

*Winding AC loss reduction techniques in  
the slot of High – frequency Electrical  
Machines*



The University of  
**Nottingham**

UNITED KINGDOM • CHINA • MALAYSIA

Anuvav Bardalai, BEng (Hons.)

Thesis submitted to The University of Nottingham for the  
degree of Doctor of Philosophy

June – 2019



Dedicated to my parents, brother and my family.

*“It is not the critic who counts; not the man who points out how the strong man stumbles, or where the doer of deeds could have done them better. The credit belongs to the man who is actually in the arena, whose face is marred by dust and sweat and blood; who strives valiantly; who errs, who comes up short again and again because there is no effort without error and shortcoming; but who does actually strive to do the deed; who knows great enthusiasms, the great devotions; who spends himself in a worthy cause; who at the best knows in the end the triumph of high achievement, and who at the worst, if he fails, at least fails while daring greatly, so that his place shall never be with those cold and timid souls who neither know victory no defeat.”*

*Theodore Roosevelt*

# ACKNOWLEDGEMENT

My first debt of gratitude must go to Professor Chris Gerada, who gave me the great opportunity to start this journey.

I would like to express my heartfelt gratitude to my supervisors Dr. David Gerada, Dr. He Zhang and Dr. Jing Li for their encouragement and patience. I am indebted and grateful to my mentors Dr. David Gerada, Dr. Xiaochen Zhang, Dr. Dmitry Golovanov and Dr. Zeyuan Xu, who are inspirational, supportive and patient. They provided the vision, encouragement and advice necessary for me to proceed through the research and complete my thesis.

I would like to thank my examiners, Dr. Michele Degano and Dr. Davide Barater, who provided encouraging and constructive feedback. I am grateful for their thoughtful and detailed comments.

I would also like express my gratitude to all those who helped and were part of the long journey towards realizing and implementing the work outlined in this thesis. Special thanks to my fellows, Dr. Weiduo Zhao, Dr. Bowen Shi, Dr. Tianhao Wang, Yuli Bao, Chuan Liu, Fengyu Zhang, Yinli Wang, Wei Dai, Tianru Zhang, Xuchen Wang and Jiaqi Li for all the great time we shared.

I am deeply thankful to my Mom, Dad and my twin brother for their love, support and sacrifices.

# ABSTRACT

In recent years, the demand for high performance electrical machines that combine high power density (kW/kg or kW/L), light – weighting and high efficiency have become more and more important. High power density reduces the volume, weight of the machines and offers great potentials to reduce cost. Increasing the rotational speed of the machines provides a straightforward solution to reduce the size of the machine. However, increasing the rotational speed increases the fundamental frequency of the machine. These elevated frequencies lead to parasitic effects such as skin and proximity effect, causing the losses in the winding to increase significantly. For traction applications, often low voltage high power density machines combined with low-cost manufacturing are desired. As such, solid straight round magnet wires are employed which offer great potential in ease of manufacturing and overall cost reduction. However, these wires are subjected to high AC losses in the high frequency operations where the machine often needs to operate. Therefore, mitigation of these AC losses in these machines have become the subject of prime importance in the recent years.

In this work, the main aim is to investigate these AC losses in the windings of a high – frequency interior permanent magnet machine and propose possible methods to mitigate the losses generated in the windings. An in-depth investigation into the effects of these losses in the winding is presented and it is shown that while the skin and proximity effects losses in the strands do not depend on the shape and position of the bundles, the circulating currents are very sensitive to the bundle shape. Using Finite Element Method, it is shown how for a given slot geometry, by selecting optimum strand diameter and winding height, the effects of AC losses in the winding

can be mitigated. A reduction of 34% of the total losses in the winding is achieved by selection of optimum strand size and winding height in the machine investigated in this thesis. Taking advantage of the advancements in 3D printing technology, slot formers with holes along the length are manufactured to achieve accurate placement of each strand to match the corresponding positions as in the FE model. With these motorettes, it is shown that FE models can be validated by experimental results. In this work, the accuracy is within 10% of the experimental test results. Using FEM, it is shown that by carefully controlling the shape of the conductors near the slot top (area of the machine slot towards the slot opening), the AC losses in the winding can be significantly reduced. In this work, a reduction of 36% in the AC losses at the active length (stack length of the machine) is achieved. It is also shown that the effect of individual strand positions within a bundle shape is not critical if the bundle shapes are fixed. Using experimental motorette setups with randomly wound winding, a relationship between copper filling factor and AC losses is presented where the trend shows that for the same strand diameter size, with increase in slot filling factor the ratio of total loss in the winding to equivalent loss if only DC was flowing ( $Total/DC$ ) increases. Comparing the motorettes with the same winding specification as of the prototype machine, this analysis shows that for random wound winding the losses in the winding can be unpredictable and with smaller strands diameters/ more strands – in – hand, the losses in the windings can be significantly high.

# List of Publications

- A. Bardalai et al., "The Influence of Strands and Bundle-Level Arrangements of Magnet Wires on AC Losses in the Winding of High — Speed Traction Machine," 2018 21st International Conference on Electrical Machines and Systems (ICEMS), Jeju, 2018, pp. 65-69.

## Accepted conference papers:

- **ICEMS 2019, Harbin, China**  
“Comparative Analysis of AC losses with round magnet wire and Litz wire winding of a High –Speed PM Machine”.
- **ISEF 2019, Nancy, France**  
“The Effects of AC Losses on Back-iron Extension Thermal Benefits”.

## Under review and planned journals:

- “Reduction of winding AC losses by accurate conductor placement in High frequency Electrical Machines”.
- “Sensitivity Analysis of AC losses in the winding of Electrical machines with varying strands – in – hand and bundle configurations”.
- “Comparative Study of AC losses in the winding of Electrical machines with fixed strands positions, fixed conductor shapes and random winding”.
- “Optimised magnet wire size and slot winding height for minimum winding loss with in – slot cooling”.
- “Practical Guideline for use of Litz Wire in High – Frequency Electrical Machines”.

# Contents

<b>ACKNOWLEDGEMENT .....</b>	<b>ii</b>
<b>ABSTRACT .....</b>	<b>iii</b>
<b>List of Publications.....</b>	<b>v</b>
<b>Contents.....</b>	<b>vi</b>
<b>List of Figures .....</b>	<b>xii</b>
<b>List of Tables.....</b>	<b>xix</b>
<b>Chapter 1.....</b>	<b>1</b>
<b>Introduction .....</b>	<b>1</b>
<b>1.1. General Introduction.....</b>	<b>1</b>
<b>1.2. Key components of PMSM .....</b>	<b>3</b>
<b>1.3. Types of stator winding.....</b>	<b>5</b>
<b>1.3.1. Random – wound stators .....</b>	<b>5</b>
<b>1.3.2. Form – wound stators .....</b>	<b>6</b>
<b>1.4. Conductors .....</b>	<b>7</b>
<b>1.4.1. Magnet Wire .....</b>	<b>7</b>
<b>1.4.2. Litz Wire .....</b>	<b>12</b>
<b>1.5. Problem Description.....</b>	<b>14</b>
<b>1.6. Aim and objective .....</b>	<b>21</b>

1.7. Key findings of the thesis .....	21
1.8. Thesis outline.....	22
<b>Chapter 2.....</b>	<b>25</b>
<b>Losses in Permanent Magnet Machines .....</b>	<b>25</b>
2.1. Core losses .....	26
2.1.1. Hysteresis Loss.....	26
2.1.2. Eddy current Loss .....	28
2.2. Copper loss in the winding.....	29
2.3. DC copper loss.....	30
2.3.1. Calculation of DC resistance .....	31
2.3.2. Calculation of winding DC resistance .....	32
2.3.3. Mitigation of DC copper loss.....	34
2.4. AC Copper Loss.....	34
2.5. Skin Effect .....	35
2.6. Proximity effect.....	38
2.7. Circulating Current Loss .....	40
2.8. Finite Element Analysis of the fundamental losses in the winding ....	44
2.8.1. Skin Effect .....	45
2.8.2. Proximity Effect.....	46
2.8.3. Circulating Current .....	47
<b>Chapter 3.....</b>	<b>50</b>

<b>Sensitivity Analysis of AC losses with varying ‘strands – in – hand’ and bundle shape .....</b>	<b>50</b>
<b>3.1. Specification of the prototype machine.....</b>	<b>50</b>
<b>3.2. Methodology .....</b>	<b>52</b>
<b>3.2.1. Description .....</b>	<b>52</b>
<b>3.2.2. Calculation of DC loss in the winding .....</b>	<b>54</b>
<b>3.2.3. Calculation of AC + DC losses in the winding .....</b>	<b>54</b>
<b>3.2.4. Mitigation of circulating current .....</b>	<b>55</b>
<b>3.3. Horizontal Arrangement (ARR1) .....</b>	<b>56</b>
<b>3.3.1. Losses in conductors.....</b>	<b>57</b>
<b>3.3.2. (AC+DC) /DC Loss ratio.....</b>	<b>59</b>
<b>3.3.3. Investigating the effect of circulating current .....</b>	<b>60</b>
<b>3.3.4. Comparison of the cases.....</b>	<b>67</b>
<b>3.4. Vertical Bundled (ARR2).....</b>	<b>72</b>
<b>3.4.1. Losses in the conductors .....</b>	<b>72</b>
<b>3.4.2. Investigating the effect of circulating current in Vertical bundled configuration.....</b>	<b>74</b>
<b>3.4.3. Conclusion.....</b>	<b>77</b>
<b>3.5. Horizontal Bundled (ARR3) .....</b>	<b>77</b>
<b>3.6. Comparison of loss components in the configurations.....</b>	<b>78</b>
<b>3.7. Proof for <math>P_{Total} = P_{DC} + P_{skin\ and\ proximity} + P_{circulating\ current}</math> .....</b>	<b>81</b>
<b>3.8. Conclusion .....</b>	<b>84</b>

<b>Chapter 4.....</b>	<b>85</b>
<b>Optimisation of winding height in the slot for minimum winding loss .....</b>	<b>85</b>
<b>4.1. Model Simplification .....</b>	<b>85</b>
<b>4.1.1. Investigation of big discrepancy between the 3 slot 1 phase stranded model and the baseline model .....</b>	<b>88</b>
<b>4.1.2. Comparison of 1 slot stranded model with the baseline model ...</b>	<b>91</b>
<b>4.2. Methodology .....</b>	<b>93</b>
<b>4.3. FEM Results .....</b>	<b>97</b>
<b>4.3.1. Height (H1).....</b>	<b>97</b>
<b>4.3.2. Height (H2).....</b>	<b>101</b>
<b>4.3.3. Height (H3).....</b>	<b>104</b>
<b>4.3.4. Height (H4).....</b>	<b>108</b>
<b>4.3.5. Height (H5).....</b>	<b>113</b>
<b>4.4. Comparison and discussion .....</b>	<b>116</b>
<b>Chapter 5.....</b>	<b>120</b>
<b>Experimental validation of finite element modelling .....</b>	<b>120</b>
<b>5.1. Motorette with 33 ‘strands – in – hand’ .....</b>	<b>120</b>
<b>5.2. Motorette with slot formers .....</b>	<b>126</b>
<b>5.2.1. Motorette 1 .....</b>	<b>127</b>
<b>5.2.2. Motorette 2 .....</b>	<b>136</b>
<b>5.3. Conclusion .....</b>	<b>141</b>
<b>Chapter 6.....</b>	<b>142</b>

<b>The Influence of bundle shapes and positions on the AC losses in the slot....</b>	<b>142</b>
<b>6.1. Methodology .....</b>	<b>142</b>
<b>6.1.1. Selection of optimum strand diameter .....</b>	<b>142</b>
<b>6.1.2. Clustering of strands into bundles and positioning.....</b>	<b>143</b>
<b>6.2. Finite – Element model (15 parallel strands) .....</b>	<b>145</b>
<b>6.3. Validation .....</b>	<b>151</b>
<b>6.3.1. FE Modelling and Analysis.....</b>	<b>152</b>
<b>6.3.2. Experimental validation.....</b>	<b>158</b>
<b>6.4. Conclusion .....</b>	<b>162</b>
<b>Chapter 7.....</b>	<b>163</b>
<b>Experimental Analysis .....</b>	<b>163</b>
<b>7.1. Comparative analysis of fixed strands positions and fixed conductor shapes motorette .....</b>	<b>163</b>
<b>7.2. Relationship between copper filling factor and AC losses .....</b>	<b>169</b>
<b>Chapter 8.....</b>	<b>176</b>
<b>Conclusion and Future Works .....</b>	<b>176</b>
<b>References .....</b>	<b>181</b>
<b>APPENDICES .....</b>	<b>188</b>
<b>Appendix – A .....</b>	<b>188</b>
<b>Appendix – B.....</b>	<b>189</b>
<b>Calculation of DC resistance.....</b>	<b>189</b>
<b>Appendix – C .....</b>	<b>190</b>

<b>C 1. Specifications of Programmable AC power supply (chroma 61511)</b>	<b>190</b>
<b>C 2. Specification of Precision Power Analyzer (PPA 5530) [67]</b>	<b>192</b>
<b>C 3. Wiring configuration of PPA 5530</b>	<b>194</b>
<b>C 4. Specification of Precision Impedance Analyzer (KEYSIGHT E4990A)</b>	<b>198</b>
<b>Appendix – D</b>	<b>199</b>

# List of Figures

- Fig. 1.1: Exploded view of PMSM. [5]
- Fig. 1.2: Stator lamination showing various sections
- Fig. 1.3: Cross section of a trapezoidal shaped slot in a random – wound stator
- Fig. 1.4: Cross section of a rectangular shaped slot with form - wound rectangular conductors
- Fig. 1.5: (a) Insulated round magnet wire, (b) Insulated square magnet wire, (c) Insulated rectangular magnet wire
- Fig. 1.6: Slot – filling comparison with round and square magnet wire
- Fig. 1.7: Hairpin winding stator assembly
- Fig. 1.8: Breakdown Voltage of different grades of magnet wire for varied nominal diameter
- Fig. 1.9: Percentage of total strand area occupied by the insulation coat (Grade 2)
- Fig. 1.10: Litz wire [11]
- Fig. 1.11: Roadmap laid by Advanced Propulsion Centre, UK [20].
- Fig. 1.12: Electrical Machine Roadmap laid by Advanced Propulsion Centre, UK [20].
- Fig. 2.1: Isometric view of stator motorette
- Fig. 2.2: Skin effect in a conductor
- Fig. 2.3: Proximity effect [47]
- Fig. 2.4: Finite – element analysis of Skin effect in strand

- Fig. 2.5: Proximity effect in the strands (a) with no supply current in strand 2, (b) with supply current in same direction for both strands, (c) with current in the opposite directions
- Fig. 2.6: (a) Model for investigating circulating current, (b) circuital representation of the connection in model, (c) Flux function and current density in the strands
- Fig. 2.7: Waveforms of the individual current in the strands and the source current
- Fig. 3.1: Prototype of the traction machine (M1)
- Fig. 3.2: Cross – sectional view of the prototype machine
- Fig. 3.3: Quarter section model of the prototype machine with strand – level winding
- Fig. 3.4: (a) Horizontal, (b) Vertical bundled, (c) Horizontal bundled
- Fig. 3.5: Circuital representation of the strands and bundle connections in the models with (a) single source supply and (b) multi - source supplies
- Fig. 3.6: (a) Losses in individual conductors with varied number of parallel strands, (b) total losses in the machine winding with varied parallel strands
- Fig. 3.7:  $(AC+DC) / DC$  loss ratio (ARR1)
- Fig. 3.8: Supply current to the phase - one of winding
- Fig. 3.9: Individual strand currents for model with varying number of parallel strands
- Fig. 3.10: Losses in conductors with single and multi – source supply for model with 4 parallel strands

- Fig. 3.11: Individual strand current with multi – source supply in 4 parallel strands model
- Fig. 3.12: Losses in conductors with single and multi – source supply for model with 6 parallel strands
- Fig. 3.13: Losses in conductors with single and multi – source supply for model with 13 parallel strands
- Fig. 3.14: Losses in conductors with single and multi – source supply for model with 24 parallel strands
- Fig. 3.15: Breakup losses in the winding (CASE 1 and CASE 3)
- Fig. 3.16: Breakup losses in the winding (CASE 2 and CASE 4)
- Fig. 3.17: Trend of skin & proximity losses and circulating current losses with increasing number of parallel strands
- Fig. 3.18: Models with vertical bundled strands
- Fig. 3.19: Losses in individual conductors with varied number of parallel strands (Ver. Bundled)
- Fig. 3.20: (a) 3 – ph current source waveform, (b) 6 strands single source current density (J) in strands (0.00194s), and (c) 6 strands multi - source current density (J) in strands (0.00194s)
- Fig. 3.21: (a) 24 strands single source current density (J) in strands (0.00194s), (b) 24 strands multi - source current density (J) in strands (0.001934s)
- Fig. 3.22: Horizontal bundled configuration with 6 parallel strands
- Fig. 3.23: 6 parallel strands model with (a) Horizontal, (b) Vertical bundled, (c) Horizontal bundled

- Fig. 3.24: Breakup of losses in the winding into its components for ARR1, ARR2 and ARR3
- Fig. 4.1: Comparison of different modelling depth for simplification of modelling
- Fig. 4.2: Waveform of the 3-phase source current in baseline model
- Fig. 4.3: Flux distribution inside the slot (at time instant 0.00268s)
- Fig. 4.4: Current density distribution in the strands (at time instant 0.00268s)
- Fig. 4.5: Waveform of strand currents in (a) 3 slots 3 phases model, (b) 3 slots 1 phase stranded model
- Fig. 4.6: 1 slot stranded model with flux tangential boundary conditions on the teeth side
- Fig. 4.7: (a) Waveform of 3 phase source current with timeline marked at 0.0018s, (b) Flux density  $|B|$  in baseline model, (c) Flux density  $|B|$  in 1 slot stranded model, (d) Comparison of Flux density  $|B|$  inside the slot of 1 slot stranded model with the baseline model at time instant 0.0018 s
- Fig. 4.8: Representation of a slot geometry with woundable area ABCD
- Fig. 4.9: Representation of strand layout in slot geometry
- Fig. 4.10: (a) Representation of clustered strands into bundles, (b) Model with 27 strands – in – hand clustered together to form bundles
- Fig. 4.11: Reduction of winding height from  $H_1$  to  $H_n$
- Fig. 4.12: Slot filling factor against the strand outer diameter ( $H_1$ )
- Fig. 4.13: Models used for analysis for height  $H_1$
- Fig. 4.14: Losses in the conductors for models of  $H_1$
- Fig. 4.15: Slot filling factor against the strand outer diameter ( $H_2$ )

- Fig. 4.16: Models used for analysis with slot height H2
- Fig. 4.17: Slot filling factor against the strand outer diameter (H3)
- Fig. 4.18: Models used for analysis with slot height H3
- Fig. 4.19: Slot filling factor against the strand outer diameter (H4)
- Fig. 4.20: Models used for analysis with slot height H4
- Fig. 4.21: Slot filling factor against the strand outer diameter (H5)
- Fig. 4.22: Models used for analysis with slot height H5
- Fig. 4.23: Comparison of losses in components for varying slot heights (with maximum total losses for each winding height)
- Fig. 4.24: Comparison of losses in components for varying slot heights (with minimum total losses for each winding height)
- Fig. 5.1: 3D rendering of experimental motorette
- Fig. 5.2: Schematic diagram of the experimental setup
- Fig. 5.3: Representation of circuitual connection of the motorette in the experimental setup
- Fig. 5.4: Experimental setup with test motorette (33 strands – in – hand random winding)
- Fig. 5.5: Motorette representation for FEA
- Fig. 5.6: Experimental total losses in the motorette at various frequencies for different current amplitude
- Fig. 5.7: Render of motorette slot former
- Fig. 5.8: Arrangement of strands in the slots of motorette 1
- Fig. 5.9: Experimental motorette 1
- Fig. 5.10: Waveform of strand currents and supply current in motorette 1
- Fig. 5.11: Flux density  $|B|$  in the teeth and back iron of the motorette

- Fig. 5.12: Measurement of AC resistance of the motorette winding with impedance analyser
- Fig. 5.13: AC resistance of the coils in the motorette as function of frequency
- Fig. 5.14: Former used for Motorette 2
- Fig. 5.15: Experimental Motorette 2
- Fig. 5.16: Conductor positions and layout in motorette 2
- Fig. 5.17: Measured resistance of the components in motorette 2 using impedance analyser
- Fig. 6.1: Representation of strand layout in the slot geometry
- Fig. 6.2: Representation of the clustering and positioning process
- Fig. 6.3: Half side of a slot showing plausible versions of conductor positions
- Fig. 6.4: (a) Losses in the conductors, (b) Average loss in the conductors
- Fig. 6.5: Comparison of strands currents in Version #3 and #4 along with supply current
- Fig. 6.6: Comparison of current density ( $J$ ) in the strands (0.00294 s)
- Fig. 6.7: (a) Conductor 9 and 10 in Version #3, (b) Conductor 9 and 10 in Version #4, and (c) Average value of flux density  $|B|$  in the quadrants
- Fig. 6.8: Representation of motorette used for experimental validation
- Fig. 6.9: Half side of the slot showing various cases with plausible conductor positions
- Fig. 6.10: Representation of circuitual connections of strands in the validation motorette
- Fig. 6.11: (a) Average value of flux density  $|B|$  in the quadrants, (b) Conductor 7 and 8 in CASE #2, (c) Conductor 7 and 8 in CASE #5
- Fig. 6.12: Comparison of strand currents in conductor 8 for CASE #2 and #5

- Fig. 6.13: Front and Isometric views for 3D printed former used within experimental validation
- Fig. 6.14: A wound motorette with slot formers
- Fig. 6.15: AC resistance of connecting cable
- Fig. 6.16: Schematic diagram of experimental setup showing equipment and connection
- Fig. 6.17: Views of experimental setup showing various equipment used in the tests along with the test motorette
- Fig. 7.1: Motorette with fixed strand positions (CASE A)
- Fig. 7.2: Formers and motorette with fixed conductor shapes (CASE B)
- Fig. 7.3: Strands and conductor shapes in motorette (a) CASE A, (b) CASE B
- Fig. 7.4: Experimental Motorette with varied Cu. Filling Factor
- Fig. 7.5: Comparison of Total/DC Loss ratio of the motorettes
- Fig. C1: KEYSIGHT Impedance Analyzer (E4990A) [68]

# List of Tables

- TABLE 1.1:** Temperature Class of magnet wire
- TABLE 1.2:** Temperature Class and insulation material
- TABLE 3.1:** Machine Parameters
- TABLE 3.2:** Specification of components in slot
- TABLE 3.3:** Dimensions of the strands
- TABLE 3.4:** Losses in the conductors for models with varied number of parallel strands (ARR1)
- TABLE 3.5:** (AC+DC) /DC loss ratio (ARR1)
- TABLE 3.6:** Deviation of strand currents
- TABLE 3.7:** Comparison of losses in conductors using single and multi – source current supply (CASE 1)
- TABLE 3.8:** Comparison of losses in conductors using single and multi – source current supply (CASE 2)
- TABLE 3.9:** Comparison of losses in conductors using single and multi – source current supply (CASE 3)
- TABLE 3.10:** Comparison of losses in conductors using single and multi – source current supply (CASE 4)
- TABLE 3.11:** AC Loss in percentage of total loss in the winding of the machine
- TABLE 3.12:** Peak current in strand due to circulating current
- TABLE 3.13:** Losses in conductors for models with varied parallel strands (Ver. Bundled)

- TABLE 3.14:** (AC+DC)/DC loss ratio (Ver. Bundled)
- TABLE 3.15:** Comparison of losses in conductors using single and multi – source current supply (CASE A)
- TABLE 3.16:** Comparison of losses in conductors using single and multi – source current supply (CASE B)
- TABLE 3.17:** Comparison of losses in the conductors and AC+DC/DC loss ratio with single and multi – source current supplies (Hor. Bundled)
- TABLE 3.18:** Comparison of loss components for ARR1, ARR2 and ARR3
- TABLE 3.19:** Comparison of segregated loss components to DC loss ratio for the winding arrangements
- TABLE 3.20:** Verification using some of the models
- TABLE 4.1:** Comparison of models' losses and percentage difference from baseline model
- TABLE 4.2:** Strand diameters with high fill factor for H1
- TABLE 4.3:** Losses in the winding of the machine (H1)
- TABLE 4.4:** Strand diameters with high fill factor for H2
- TABLE 4.5:** Losses in the winding of the machine (H2)
- TABLE 4.6:** Strand diameters with high fill factor for H3
- TABLE 4.7:** Losses in the winding of the machine (H3)
- TABLE 4.8:** Strand diameters with high fill factor for H4
- TABLE 4.9:** Losses in the winding of the machine (H4)
- TABLE 4.10:** Strand diameters with high fill factor for H5
- TABLE 4.11:** Losses in the winding of the machine (H5)

- TABLE 4.12: Comparison of losses in components for varying slot height (maximum total losses of each slot winding height)**
- TABLE 4.13: Comparison of losses in components for varying slot height (minimum total losses of each slot winding height)**
- TABLE 5.1: Specification of motorette**
- TABLE 5.2: Experimental Losses of motorette**
- TABLE 5.3: Comparison of experimental loss and modelling loss**
- TABLE 5.4: Specification of slot in motorette 1**
- TABLE 5.5: DC Losses in the components**
- TABLE 5.6: Comparison of measured total loss and modelling loss**
- TABLE 5.7: Comparison of losses calculated from AC resistance with simulation loss**
- TABLE 5.8: Specification of slot former in motorette 2**
- TABLE 5.9: Comparison of measured total loss and modelling loss (motorette 2)**
- TABLE 6.1: Comparison of total loss to DC loss**
- TABLE 6.2: Comparison of strands currents**
- TABLE 6.3: Specification of validation motorette**
- TABLE 6.4: Comparison of Total / DC Loss in Active Machine Length**
- TABLE 6.5: Losses in Motorette CASE #2**
- TABLE 6.6: Losses in Motorette CASE #5**
- TABLE 7.1: Specifications of parameters used in the slot**
- TABLE 7.2: Comparison of measured losses in motorette with winding configurations CASE A and CASE B**

**TABLE 7.3: Specifications in the slot for motorettes with varied Copper filling factor**

**TABLE 7.4: Comparison of losses in the motorettes with varied Cu. Filling Factor**

## Chapter 1

# Introduction

## 1.1. General Introduction

Increasing prosperity in developing economies has led to an increased transportation demand. Global demand for both passenger and freight transport services are forecasted to be more than double by 2040 which is consistent across road, aviation and marine [1]. Despite increase in use of alternative fuels, particularly natural gas and electricity, the transport sector is still dominated by oil. In forecasted Evolving Transition (ET) scenario [1], oil demands accounts for around 85 percent of total transport fuel demand in 2040 while the natural gas, electricity and combination of ‘other’ types of fuels such as biofuels and hydrogen are projected to account for approximately 5 percent of transport fuel.

As such, the main challenges the contemporary world faces today, (i) increased emissions, including greenhouse gas emissions, (ii) increased energy demand versus limited non – renewable energy resources and rising prices.

To counter the challenges of emissions, the governments around the world are introducing stringent emissions standards. For example (e.g.), the Euro 6/VI vehicle emission standards. 90 percent of global vehicle sales are in the G – 20 countries, out of which 17 members follow the European regulatory pathway for vehicle emissions control [2]. Car manufacturers have chosen to satisfy these emission standards by making efficiency improvements and investing into research and

innovation on the propulsion systems. To counter the challenges of limited non – renewable resources and to achieve a sustainable transportation, national and international policy makers have been promoting greener vehicles in the recent decade. The Electric Vehicles Initiative (EVI) and EV30@30 campaign are two of such forums dedicated to accelerating the deployment of electric vehicles worldwide [3]. EVs such as Plug – in Hybrids Electric Vehicles (PHEVs) and Battery Electric Vehicles (BEVs) for road transport boost energy efficiency by using high efficiency electric – drive systems and contribute to a wide range of transport goals such as enhanced energy security, better air quality, less noise and reduced greenhouse gas emissions (in conjunction with low – carbon power generation mix).

Rotating electrical machine is one of the main components in an EV. The permanent magnet synchronous machine (PMSM) has stand out as one of the suitable candidates for traction requirements due to combination of several advantages such as high efficiency, high power factor, high torque density, high overload capability, robustness, reduced maintenance, compactness and low weight. Apart from that, the absence of rotor copper loss allows for increase in the efficiency while high energy PM excitation allows for reduced overall volume or weight. Flux – weakening capability of the PM machine allows for operating in wider range of speed. However, the PM excitation has certain drawbacks, such as risk of demagnetisation at high temperature and relatively higher cost of rare – earth permanent magnets [4].

## 1.2. Key components of PMSM

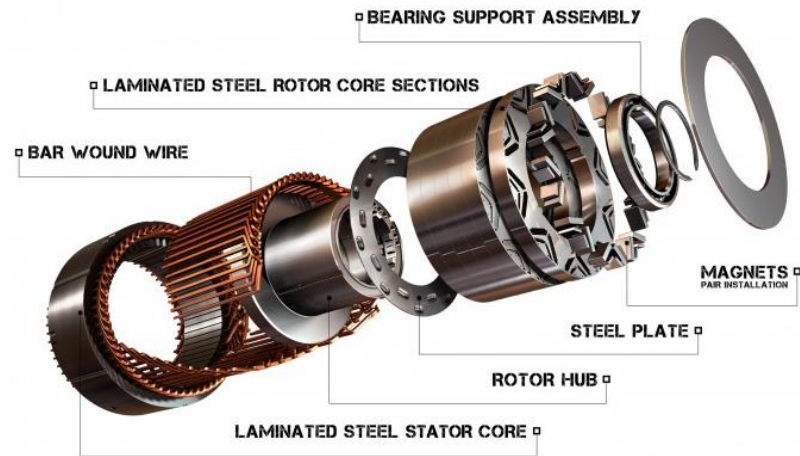


Fig.1.1: Exploded view of PMSM. [5]

Fig. 1.1 shows an exploded view of a PMSM. The key electromagnetic components of the machine are the laminated stator core, the armature winding, the laminated rotor core and the rotor magnets. The bearing support assembly, the steel plate, the rotor hub and the housing constitute the mechanical components of the machine. The housing provides support for the stator core and protect the machine components from foreign objects such as water, dust, sand and moisture. In addition to these components, the machine also employs some kind of cooling techniques to extract the heat losses. This can be passive cooling for motors with low power losses and low thermal load conditions. In this case, motor cooling primarily relies on heat conduction to transport the generated heat from the heat sources (e.g. stator winding) to the motor frame (e.g. motor housing) and then to dissipate the heat to the environment by natural convection and radiation (usually by employing various cooling fins on the external surfaces of the motor housing and endbells). In contrast, for modern motors with high power density and consequently high-power losses, active cooling is required to remove the waste heat produced. The active cooling

techniques require the use external devices such as fans, blowers, and pumps to force coolant (air or liquid) flowing through cooling channels either inside or outside, or both, of the motor [6].

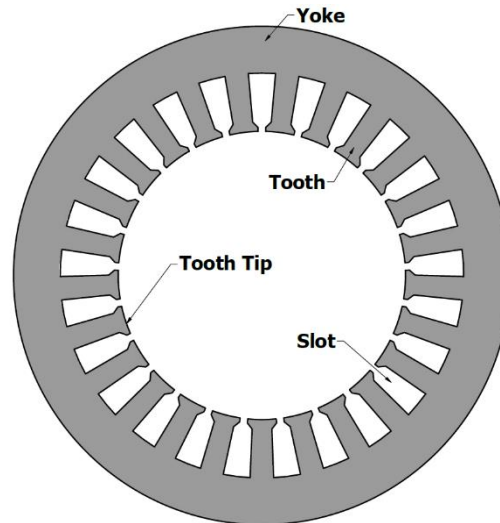


Fig. 1.2: Stator lamination showing various sections

The stator typically forms the outer body of an electric machine. It is made up of a stack of laminated steel with the inner surface usually having deep slots or grooves, which are distributed uniformly or non - uniformly in the circumferential direction. Stator windings are positioned into these slots. The sections adjacent to these slots are the teeth and the area that is radially outwards from the slots connecting the teeth is the yoke of the stator. The teeth and the yoke together form the stator core of the machine. The windings, the stator core and the insulation form the three main components in a stator. The winding and the core form the active part of the stator; creating a rotating magnetic field and concentrating the magnetic flux, respectively. The insulation is the passive component of the core. Fig. 1.2. shows a stator core lamination with its different components.

### 1.3. Types of stator winding

There are two basic types of stator winding structures employed in PMSM:

#### 1.3.1. Random – wound stators

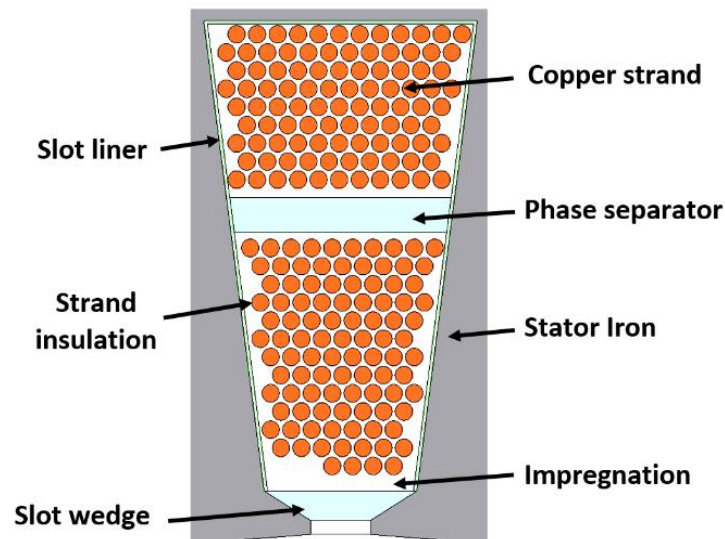


Fig. 1.3: Cross section of a trapezoidal shaped slot in a random – wound stator

Random – wound stators are typically used for machines with power rating less than several hundreds of kilowatts and operating at voltage levels less than 1000 V. Fig. 1.3. shows the cross section of a trapezoidal shaped slot in a random – wound stator. The components in the slot of a random – wound stator are the copper conductors, the slot liners, the phase separator, the wedge and the impregnation material. The round, insulated copper conductors (magnet wires) are continuously wound (usually by hand or in a former using a winding machine) through the slots in the stator core to form a coil. The slot liner provides ground insulation between the current carrying copper coils and the grounded stator slot and prevent partial discharge from happening. As the name suggest, the coil separator is to insulate the coils of the different phases in the slot. The wedge at the top of the slot is used to hold the magnet wires in place and prevent them from coming out through the slot

opening. For random – wound stator, the most common insulation for slot liners, the phase separators and the wedges are sheet of “paper” made from synthetic material “aramid”. DuPont is a major supplier of this insulation paper and uses the trade name Nomex™. Nomex is resistant to chemical attack, has excellent tear resistance and has a thermal class of 220°C. The paper thickness varies from 0.1 mm to 0.5 mm depending on the voltage class of the machine. In random – wound stator, after the coils are inserted into the slots, the stator core is impregnated with a varnish or resin. This impregnating coat imparts resistance to moisture and contamination and improves the electrical breakdown strength of the windings. The impregnation improves the transmission of heat from the windings to the stator core. In addition, this impregnating material holds the conductors tight in the slot and reduces the tendency to move/vibrate under the magnetic forces [7].

### 1.3.2. Form – wound stators

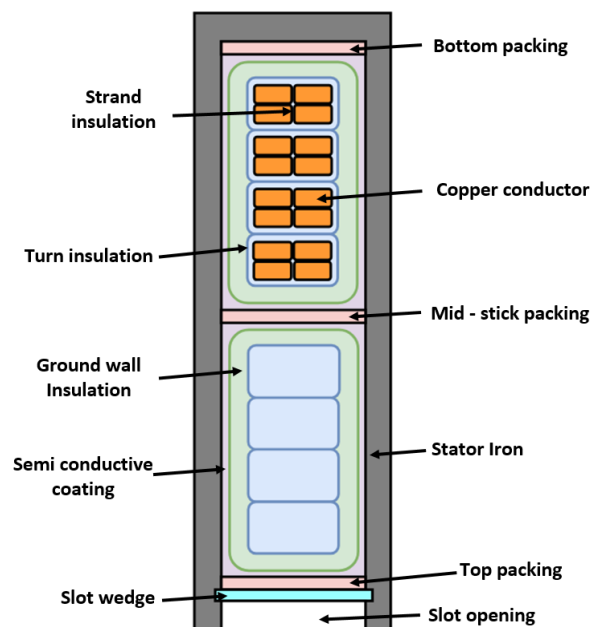


Fig. 1.4: Cross section of a rectangular shaped slot with form - wound rectangular conductors

Fig. 1.4. shows the cross section of a rectangular shaped slot with form – wound coils made of rectangular conductors. Form – wound stators are usually intended for machines operating at 1000 V and above. The windings are made from insulated rectangular magnet wire preformed and shaped into a coil before its insertion into the slots. In addition to the strand insulation, each turn is insulated with turn insulation to prevent shorts between the turns in a coil. The function of groundwall insulation is similar that of slot liners in random – wound stator slot and separates the copper conductor from the grounded stator core. However, in case of form – wound stators, the groundwall insulation has to endure rigorous electrical, thermal and mechanical stresses. In addition to that, a semi conductive stress relief coating is applied in the slot area, which is partially conductive and is usually a graphite – loaded paint or tape. This coating is essentially at ground potential because of contact with the core and prevents any partial discharge from occurring.

## **1.4. Conductors**

### **1.4.1. Magnet Wire**

The most common type and widely used electrical conductors for fabricating stator windings in small and medium sized electric motors is magnet wire. Magnet wire consists of a base metal (usually copper or aluminium) wire coated with a thin one – or multilayer of insulation materials such as enamel, fibrous polyester, fibreglass yarn, and polyamide. The insulation materials on the magnet wire allow winding wires to contact each other without forming electrical short circuits between them. The selection of the magnet wire is based on the motor operating conditions (working frequency, current, voltage, temperature, etc.), wire material properties,

wire diameter for allowing maximum current density, thermal class, coating material, thickness of coating layer, and others.

The following are the most important features of magnet wire:

- a) Small and uniform insulation thickness
- b) Good electrical characteristics such as dielectric strength and insulation resistance
- c) Tough coating, resistant to external forces such as bending, stretching and friction
- d) Heat – resistance
- e) Resistant to solvents, chemical and varnishes
- f) Resistant to hydrolytic degradation
- g) Stable when combined with insulating material
- h) Resistant to water and moisture
- i) Easy to use

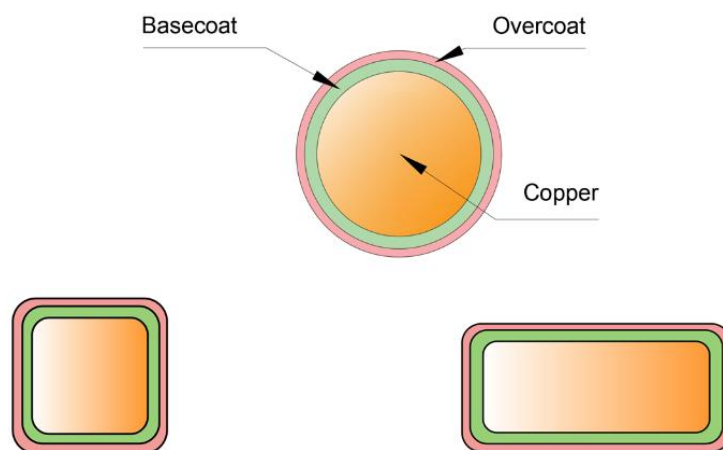


Fig. 1.5: (a) Insulated round magnet wire, (b) Insulated square magnet wire, (c) Insulated rectangular magnet wire

Fig. 1.5. shows several cross – sectional shapes of magnet wires available for stator windings. The most common magnet wire for random – wound stators in use

today is a round copper wire insulated with a polyamide – imide insulation (Class 200°C) or polyester with a polyamide – imide overcoat. The insulation thickness varies from 0.05 mm to 0.1 mm. In some magnet wires, there is an additional adhesive enamel overcoat that which has a bonding feature. When the adhesive is activated by heat or solvent, the bond coating cements the winding turn – to – turn to create a compact self – supporting coil. NEMA MW 1000, JIS C – 3202, and IEC – 60317 – 0 – 01 are commonly used standards for magnet wires.

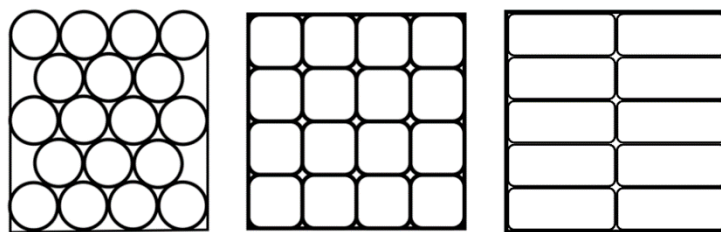


Fig. 1.6: Slot – filling comparison with round and square magnet wire

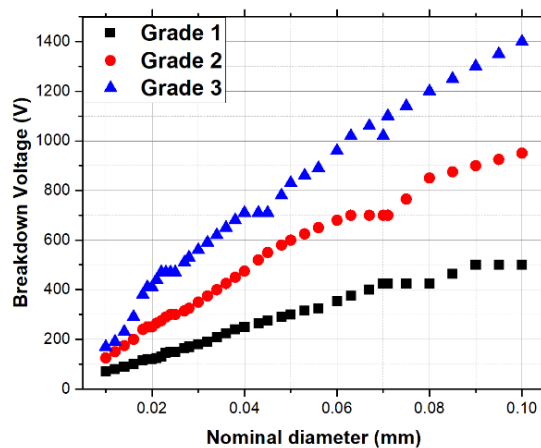
The use of square or rectangular wires can significantly increase the slot – filling factor as shown in fig. 1.6. One such example is hairpin winding shown in fig. 1.7. Apart from higher slot fill factor, it offers the advantages such as shorter end turns, easy cooling and easier and fully automatic manufacturing [8]. However, when these bar conductors are used in high frequency applications, the bulky conductors induce addition losses due skin effect, which causes the current to flow only though the outer surface of the conductors.



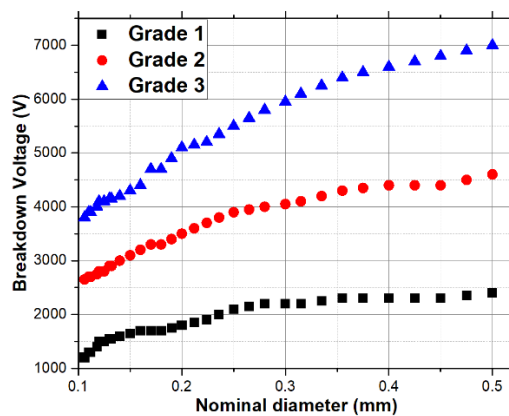
Fig. 1.7: Hairpin winding stator assembly

### A. Classification of Magnet wire

Magnet wire is classified based on diameter (American Wire Gauge (AWG) number, British Standard Wire Gauge (SWG) or millimetres or area (square millimetres), insulation class and temperature class. Based on the breakdown voltage level, which effects the thickness of the insulation overcoat on the magnet wire, it is classified as Grade 1, Grade 2 and Grade 3, with Grade 1 having the weakest endurance level of breakdown voltage. The higher the grade, the thicker the insulation and thus higher the breakdown voltage. Fig 1.8 shows the Breakdown Voltage (BDV) of different grades of the magnet wire and varied nominal diameter (according to IEC 60 317 [7]).



(a) BDV for nom. dia. 0.01 to 0.1 mm



(b) BDV for nom. dia. 0.106 to 0.5 mm

Fig. 1.8: Breakdown Voltage of different grades of magnet wire for varied nominal diameter

Based on thermal endurance capacity, magnet wire is classified as [8], [9]:

**TABLE 1.1: Temperature Class of magnet wire**

CLASS	TEMPERATURE (°C)
O	90
A	105
E	120 (IEC)
B	130
F	155
H	180
200 (K)	200
220 (M)	220
C	240+
250	250 (IEC)

Materials used in the temperature classes are as follows:

**TABLE 1.2: Temperature Class and insulation material**

TEMPERATURE CLASS	INSULATION TYPES
90	PAPER
105	PAPER, COTTON, NYLON, POLYVINYL ACETAL, FORMVAR
105 SOLDERABLE	POLYURETHANE
130	EPOXY
130 SOLDERABLE	POLYURETHANE
155	POLYESTER, GLASS
155 SOLDERABLE	POLYURETHANE
180	POLYESTER
180 SOLDERABLE	PLOYESTER IMIDE, POLYURETHANE
200	PLOYESTER/AMIDE IMIDE, AI
220	AMIDE – IMIDE
240	POLYIMIDE

It is worth noting that the magnet wire thickness insulation does not depend on the temperature classes of the magnet wire but depends on the breakdown voltage i.e. if a strand diameter of a specific grade is selected, the insulation thickness will remain the same across all thermal classes of that explicit wire diameter.

### B. Insulation versus strand diameter

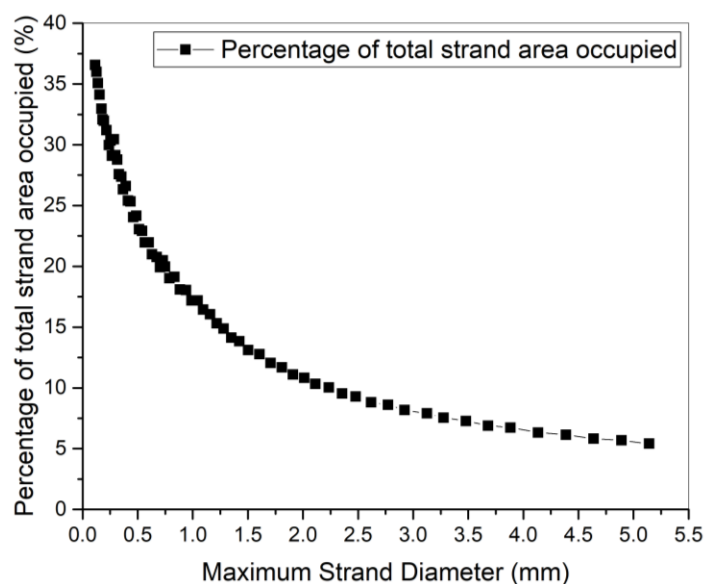


Fig. 1.9: Percentage of total strand area occupied by the insulation coat (Grade 2)

In fig. 1.9, the abscissas show the total diameter (conductor area + insulation area) of strands and the axis of ordinates shows the percentage of total strand area that is being occupied by the insulation coat on it. With the smallest strand diameter of 0.113 mm, the insulation coat occupied about 36% of the total strand area. The area occupied by insulation decreases exponentially as the strand diameter increases. For largest strand diameter considered in the plot of 5.141 mm, the insulation only occupies approximately 5.4% of the total strand area. Thus, using larger cross – sectional magnet wire, better slot filling factor can be achieved. The data used in the plot is acquired from a standard magnet wire catalogue [10]. Grade 2 magnet wire is used for the aforementioned analysis.

#### 1.4.2. Litz Wire

Litz wire is constructed from thin individual insulated magnet wires intertwined into a uniform pattern as shown in fig. 1.10.

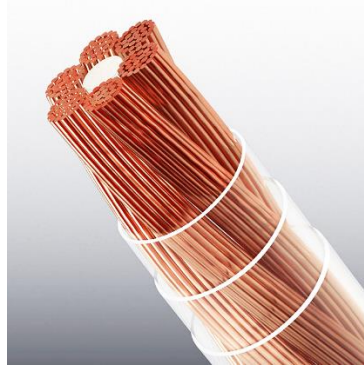


Fig. 1.10: Litz wire [11]

Litz wire is essentially used for high – frequency applications. It utilises the full cross – sectional area of the wire to carry current. Because each individual strand is thinner than the skin depth, the use of Litz wire can greatly minimise the skin and proximity effect losses in high – frequency windings. However, when used in high performance electrical machines operating in demanding environments, Litz wires have some manufacturing and assembling disadvantages such as [6], [12]:

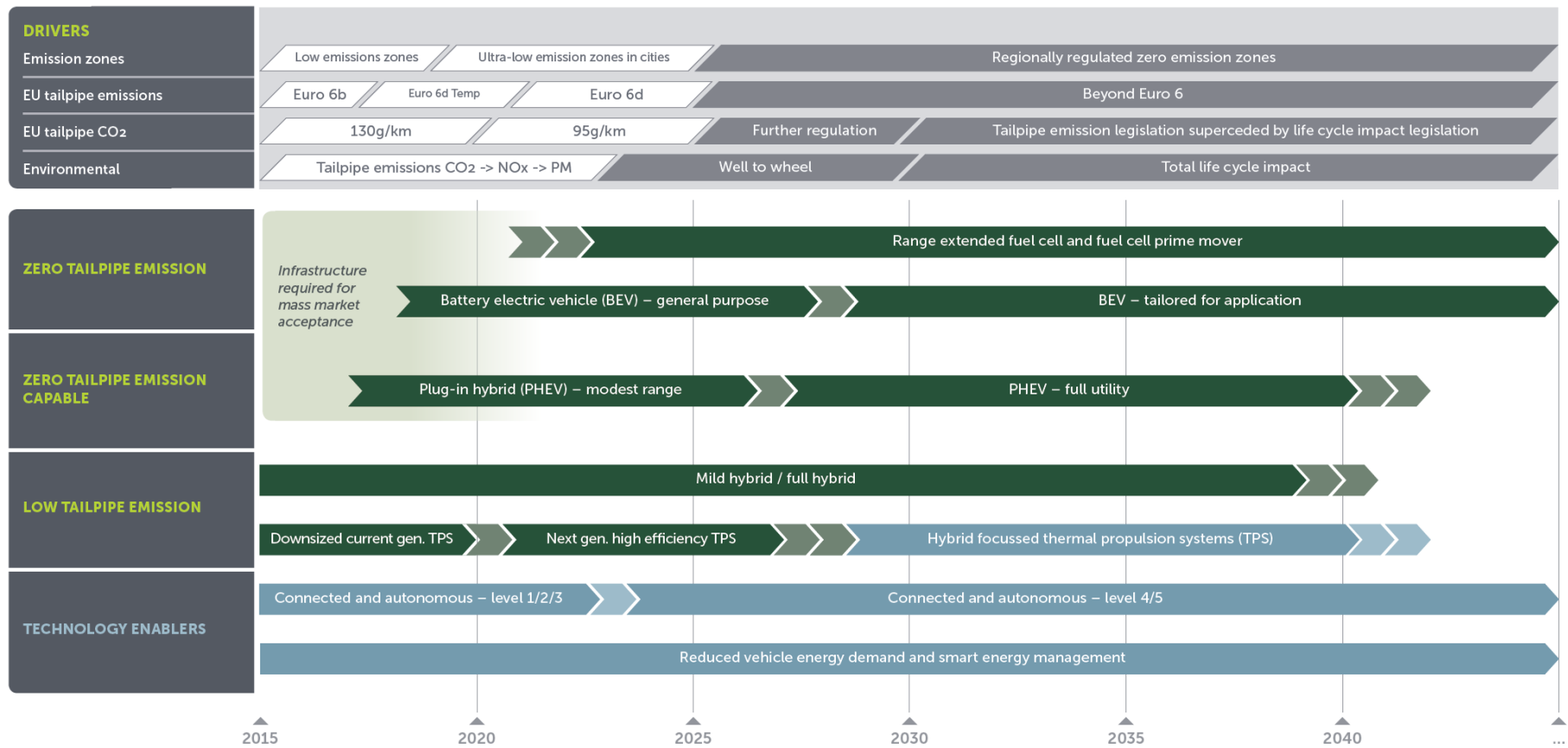
- a) It is difficult to ensure full impregnation of varnish because strands are closely knit.
- b) Encasing layer of insulation layer is often required to ensure a high degree of inter – coil insulation integrity as the insulation layer on the individual wire strands is very thin.
- c) The manufacturing cost of Litz wire is higher as compared to conventional round magnet wires
- d) Litz winding has a low copper fill factor and poor heat transfer across the winding bundle in comparison to winding former from single conductor turns.

## 1.5. Problem Description

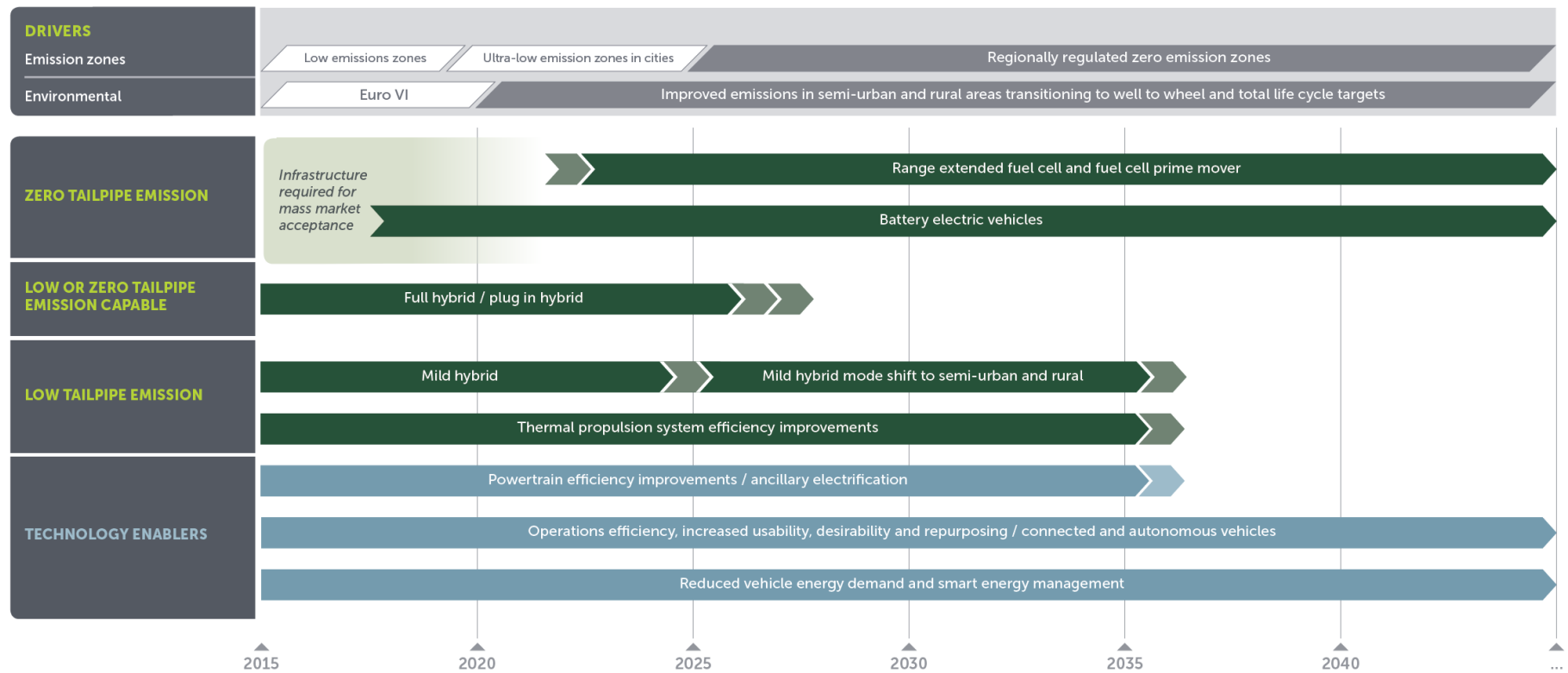
Increasing demands and widespread adoption of electrical drives in aircraft, automobiles and machine tools have intensified the efforts in design and development of high-performance electrical machines that combine high power density (kW/kg or kW/L), light-weighting and high efficiency [13]. With the majority of the power loss within high power density electrical machines often being generated in the stator winding [14], it is necessary to reduce the copper losses and improve the heat transfer mechanisms for such losses. One general way of reducing the copper losses is by maximizing the slot filling and achieving better thermal conductivity within the slot [15]. Using rectangular conductors, with higher cross-sectional areas and evenly laying them around segmented stator teeth in the form of preformed coils, coupled with the use of higher thermal conductivity materials can result in achieving the best slot fill and a good thermal performance [16]. However, the problem with the use of such bulky conductors in high frequency applications is that, the increase in apparent resistance of the windings is quite significant and the copper loss is many folds larger than the DC copper loss. The higher concentration of these added losses due to AC effects is usually accompanied by higher localised temperature variations [14], [17], [18], and earlier winding failures. The main cause for winding failure is deterioration of insulation property. It is been reported that 30% of motor failures are due to insulation failure, 60% of which are caused by overheating. For every 10°C of additional heat to the windings, the insulation lifetime is halved [19]. Traditionally, to mitigate the loss associated with AC effects in bulk conductors, the solution is to split the large conductor cross-section into smaller sections using thin magnet wires connected in parallel. These magnet wires are then randomly inserted into the slot to fill up the slot area. The effects of AC in

the windings of the smaller machines has been mostly neglected or given secondary concern. This is especially true for machines with random – wound winding. The presence of slot flux – leakage that links each individual strands of the conductor differently causes the impedance of the individual strands to differ. This result in uneven current sharing among the parallel strands or ‘strands – in – hand’ of a conductor and causes circulating current loops to form. These current loops in turn cause the apparent resistance of the winding to increase. The Advanced Propulsion Centre, UK has laid a roadmap for automotive propulsion technologies and is illustrated in Fig. 1.11 [20]. It predicts that the BEVs will displace the conventional propulsion systems in the next 5 – 10 years, if they become cost competitive on a total – cost of ownership basis It also predicts that BEVs would dominate beyond 2040, depending on the availability of sufficient charging infrastructures. For future transportation with hybrid and electric propulsion, the power density of the machines needs to be markedly higher than the currently available state of the art machines as reported in the Advanced Propulsion Centre in roadmap for electrical machines. The roadmap illustrates that developments in electrical machines broadly focus on three main areas: (a) achieving a step change in performance (power – density or efficiency) for high – end applications, (b) reducing cost mass market applications and (c) minimising the environmental impact of manufacturing and end of life recycling. Fig. 1.12a illustrates the roadmap for electrical machines. Technology evolutions that reduce the compromise between reduced costs and improved performance are shown from 2025 in the roadmap. Fig. 1.12b shows the performance targets set by the Electrical Machine roadmap for passenger car traction motor and Truck and Bus traction motor. The roadmap has identified that for lower cost electrical machines, more effective utilisation of existing materials, reducing copper

losses through better winding designs and reducing iron losses are required. As losses in copper windings are one of the major sources of efficiency loss in electrical machines, development has been intensely focussed on reducing these losses wherever possible.



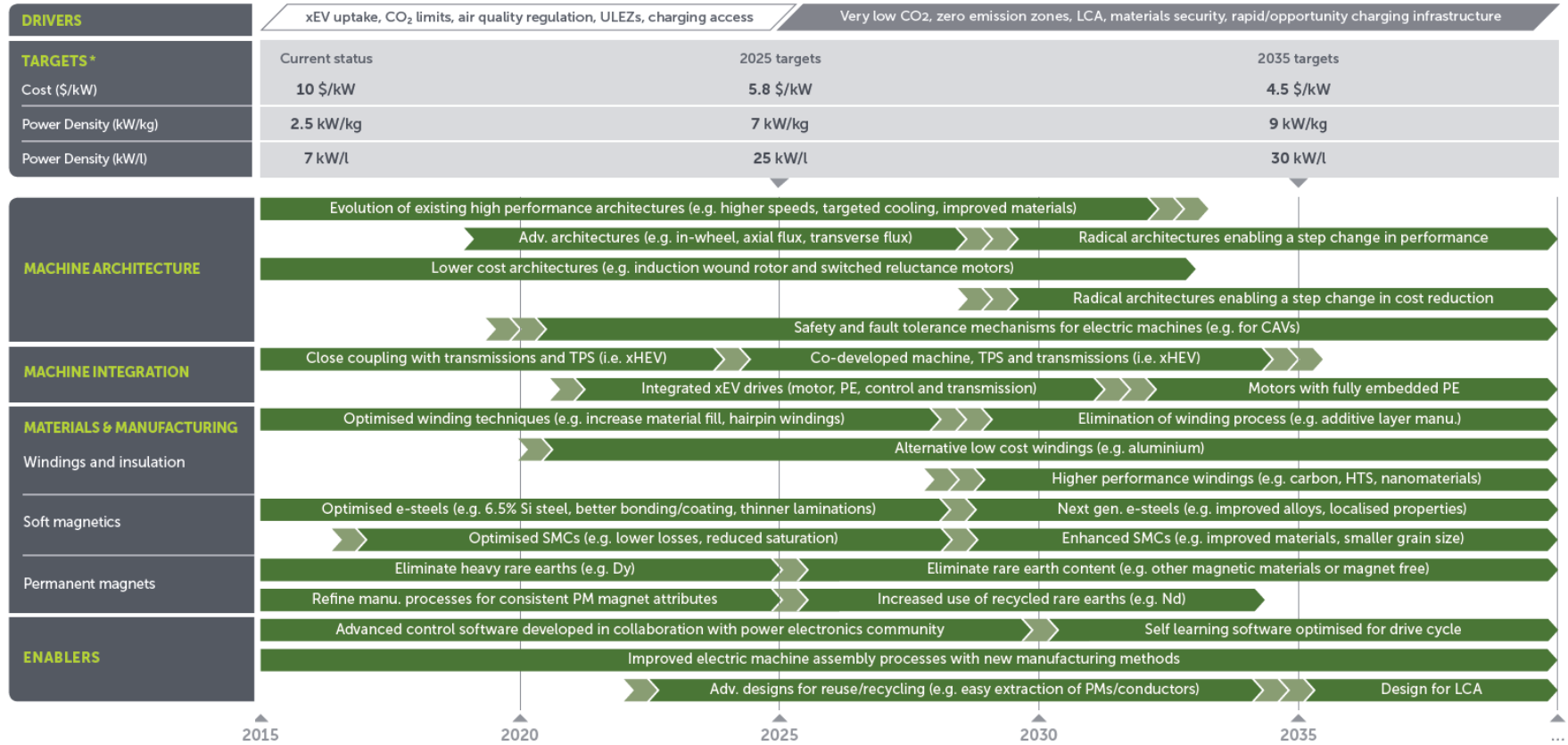
(a) Roadmap for passenger vehicles



(b) Roadmap for buses

Fig. 1.11: Roadmap laid by Advanced Propulsion Centre, UK [20].

## ELECTRIC MACHINES



(a) Roadmap for Electrical Machines

	2017	2025	2035
<b>Passenger Car Traction Motor <sup>1</sup></b>			
Cost (\$/kW) <sup>2</sup>	10	5.8	4.5
Continuous power density (kW/kg)	2.5	7	9
Continuous power density (kW/l)	7	25	30
Drive cycle efficiency (%) <sup>3</sup>	86.5	92.5	93
<b>Truck and Bus Traction Motor <sup>1</sup></b>			
Cost (\$/kW) <sup>2</sup>	60	15	12
Continuous power density (kW/kg)	1.5	2	2.5
Continuous power density (kW/l)	4.5	6	7
Drive cycle efficiency (%) <sup>3</sup>	83	88	90

1. All assume 350V / 450 Amps @ 65°C inlet
2. Prices are 300% mark-up on material costs
3. Drive cycle bases on Worldwide Harmonised Light Vehicle Test Procedure (WLTP)

(b) Targets set for Traction Motors

Fig. 1.12: Electrical Machine Roadmap laid by Advanced Propulsion Centre, UK [20].

## **1.6. Aim and objective**

The main purpose of this work is to investigate the effects of AC losses in the winding of an Interior Permanent Magnet (IPM) traction machine using numerical methods and to develop solutions to mitigate the aforesaid losses with the geometry of the slot being constrained.

## **1.7. Key findings of the thesis**

The key findings of the thesis are presented as below:

- Through FE analyses it is established that Skin and proximity losses are largely independent of the bundle shapes and positions in the slot geometry and the circulating current losses are very sensitive to the shapes of the bundle.
- A prove for loss segregation into components is derived and it is proposed that the skin and proximity losses cannot be neglected even when the wire diameter is smaller than the skin depth.
- Optimisation of winding height on the slot combined with optimal strand diameter size and bundling of strands to minimize the AC losses in the slot.
- Validation of the finite –element modelling by experimental motorettes with 3D printed slot formers.
- Using simplified experimental motorette section, it shown by accurately controlling the strand positioning within the slot top the losses in the windings can be significantly be reduced.

- Using experimental motorette, it is shown that that the shape of the bundles is more sensitive than the positions of the individual strands within the bundle.
- Using experimental motorette, it is shown that at elevated frequencies, as the copper filling factor increase the AC losses in the winding increase. For randomly wound winding, the losses in the winding can be unpredictable and for the same slot filling factor with smaller strands size/more strands – in hand, the losses in the windings can be significantly high.

## **1.8. Thesis outline**

Chapter 2 presents an introduction to the losses in PM machine. A brief description of each of the losses is presented followed with the analytical calculation methods available in the literature. With the major focus of this work being the AC losses in the winding of the machine, in – depth review of each of the components these losses are presented along with the literature review of the work done so far by the experts in this field. Finally, using commercially available finite – element (FE) software, Infolytica MagNet (now Mentor Graphics), analysis of these losses is presented using simplified models.

Chapter 3 introduces the existing prototype machine considered for the purpose of this thesis. Keeping the slot filling factor constant as the prototype machine, 3 types of strands/ bundles arrangements with various strand numbers are introduced and comparative analysis made using Finite – Element Analysis (FEA). A methodology for segregation of the losses into the components is introduced. Using analytical methodology aided with the FE results of the above arrangements, a proof

of the loss segregation is presented. Also, it is shown that the skin and proximity effects losses in the strands do not depend on the shape and position of the bundles, whilst the circulating currents are very sensitive to the bundle shape.

In chapter 4, a methodology for simplification of modelling is presented. It is shown that for the machine considered in this thesis, the strand -level modelling of the machine be reduced to one slot. Using this simplification methodology, significant reduction in computational time is achieved with the loss in some accuracy in loss calculation when compared with the baseline model. An investigation into validity of this simplification is also presented. An optimisation methodology to reduce the effects of ac losses in the winding is discussed. In this chapter, using FEM it is shown for a given slot geometry, by selecting optimum strand diameter and winding height, the effects of AC losses in the winding can be mitigated. The FE results shows that with the optimum winding height of H4 aided with appropriate wire size, the total losses in the windings can be reduced by 34%.

It is a well-established phenomenon that estimation/modelling of AC losses and experimental test results of it vastly differs. Therefore, Chapter 5 presents a meticulous but accurate approach for the experimental validation of the FE modelling. Taking advantage of the advancements in 3D printing technology, slot formers with holes along the length were manufactured. By placing each strand of the winding in the slot at exactly the same position as of the FE model, it is shown that FE models can be validated by experimental results in the position of each conductor is well defined. For the case in this chapter, the accuracy is within 10% of the experimental test results.

In chapter 6, the influence of bundle shapes and position in the AC losses is being presented. Using FEM, it is shown that by carefully controlling the shape of the conductors near the slot top, the ac losses in the winding can be significantly reduced. A qualitative explanation for relationship between the reduced losses and bundle shapes is presented and using single experimental validation motorette, a reduction of 36% in the AC losses at the active length (stack length of the machine) is achieved.

Chapter 7 presents comparative analysis of fixed strand positions and fixed conductor shapes in the slot using experimental approach. It shows that the effect on individual strand positions within a bundle shape is not critical as long as the bundle shapes are fixed. For both cases the results are within 10% of each other. Using experimental motorette setups with randomly wound winding, a relationship between copper filling factor and AC losses is presented. The trend shows that for the same strand diameter size, with increase in slot filling factor the Total/DC loss ratio increase. Comparing the motorettes with the same winding specification as of the prototype machine, this analysis shows that for random wound winding the losses in the winding can be unpredictable and with smaller strands diameters/ more strands – in – hand, the losses in the windings can be significantly high.

Chapter 8 summarises the conclusions of the work undertaken for this PhD and suggests possible future work.

## Chapter 2

# Losses in Permanent Magnet Machines

Electric motors are electromechanical devices that convert electrical energy to mechanical energy. However, in doing so, not all the electrical energy is converted to useful mechanical energy. This consumed energy is referred to as motor power loss. In motor design, it is important to consider motor power losses and it is desired to understand the mechanisms of various power losses associated with electric motors. The motor efficiency is defined as the ratio of the power output to the power input where power output equals input power minus power loss. Therefore, reduced power losses relate to higher motor efficiency. From economic standpoint, higher losses are always associated with increased motor costs. A vast majority of those are converted into heat energy, which can substantially increase the temperature in the windings and deteriorate the motor performance. Temperature is a major cause of degradation of insulation materials and accelerates the aging of the winding insulations; thus, reducing their lifetime. High temperature can significantly reduce magnetic properties of permanent magnets (PMs) to lower the performance of PMSM and may lead to risk of the permanent magnets to demagnetise permanently. The high temperature caused by the motor power loss adversely effects the bearing of the machines. To keep the machine temperature below the maximum allowed value, all the heat energy produced because of motor loss needs to be dissipated to the surrounding. Thus, selection of cooling method of machine is strongly affected by the power loss in the machine.

The power losses in PM machine can be categorised as no – load and load losses. As the name suggests, no – load losses do not require load currents. The major no – load losses includes (a) core losses (also called magnetic losses), caused by the alternating magnetic flux in the stator and rotor cores, magnets and other machine components, (b) frictional and windage losses together grouped as mechanical losses. The load losses include (i) resistive losses in the stator windings, (ii) stray losses that consists of various kinds of losses that cannot be accounted for.

Contribution of each type of losses to the total power loss has been estimated in [21]. The power loss largely depends on the frequency and materials used. The largest contribution comes from the stator windings of about 35% of the total power loss. The core losses contribute about 20% and the mechanical loss of about 10%. Similar contribution of 33% of the total losses from the stator winding is reported in [22].

## **2.1. Core losses**

### **2.1.1. Hysteresis Loss**

In electrical machines, stator core is made of ferromagnetic materials, which typically are composed of iron and alloys of iron with cobalt, tungsten, nickel, aluminium, and other metals. Ferromagnetic material contains a large number of domains, i.e. regions in which the magnetic moments of all the atoms are parallel, giving rise to a net magnetic moment for that domain. In an unmagnetised sample of material, the domain magnetic moments are randomly oriented, and the net resulting magnetic flux in the material is zero. When an external alternating magnetic field is applied to a ferromagnetic material, it forces the atomic dipoles in the material to

align themselves with the magnetic field. If the applied magnetising force is reduced to zero, the domain magnetic moments relax to the direction of easy magnetism nearest to that of the applied field. Although, the dipoles tend to orient towards their initial orientation, due to phenomenon known as magnetic hysteresis they will no longer be randomly oriented and will retain a net magnetisation component along the applied field direction. When the magnetic field suddenly changes its orientation relatively with the material, the atomic dipoles must realign themselves to accommodate such change. This takes certain amount of energy to overcome the magnetic hysteresis effect to adjust the atomic dipoles according to the change of the external magnetic field. Hysteresis loss depends on the power frequency, peak flux density, material properties, and the orientation of the magnetic flux with respect to the grain structure of the steel [6], [23], [24].

The empirical formula expressing hysteresis loss per unit volume is given by Steinmetz and Bertotti equation as follows:

$$P_h = K_h V_c B^n f \quad (2.1)$$

where

$K_h$  is the hysteresis coefficient

$n$  is the Steinmetz coefficient, which has a value between 1.6 and 2.3 for most modern magnetic materials

$f$  is the frequency of magnetisation

### 2.1.2. Eddy current Loss

Faraday's law of induction states that, "*Any change in the environment of a coil of wire will cause a voltage to be induced in the coil, regardless of how the magnetic change is produced.*". This induced voltage (emf) causes circulating currents to flow referred as eddy currents. The power loss caused by these currents is known as eddy current loss. In electric motors, eddy – currents are affected by the electrical resistance of ferromagnetic materials in which eddy currents flow. These local circulating currents induced in conductive core components caused eddy – current loss and results in the rise in temperature. To mitigate the effects of eddy – currents, both the stator and the rotor cores are built by stacking thin sheets of lamination, which are insulated from each other by non – conducting materials such as an oxide layer on their surfaces or by a thin coat of insulating enamel or varnish. This layered structure prevents large current loops and effectively confines eddy currents to small loops in individual layers. The sum of the individual eddy current in each piece of the laminated core is less than the in the solid iron core. In addition, infusion of silicon element into the steel core increases the electrical resistance of the material, leading to the further decrease of eddy current [6], [25], [26].

Eddy – current loss of magnetic core (in unit of W ) can be derived as

$$P_e = \frac{\pi^2}{6} V_c B^2 f^2 a^2 \sigma = K_e V_c B^2 f^2 \quad (2.2)$$

$$K_e = \frac{\pi^2 a^2 \sigma}{6} \quad (2.3)$$

where

$V_c$  is the volume of magnetic core in unit of  $m^3$

$a$  is the lamination thickness in unit of m

$B$  is the peak flux density

## 2.2. Copper loss in the winding

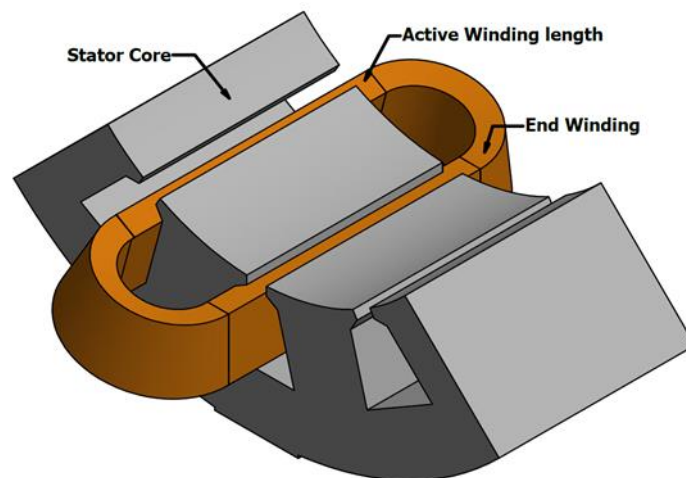


Fig. 2.1: Isometric view of stator motorette

Fig. 2.1 shows an isometric view of a stator motorette with a single layer concentric winding on the teeth. The winding can be divided into two parts: the active winding length contained within the stator stack, responsible for creating useful torque producing flux; and the overhang area (or the end - winding), which does not contribute any useful flux but is necessary to form close loops of the coils. Apart from these parts, in case of the three - phase machines, there may be lead wires connecting the terminals of the machine with the three - phase winding. Since, very few leakage fluxes interact with the lead wires and the end - winding region, the losses in these parts can be considered mainly due to DC component of copper loss.

However, the part of the winding laying inside the slot are subjected to varying flux linkage. This result in apparent increase in the resistance of the winding due the AC effects, namely, skin and proximity effect and circulating current described in detail in later sections.

### 2.3. DC copper loss

When DC current passes through a conductor (or copper coil), heat is generated in the conductor. This heating is known as ohmic/resistive heating or DC copper loss. The power of heating generated by an electrical conductor (Joule's first law) is given as the product of the resistance of the material (copper conductor) and the square of the current.

$$P_{DC} = I^2 R_{DC} \quad (2.4)$$

where

$P_{DC}$	DC power loss
$I$	DC current flowing through the conductor
$R_{DC}$	DC resistance of the conductor

The ohmic loss in a conductor can also be given as [27]:

$$P_{ohmic} = \int_v \rho J \cdot J dv = \int_v \frac{J \cdot J}{\sigma} dv \quad (2.5)$$

where

$V$  is the volume of the conductor

$\rho$  is the resistivity of the conductor material

$J$  is the current density in the conductor

$\sigma = \frac{1}{\rho}$  is the conductivity of the conductor material

### 2.3.1. Calculation of DC resistance

The electrical resistance,  $R_{DC}$ , of a material is proportional to the resistivity of the material  $\rho$  (in  $\Omega\text{-}m$ ) and the material length  $l$  (in  $m$ ) and inversely proportional to the cross – sectional area of the material  $A$  (in  $m^2$ ), that is

$$R_{DC} = \frac{\rho l}{A} \quad (2.6)$$

Where  $\rho$  is a function of temperature  $T$ ,

$$\rho(T) = \rho_0(T_0)[1 + \alpha(T - T_0)] \quad (2.7)$$

Where

$\alpha$  is the temperature coefficient of resistance of the material

$T_0$  is the reference temperature

Substituting Equation 2.7 into Equation 2.6, yields

$$R_{DC}(T) = \frac{1}{A} \rho_0(T_0)[1 + \alpha(T - T_0)] = R_{DC(T_0)}[1 + \alpha(T - T_0)] \quad (2.8)$$

Thus, a measured resistance,  $R_{DC(m)}$ , at an arbitrary measuring temperature  $T_m$  can be converted into the resistance at the reference temperature  $T_o$  :

$$R_{DC}(T_o) = \frac{R_{DC(m)}(T_m)}{1 - \alpha(T_m - T_o)} \quad (2.9)$$

### 2.3.2. Calculation of winding DC resistance

The resistance of a coil can be given as

$$R_{coil} = T_c \frac{\rho L_{av}}{n A_{strand}} \quad (2.10)$$

where

$T_c$  is number of turns in a coil

$\rho$  is resistivity of the material in the coil

$L_{av}$  is the average length of a coil turn

$n$  is the number of parallel strands/ strands – in - hand

$A_{strand}$  is the copper area of one strand

$$A_{strand} = \pi r_{strand}^2 \quad (2.11)$$

where

$r_{strand}$  is the copper radius of one strand

The phase resistance is given as

$$R_{ph} = \frac{N_c}{a^2} R_{coil} \quad (2.12)$$

where

$N_c$  is number of coils per phase

$a$  is number of parallel paths

The number of turns in series per phase is

$$T = N_c \frac{T_c}{a} \quad (2.13)$$

Therefore, phase resistance can be given as

$$R_{ph} = \frac{T_{ph}}{a} \frac{\rho L_{av}}{nA_{strand}} \quad (2.14)$$

The average length,  $L_{av}$ , of a coil turn in a slot of low – voltage machine with round enamelled magnet wires is given approximately as [28],

$$L_{av} = 2l + 2.3\tau_p \quad (2.15)$$

Where,  $l$ , is length of stator stack of the machine and

$$\tau_p = \pi \times \frac{statorID}{p} \quad (2.16)$$

Where,

$statorID$  is the stator inner diameter

$p$  is the number of poles

### 2.3.3. Mitigation of DC copper loss

Copper filling factor in a slot is defined as:

$$\text{Copper fill factor} = \frac{\text{Total copper area per slot}}{\text{Slot area}}$$

One general way of reducing DC copper loss is to aim for achieving high copper filling factor [15], [17]. Resistance of a material is inversely proportional to the area of the material; increasing the copper area in the slot reduces the resistance. Since DC copper loss is proportional to resistance of the copper conductor, therefore increase in copper area results in reduction in DC copper loss. However, this increases the motor weight and cannot solve the conflict between efficiency and power density, especially in case of electric and hybrid vehicles where weight and space are premium [29]. Using rectangular conductors, representing big cross – sectional areas in the slots of electrical machines provides an opportunity to reduce DC losses.

## 2.4. AC Copper Loss

Recent development and demand in electric and hybrid vehicles have created a trend of high - speed electrical machines. Increasing the rotational speed of PM machines increases the power density of the machines [30]. Higher power density reduces the volume and weight of the electric motor, and offers great potentials to reduce costs [29], [31]. High – speed machines often have few series turns because of high rate of change of flux linkage so they can have many parallel turns or strands – in – hand [32]. With trend for high – speeds and therefore high electrical frequencies, consideration of the AC effects such as skin and proximity effects, and

circulating currents in the ‘strands – in – hand’ is getting more and more important [17].

In later sections, each of these AC effects are discussed in details and a literature review of the work carried out so far in analysis, modelling and mitigation of these losses is presented.

## 2.5. Skin Effect

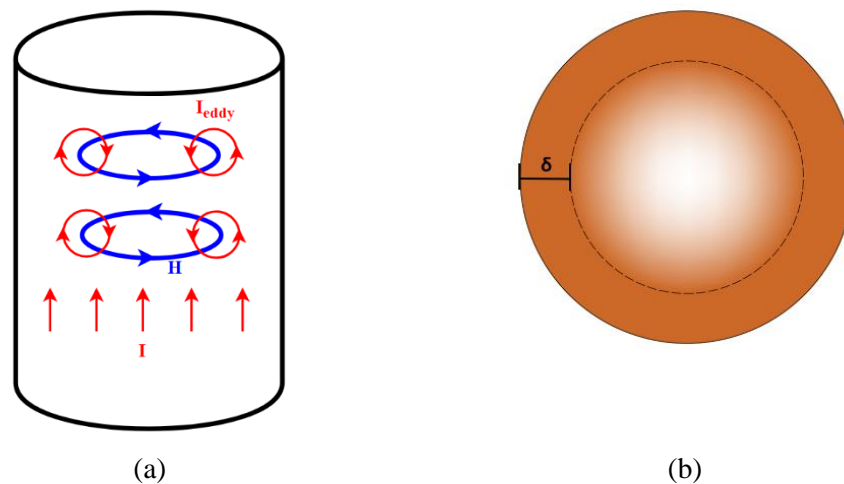


Fig. 2.2: Skin effect in a conductor

Skin effect is the tendency of the AC current to flow towards the outer periphery/surface of the conductor. The skin effect is due to opposing eddy currents induced by the changing magnetic field resulting from the alternating current. As shown in Fig. 2.2a, an AC current,  $I$ , flowing through a conductor produces magnetic field,  $H$ , which in turn creates circulating currents inside the conductor. These eddies cancel the current flow in the centre of the conductor and reinforce the current flow towards the outer skin of the conductor, resulting in the current to distribute more towards the outer surface, as shown in Fig. 2.2b. Thus, the effective resistance of the conductor increases.

The skin depth is defined as the distance from the conductor surface where the current density decreases exponentially to 36.8 percent as compared to current density at the surface of the conductor ( $e = 2.71828$ ) [33], [34]. The skin depth ( $\delta$ ), can be calculated as [35],

$$\delta = \sqrt{\frac{\rho}{\pi f \mu_0 \mu_r}} \quad (2.17)$$

Where,  $\rho$  and  $\mu_r$  are the electrical resistivity and the relative permeability of the conductor respectively, and  $\mu_0$  is the permeability of the free space.

The effective resistance of the conductor increases due to skin effect and the factor by which the DC resistive losses have to be multiplied to get the AC resistive losses is the resistance factor  $k_{skin}$ . It is also the ratio of the AC and DC resistances of the conductor. The resistance factor in the slot area is [24],

$$k_{Skin u} = \frac{R_{AC}}{R_{DC}} = \frac{P_{AC}}{P_{DC}} \quad (2.18)$$

The average resistance factor  $k_{Skin u}$ , over the slot can be calculated as [17], [24],

$$k_{Skin u} = \varphi(\xi_s) + \frac{Z_n^2 - 1}{3} \psi(\xi_s) \quad (2.19)$$

Where  $\varphi$  and  $\psi$  are auxiliary functions specified as

$$\varphi(\xi_s) = \xi_s \frac{\sinh 2\xi_s + \sin 2\xi_s}{\cosh 2\xi_s - \cos 2\xi_s} \quad (2.20)$$

$$\Psi(\xi_s) = 2\xi_s \frac{\sinh \xi_s - \sin \xi_s}{\cosh \xi_s + \cos \xi_s} \quad (2.21)$$

and the reduced strand height  $\xi_s$ , can be calculated as

$$\xi_s = d_s \frac{\pi}{2} \sqrt{f \mu \sigma_c \sqrt{\frac{SF_{Cu}}{A_s}}} \quad (2.22)$$

Where

- $d_s$  is the strand diameter
- $f$  is the supply frequency
- $\mu$  is the permittivity
- $\sigma_c$  is the electrical conductivity
- $SF_{Cu}$  is the copper filling factor
- $A_s$  is the cross – sectional area of one strand

One way to mitigate the copper losses in electrical machines due to the skin effect, is by selecting the size of the strands properly [34], [36], [37]. For an operating frequency, if the diameter of the round magnet wire is equal to or smaller than the skin depth, the AC resistance tends to be close to the DC resistance. The optimal stranding to minimise the copper losses is defined by  $k_{skin}$  [38]. Another technique to reduce the skin effect is to transpose the coil along the slot [12], [32], [39], [40] or use Litz Wire [41] – [43]. However, with Litz wire, since the wire is stranded, the net copper area reduces. Twisting the strands reduces the slot fill factor, increasing the DC resistance and thus the DC losses. Furthermore, twisting the strands

adversely effects the thermal performance and the mechanical flexibility of the strands – in – hand [44] – [46].

## 2.6. Proximity effect

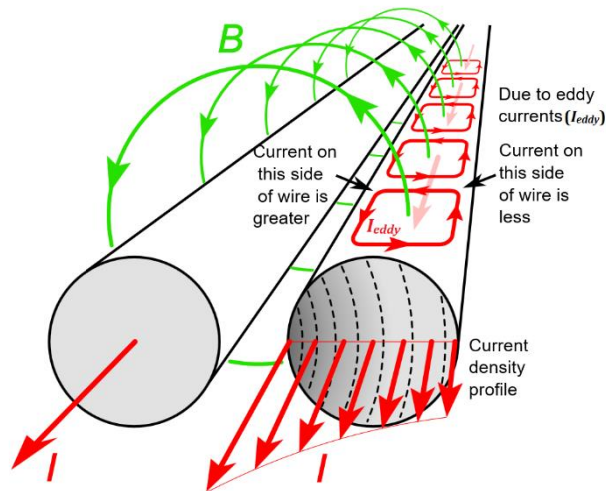


Fig. 2.3: Proximity effect [47]

The proximity effect is the tendency for current to flow in other undesirable patterns that form localised current loops or concentrated distributions due to the presence of a magnetic field generated by nearby conductors [37]. Fig. 2.3 shows the process of proximity effect. Current,  $I$ , flowing through conductor on left creates a magnetic field,  $B$  and the flux created by this field induced eddy current loops  $I_{eddy}$ , in the conductor on the right. Thus, if the right conductor is carrying current in the same direction as the left conductor, the eddy loops reinforces the main current in the conductor towards the side closer to the conductor on the left and opposes on the side further away. This creates uneven current distribution inside the conductor increasing the losses in the conductor.

According to [48], [49], the proximity effect losses for all the strands in the slot can be calculated as

$$P_{proximity} = \frac{\pi \omega_e^2 l_{eff} d_s^4 B^2}{128 \rho_c} \quad (2.23)$$

Where,

- $P_{proximity}$  is the strand – level proximity loss
- $\omega_e$  is the excitation frequency
- $l_{eff}$  is the effective length of the strand
- $d_s$  is the strand diameter
- $B$  is the flux density amplitude at the strand location in the slot
- $\rho_c$  is the conductor resistivity

Proximity losses in high speed electrical machines is a well – studied and researched area. Klauz in [50] investigated the losses in the windings of a Switched Reluctance Machine (SRM) due to proximity effect using FEA. Authors in [48] presented a 2D analytical model of the stator slots to predict the proximity losses in Surface PM machines including the effects of slot openings. In this paper, the difference between the AC losses in machines with single- and double-layer windings were investigated, and it is shown that the 2D analytical model provide good matches for the predicted flux densities at the AC losses in comparison to the FE results. Reddy [49] presented an integrated analytical tool for estimating the total proximity losses in stator windings for machines operating at high speeds. In [37], authors have noted that high ratios of ac to dc resistance can be exhibited in permanent magnet machines with fractional – slot concentrated windings due to proximity effects at high frequencies despite the adoption of stranded bundles. It is

shown in the paper that the proximity effect can be significantly reduced with an appropriate choice of conductor shape, by placing the conductors towards the bottom of the slot and by minimising height in the radial direction of the parallel conductor bundle forming each turn. In [51], authors calculated the winding losses of inductors with rod cores caused by eddy currents in adjacent windings. The paper shows that the proximity losses in a turn depend on both the position of the turn in the winding and the geometry of the whole winding layout and proposed a winding geometry to reduce losses. Authors in [52] presented an investigation into proximity losses in the end – winding region of an ac power inductor using 3D FEA. They conclude that simpler 2D approach tends to overpredict the  $R_{ac}/R_{dc}$  ratio and show that end-winding proximity losses are lower than that generated in the active length of conductors. Iwasaki [53], investigated the effect of high frequency current ripples induced by PWM on the proximity effect losses and concludes that the skin and proximity losses increase significantly due to PWM. Authors in [54], developed a hybrid analytical – numerical loss calculation method which is computationally efficient for the deriving ac loss in the winding and provides a reasonable compromise between computational time and accuracy.

## **2.7. Circulating Current Loss**

Parallel strands for coil turns located in the slot top and slot bottom experience proximity effect since there is different flux linkages between them due to leakage. Due to the slot flux leakage, each strand sees a different flux linkage and thus have a different inductance. This leads to a difference in the total current of each parallel current, increasing the total resistive losses. The difference between the individual and average strand currents is the circulating currents and result in circulating current

losses [30], [32], [55], [56]. The leakage may originate from the excitation field or the armature field. The losses induced by the excitation field primarily effects machines with windings in direct exposure to the field flux, such as slotless machines and these losses induced by the excitation field greatly diminish in the presence of the tooth tip [57].

According to [30], [58], the induced losses inside a strand subjected to an external magnetic field  $H_e$ , can be given as

$$P_{cc} = \rho l \hat{H}^2 D_s \quad (2.24)$$

with

$$D_s = 2\pi \operatorname{Re} \left\{ \frac{\alpha r I_1(\alpha r)}{I_0(\alpha r)} \right\} \quad (2.25)$$

Where

- $P_{cc}$  is power in one strand
- $\rho$  is the resistivity
- $l$  is the length
- $\hat{H}$  is the peak of the magnetic field
- $\alpha = \frac{1+j}{\sqrt{2\rho}} \sqrt{\omega\mu}$
- $r$  is radius of the strand
- $I_0$  and  $I_1$  are modified Bessel functions

Circulating currents resulting from imbalances in the linked field flux by the strands in the slot cause the source current to be shared unevenly among the parallel strands. To minimise the effects of circulating current, each strand should be placed in various positions inside the slot, so that the impedance of all the strands are similar.

Reddy [44], used 3D FEA to investigate the effects of transposition of magnet wires in stator winding bundles on the copper losses in high – speed machines. The paper has shown that straight un-transposed bundles have highest losses while bundles with  $360^\circ$  transpositions over the length of the slots produce the least losses. The authors in [59], proposed an analytical model for circulating current loss and compared stators with Litz and stranded conductors' windings to highlight the effect of circulating current losses. Popescu [32], studied the effect of circulating currents in the parallel rectangular strands using FEA and showed that the ac/dc loss ratio is over 50 for a leading-edge conductor at the top of a slot, at high speeds. Van der Geest [30], investigated several techniques to reduce circulating current in the strands in the slot. This includes increasing the number of parallel strands, partially filling the slot, changing the strand shapes, and decreasing the slot size. His findings with increasing number of parallel strands shows that a high number of parallel strands is unattractive, because small differences in strand placement lead to large loss variations. With partially filling slots, the author showed that it is beneficial to not fill the complete slot and place the strands towards the slot bottom. With varied strand shape, it is shown that maximising the slot fill factor does not result in immediate benefits and neither do changing the slot shape. However, the authors didn't take into account bundle shapes and no experimental validation was presented. In [45], the author presented a method based on impedance matrix (from 3D FEA) of the windings to estimate the uneven distribution of current across the strands. The paper showed that a  $360^\circ$  transposition in the winding over the length of the slot significantly reduces the losses. To reduce circulating current loss, authors in [55] proposed (a) comparison of designs with different number of parallel paths in the winding, (b) partially filling the slot, leaving the slot top area unfilled, (c), varying

the slot winding height and tooth width simultaneously, keeping the slot fill factor constant and plotting it against the resistance ratio. Although, the authors presented a simplified experimental verification of finite element modelling by placing two wires in the stator core without winding, comparison and validation of FE modelling considering realistic winding is not presented. Authors in [17], investigated the influence of circulating currents in parallel wires' placement. In this paper, the authors considered two winding cases for a machine. It is experimentally shown that the bad winding has additional loss of 65% at high speed (11 krpm). However, a simplified non-realistic winding arrangement was considered. Authors in [60] showed that for coils made with solid flat conductors, the circulating current losses can be minimised by transposing a single conductor at about 70% of the coil height (from bottom to the top of the slot) at the endwinding. Authors in [18], studied the AC loss distribution in the winding with and without parallel strands and the impact on the insulation lifetime of the winding. The paper argues that although the AC loss is greater with higher parallel strands than with single solid conductor, the localised hotspot in case of solid conductor may lead to relatively faster insulation failure. Arumugam in [61], investigated the influences of the winding arrangements on frequency – dependent resistances along with other investigation points and showed that by adopting winding arrangement that shares the slot leakage flux, the ac losses in the winding are minimized. For the experimental verification, no parallel strands/strands – in – hand and realistic bundle shapes were considered. Lehtikoinen in [56], proposed two alternative FE formulations, point – strand method and polygon – strand method to calculate circulating currents in thin parallel strands. Based on simulations, the author showed that both methods yield reasonable accuracy results and is computationally efficient compared to brute – force approach

where the strands are finely meshed to obtain accurate skin – and proximity – effect losses. In [62], the author proposed a circuit – based model and a computationally efficient FE model to calculate circulating current in random – wound electrical machines. The author also proposed a process to generate random winding based on Monte Carlo analysis.

In the work carried out by the previous authors, minimisation of the winding losses were realised by:

- Only through finite – element simulation with no experimental validation [30], [56] and [62].
- Transposing of the coil over the length of the slots [44], [45] and [60], which effects the slot filling factor.
- Experimental test setup with simplified and idealistic winding arrangements which do not fully comprehend/ represent realistic randomly wound winding.

## **2.8. Finite Element Analysis of the fundamental losses in the winding**

In this section, the fundamental losses described in the above sections are analysed using finite – element, with commercially available software package, MagNet from Mentor Graphics. The parameters used for the purpose of this analysis are as following:

Parameter	Value
Strand diameter	1 mm
Current amplitude	100 A
Frequency	10 kHz

### 2.8.1. Skin Effect

Fig. 2.4 shows the skin effect on a strand placed in air. The skin depth at the frequency of 10 kHz is 651.955 micrometre ( $\mu\text{m}$ ) and the diameter of the strand is 1 mm. In Fig. 2.4, it can be clearly observed that the current density towards the periphery of the strand increases.

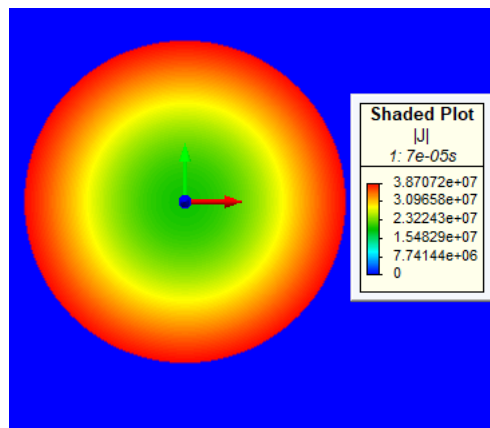
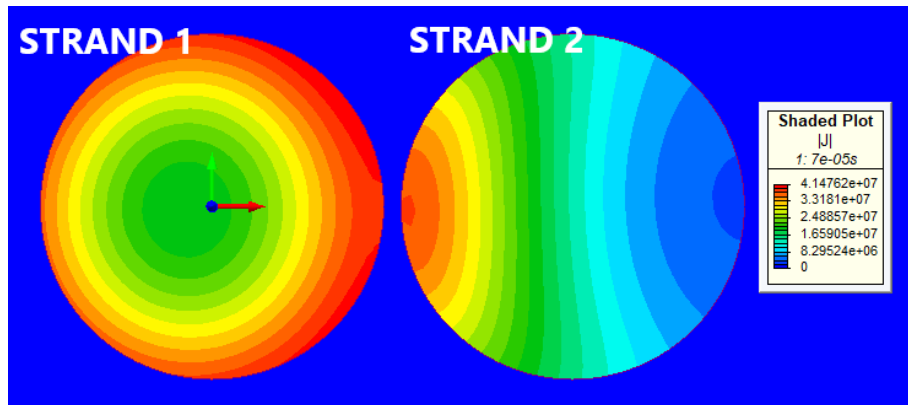
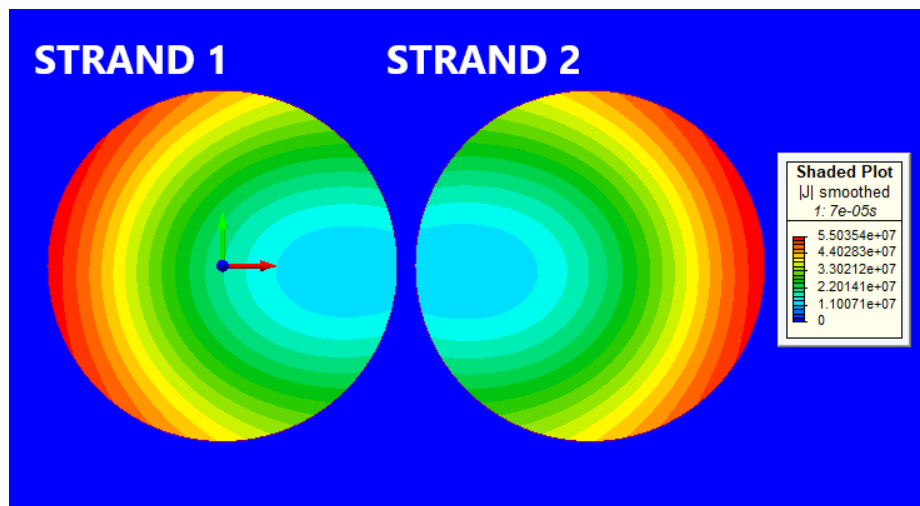


Fig. 2.4: Finite – element analysis of Skin effect in strand

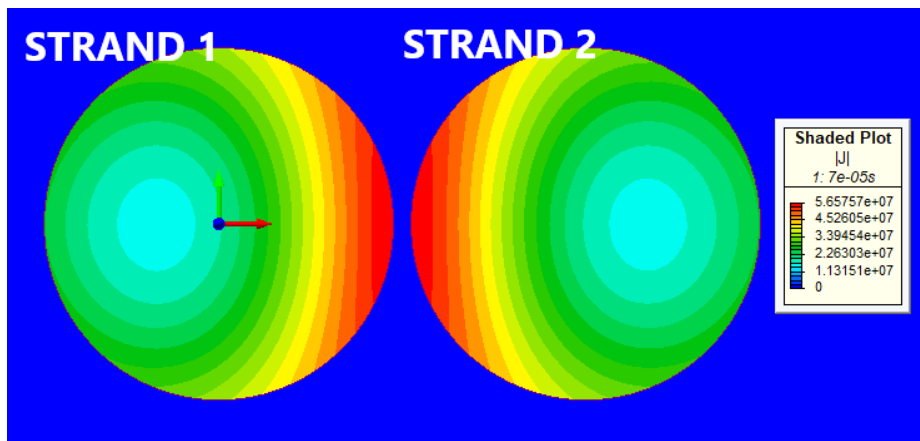
## 2.8.2. Proximity Effect



(a)



(b)

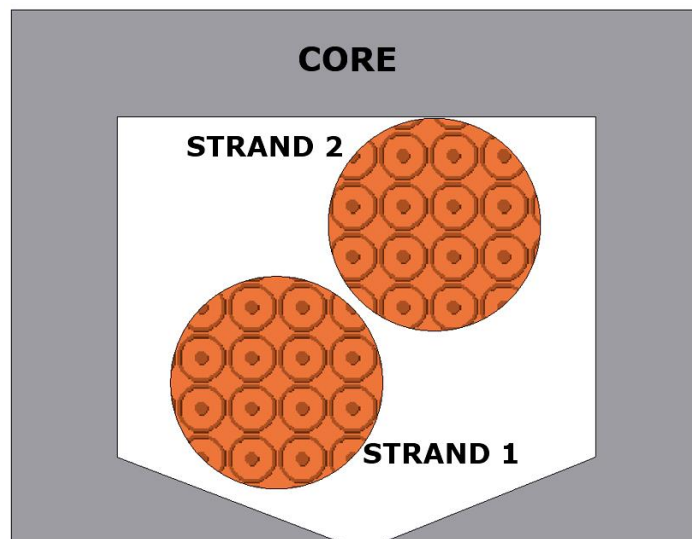


(c)

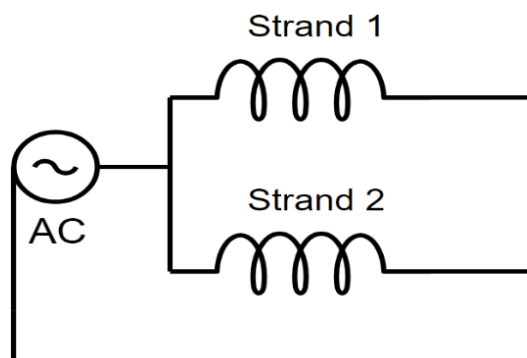
Fig. 2.5: Proximity effect in the strands (a) with no supply current in strand 2, (b) with supply current in same direction for both strands, (c) with current in the opposite directions

Fig. 2.5 shows the current density distribution in the strands due to proximity effect. For currents in the strands flowing in the same direction, the regions of higher current density are located towards the far side of each strand. In the case, where the currents in the strands are in opposite directions, the higher current density regions are towards the near side of the strands as shown in fig. 2.5b and fig. 2.5c respectively.

### 2.8.3. Circulating Current



(a)



(b)

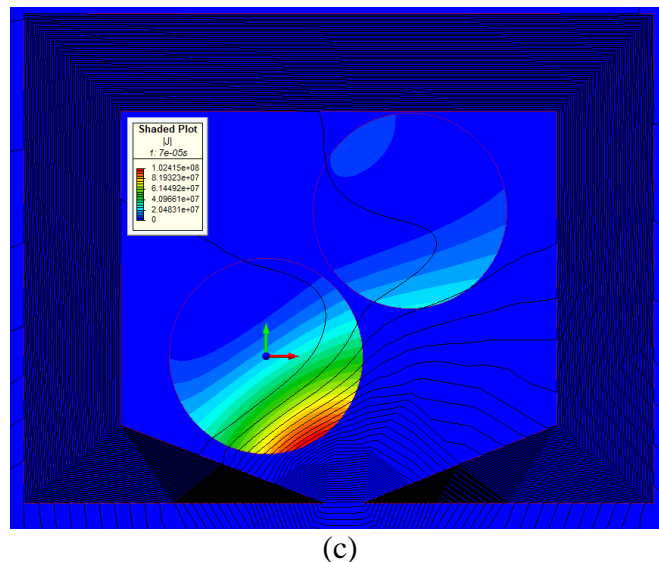


Fig. 2.6: (a) Model for investigating circulating current, (b) circuitual representation of the connection in model, (c) Flux function and current density in the strands

Fig. 2.6a shows a model of a semi - closed slot core with two strands placed inside it. The strands are connected in parallel and the supply is fed from a current source as shown in fig. 2.6b. Fig. 2.6c shows the current distribution in the strands at a time instant. The concentration of the slot leakage flux is higher towards the slot top (near the slot opening) than towards the bottom of the slot. The strand (Strand 1) placed near the slot top links with a different flux compared to the strand (Strand 2) placed towards the slot bottom. This causes a difference in the inductance of the parallel strands, the supply current is unevenly shared by them. Fig. 2.7 shows the current in the individual strands. It can be seen that, strand 1 is carrying the bulk of the supply current which may lead to hotspot and premature insulation failure of the strand.

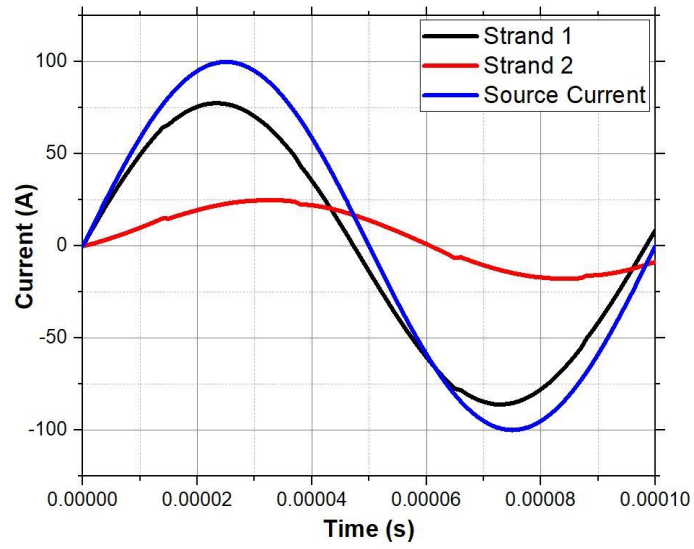


Fig. 2.7: Waveforms of the individual current in the strands and the source current

## Chapter 3

# Sensitivity Analysis of AC losses with varying ‘strands – in – hand’ and bundle shape

## 3.1. Specification of the prototype machine

An existing prototype interior permanent magnet synchronous machine (IPMSM) is used for analyses in the chapter. The machine is shown in Fig. 3.1 and details of it are listed in TABLE 3.1.

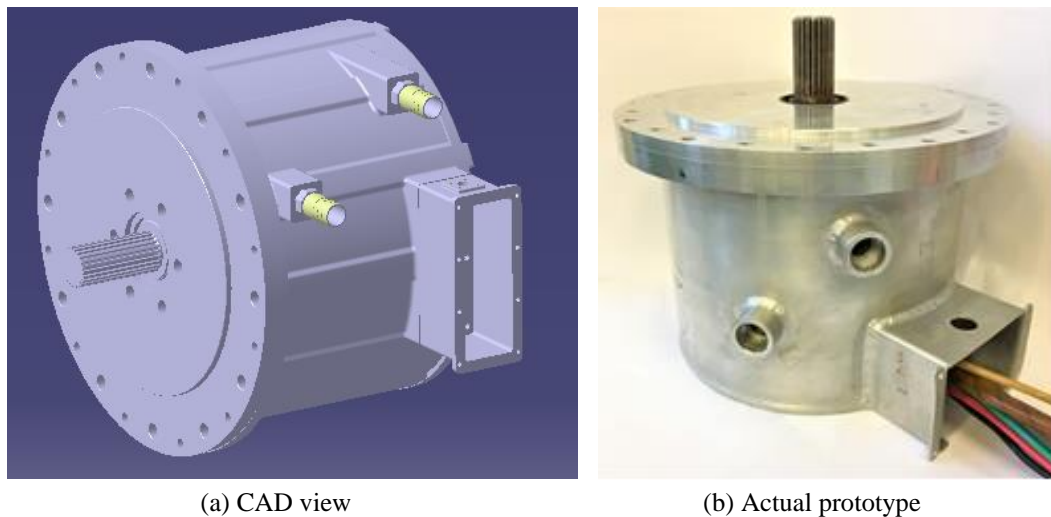


Fig. 3.1: Prototype of the traction machine

**TABLE 3.1: Machine Parameters**

Machine Type		Three – phase PMSM	
Voltage	384V / 480V	Number of phases	3
Rated/Peak power	37 / 74 kW	Winding type	concentrated
Rated/Peak Torque	126/382 Nm	Layers	2
Rated/ Peak base speed	2800 /1750 rpm	Turns/Slot	20
Highest Speed	10000 rpm	Working temperature	-40°C ~ 105°C
Working time at peak power	$\geq 60$ s	<b>Cooling:</b>	Water cooled
Efficiency	$\geq 95\%$	<b>Materials:</b>	
<b>Geometry:</b>		Magnet	N38EH
Outer diameter	245 mm	Iron Sheets	M235 – 35A
Active length	140 mm	Winding	Copper

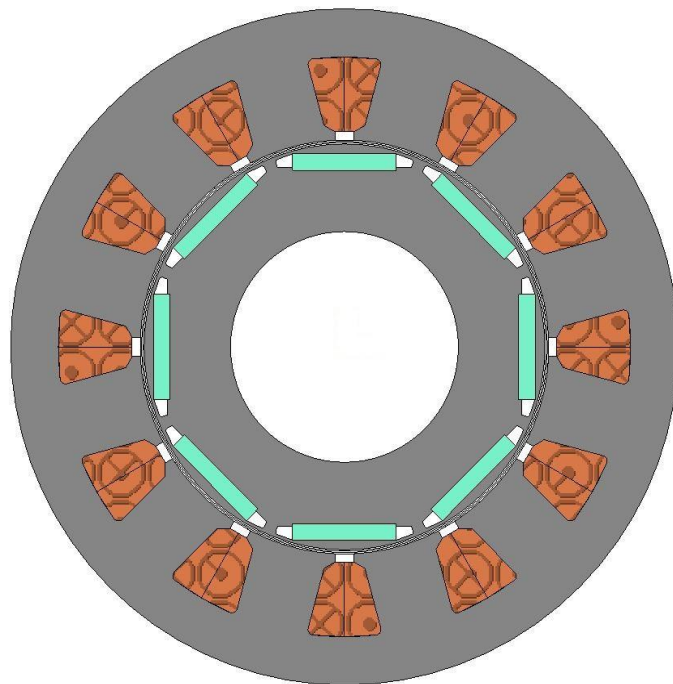


Fig. 3.2: Cross – sectional view of the prototype machine

Fig. 3.2 shows the cross-sectional view of the prototype machine. The machine has 8 poles / 12 slots with three – phase concentrated winding wound around the stator teeth. The rated current of the machine is 84 Arms. The machine is liquid cooled with a water jacket wrapped around the housing. In TABLE 3.2, the specifications of the constituent elements in the slot of machine are detailed.

**TABLE 3.2: Specification of components in slot**

Components	Material	Specification
Slot liner	DuPont™ Nomex® 410	Thickness : 0.3 mm
Coil separator	DuPont™ Nomex® 410	Thickness : 0.3 mm
Wedge	DuPont™ Nomex® 410	Thickness : 0.3 mm
Magnet wire	DAMID 200 – Gr 2	Outer diameter: 0.704 mm Nominal diameter : 0.63 mm
Conductors / slot		20
Strands – in - hand		33
Total strands / slot		660
Slot Filling factor		42%

## 3.2. Methodology

### 3.2.1. Description

For the purpose of this analysis, keeping the conductor area for each turn approximately the same and hence maintaining approximately a similar slot filling factor as in the original prototype machine, the strands – in – hand are increased in steps from 1 strand per conductor to 33 strands – in – hand. The models are built at the strand – level and analyses are carried out at operating point of 10000 rpm, which translates to fundamental frequency of 666.67 Hz. Due to symmetry, a quarter

section of the machine is modelled, and the models are solved using finite – element package, MagNet from Mentor Graphics. Fig. 3.3 shows the strand – level quarter section model of the machine with 3 slots and 2 poles.

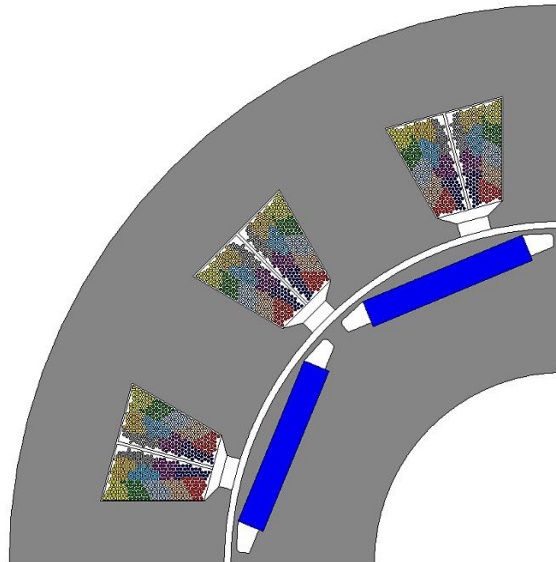


Fig. 3.3: Quarter section model of the prototype machine with strand – level winding

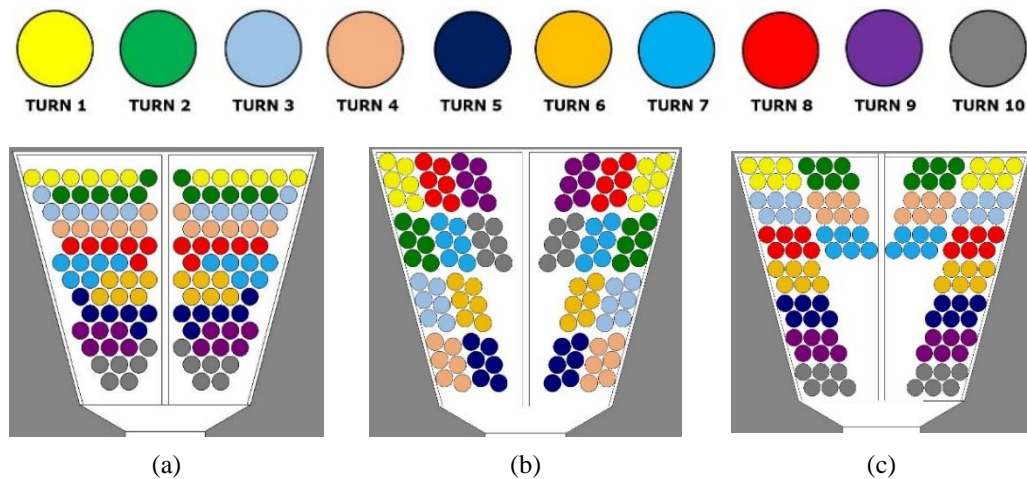


Fig. 3.4: (a) Horizontal, (b) Vertical bundled, (c) Horizontal bundled

Three arrangements of strands and bundles configurations are considered, namely: (a) horizontal (ARR1), (b) vertical bundled (ARR2), and (c) horizontal bundled (ARR3). Fig. 3.4 shows a slot of the model with the three arrangements. Here, each coloured disc represents a strand. The different coloured discs represent the turns

and the discs with same colour represents strands – in – hand of a turn. For example, the models in Fig. 3.4 have 10 turns represented by 10 different coloured discs and 6 same coloured discs representing the six strands of a turn connected in parallel. This result in 60 strands per coil side in the slot. In the case of horizontal arrangement (ARR1), the strands are laid horizontally across the slot geometry with no constraints on the bundle shape. For the case of vertical bundled arrangement (ARR2), the parallel strands on each turned are bundled and placed along the vertical direction (through the height) of slot. In the case of horizontal bundled arrangement (ARR3), the bundled strands are positioned across the slot geometry (through the slot width).

### **3.2.2. Calculation of DC loss in the winding**

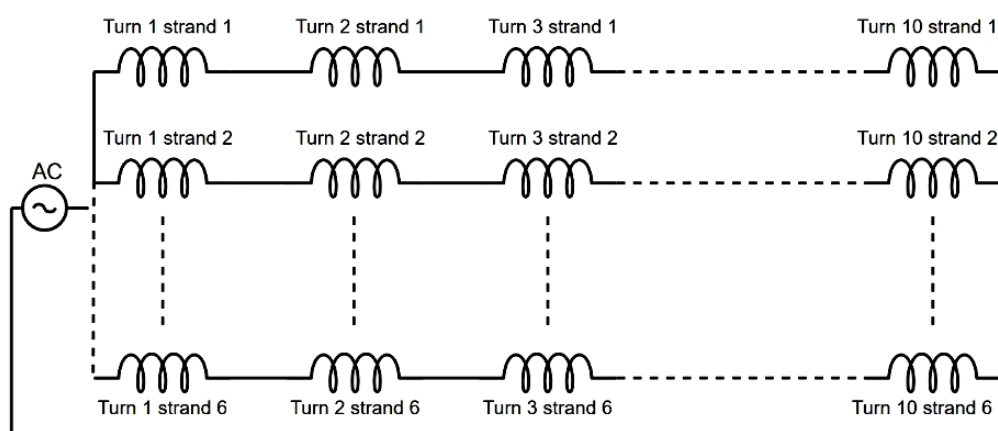
The DC loss in the winding is calculated using analytical approach. The resistance of each strand is calculated and using Eq. (2.4), the power loss in each strand is calculated for DC current equivalent to the AC rms current. Alternatively, the power loss in the strands are also calculated by solving the models using FE static 2D solver.

### **3.2.3. Calculation of AC + DC losses in the winding**

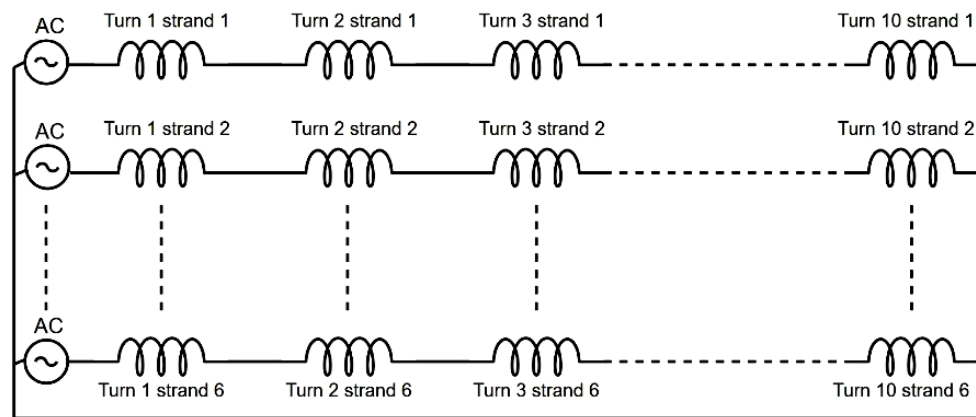
Calculation of the AC ohmic loss in strands are carried out by solving each model using transient analysis in the FEM package which in turn uses Eq. (2.5) to calculate the power loss in the strands. Each model is solved over the period of one electrical cycle and the average ohmic loss in each strand over that time – period is obtained. The losses of the strands forming parallel strands of a conductor are summed up to give the losses in the conductor.

### 3.2.4. Mitigation of circulating current

When strands are connected in parallel, they see different inductances due to variation of flux linkage. When these strands are connected in parallel with a sinusoidal source (single source), the current is unevenly shared by the strands and there is a significant difference in the amplitude and phase of the current in each strand caused by the circulating current. In order to eliminate the effect of circulating current (at simulation level), each strand is supplied with its own current source (multiple sources) so that to distribute the supply current equally among the parallel strands. The multiple source supply is an ideal case scenario and cannot be realised in practice as it would require a source to be added to each parallel strand of a coil. However, at simulation level the losses caused by the circulating currents can be mitigated using multi-source supplies as the main current is divided equally among the individual strands with same amplitude and phase. Fig. 3.5 shows the circuitual representation of the strands and bundle connections in the models with a single source supply and supply sources connected to each individual strand (multi-source supply). Supplying each strand with its individual source eradicate the effects from slot leakage flux and so thus the circulating current at the simulation level.



(a) Single source supply



(b) Multi - source supplies

Fig.3.5: Circuitual representation of the strands and bundle connections in the models with (a) single source supply and (b) multi - source supplies

### 3.3. Horizontal Arrangement (ARR1)

TABLE 3.3 lists the strand diameters that are used the analysis for this section. The total number of strands are adjusted to maintain a similar slot filling factor.

**TABLE 3.3: Dimensions of the strands**

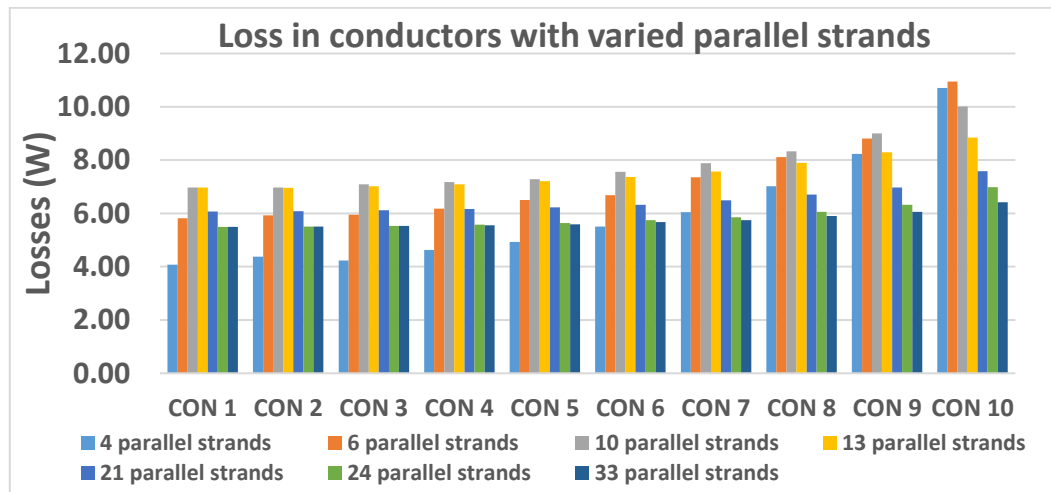
Number of parallel strands	Strand Copper diameter (mm)	Total strands per slot	Slot Filling Factor (%)
4	1.8	80	41.7%
6	1.5	120	43.46%
10	1.18	200	44.82%
13	1	260	41.7%
21	0.8	420	43.26%
24	0.75	480	43.46%
33	0.63	660	42.16%

### 3.3.1. Losses in conductors

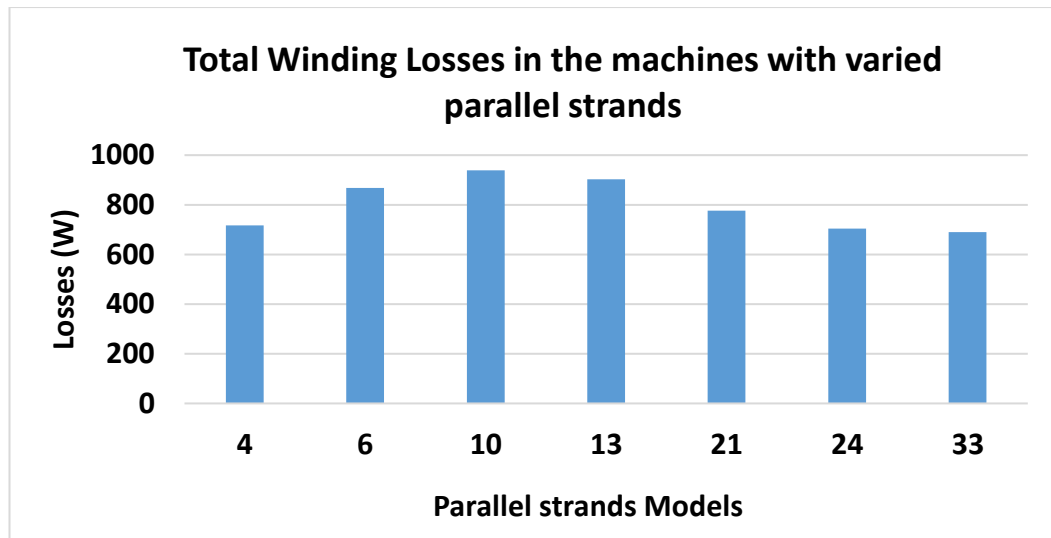
**TABLE 3.4: Losses in the conductors for models with varied number of parallel strands (ARR1)**

Pr. St ds	CON 1	CON 2	CON 3	CON 4	CON 5	CON 6	CON 7	CON 8	CON 9	CON 10	Total Loss (W)
4	4.07	4.38	4.23	4.63	4.93	5.50	6.05	7.02	8.23	10.70	716.92
6	5.81	5.92	5.95	6.18	6.50	6.68	7.35	8.11	8.81	10.94	867.36
10	6.98	6.97	7.09	7.18	7.28	7.56	7.88	8.33	9.01	10.02	939.33
13	6.97	6.96	7.02	7.10	7.22	7.37	7.57	7.89	8.29	8.85	902.75
21	6.07	6.09	6.12	6.16	6.23	6.32	6.49	6.71	6.98	7.58	776.96
24	5.49	5.50	5.53	5.57	5.64	5.74	5.85	6.06	6.33	6.99	704.52
33	5.50	5.51	5.53	5.56	5.59	5.67	5.75	5.90	6.06	6.41	689.89

\* Pr. Stds = Number of parallel strands



(a)



(b)

Fig. 3.6: (a) Losses in individual conductors with varied number of parallel strands, (b) total losses in the machine winding with varied parallel strands

TABLE 3.4 shows the losses in the individual conductors for the models with varied number of parallel strands. In this table, the column highlighted in green lists the models with varied parallel strands. The column highlighted in yellow shows losses in individual conductors for the models, while the column in blue lists the total AC + DC losses in the winding of the models. Fig. 3.6a shows the losses in the conductors for the models and Fig. 3.6b shows the total losses in the machine winding (active length of winding) for the models in the form of bar plots. The DC ohmic loss in the winding of the models is 412 W. In fig. 3.6a, the general trend suggests that as the conductors get positioned closer to the slot top (towards the slot opening, where flux leakage is higher), the losses in the individual conductors increase. This is true across all the models with varied number of parallel strands i.e. the losses in individual conductors increase from conductor 1 to conductor 10. In addition, the trend suggests that as the number of parallel strands forming a conductor increase, the difference in the losses in the conductors at the slot top and slot bottom gradually decrease. This is evident from Fig. 3.6a, where there is 162.74%

increase in the losses in conductor 10 as to the losses in conductor 1 for model with 4 parallel strands, whereas in case of model with 33 parallel strands, the increase in the losses in conductor 10 to the losses in conductor 1 is 16.64%. Fig. 3.6a also indicates that as compared to the losses in the conductors (1 – 6) for the model with 4 parallel strands, the losses in the individual conductors (1 – 6) for other models are higher. This may be due to the increasing effect of circulating current within the strands as the number of parallel strands in the models increase and will be investigated in later sections.

### 3.3.2. (AC+DC) /DC Loss ratio

**TABLE 3.5: (AC+DC) /DC loss ratio (ARR1)**

MODELS	(AC+DC)/DC loss ratio
4 parallel strands	1.74
6 parallel strands	2.20
10 parallel strands	2.45
13 parallel strands	2.20
21 parallel strands	2.05
24 parallel strands	1.78
33 parallel strands	1.75

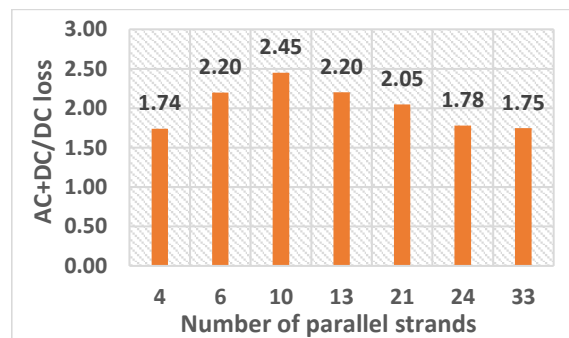


Fig 3.7: (AC+DC) /DC loss ratio (ARR1)

Table 3.5 and Fig. 3.7 shows the (AC+DC)/DC loss ratio for each model. The loss ratio trends suggest that as the parallel strands increases the (AC+DC)/DC loss ratio increases and then it decreases again. The maximum (AC+DC)/DC loss ratio is in the case of 10 parallel strands model with AC+DC loss value 2.45 times greater than the DC loss. This might be because of the combined effect of higher skin effect in the relatively larger strands in the models with fewer parallel strands (model with 10 or 13 parallel strands compared to 24 or 33 parallel strands) and the circulating currents within the strands. To investigate the cause of skin effect, using Eq. (2.17)

the skin depth is calculated to be 2.59 mm at the fundamental frequency of 666.67Hz. This is significantly larger than the strand diameters used in this analysis. Therefore, a question arises, if it is appropriate to neglect the skin and proximity effects for strand diameter smaller than the skin depth as the literature suggests?

### 3.3.3. Investigating the effect of circulating current

To investigate the effect of circulating current in the parallel strands of the models, the current amplitude in each strand of the models is plotted against time. Fig. 3.8 shows the supply current to a phase of the winding and Fig. 3.9 shows the individual strand currents for the models with varied number of parallel strands.

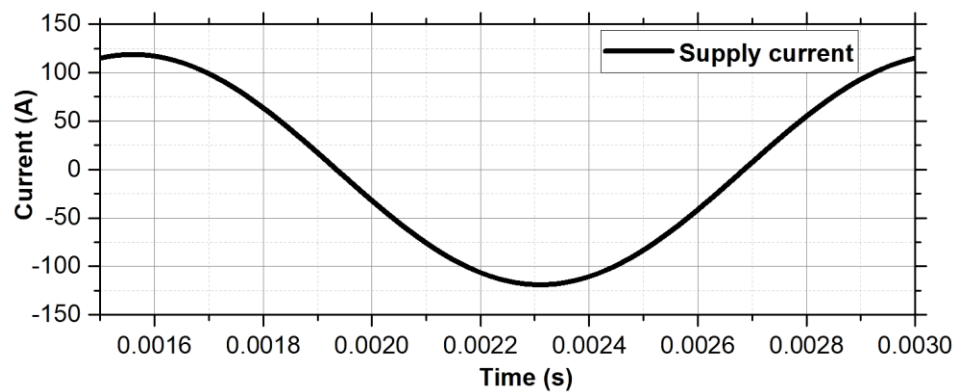
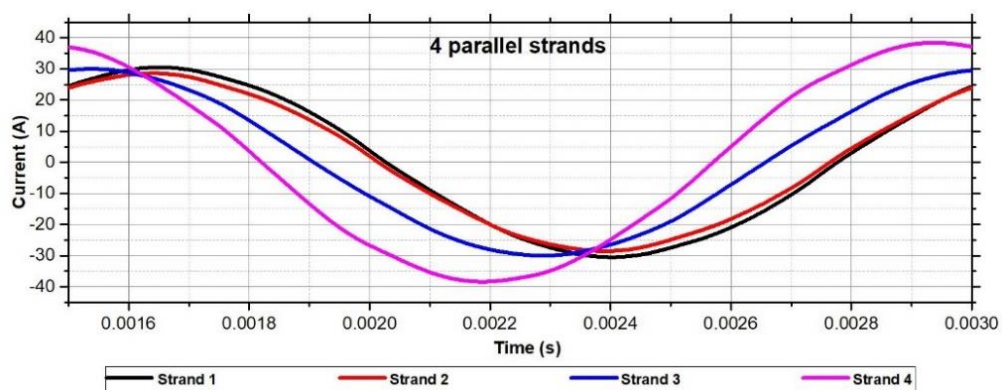
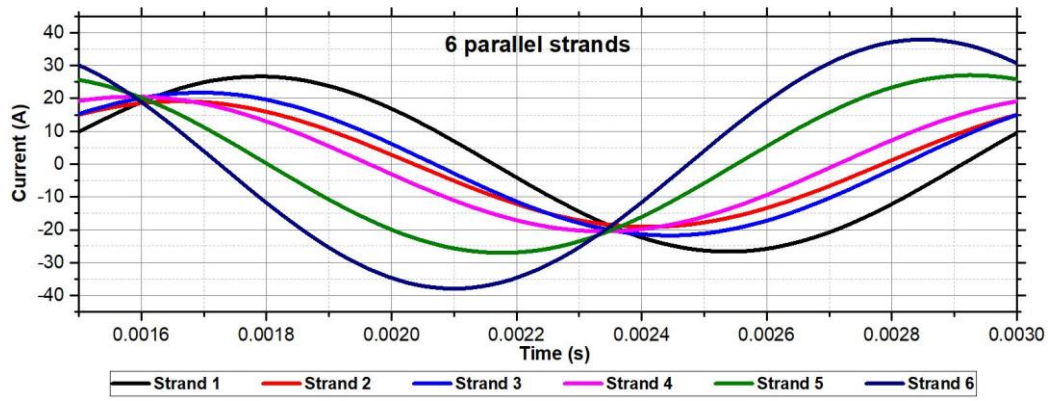


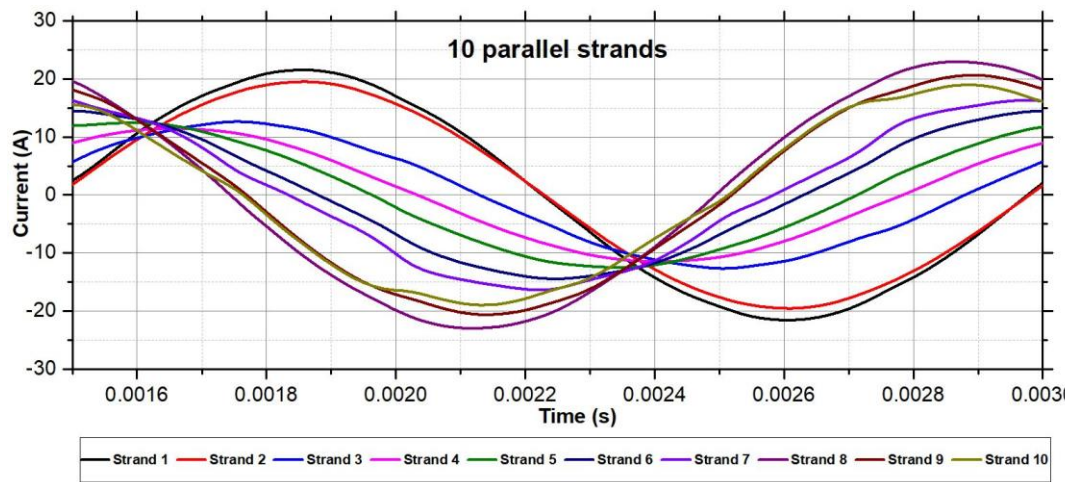
Fig. 3.8: Supply current to the phase - one of winding



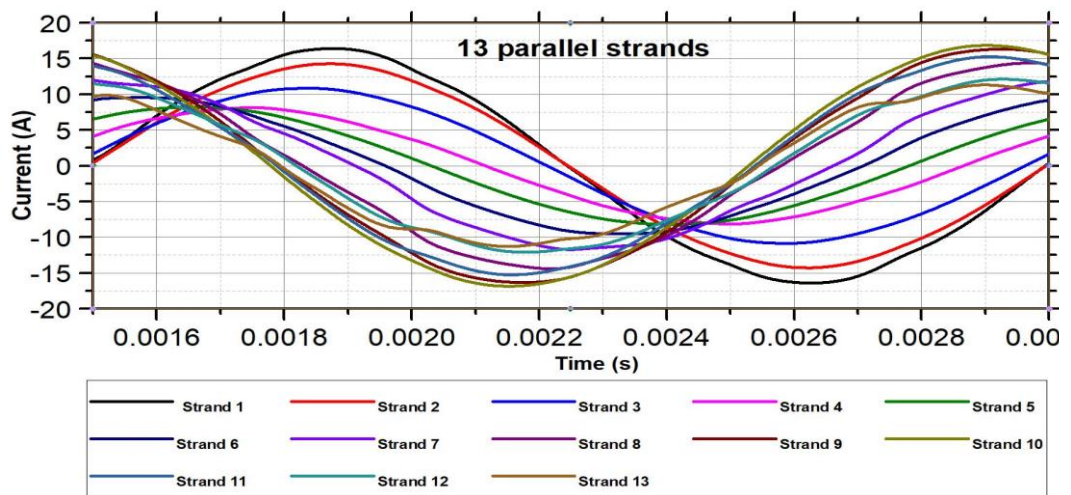
(a)



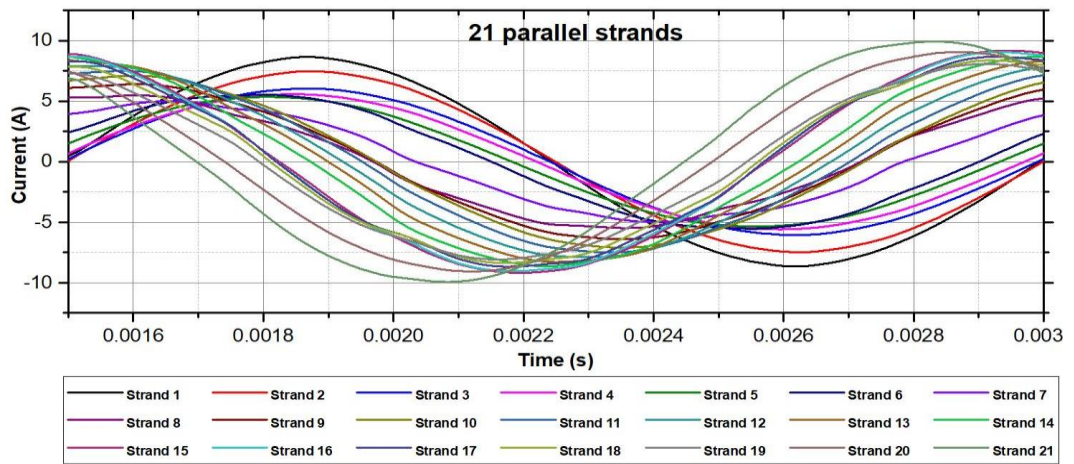
(b)



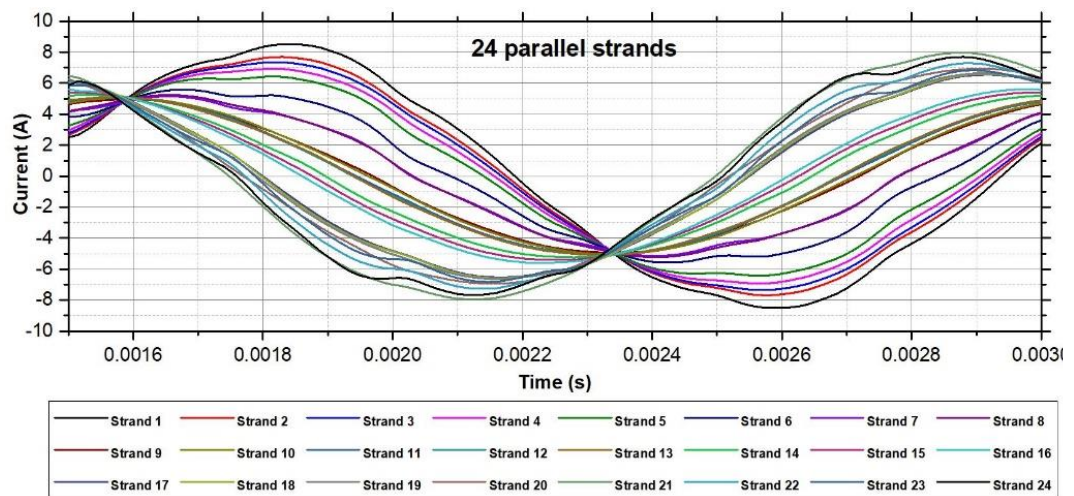
(c)



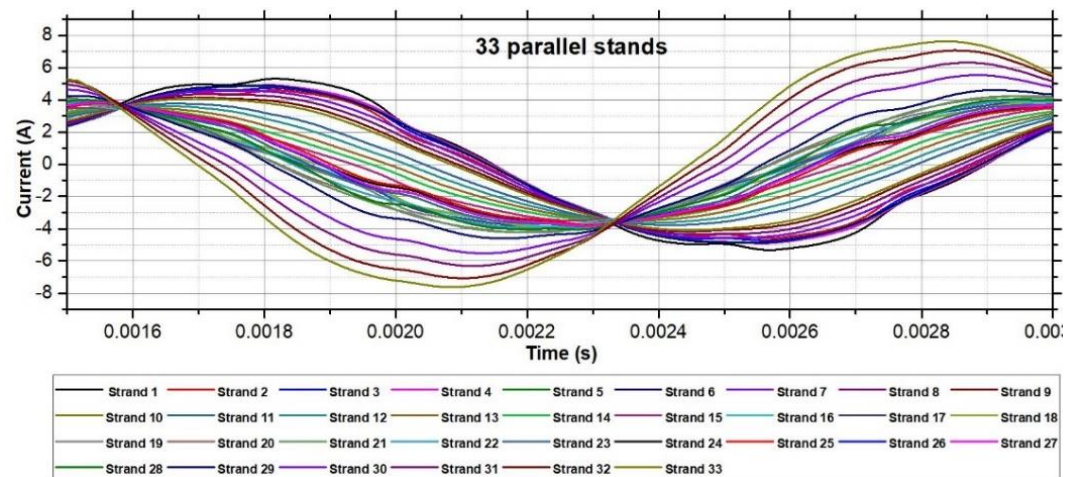
(d)



(e)



(f)



(g)

Fig. 3.9: Individual strand currents for model with varying number of parallel strands

Fig. 3.9 illustrates that the main supply current (reference) is unevenly distributed among the parallel strands and the individual strand current waveforms are displaced

in time as compared to the reference current waveform. This is due to the circulating current in the parallel strands arising from non-uniform flux linkage by the strands in the slots. Although, the trend is not very definitive, it can be said that the circulating current effect become more prominent with increasing number of strands. TABLE 3.6 lists the percentage deviation of the maximum and minimum current amplitude in the parallel strands of the models and the maximum percentage deviation of the strand current from the ideal strand current.

**TABLE 3.6: Deviation of strand currents**

<b>MODELS</b>	<b>% dev. (max. and min. current carrying strands)</b>	<b>Max % dev. (from ideal strand current)</b>
4 parallel strands	34.45	29.38
6 parallel strands	98.44	91.68
10 parallel strands	100.8	93.38
13 parallel strands	106.69	84.23
21 parallel strands	99.09	75.63
24 parallel strands	72.06	71.96
33 parallel strands	121.1	111.97

To mitigate the effects of circulating current, the parallel strands are connected with individual current source as described in subsection 3.2.4 and the methodology carried out in the earlier subsection is repeated for the following cases:

<b>CASES</b>	<b>MODELS</b>
CASE 1	4 parallel strands
CASE 2	6 parallel strands
CASE 3	13 parallel strands
CASE 4	24 parallel strands

**CASE 1: 4 parallel strands (multi – source current supply)****TABLE 3.7: Comparison of losses in conductors using single and multi – source current supply (CASE 1)**

Source	CONDUCTOR NUMBER										Total Loss (W)	(AC+DC) /DC loss
	1	2	3	4	5	6	7	8	9	10		
single	4.07	4.38	4.23	4.63	4.93	5.5	6.05	7.02	8.23	10.7	716.92	1.74
multi	3.5	3.8	3.66	4.05	4.36	4.94	5.49	6.48	7.73	10.3	651.54	1.58

\* single = single source, multi = multi - source

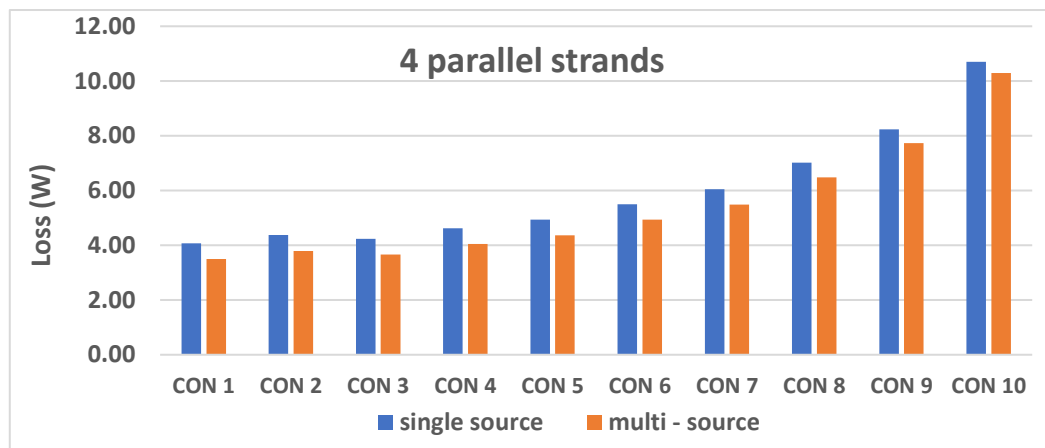


Fig. 3.10: Losses in conductors with single and multi – source supply for model with 4 parallel strands

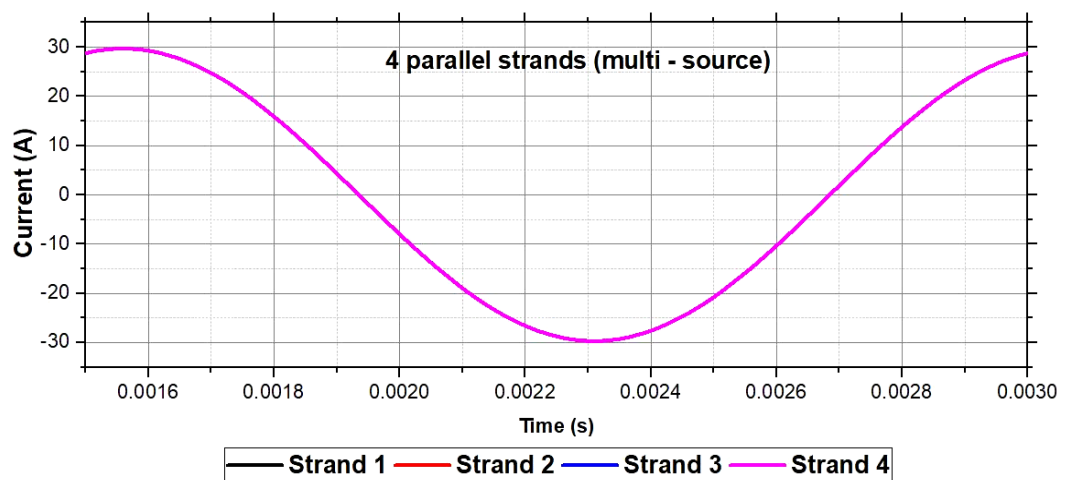


Fig. 3.11: Individual strand current with multi – source supply in 4 parallel strands model

TABLE 3.7, Fig. 3.10 and Fig. 3.11 summarize the results using multi – source current supply. In TABLE 3.7 and Fig. 3.10, the comparison of losses in the conductors with single – source and multi – source current supplies is presented along with the (AC+DC)/DC loss ratio. By mitigating the circulating current effects, the total loss reduces by 9.1% for the model with multi – source current supplies. Fig. 3.11 shows the individual strand currents that superimpose in the event of absence of circulating currents.

**CASE 2: 6 parallel strands (multi – source current supplies)**

**TABLE 3.8: Comparison of losses in conductors using single and multi – source current supply (CASE 2)**

Source	CONDUCTOR NUMBER										Total Loss (W)	(AC+DC)/DC loss
	1	2	3	4	5	6	7	8	9	10		
single	5.81	5.92	5.95	6.18	6.5	6.68	7.35	8.11	8.81	10.94	867.36	2.196
multi	3.36	3.47	3.5	3.73	4.06	4.25	4.93	5.68	6.41	8.52	574.93	1.455

\* single = single source, multi = multi - source

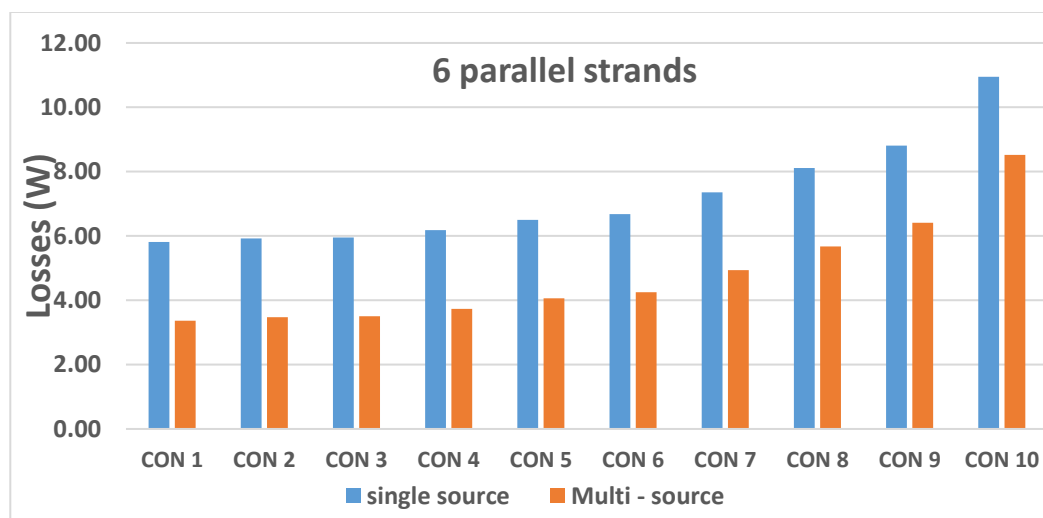


Fig. 3.12: Losses in conductors with single and multi – source supply for model with 6 parallel strands

In TABLE 3.8 and Fig. 3.12, the comparison of losses in the conductors with single – source and multi – source current supplies is presented along with the (AC+DC)/DC loss ratio for model with 6 parallel strands. By mitigating the circulating current effects, the total loss reduces by 33.7% for the model with multi – source current supplies.

**CASE 3: 13 parallel strands (multi – source current supplies)**

**TABLE 3.9: Comparison of losses in conductors using single and multi – source current supply (CASE 3)**

Source	CONDUCTOR NUMBER										Total Loss (W)	(AC+DC) /DC loss
	1	2	3	4	5	6	7	8	9	10		
<b>single</b>	6.97	6.96	7.02	7.1	7.22	7.37	7.57	7.89	8.29	8.85	902.75	2.2
<b>multi</b>	3.47	3.46	3.53	3.61	3.73	3.88	4.09	4.42	4.84	5.42	485.65	1.18

\* single = single source, multi = multi - source

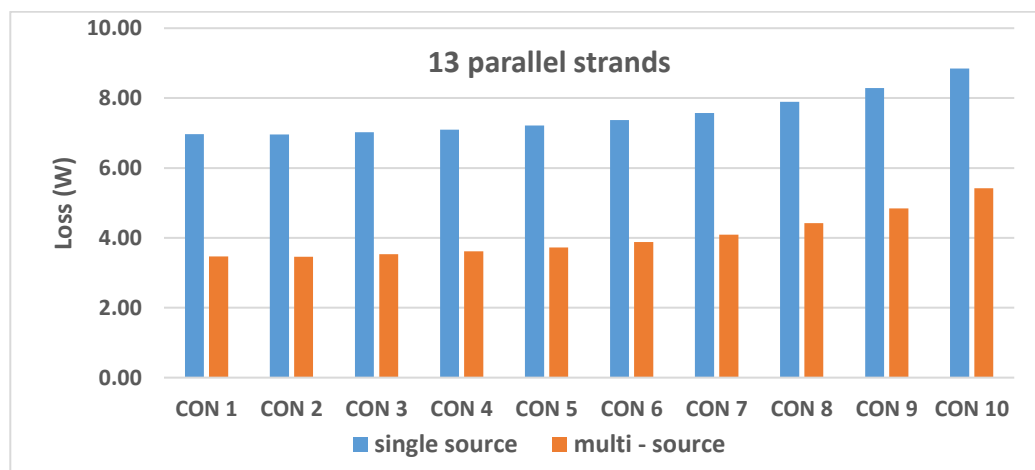


Fig. 3.13: Losses in conductors with single and multi – source supply for model with 13 parallel strands

In TABLE 3.9 and Fig. 3.13, the comparison of losses in the conductors with single – source and multi – source current supplies is presented along with the (AC+DC)/DC loss ratio for model with 13 parallel strands. The total loss for this case reduces by 46.2%.

**CASE 4: 24 parallel strands (multi – source current supplies)****TABLE 3.10: Comparison of losses in conductors using single and multi – source current supply (CASE 4)**

Source	CONDUCTOR NUMBER										Total Loss (W)	(AC+DC) /DC loss
	1	2	3	4	5	6	7	8	9	10		
<b>single</b>	5.49	5.5	5.53	5.57	5.64	5.74	5.85	6.06	6.33	6.99	704.52	1.78
<b>multi</b>	3.32	3.33	3.35	3.4	3.47	3.57	3.68	3.9	4.17	4.89	445.06	1.13

\* single = single source, multi = multi - source

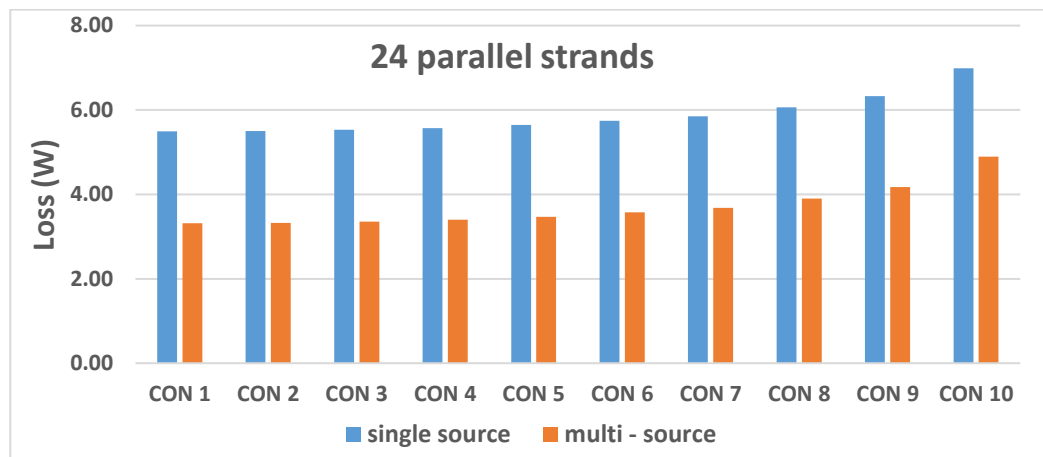


Fig. 3.14: Losses in conductors with single and multi – source supply for model with 24 parallel strands

In TABLE 3.10 and Fig. 3.14, the comparison of losses in the conductors with single – source and multi – source current supplies is presented along with the (AC+DC)/DC loss ratio for model with 24 parallel strands. The total loss for this case reduces by 36.52%.

### 3.3.4. Comparison of the cases

The total loss in the conductor is the summation of DC loss and the additional loss due to AC effects, i.e.

$$P_{Total} = P_{DC} + P_{AC} \quad (3.1)$$

Where,

$$P_{AC} = P_{skin\ and\ proximity} + P_{circulating\ current} \quad (3.2)$$

Therefore,

$$P_{Total} = P_{DC} + P_{skin\ and\ proximity} + P_{circulating\ current} \quad (3.3)$$

Where

$P_{Total}$  is the actual resistive loss

$P_{DC}$  is the ideal resistive loss from dc approximation

### ***Comparison of CASE 1 and CASE 3***

Comparing CASE 1 (4 parallel strands model) and CASE 3 (13 parallel strands model), both CASES have the slot fill factor of 41.7% and total DC loss in the winding for each model is 412 W. However, with the single current source (AC+DC)/DC loss ratio are 1.74 for CASE 1 model and 2.2 for CASE 3. When the losses due to circulating currents are eliminated using multi - current sources, the (AC+DC)/DC loss ratio drops to values of 1.58 for CASE 1 and 1.18 for CASE 3. This means for CASE 3, skin and proximity effects only added an extra of 18% in addition to the DC losses while for CASE 1 the additional loss is as high as 58%. The breakup of the losses into its components is summarised in Fig. 3.15.

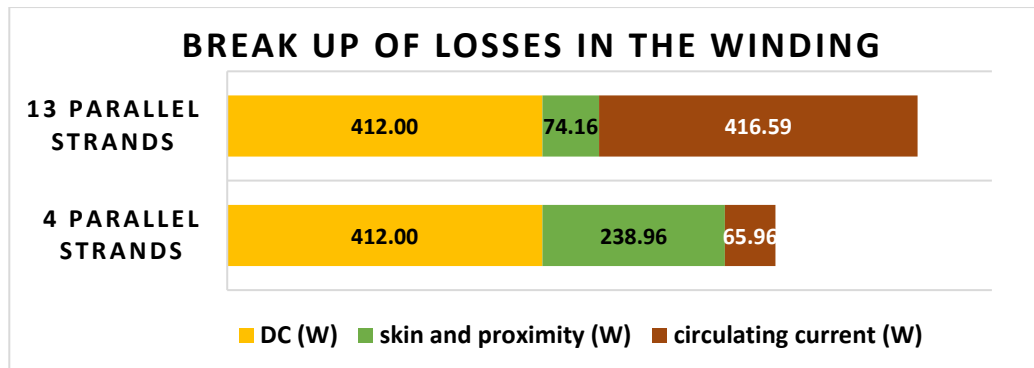


Fig. 3.15: Breakup losses in the winding (CASE 1 and CASE 3)

### *Comparison of CASE 2 and CASE 4*

Comparing CASE 2 (6 parallel strands model) and CASE 4 (24 parallel strands model), both CASES have the slot fill factor of 43.46% and total DC loss in the winding for each model is 395 W. However, with the single current source (AC+DC)/DC loss ratio are 2.196 for CASE 2 model and 1.78 for CASE 3. When the losses due to circulating currents are eliminated using multi - current sources, the (AC+DC)/DC loss ratio drops to values of 1.455 for CASE 1 and 1.13 for CASE 4. This means for CASE 2, skin and proximity effects added an addition loss of 45.5% along with the DC losses while for CASE 4, the additional loss is mere 13%. This breakup of the losses into the components is summarised in Fig. 3.16.

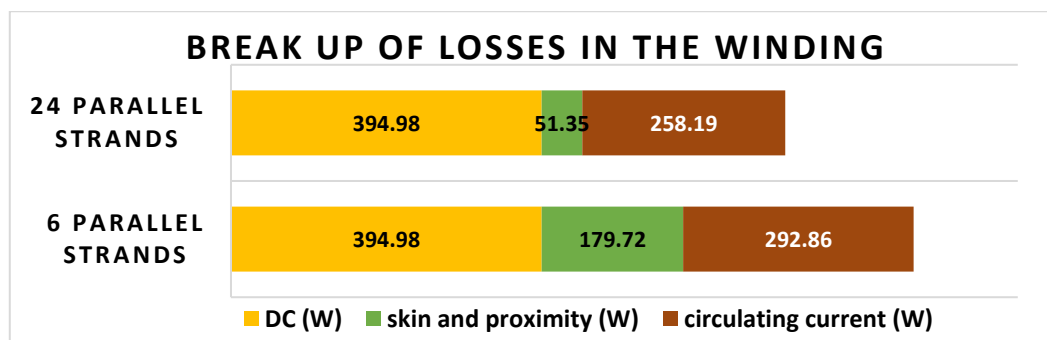


Fig. 3.16: Breakup losses in the winding (CASE 2 and CASE 4)

*Discussion and Conclusion***TABLE 3.11: AC Loss in percentage of total loss in the winding of the machine**

Case	Total Loss	Skin and proximity (W)	Circulating current (W)	Skin and proximity (% of total loss)	Circulating current (% of total loss)
Case 1	716.92	238.96	65.96	33.33	9.2
Case 2	867.56	179.72	292.86	20.72	33.76
Case 3	902.75	74.16	416.59	8.21	46.15
Case 4	704.52	51.35	258.19	7.29	36.65

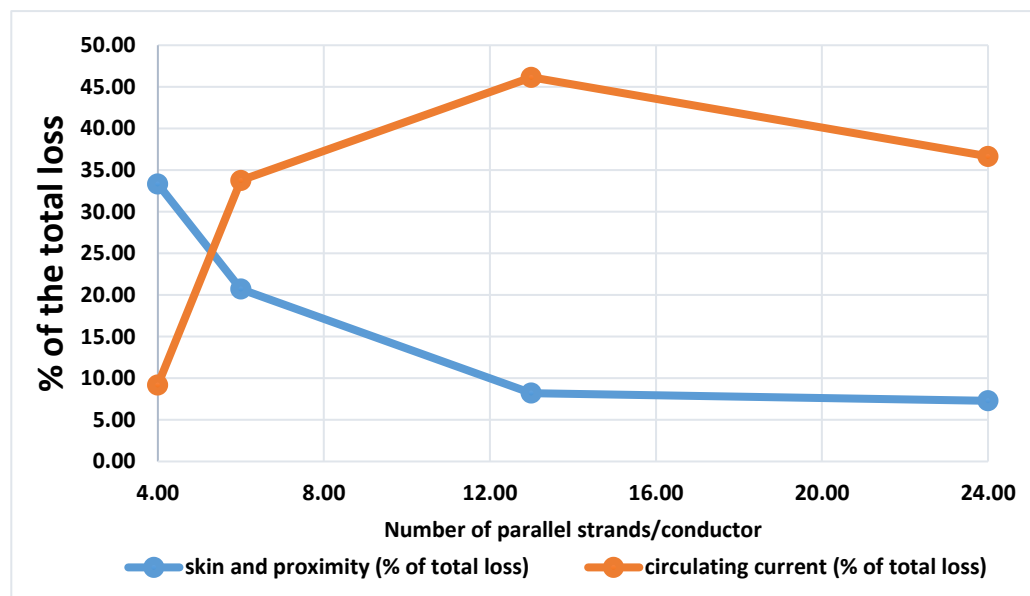


Figure: 3.17: Trend of skin & proximity losses and circulating current losses with increasing number of parallel strands

TABLE 3.11 and Fig. 3.17 shows the breakup of the AC losses in percentage of total loss in the winding for each case. A question was raised in subsection 3.3.2 as to whether it is safe to neglect the skin and proximity effects for strand diameter smaller than the skin depth as the literature suggests? The analysis presented in TABLE 3.11 and Fig. 3.17 suggests although the strand diameters considered were

significantly smaller than the skin depth, the losses due skin and proximity effects cannot be neglected. However, these losses reduce significantly, as the strand diameter gets thinner. Moreover, the combination of skin and proximity effects, and circulating currents resulted in significant increase in (AC+DC)/DC loss ratio for models with (6 – 21) parallel strands.

**TABLE 3.12: Peak current in strand due to circulating current**

Case	Strand number	Ideal current (A peak)	Single source (A peak)	Single/ideal ratio
Case 1	4	29.7	38.42	1.29
Case 2	6	19.8	37.4	1.89
Case 3	1	9.14	16.83	1.84
Case 4	1	4.95	8.45	1.71

TABLE 3.12 lists the strand number for the cases that carry the maximum current. For case 2 - 4, the strand 6, 1 and 1 respectively are carrying 1.89, 1.84 and 1.71 times the ideal current that it should be carrying if there is no circulating current. This result in hotspot creation, which may lead to machine failure due to insulation deterioration.

### 3.4. Vertical Bundled (ARR2)

The following models are considered for vertical bundled configuration:

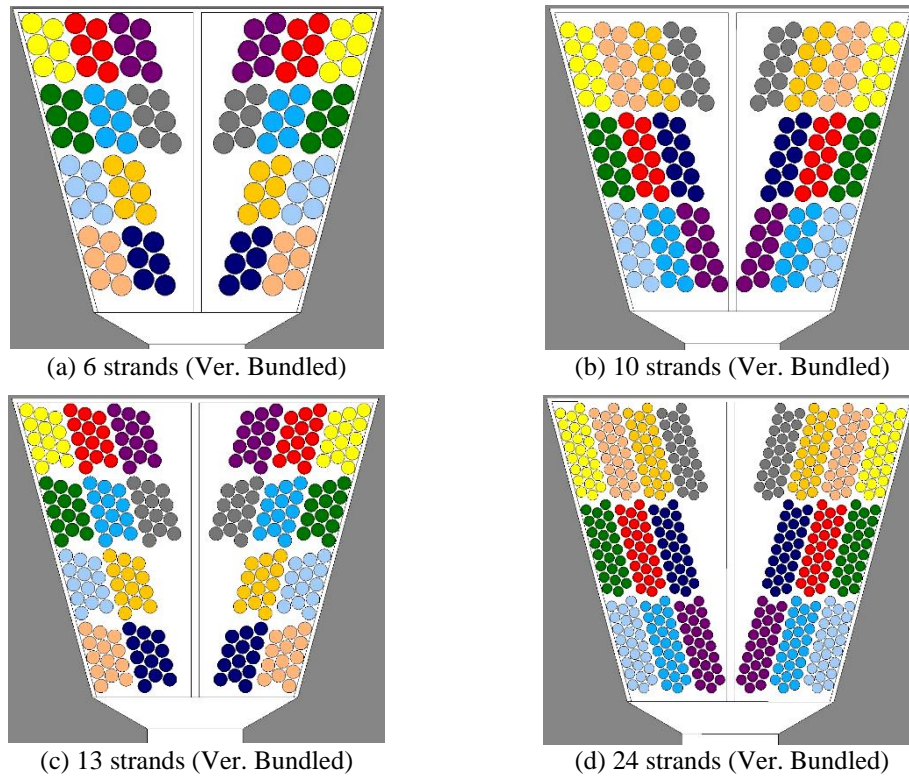


Fig. 3.18: Models with vertical bundled strands

#### 3.4.1. Losses in the conductors

**TABLE 3.13: Losses in conductors for models with varied parallel strands (Ver. Bundled)**

Pr. Stds	CON 1	CON 2	CON 3	CON 4	CON 5	CON 6	CON 7	CON 8	CON 9	CON 10	Total Loss (W)
6	13.21	13.59	14.6	16.24	13.28	13.74	14.96	17.86	13.4	13.92	1737.82
10	17.71	18.1	19.1	17.8	18.2	19.7	17.84	18.3	20.25	17.88	2219.48
13	13.01	13.17	13.63	14.29	13.04	13.24	13.79	15.26	13.09	13.31	1629.96
24	18.7	18.91	19.29	18.8	18.95	19.58	18.81	18.99	19.85	18.82	2289.43

\* Pr. Stds = Number of parallel strands

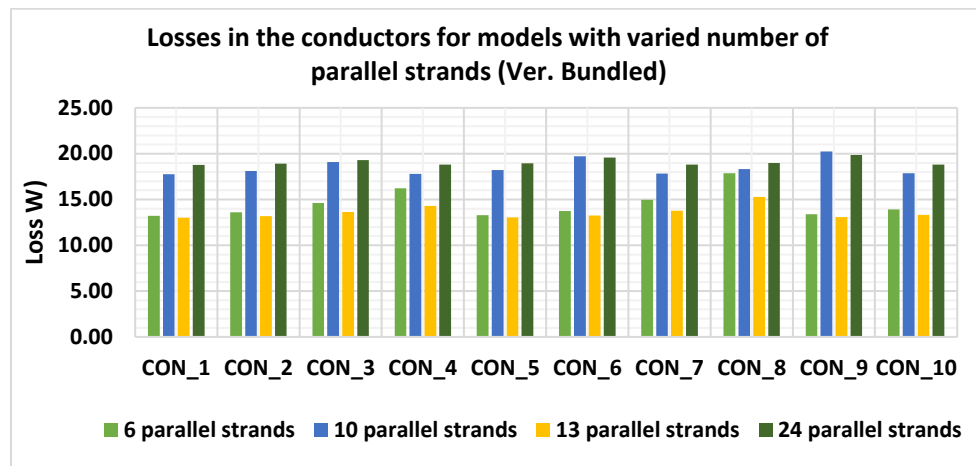


Fig. 3.19: Losses in individual conductors with varied number of parallel strands (Ver. Bundled)

**TABLE 3.14: (AC+DC)/DC loss ratio (Ver. Bundled)**

Models (Ver. Bundled)	(AC+DC) / DC loss
6 parallel strands	4.4
10 parallel strands	5.8
13 parallel strands	3.97
24 parallel strands	5.8

TABLE 3.13 and Fig. 3.19 shows the losses in individual conductors with varied number of parallel strands for models with strands bundled vertically. From Fig. 3.18, it is observed that the conductor closer to the slot top (towards the slot opening), incur more loss compared to the ones towards the slot bottom. This trend is also present in the horizontally placed strands models (ARR1) described in the previous section. TABLE 3.14 lists the (AC+DC)/DC loss ratio, which are high when compared to the ARR1, and is being compared in detailed in later sections.

### 3.4.2. Investigating the effect of circulating current in Vertical bundled configuration

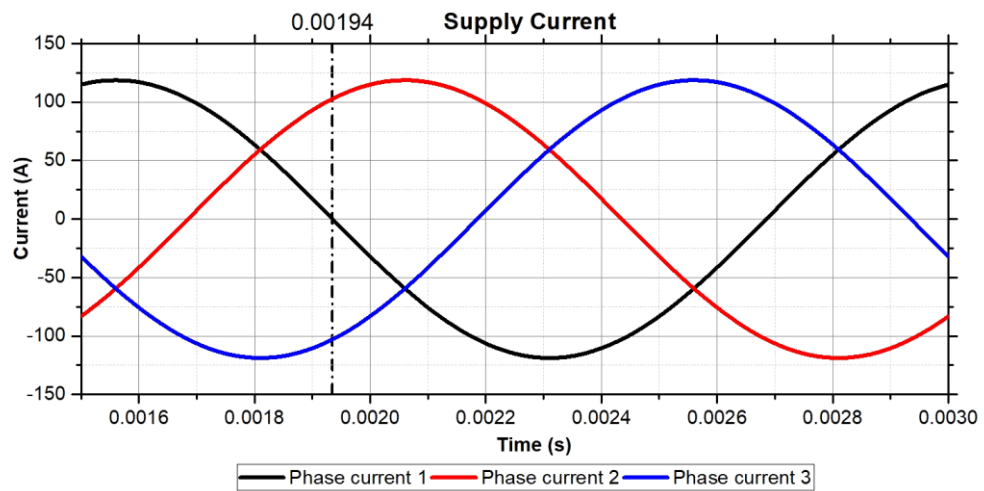
Two models with strands vertically bundled configuration are considered here: 6 parallel strands model (CASE A) and 24 parallel strands model (CASE B).

#### *CASE A: 6 parallel strands model (Ver. Bundled)*

**TABLE 3.15: Comparison of losses in conductors using single and multi – source current supply (CASE A)**

Source	CONDUCTOR NUMBER										Total Loss (W)	AC+DC /DC loss
	1	2	3	4	5	6	7	8	9	10		
<b>single</b>	13.21	13.59	14.62	16.24	13.28	13.74	14.96	17.86	13.4	13.92	1737.82	4.4
<b>multi</b>	3.37	3.85	4.98	6.69	3.46	4.03	5.33	8.32	3.61	4.22	574.45	1.45

\* single = single source, multi = Multi - source



(a)

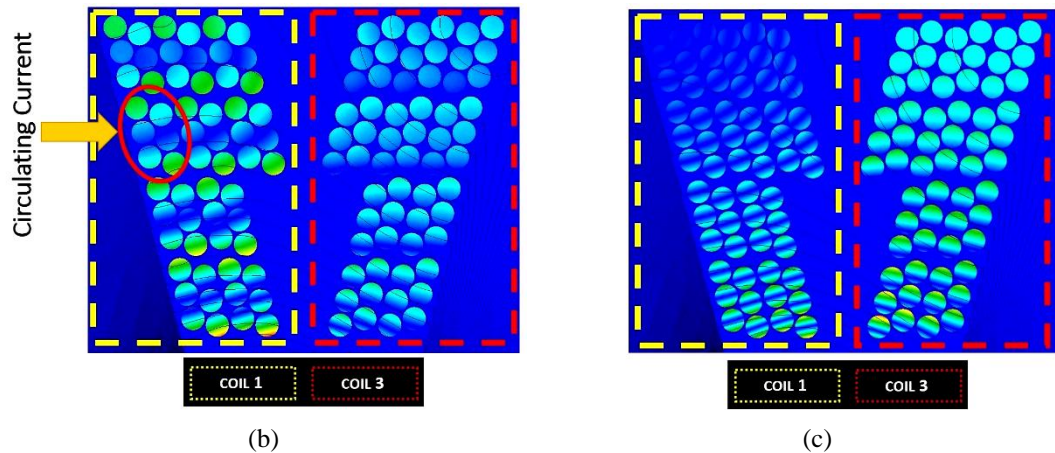


Fig. 3.20: (a) 3 – ph current source waveform, (b) 6 strands single source current density (J) in strands (0.00194s), and (c) 6 strands multi - source current density (J) in strands (0.00194s)

Fig. 3.20 shows the comparison of current density (J) inside the strands for single and multi – source models. At time instant 0.00194 s (marked by dash dot line in Fig. 3.20a), the current in phase A (coil side 1) is zero, while the other two phases have some amplitude. In Fig. 3.20b shows the current density in the strands in a slot from single – source model, while Fig. 3.20c shows the same for the multi – source. In both the subfigures 3.20(b & c), the coil side 1 connected to phase A of the current source is highlighted by enclosing the side in area with yellow dash boundary, while the coil side 3 connected to the phase B of the current source is highlighted by enclosing the coil side in area with red dashed boundary. The Fig. 3.20b shows that at time instant 0.00194s, even when the supply current in phase A is zero, there are currents circulating through the peripheral strands of each bundle. In case of the multi – source model, these currents are absent at the same time instant.

**CASE B: 24 parallel strands model (Ver. Bundled)****TABLE 3.16: Comparison of losses in conductors using single and multi – source current supply (CASE B)**

Source	CONDUCTOR NUMBER										Total Loss (W)	AC+DC /DC loss
	1	2	3	4	5	6	7	8	9	10		
<b>single</b>	18.78	18.91	19.29	18.8	18.95	19.58	18.81	18.99	19.85	18.82	2289.43	5.8
<b>multi</b>	3.32	3.53	3.99	3.34	3.57	3.36	3.36	3.62	4.58	3.39	444.15	1.12

\* single = single source, multi = Multi - source

TABLE 3.16 shows the comparison of losses in conductors using single and multi – source current supplies for CASE B. For single source model, the total losses in the winding are 5.8 times higher than the DC loss value. Eliminating the circulating currents in the strands, the (AC+DC)/DC Loss ratio drops to 1.12.

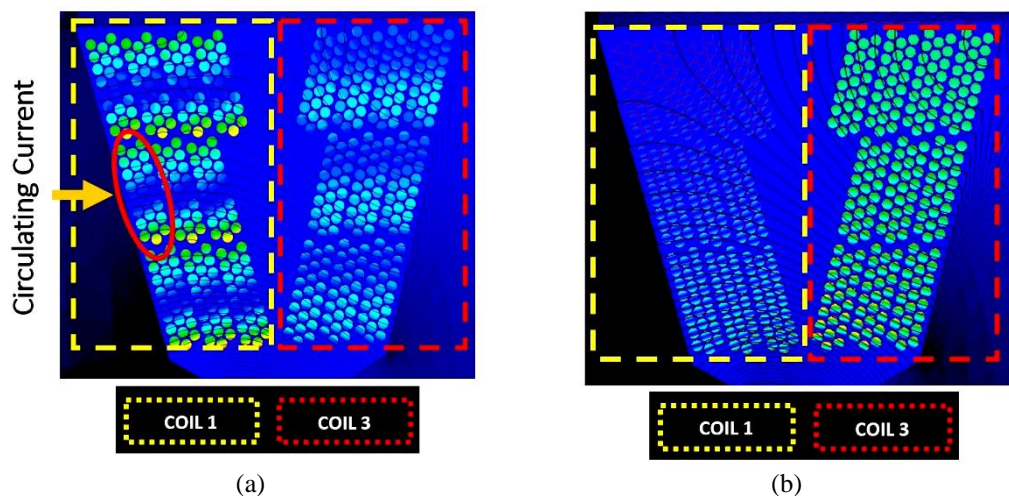


Fig. 3.21: (a) 24 strands single source current density (J) in strands (0.00194s), (b) 24 strands multi - source current density (J) in strands (0.001934s)

Similar as in CASE A, Fig. 3.21 shows the comparison of current densities in the strands for CASE B models with single and multi – source current supplies. At time instant 0.00194s, when the applied current in coil 1 is zero, circulating currents flowing through the peripheral strands of the bundles are present as shown in Fig.

3.21a. Again, this circulating current effect is absent in multi – source model (shown in Fig. 3.21b).

### **3.4.3. Conclusion**

The above sections showed that, bundling the strands in vertical configuration resulted in high losses in the winding of the machine. These additional losses were largely due to contribution from the bundle – level losses that are caused by the current circulating in parallel strands of the conductors. Eliminating the circulating current effects in the strands as in for CASE A and CASE B reduce the losses significantly and are comparable to the losses obtained in case of horizontal configuration. This demonstrates that the skin and proximity effect losses are not affected significantly by the shape and position of the bundles inside the slot geometry.

### **3.5. Horizontal Bundled (ARR3)**

For this arrangement, only the model with 6 parallel strands is considered as the circulating current effects for models with lesser parallel strands is insignificant. Because of the slot geometry constraints, models with higher number of parallel strands in horizontal bundled configuration is not feasible and is not being considered in the analysis. Fig. 3.22 shows the model with 6 parallel strands with bundles configured in horizontal direction.

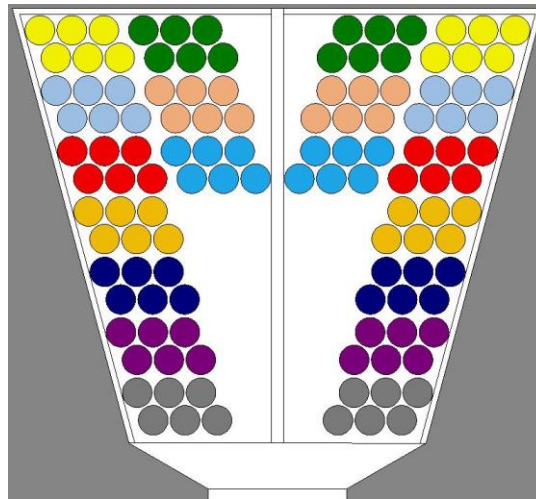


Fig. 3.22: Horizontal bundled configuration with 6 parallel strands

**TABLE 3.17: Comparison of losses in the conductors and AC+DC/DC loss ratio with single and multi – source current supplies (Hor. Bundled)**

Source	CONDUCTOR NUMBER										Total Loss (W)	AC+DC /DC loss
	1	2	3	4	5	6	7	8	9	10		
<b>single</b>	8.51	8.66	8.69	8.89	9.11	9.44	9.75	10.57	11.66	13.79	1188.7	3.01
<b>multi</b>	3.35	3.54	3.55	3.77	3.99	4.34	4.66	5.48	6.60	8.77	576.42	1.46

\* single = single source, multi = Multi - source

TABLE 3.17 shows the comparison of losses in the conductors with the loss ratio comparison for 6 parallel strands (Hor. Bundled) models with single and multi – source current input. Similar to case of vertical bundled configuration (ARR2), when the circulating current effects are eliminated, the losses in the winding become comparable to the horizontal and vertical bundled configurations. A detailed comparative analysis of this is carried out in the next section.

### 3.6. Comparison of loss components in the configurations

In this section, the losses in the winding are segregated into its constitutive components and are compared for all the three arrangements. The analysis is carried

out using the results from the 6 parallel strands model for all three strands/bundles arrangements.

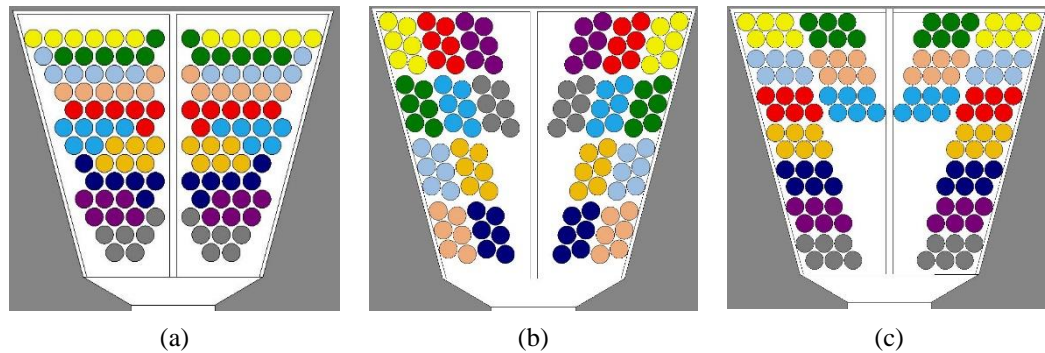


Fig. 3.23: 6 parallel strands model with (a) Horizontal, (b) Vertical bundled, (c) Horizontal bundled

**TABLE 3.18: Comparison of loss components for ARR1, ARR2 and ARR3**

Arrangement	Total Loss(W)	DC Loss (W)	Skin and Proximity Loss (W)	Circulating Current Loss (W)
<b>Horizontal (ARR1)</b>	867.56	394.88	179.72	292.86
<b>Vertical Bundled (ARR2)</b>	1737.82	394.88	177.7	1165.24
<b>Horizontal Bundled (ARR3)</b>	1188.7	394.88	181.84	612.28

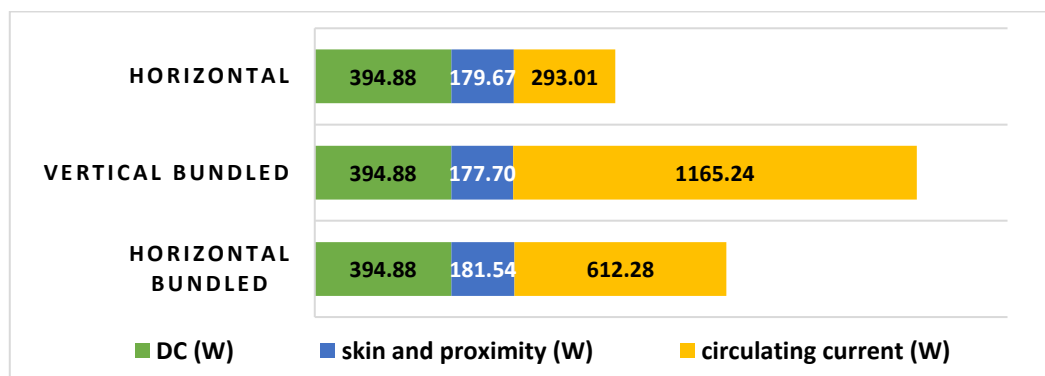


Fig. 3.24: Breakup of losses in the winding into its components for ARR1, ARR2 and ARR3

Let,

$$P_{skin\ and\ proximity} = P_{SP}$$

$$P_{circulating\ current} = P_{cc}$$

Dividing both sides of eq. (3.3) by  $P_{DC}$ , we get

$$\frac{P_{Total}}{P_{DC}} = \frac{P_{DC}}{P_{DC}} + \frac{P_{SP}}{P_{DC}} + \frac{P_{cc}}{P_{DC}} \quad (3.4)$$

Therefore, the ratio of each loss component in the strands to the DC loss for the three arrangements can be listed as in TABLE 3.19.

**TABLE 3.19: Comparison of segregated loss components to DC loss ratio for the winding arrangements**

	<b>ARR1</b>	<b>ARR2</b>	<b>ARR3</b>
$(AC + DC)/DC$	2.196	4.4	3.01
$P_{DC}/P_{DC}$	1	1	1
$P_{SP}/P_{DC}$	0.456	0.45	0.46
$P_{cc}/P_{DC}$	0.74	2.96	1.56

TABLE 3.19 shows that the skin and proximity effects losses in the strands do not significantly depend on the shape and position of the bundles, as these losses for all the three arrangements are approximately similar. However, the circulating currents are very sensitive to the bundle shape and careful consideration should be made while laying the bundled conductors in the slot. The data also shows that the ARR1 causes the least increase of AC effects in the winding, followed by ARR3 and the worst configuration being the ARR2. Although, the ARR1 would be ideal for lower

loss in winding of the machine, in practice, arranging the strands of a random – wound machine as ARR1 is impractical. In case of ARR3, the losses are comparatively lesser than ARR2. However, it does not provide flexibility in terms of configuring the bundles in the given slot geometry. Therefore, a trade – off between all three arrangements with the least loss would be an optimal solution.

### 3.7. Proof for $P_{Total} = P_{DC} + P_{skin\ and\ proximity} + P_{circulating\ current}$

According to [62], [63], if skin and proximity effect losses are neglected, the circulating current losses  $P_{cc}$ , can be obtained as

$$P_{cc} = P_{Total} - P_{DC} \quad (3.5)$$

The circulating current loss factor,  $k_{cc}$ , is a practical indicator of the circulating current losses and is the ratio between  $P_{Total}$  and  $P_{DC}$ , i.e. it is equal to the loss produced in the case where circulatory current exists relative to the situation where the sum of the current is equally divided between the strands.

The loss factor,  $k_{cc}$  can be obtained as

$$k_{cc} = N_p \frac{\sum_{n=1}^{N_p} \left| \underline{i}_n \right|^2}{\left| \sum_{n=1}^{N_p} \underline{i}_n \right|^2} = \frac{P_{Total}}{P_{DC}} = \frac{P_{cc} + P_{DC}}{P_{DC}} \quad (3.6)$$

Where,

$N_p$  is number of parallel strands

$\dot{i}_n$  is the complex value of current in strand  $n$

Now, let's consider the 6 parallel strands model with ARR2 configuration (ver. Bundled). Since, the strand diameter is less than the skin depth at the fundamental frequency, assume that the skin and proximity effect losses are mitigated and can be neglected. Therefore, using equation (3.6) for the model we obtained  $k_{cc} = 3.96$ . In

the absence of skin and proximity effect the value of  $k_{cc}$  should be same as  $\frac{P_{Total}}{P_{DC}}$

from equation (3.4). However, for this particular model,  $\frac{P_{Total}}{P_{DC}} = 4.4$ .

From equation (3.6),

$$\frac{P_{cc}}{P_{DC}} = k_{cc} - \frac{P_{DC}}{P_{DC}} \quad (3.7)$$

Using equation (3.7) in (3.4) for this model we get,

$$\frac{P_{SP}}{P_{DC}} = \frac{P_{Total}}{P_{DC}} - \frac{P_{DC}}{P_{DC}} - \frac{P_{cc}}{P_{DC}} = 0.44 \quad (3.8)$$

Now, from multi – source model, where there is no circulating current, we have,

$\frac{P_{Total}}{P_{DC}} = 1.45$ . With no circulating current equation (3.4) can be written as

$$\frac{P_{Total}}{P_{DC}} = \frac{P_{DC}}{P_{DC}} - \frac{P_{SP}}{P_{DC}} \quad , P_{cc} = 0 \quad (3.9)$$

Therefore,  $\frac{P_{SP}}{P_{DC}} = 0.45$ . This is approximately close to the value obtained in equation

(3.8). Repeating the above methodology for other models, we get following as listed in the TABLE 3.20.

**TABLE 3.20: Verification using some of the models**

MODEL	$\frac{P_{Total}}{P_{DC}}$	$k_{cc}$	$\frac{P_{SP}}{P_{DC}}$ (calculated)	$\frac{P_{SP}}{P_{DC}}$ (multi – source)
6 strands (ARR2)	4.4	3.96	0.44	0.45
24 strands (ARR2)	5.8	4.67	0.13	0.12
4 strands (ARR1)	1.74	1.175	0.565	0.58
6 strands (ARR1)	2.196	1.74	0.456	0.455
13 strands (ARR1)	2.2	2.024	0.176	0.18
24 strands (ARR1)	1.78	1.66	0.12	0.13

The value of  $\frac{P_{SP}}{P_{DC}}$  calculated using eq. (3.8) and eq. (3.9) seems to be close. Thus,

the following conclusions can be made:

- The skin and proximity effect cannot be neglected for straight conductors, even when the strand diameter is smaller than the skin depth.
- The losses in the strands of the winding can be segregated into its components using  $P_{Total} = P_{DC} + P_{skin\ and\ proximity} + P_{circulating\ current}$

### 3.8. Conclusion

In this chapter, the sensitivity of AC losses in the winding with varying strand numbers were analysed for an existing prototype traction machine. A methodology to segregate the total loss in the winding into components was described. Three different winding configurations (ARR1 – AAR3) were studied and the circulating current associated with them were investigated. Comparative case studies were made for some models and it is shown that even with strand diameter smaller than the skin depth, the skin and proximity effect exist, albeit these rapidly reduce with decrease in the strand diameter. It is also shown by comparative analyses of the strands/bundles configurations that while the skin and proximity is largely independent of the bundle shape and position, the circulating current is significantly affected by the shapes of the bundle. Finally, it is presented by proving that the loss segregation equation holds true and re – confirmed that even with strands' diameter less than skin depth, the skin and proximity effects cannot be neglected.

## Chapter 4

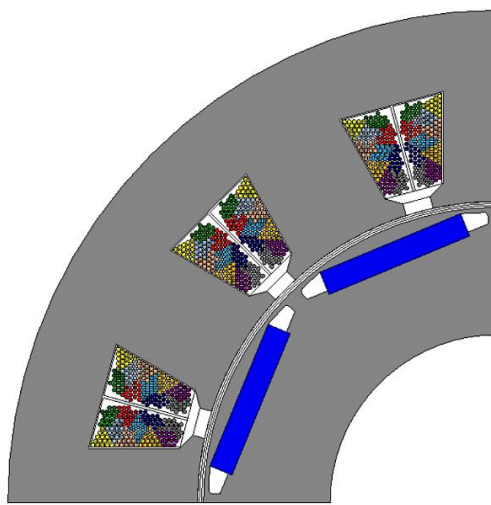
# Optimisation of winding height in the slot for minimum winding loss

Maximizing the slot filling factor decrease the DC loss. However, authors in [30] have shown that it is beneficial to not fill the complete slot and place the strands towards the slot bottom. In the previous works, optimisation of strand diameter and bundling with the winding height hasn't been considered. In this chapter, optimisation is carried out considering both strand diameter and winding height. Besides, the strands are grouped together in bundles to resemble randomly wound winding.

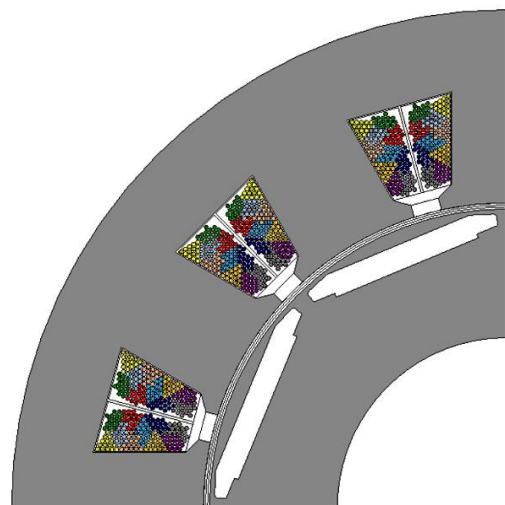
## 4.1. Model Simplification

Finite – element analysis of the strand – level models provide accurate estimation of the AC losses in the winding of the machine. However, it is computationally highly expensive with regards to the time required and at times not possible. In order to reduce the computation time, simplification of models is desired. Simplification of models often means a trade – off between computation time and calculation accuracy and for this purpose, an investigation has been made in this section on how the models can be simplified for faster solving time without a significant loss in accuracy. The same prototype machine dimensions as described in the previous chapter is being used and the process of simplification of the models are realised in stages with the results of each stage compared comprehensively.

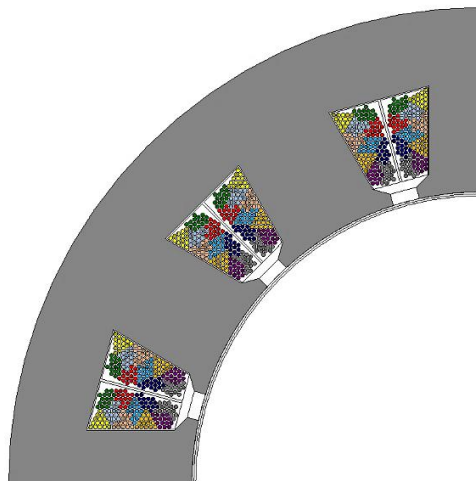
Fig. 4.1 shows the comparison of different modelling depth for simplification of modelling. The first level of simplification involves modelling all the strands within the slots while exploiting periodic symmetry as common with the FEA analysis of all electrical machines, as shown in Fig. 4.1a, where a quarter of the machine is modelled. This is used as a baseline for evaluating the loss of accuracy with further simplification levels, as shown in Fig. 4b to Fig. 4e, and subsequently quantified in TABLE 4.1.



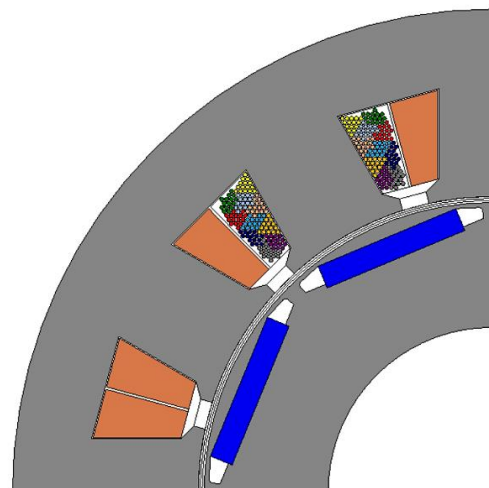
(a) 3 slots 3 phases



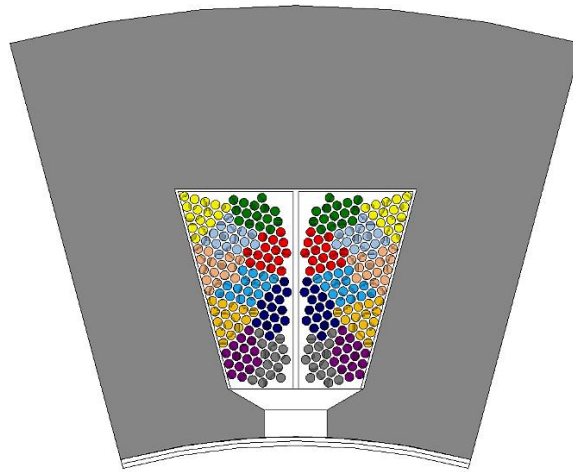
(b) 3 slots no magnet



(c) 3 slots no rotor



(d) 3 slots 1 phase stranded



(e) 1 slot stranded model

Fig. 4.1: Comparison of different modelling depth for simplification of modelling

In Fig. 4b, the magnets (source of excitation flux) are removed in comparison to the baseline model, while in Fig. 4c the rotor is removed altogether, with marginal reduction in AC loss prediction accuracy, confirming that the effect of excitation field is insignificant in machines with tooth tips and smaller slot opening as it only reduces the losses by 1.3% in comparison to the baseline model. For Fig. 4d, only one phase is modelled at the strand – level and the currents in the two other phases are adjusted to maintain the same ampere – turns as in the baseline model, however this result in a significant drop in accuracy because of flux distribution in the slot associated with modelling solid lumped conductors. In Fig. 4e, only a single slot with half coil sides of either phase is modelled, resulting in a marked reduction in simulation time of 85% and less than 5% difference in loss prediction with respect to the baseline model. However, this simplification of modelling is only true for this specific machine and cannot be generalised for all machines.

**TABLE 4.1: Comparison of models' losses and percentage difference from baseline model**

Models	Total losses in active length of machine (W)	% difference from baseline model	Simulation Time (s)
3 slots 3 phases	623.12	0	5760.42
3 slots no magnet	612.15	-1.76	4505.58
3 slots no rotor	615.03	-1.30	4340.99
3 slots 1 phase stranded	445.16	-28.56	1504.25
1 slot stranded	652.38	4.7	843.21

#### 4.1.1. Investigation of big discrepancy between the 3 slot 1 phase stranded model and the baseline model

The losses in winding estimated the 3 slots 1 phase stranded is approximately 28% less than the baseline model. In order to find the root of this discrepancy, the flux density and current density plot of both the models are compared. Fig. 4.2 shows the waveform of the 3-phase current source connected to the baseline model. At time instant 0.00268 s (marked by dot dashed line in Fig. 4.2), the current in phase 1 is zero, while the other two phases have amplitude of -100 A and 100 A.

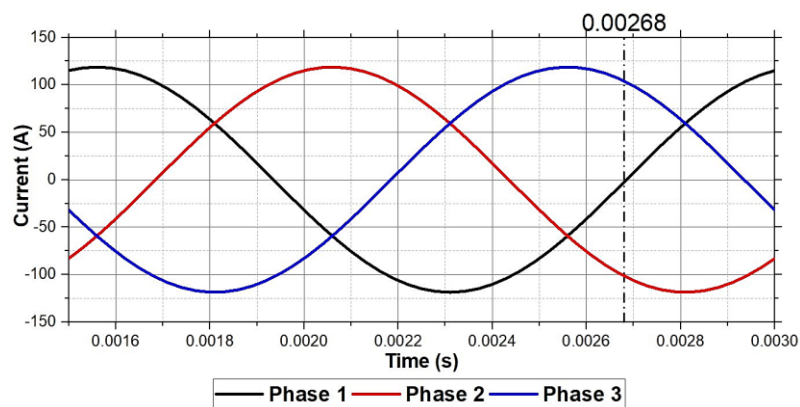
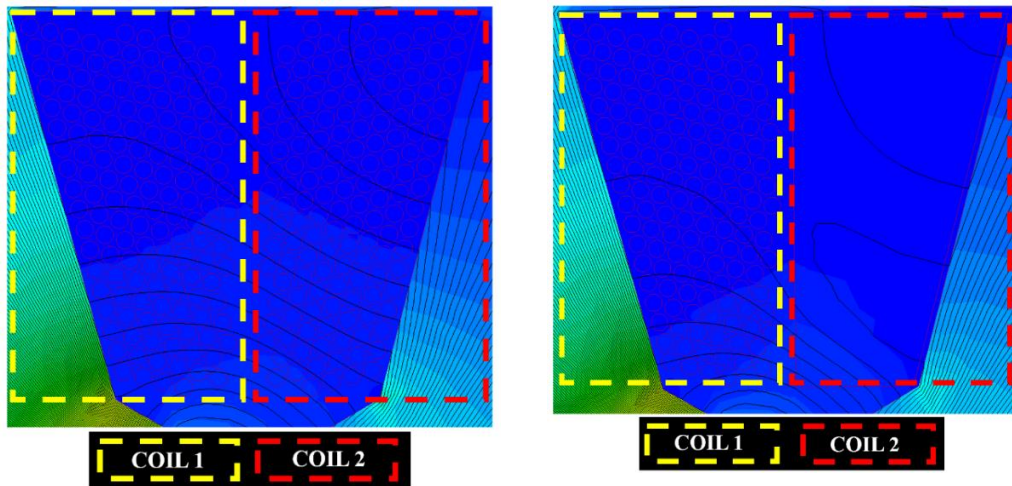


Fig. 4.2: Waveform of the 3-phase source current in baseline model

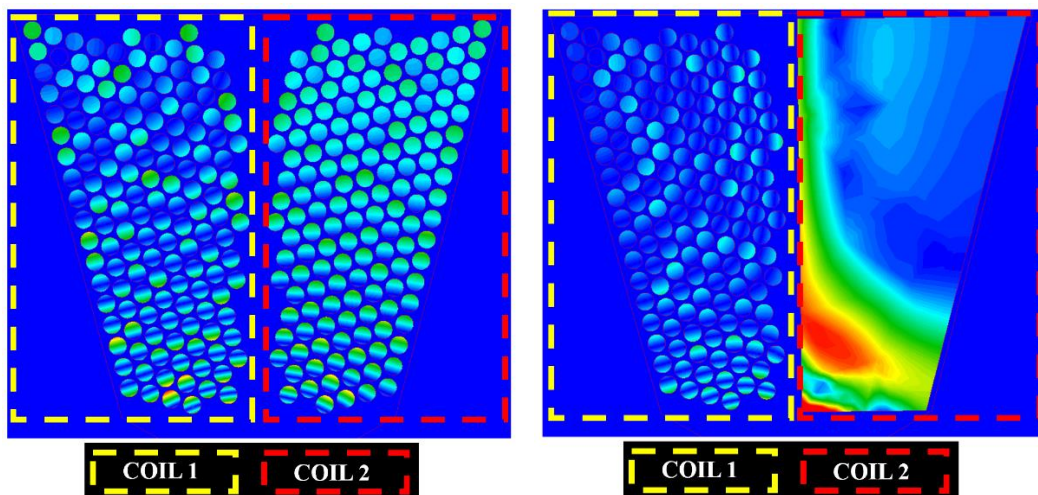


(a) 3 slots 3 phases

(b) 3 slots 1 phase stranded

Fig. 4.3: Flux distribution inside the slot (at time instant 0.00268s)

Fig. 4.3 shows the flux function distribution inside the slot. At time instant 0.00268 s, the current in coil 1 connected to phase 1 is zero, while coil 3 has amplitude. As seen in Fig. 4.3, due to the lumped conductor model of coil 3 in case of 3 slots 1 phase stranded model, the flux distribution inside the slot isn't similar to as in the baseline model, causing difference in flux linkage and lesser loss in the winding.



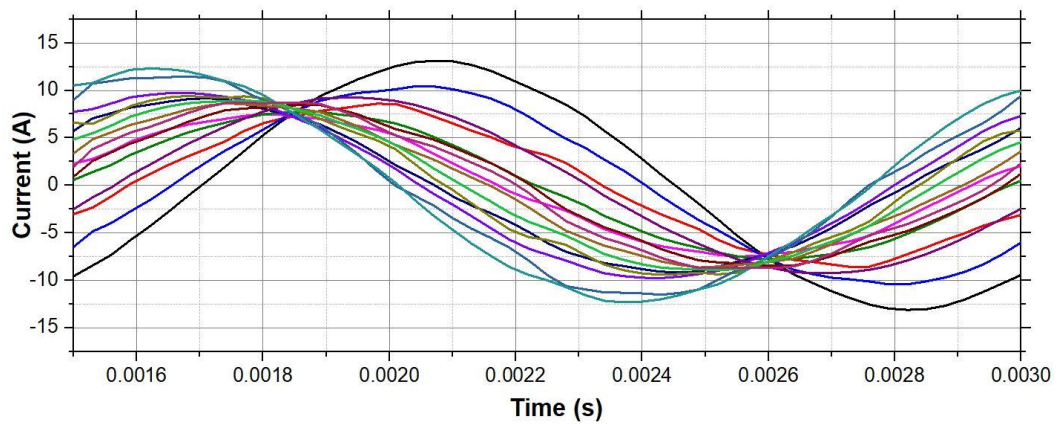
(a) 3 slots 3 phases

(b) 3 slots 1 phase stranded

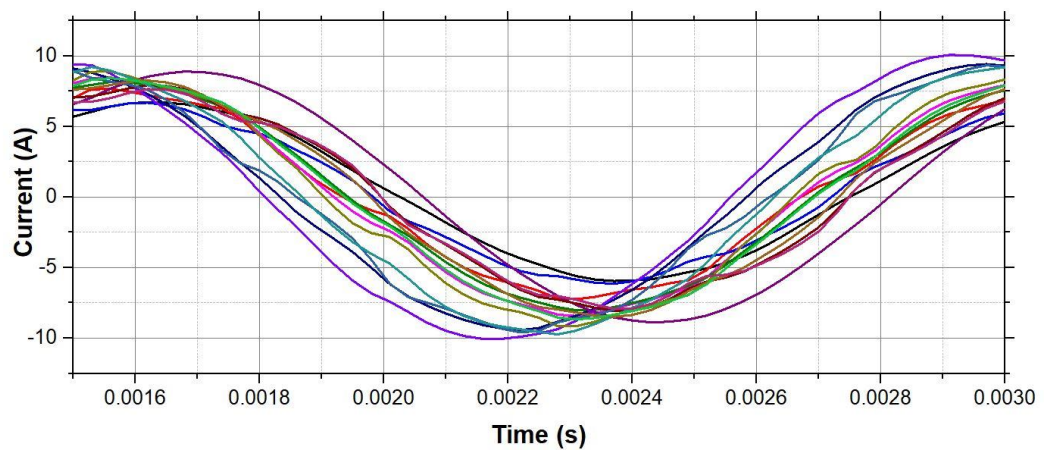
Fig. 4.4: Current density distribution in the strands (at time instant 0.00268s)

Fig. 4.4 shows the current density distribution in the strands for both the models.

The difference in the current distribution is apparent in the figure.



(a)



(b)

Fig. 4.5: Waveform of strand currents in (a) 3 slots 3 phases model, (b) 3 slots 1 phase stranded model

Fig. 4.5 shows the waveforms of the individual strand currents for both the waveforms. The circulating currents with individual strand currents displaced in time and the uneven current sharing by the strands are apparent in case of the baseline model as compared to the 3 slots 1 phase stranded model. Thus, simplifying model as the 3 slots 1 phase stranded model will not yield accurate results for losses in the winding.

#### 4.1.2. Comparison of 1 slot stranded model with the baseline model

The 1 slot stranded model gives an additional 5% loss when compared to the baseline model. However, by doing so, the computation time is reduced by 85%. This section compares both models.

Fig. 4.6 shows the 1 slot stranded model. Since the flux flows through the teeth radially, flux tangential boundary is applied to the side of the half tooth on either side of the slot.

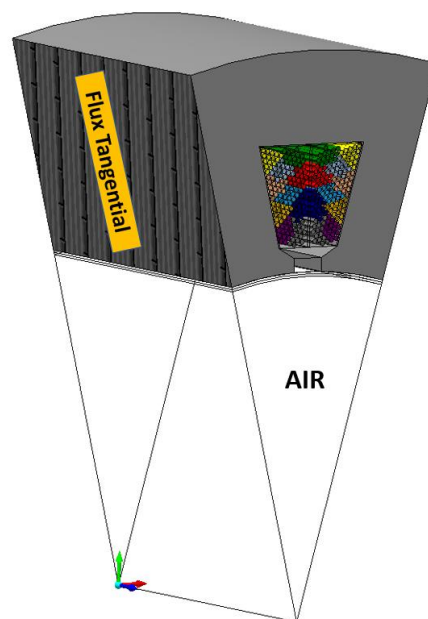
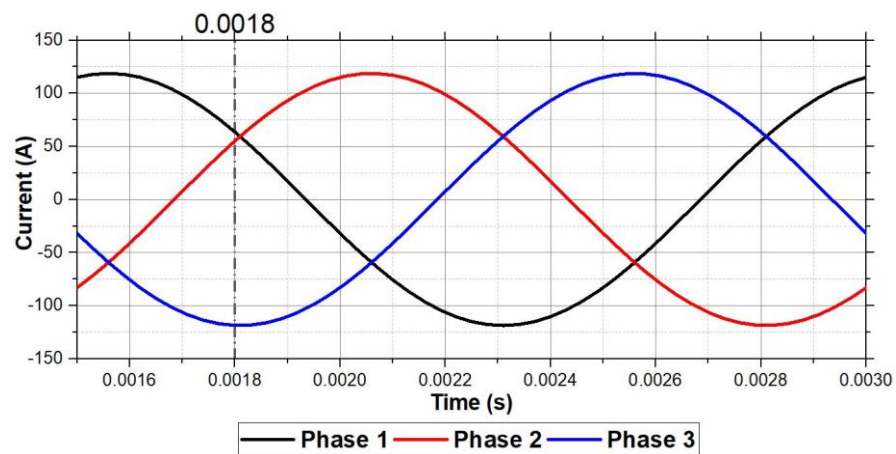
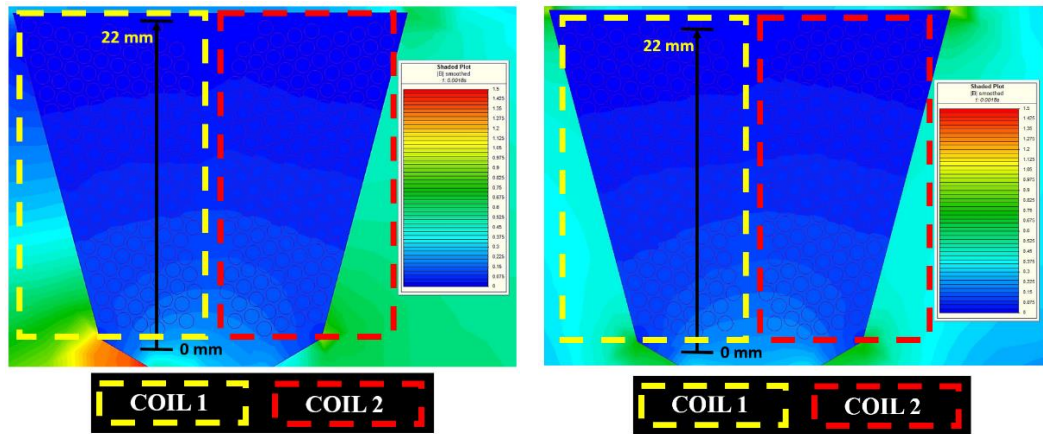


Fig. 4.6: 1 slot stranded model with flux tangential boundary conditions on the teeth side

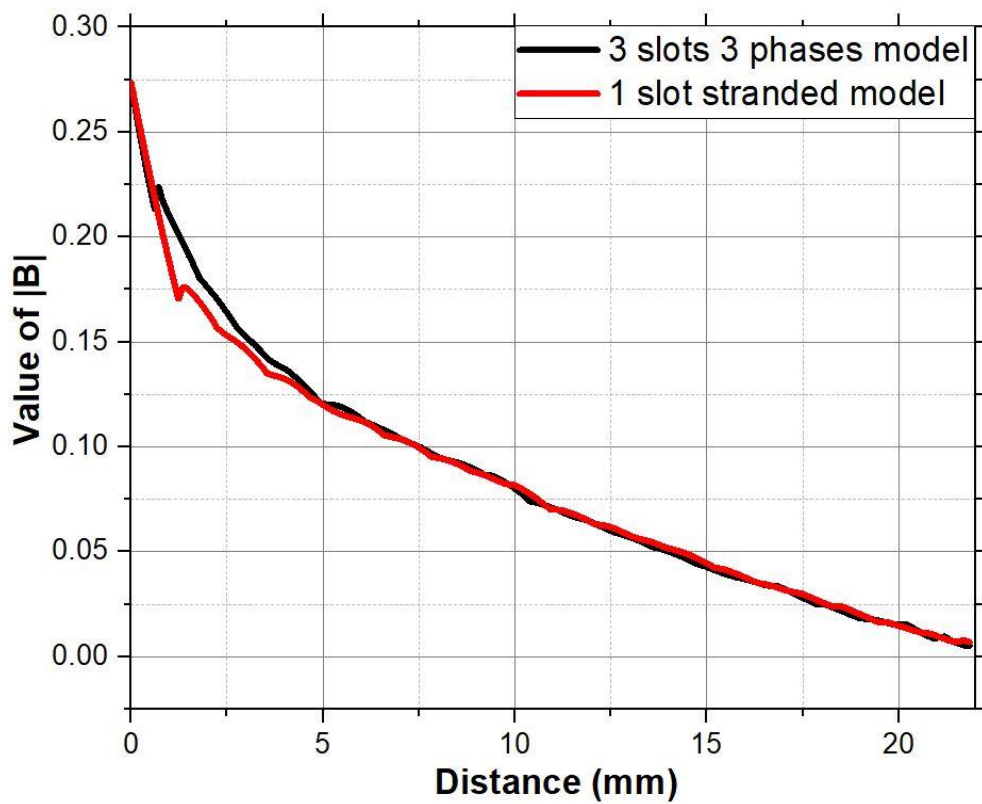


(a)



(b)

(c)



(d)

Fig. 4.7: (a) Waveform of 3 phase source current with timeline marked at 0.0018s, (b) Flux density  $|B|$  in baseline model, (c) Flux density  $|B|$  in 1 slot stranded model, (d) Comparison of Flux density  $|B|$  inside the slot of 1 slot stranded model with the baseline model at time instant 0.0018 s

Fig. 4.7 shows the comparison of flux density  $|B|$  inside the slot of the 1 slot stranded model with the baseline model at time instant 0.0018 s. Fig. 4.7a and Fig.

4.7b shows the flux density  $|B|$  inside the slot for both the baseline model and the 1 slot stranded model. The flux density values are obtained from inside the slot where coil 1 is slot placed (along the line marked at 0 mm at the slot top till the distance of marked at 22 mm towards the slot bottom). In Fig. 4.7d, the flux density  $|B|$  values inside the slot for both the models are compared along the path described before. The values for both the curves with respect to the distance are comparable and this result in the comparable losses in the windings. Therefore, for this machine, the model can be simplified to 1 slot without the significant loss in accuracy for estimating the losses in the windings due to AC effects while saving 85% in computational time. Hence, in this chapter, 1 slot stranded model is used for further analysis.

## 4.2. Methodology

The methodology used to carry out this optimisation is described in the following subsections.

### 4.2.1. Selection of optimum strand diameter

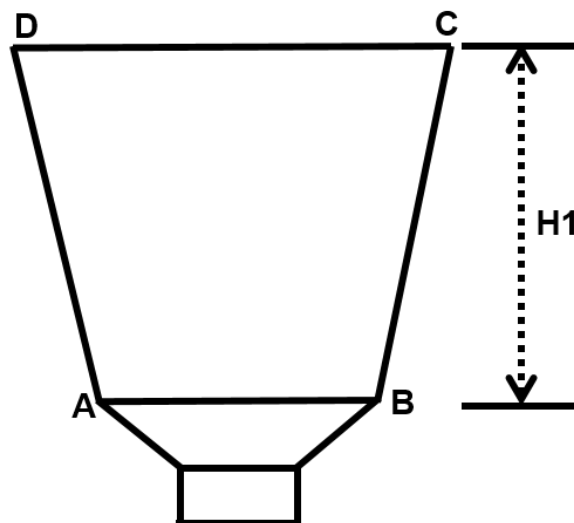


Fig. 4.8: Representation of a slot geometry with woundable area ABCD

Consider the geometry shown in Fig. 4.8 representing a slot of an electrical machine. The slot geometry has a woundable area (area which can be filled by the windings of the machine) marked by the four corners of the quadrilateral ABCD and the height of the slot is  $H_1$ . As described in literature, for high power density a higher slot filling factor is desired. However, measures against AC effects oppose higher fill factor. Therefore, for any given slot geometry, selection of an optimum strand diameter that satisfy both the need of higher fill factor and lower AC effects, combined with mechanical flexibility and ease of manufacturing become a process of paramount importance. Considering practical filling of slot in electrical machines, data of magnet wire strand size is selected from magnet wire company datasheets [10]. Then, with the strand layout as shown in Fig. 4.9, the slot area ABCD is filled with discs resembling magnet wire cross section. Varied diameter from the smallest available in the datasheet to the bulkiest strand that fits into the given slot geometry and satisfy the minimum number of turns in the slot are considered. Additional constraint is applied which accounts for the total strands in the slot to be divisible by the number of turns in the slot.

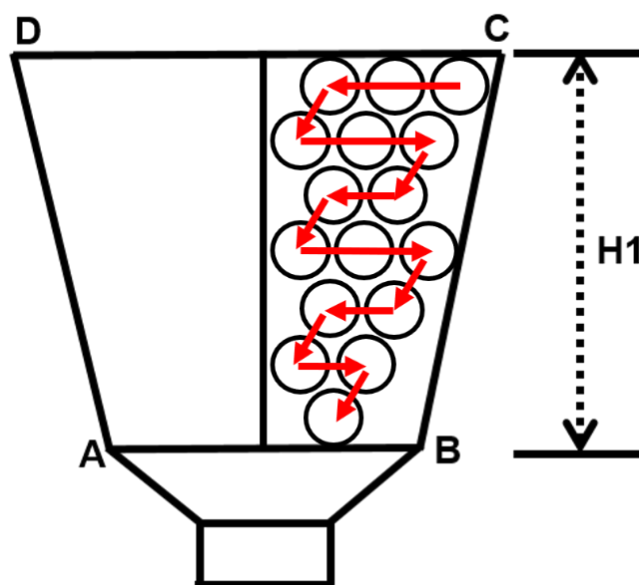
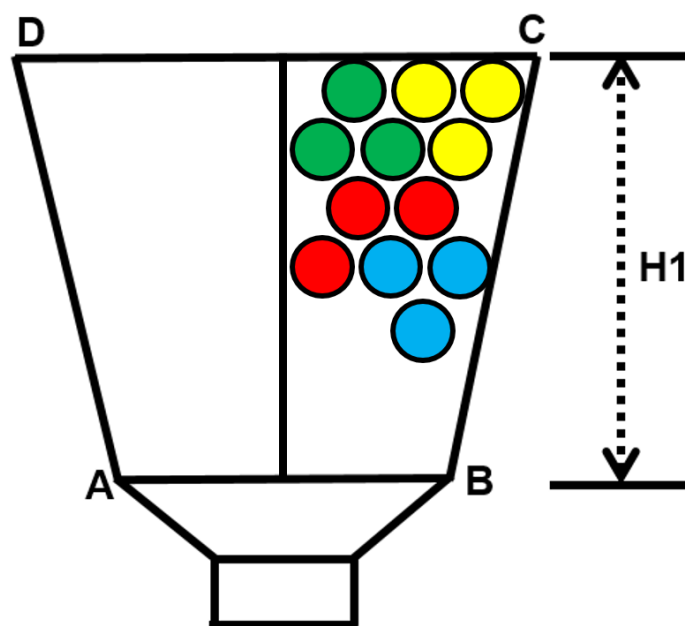


Fig. 4.9: Representation of strand layout in slot geometry

Fig. 4.9 shows a representation of how the strands are laid in the slot geometry. The arrows coloured in red mark the path of strand laying. This is similar to the ARR1 described in chapter 2. Then, the slot filling factor obtained for strand diameter is plotted to select the magnet wire diameters which exhibits high fill factor, have potential to incur lower AC effects and will provide for mechanical flexibility and ease of manufacturability. Here, the slot filling factor is defined as the total copper area divided by the available winding area (Area ABCD).

#### 4.2.2. Clustering of strands to form bundles

After the strands are laid in the slot geometry, they are divided and grouped together to form parallel strands of conductors. To imitate the strands in actual random – wound machines, the strands are grouped together as such that the strands nearby cluster together to form bundle. To keep as real as possible, the shapes of the bundles are not constrained in this case. This allows for the bundles inside the slot geometry to take any shape.



(a)

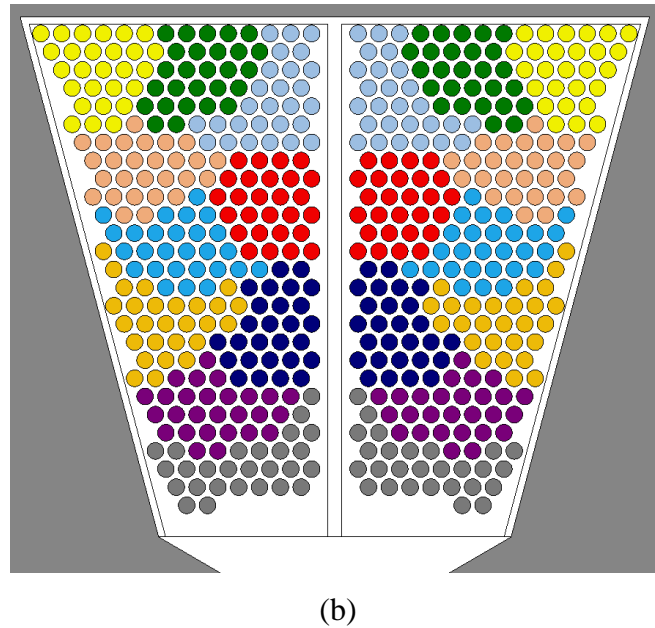


Fig. 4.10: (a) Representation of clustered strands into bundles, (b) Model with 27 strands – in – hand clustered together to form bundles

Fig. 4.10 shows the clustering of the strands into bundles. Fig. 4.10b shows a model with 27 strands – in – hand. The bundles shapes are not constrained and take shapes that reproduce a random – wound winding of a machine.

### 4.2.3. Selection of winding height

In order to find the optimum winding height, the winding is pushed towards the slot bottom in steps. The steps are chosen as percentage of height  $H_1$  and are as follows: 100%, 85%, 75%, 65% and 55%. Fig. 4.11 shows the reduction of the slot height to  $H_n$ , where  $H_n$  is  $x\%$  of  $H_1$ . Reducing the winding height reduces the available winding area to  $A'B'CD$ . The process of selecting the optimum strand diameters and clustering are repeated for the new area and the losses in winding are calculated. As the area available for winding reduces, the strand diameters and thus the available copper area reduces. This increases the DC loss while pushing the winding towards the slot bottom reduces the AC effects. Thus, a critical height is reached where advancing the strands towards the slot bottom does not yield lower

total loss in the winding as the DC loss overshadows the gain from reduction in AC losses.

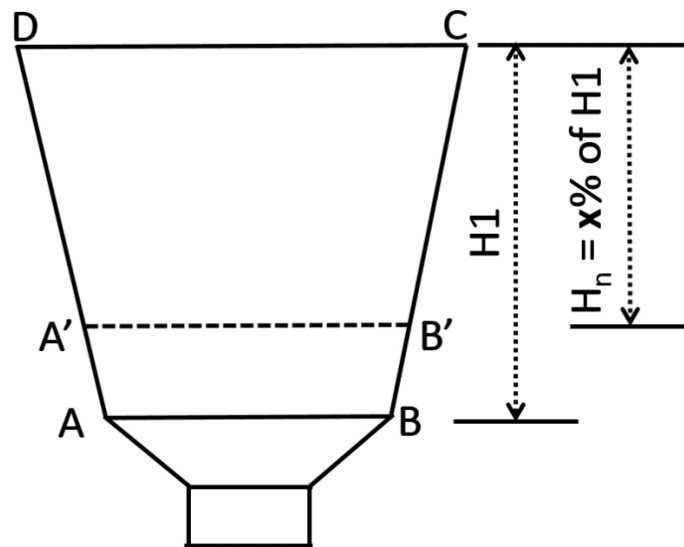


Fig. 4.11: Reduction of winding height from  $H_1$  to  $H_n$

### 4.3. FEM Results

This section details the results obtained from the finite element analysis.

#### 4.3.1. Height ( $H_1$ )

Following the methodology described above, the slot filling factor are plotted against the strand diameters for the slot height,  $H_1$  and the available winding area ABCD (area  $A_1$ ) associated with it. Fig. 4.12 shows the slot filling curve against the outer diameters of the strands for  $H_1$ . As the strand diameter increases, there is a gain in the slot filling factor first and then as the strand diameter gets large enough and the strands can no longer be equally divided by the number of turns, the slot filling factor drops. In Fig. 4.12, the data points marked in red are the point of interest as these strands provide higher filling factor, the diameters are well under the skin depth value at the fundamental frequency of 666.67 Hz and provide mechanical

flexibility to wound around the teeth with relative ease. Apart from these strands size, the strands with diameters 2.35 mm (marked with dot dashed line) and 3.883 mm (marked by dashed line), produce higher fill factor. However, these sizes are either greater than the skin depth value or/and impair the advantage of flexibility provided by the thinner strands.

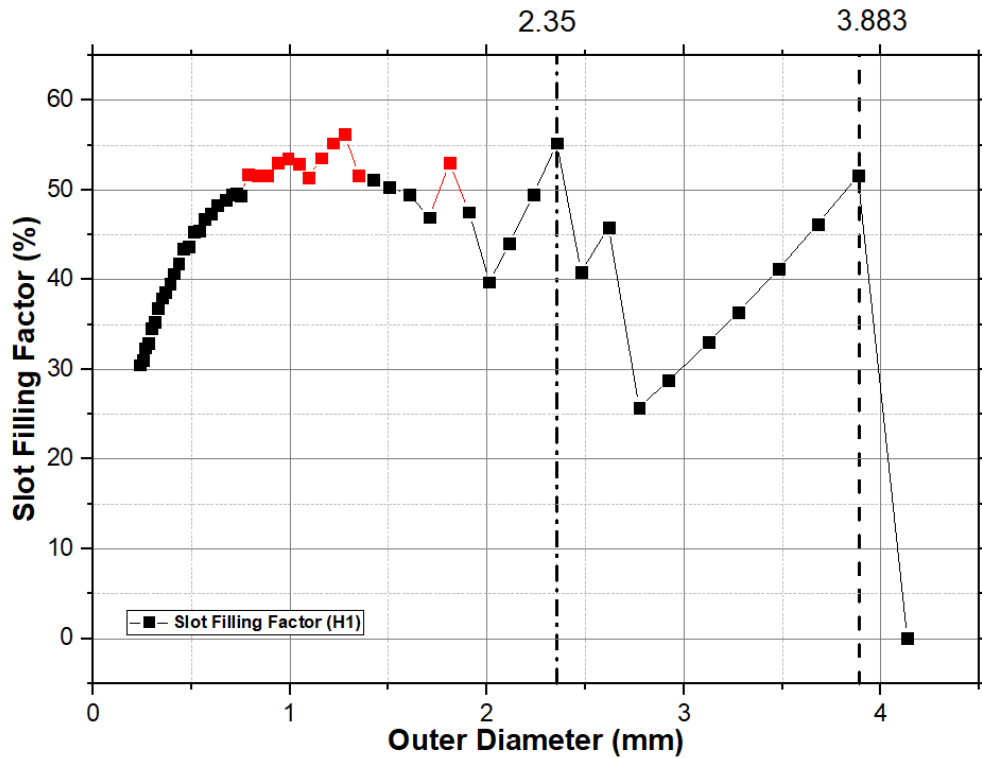


Fig. 4.12: Slot filling factor against the strand outer diameter (H1)

**TABLE 4.2: Strand diameters with high fill factor for H1**

Strand nominal diameter (mm)	Total conductors per slot	Slot Filling Factor (%)	Number of parallel strands
1.7	100	53.013	5
1.18	220	56.192	11
1.06	260	53.58	13
0.9	320	53.49	18
0.71	560	51.78	28

TABLE 4.2 lists the strand diameters, which result in high slot filling factor and are selected for further finite element analysis.

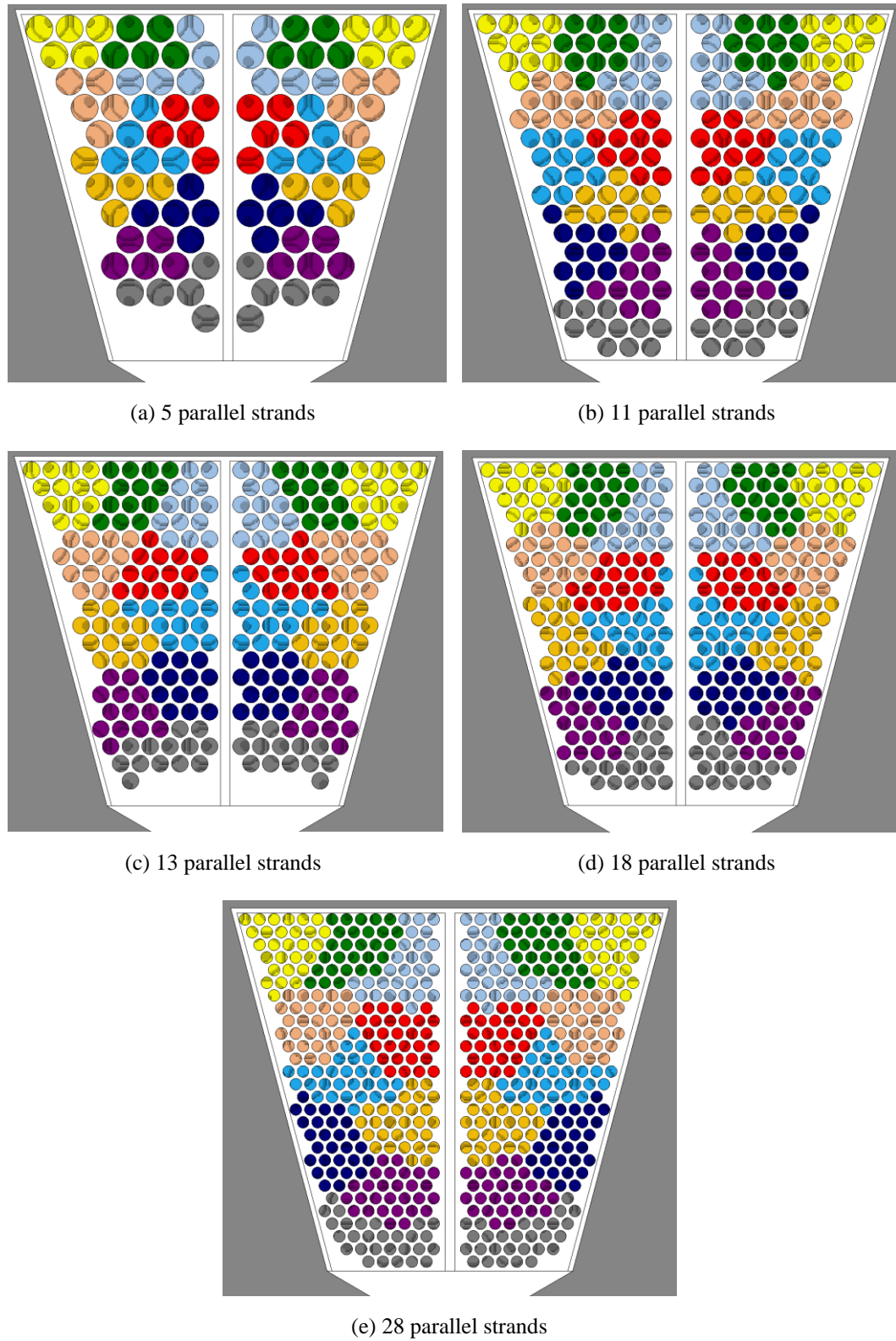


Fig. 4.13: Models used for analysis for height H1

Fig. 4.13 shows the models used for analysis for the height H1 and TABLE 4.3 lists the losses in the winding of the machine for the models with slot height H1.

**TABLE 4.3: Losses in the winding of the machine (H1)**

<b>Model with parallel strands</b>	<b>Total Loss in Active Length (W)</b>	<b>DC loss in Active Length (W)</b>	<b>DC Loss in the end winding (W)</b>	<b>Total loss (W)</b>
5	1143.80	369.00	178.00	1321.80
11	1604.31	348.12	168.00	1772.31
13	1094.64	365.04	176.00	1270.64
18	1310.54	365.76	176.00	1486.54
28	1444.06	377.76	182.00	1626.06

In TABLE 4.3, the column ‘Total Loss in Active Length’ lists the total losses in the active length of the winding of the machine models with varied parallel strands listed in the first column, ‘Model with parallel strands’. The column titled, ‘DC loss in Active Length’, lists the DC loss in the active winding length calculated analytically and the column next, ‘DC Loss in the end winding’, lists the DC losses in the ending windings for models. Since, it is assumed that the significant AC losses occur only at the active winding length of the machine, the last column, ‘Total loss’, lists the Total loss (Total Active winding + DC endwinding loss) of the winding. The highest loss (approximately 1772 W), is incurred in the active winding length of 11 parallel strands with Total / DC Loss of 4.61, i.e. the AC losses in the active length for this model is as high as 3.61 times the DC loss value. The minimum losses occur with 5 and 13 parallel strands models with Total / DC Loss ratio of 3.1 and 3.0 respectively. The lower losses in these two models is the result of the strands in these

two models positioned slightly towards the slot bottom as compared to the other models with the height H1. This is evident from Fig. 4.13, where the models with 5 and 13 parallel strands have lesser strands towards the slot top.

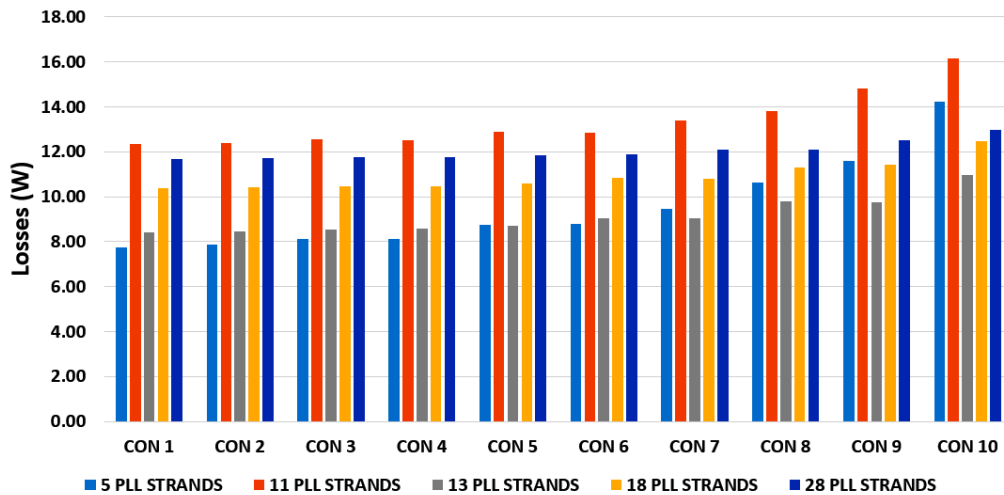


Fig. 4.14: Losses in the conductors for models of H1

Fig. 4.14 shows the losses in the individual conductors for models used in FEA with height H1. The different colours represent the different models and the coloured bars represent the losses in the individual conductors for each model for each conductor plotted in the abscissa.

#### 4.3.2. Height (H2)

For H2, the winding height is reduced to 85% of H1 towards the slot bottom. The slot is filled with strands of all possible diameters and slot filling factor is obtained. Similar to the previous section, strands diameters are selected and losses in the windings for these models are analysed.

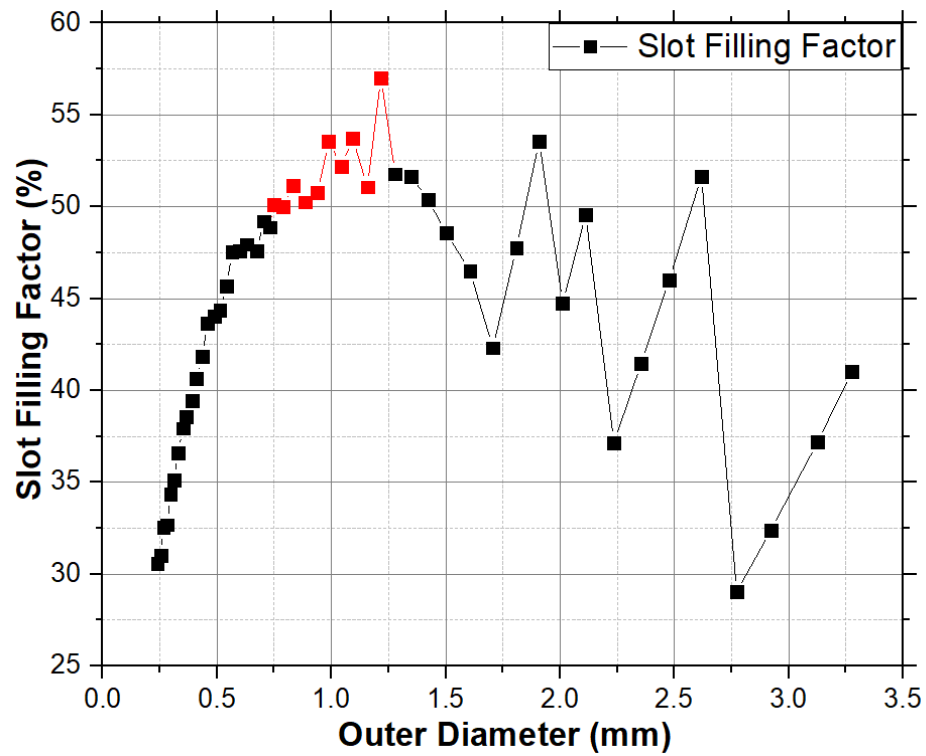


Fig. 4.15: Slot filling factor against the strand outer diameter (H2)

**TABLE 4.4: Strand diameters with high fill factor for H2**

Strand nominal diameter (mm)	Total conductors per slot	Slot Filling Factor (%)	Number of parallel strands
1.12	220	57.02	11
1	260	53.71	13
0.9	320	53.55	16
0.75	440	51.13	22
0.67	540	50.08	27

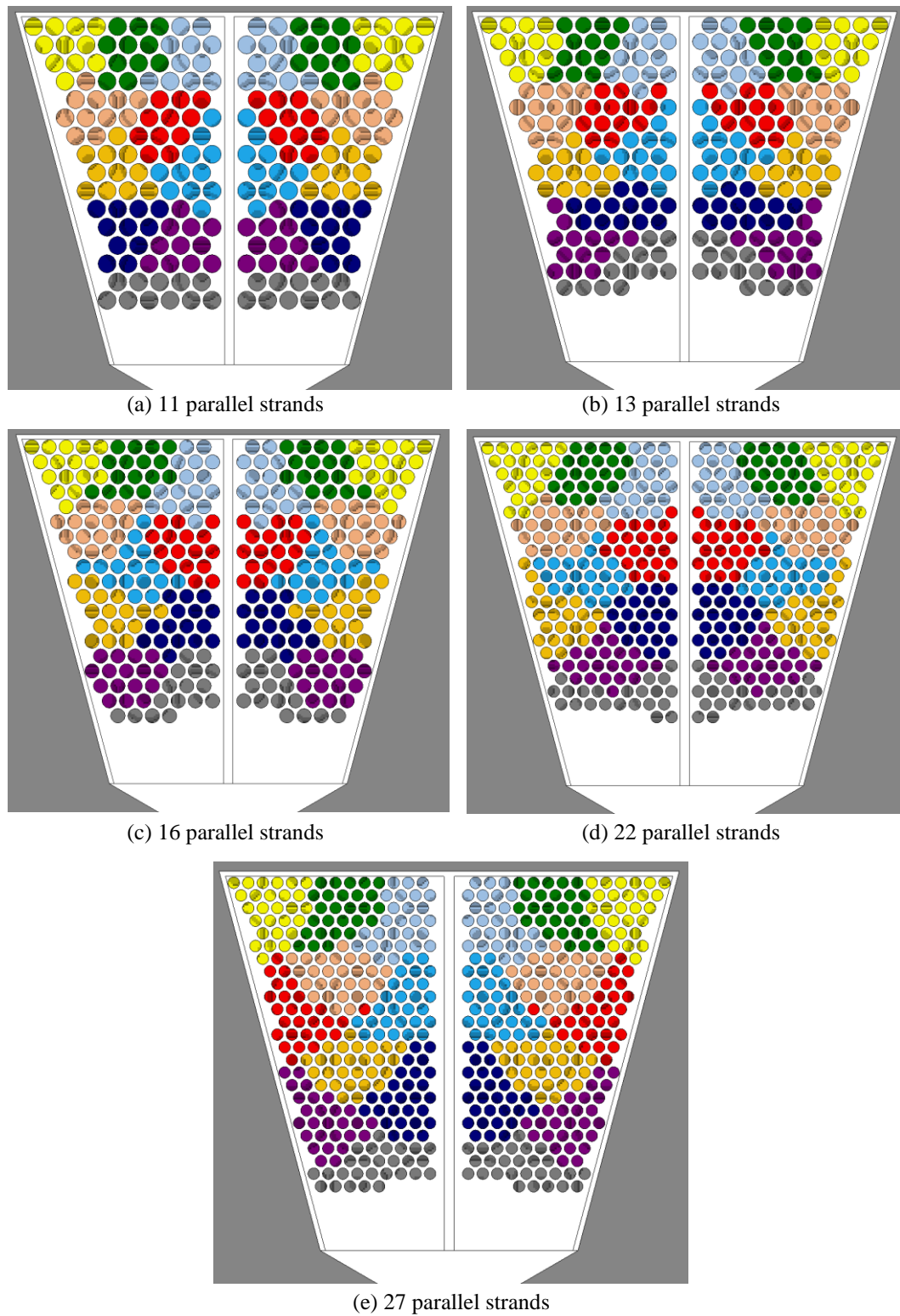


Fig. 4.16: Models used for analysis with slot height  $H_2$

Fig. 4.16 shows the models used for analysis with slot height  $H_2$  and TABLE 4.5 lists the losses in the winding of the machine with slot height  $H_2$ .

**TABLE 4.5: Losses in the winding of the machine (H2)**

<b>Model with parallel strands</b>	<b>Total Loss in Active Length (W)</b>	<b>DC loss in Active Length (W)</b>	<b>DC Loss in the endwinding (W)</b>	<b>Total loss (W)</b>
11	1035	385	186	1221
13	948.02	409	198	1146.02
16	1082.54	410	195	1277.54
22	845.05	429	208	1053.05
27	1142.4	438	212	1354.4

Similar to TABLE 4.3, which lists the losses in winding for H1, the columns in TABLE 4.5 lists the losses in with winding for H2 against each of the corresponding column headings. The highest loss of 1142.4 W is incurred in the active length of the winding of the model with 27 parallel strands for H2. Model with 22 parallel strands shows the lowest losses in the active length for H2, which 26% drop in the total loss in the active winding length when compared to the model with greatest loss (27 parallel strands model for H2). The 27 parallel strands model have total winding loss of 1354.4 W while the 13 parallel strands model have a total loss of 1146.02 W.

### **4.3.3. Height (H3)**

For H3, the winding height is reduced to 75% of H1 towards the slot bottom. Following the methodology described in the previous sections and carried out for H1 and H2, the processes are carried out for height H3.

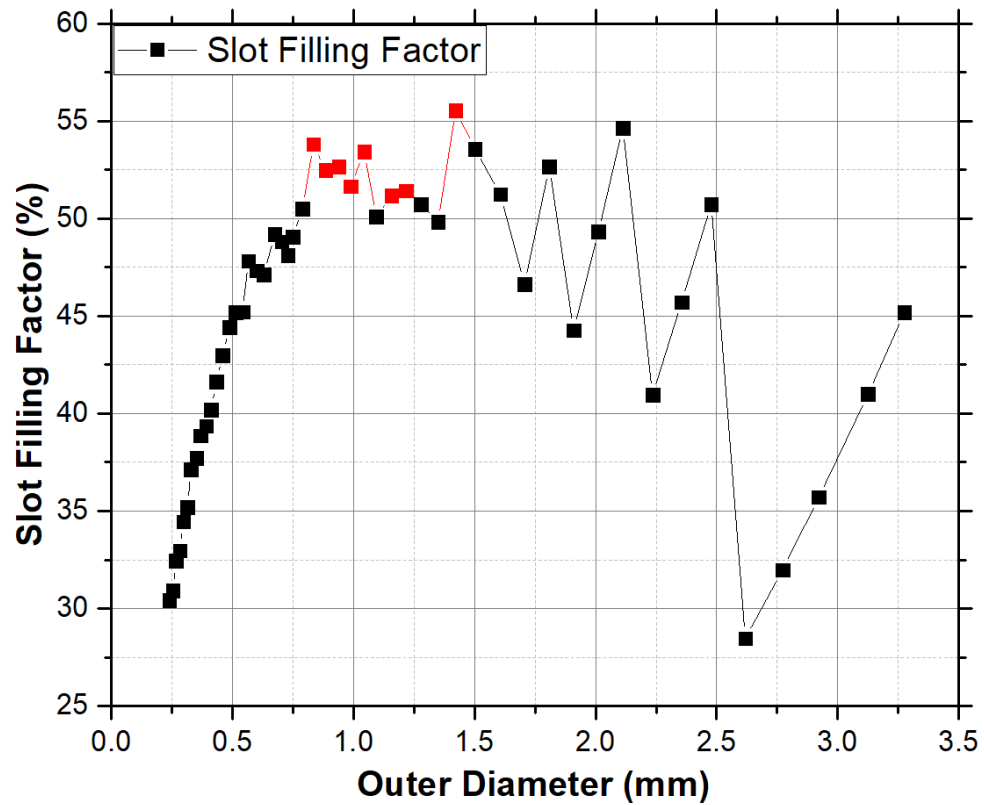
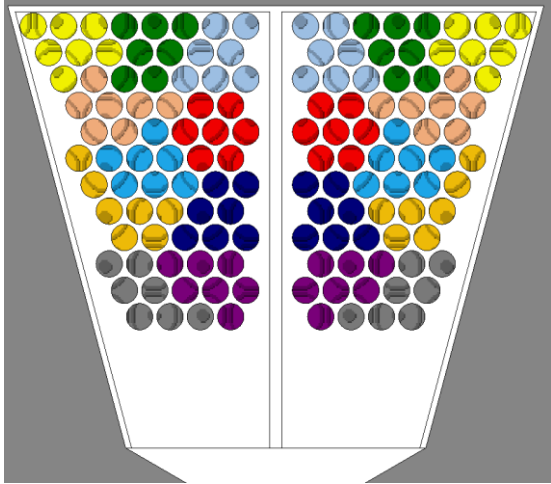


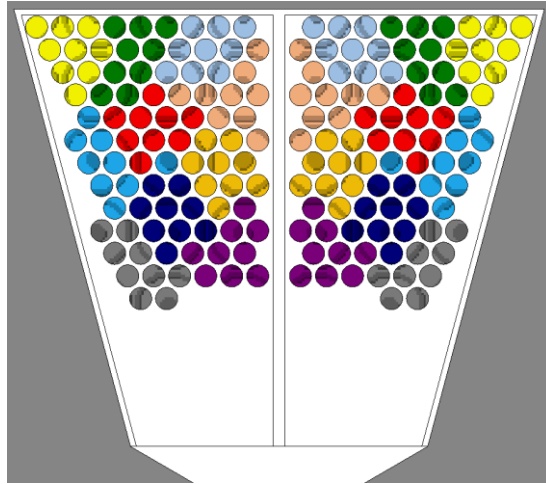
Fig. 4.17: Slot filling factor against the strand outer diameter (H3)

**TABLE 4.6: Strand diameters with high fill factor for H3**

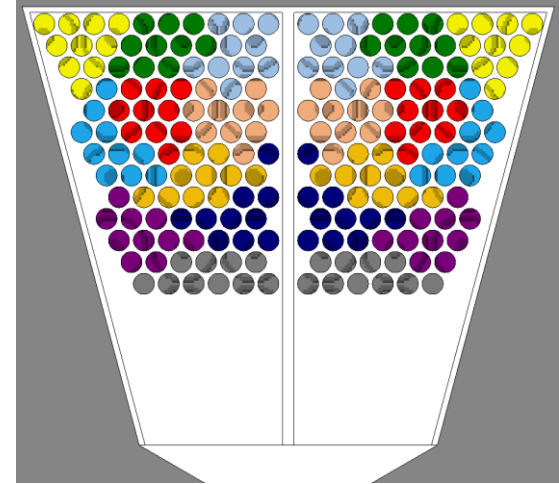
Strand nominal diameter (mm)	Total conductors per slot	Slot Filling Factor (%)	Number of parallel strands
1.32	140	55.55	7
1.12	180	51.42	9
1.06	200	51.17	10
0.95	260	53.44	13
0.9	280	51.65	14
0.85	320	52.65	16
0.8	360	52.46	18
0.75	420	52.80	21



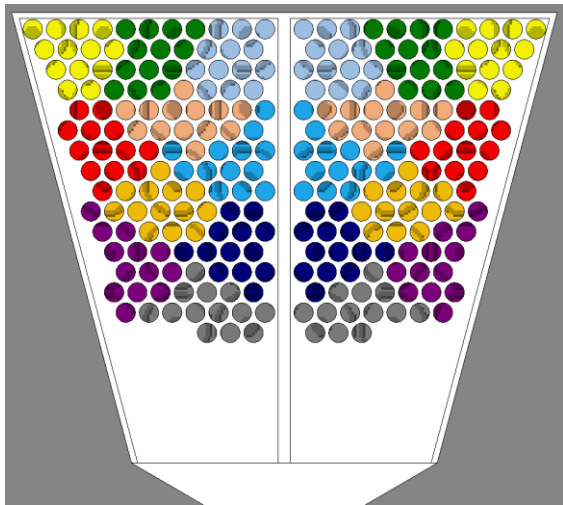
(a) 7 parallel strands



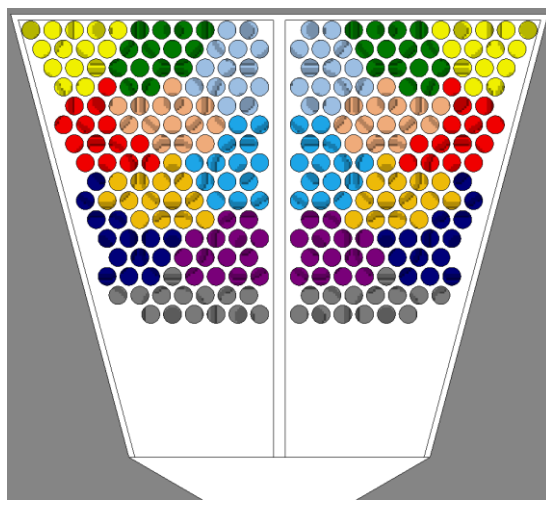
(b) 9 parallel strands



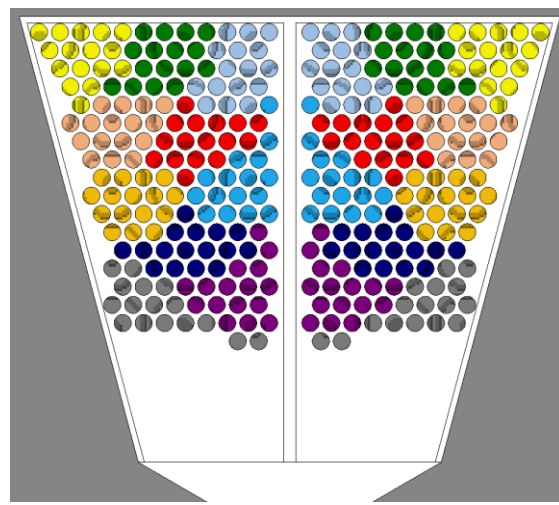
(c) 10 parallel strands



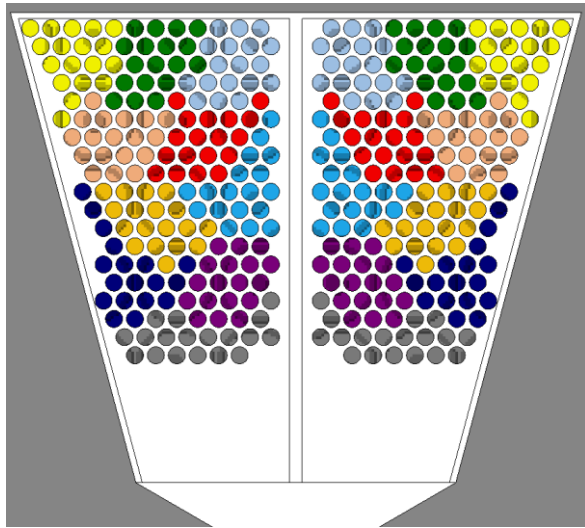
(d) 13 parallel strands



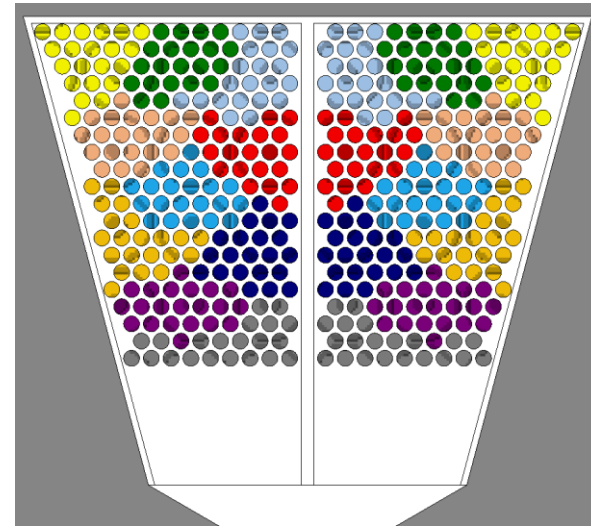
(e) 14 parallel strands



(f) 16 parallel strands



(g) 18 parallel strands



(h) 21 parallel strands

Fig. 4.18: Models used for analysis with slot height H3

Fig. 4.17 shows the slot filling factor vs the strand outer diameter for height H3 and TABLE 4.6 lists the strand diameters used for modelling with height H3. Fig. 4.18 shows the models with parallel strands used for analysis of the losses in the winding with height H3.

**TABLE 4.7: Losses in the winding of the machine (H3)**

<b>Model with parallel strands</b>	<b>Total Loss in Active Length (W)</b>	<b>DC loss in Active Length (W)</b>	<b>DC Loss in the endwinding (W)</b>	<b>Total loss (W)</b>
7	1070.58	435	211	1281.58
9	1052.87	470	228	1280.87
10	791.79	473	229	1020.79
13	1053.31	453	219	1272.31
14	955.08	468	227	1182.08
16	1026.97	459	222	1248.97
18	844.67	461	223	1067.67
21	844.35	450	218	1062.35

TABLE 4.7 lists the losses in the winding of the machine with slot height H3. Here, the maximum total winding loss of approx. 1280 W is exhibited by 7 and 9 parallel strands model while the minimum total winding loss is shown by the 10 parallel strands model, followed closely by the 21 and 18 strands models respectively.

#### **4.3.4. Height (H4)**

For H4, the height of the winding is reduced to 65% of H1 and the analysis is carried out.

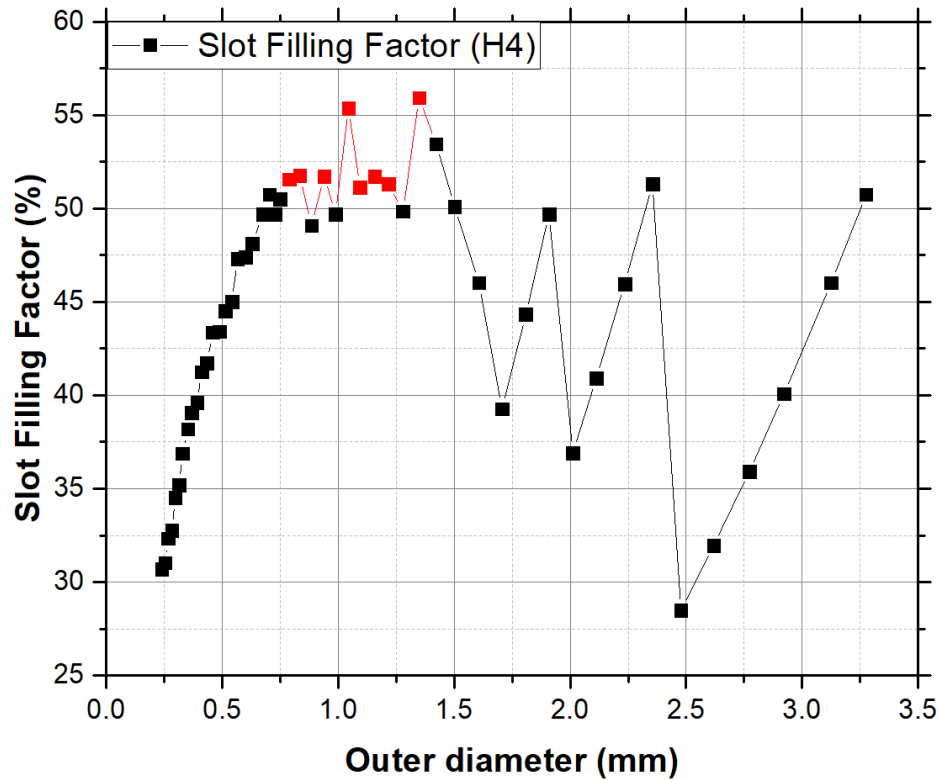
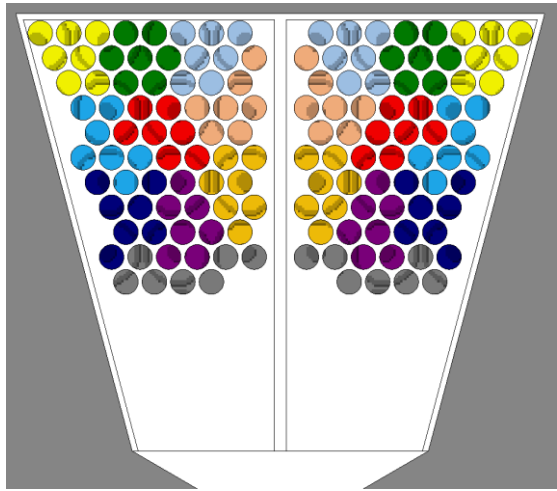


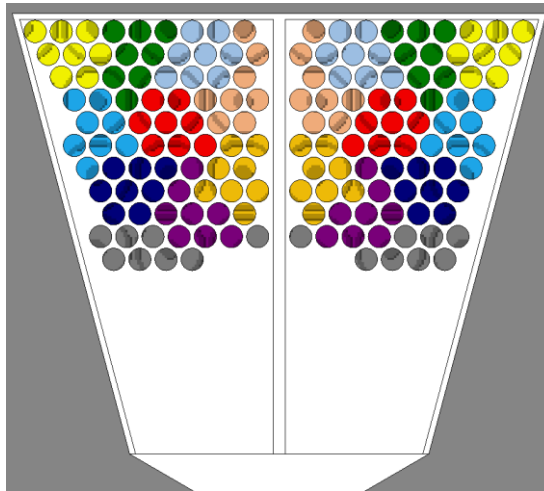
Fig. 4.19: Slot filling factor against the strand outer diameter (H4)

**TABLE 4.8: Strand diameters with high fill factor for H4**

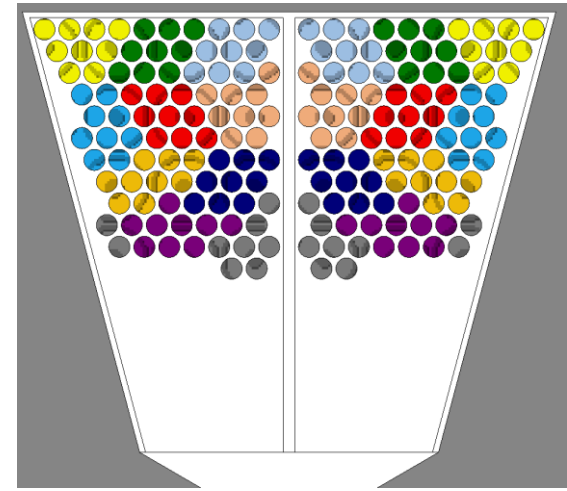
Strand nominal diameter (mm)	Total conductors per slot	Slot Filling Factor (%)	Number of parallel strands
1.32	120	53.46	6
1.25	140	55.93	7
1.12	160	51.31	8
1.06	180	51.71	9
1	200	51.13	10
0.95	240	55.38	12
0.85	280	51.72	14
0.75	360	51.77	18
0.71	400	51.55	20



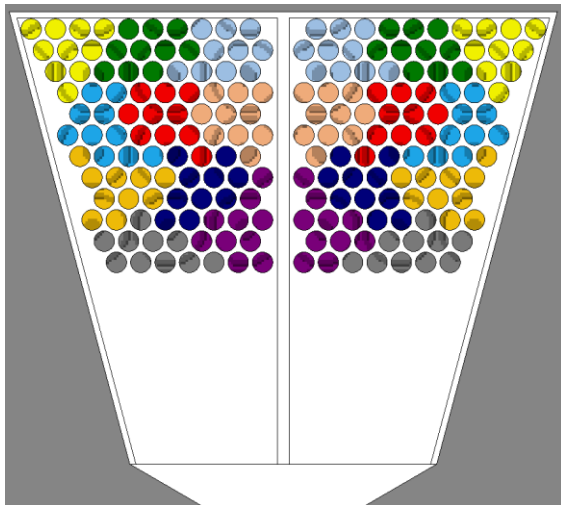
(a) 7 parallel strands



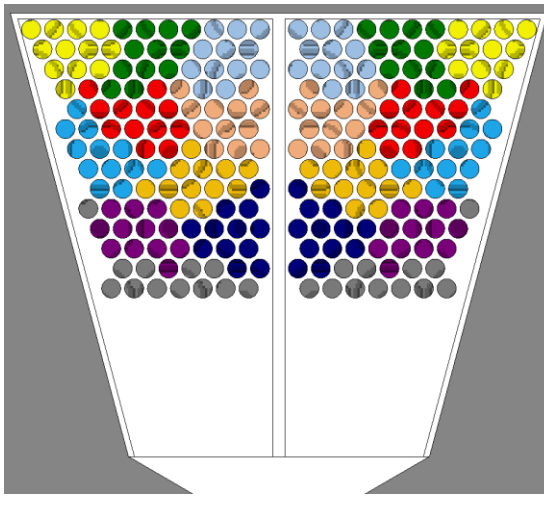
(b) 8 parallel strands



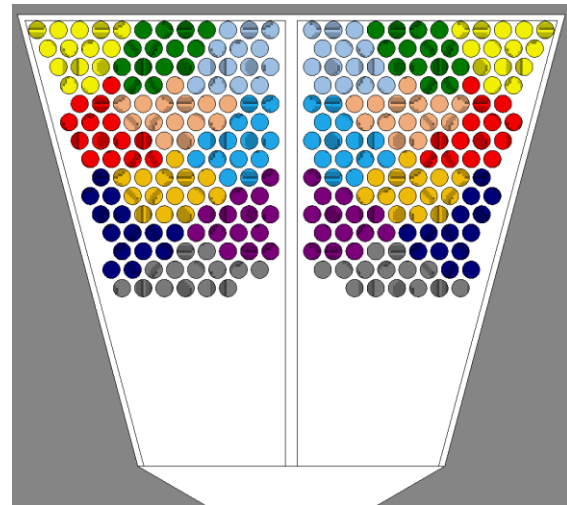
(c) 9 parallel strands



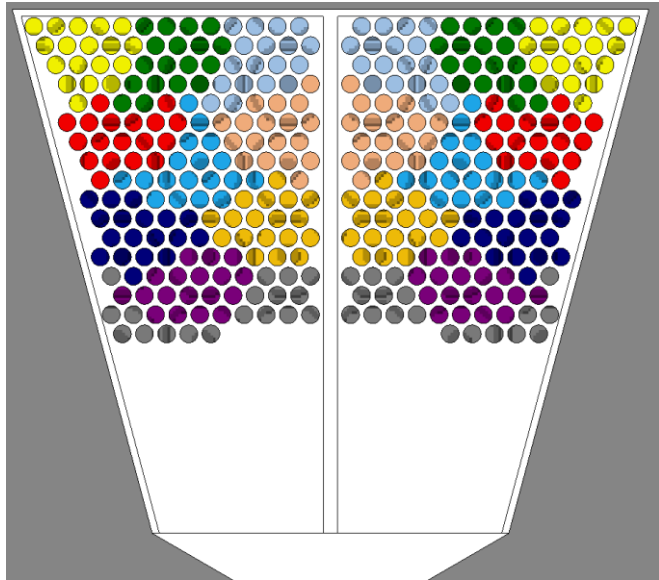
(d) 10 parallel strands



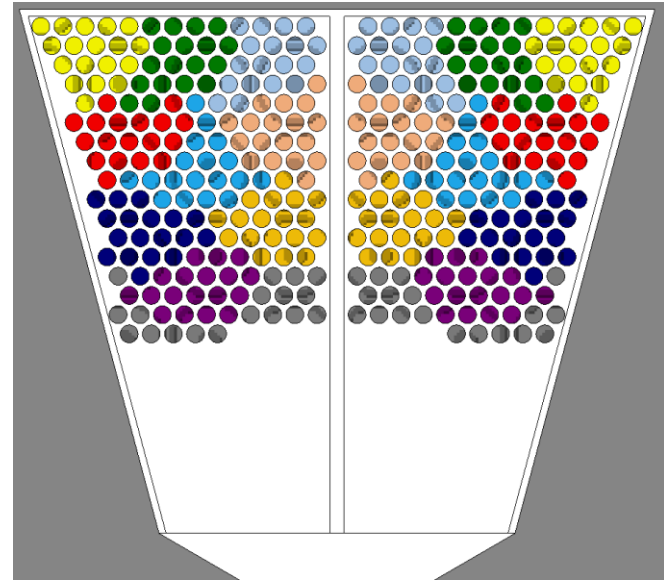
(e) 12 parallel strands



(f) 14 parallel strands



(g) 18 parallel strands



(h) 20 parallel strands

Fig. 4.20: Models used for analysis with slot height H4

Fig. 4.19 shows the slot filling factor vs the strand outer diameter for height H4 and TABLE 4.8 lists the strand diameters used for modelling with height H3. Fig. 4.20 shows the models with parallel strands used for analysis of the losses in the winding with height H3.

**TABLE 4.9: Losses in the winding of the machine (H4)**

<b>Model with parallel strands</b>	<b>Total Loss in Active Length (W)</b>	<b>DC loss in Active Length (W)</b>	<b>DC Loss in the endwinding (W)</b>	<b>Total loss (W)</b>
6	859.26	508	246	1105.06
7	878.76	486	235	1113.70
8	768.01	529	256	1024.07
9	764.72	525	254	1018.83
10	905.00	531	257	1161.97
12	895.04	490	237	1132.31
14	898.55	525	254	1152.60
18	765.66	525	254	1019.45
20	832.18	527	255	1087.06

TABLE 4.9 lists the losses in the winding of the machine with slot height H4. Here, the maximum total winding loss of approx. 1160 W is exhibited by 10 parallel strands model while the minimum total winding loss is shown by the 9 parallel strands model, followed closely by the 18 and 8 strands models respectively.

#### 4.3.5. Height (H5)

For H5, the height of the winding is reduced to 55% of H1 and the analysis is carried out.

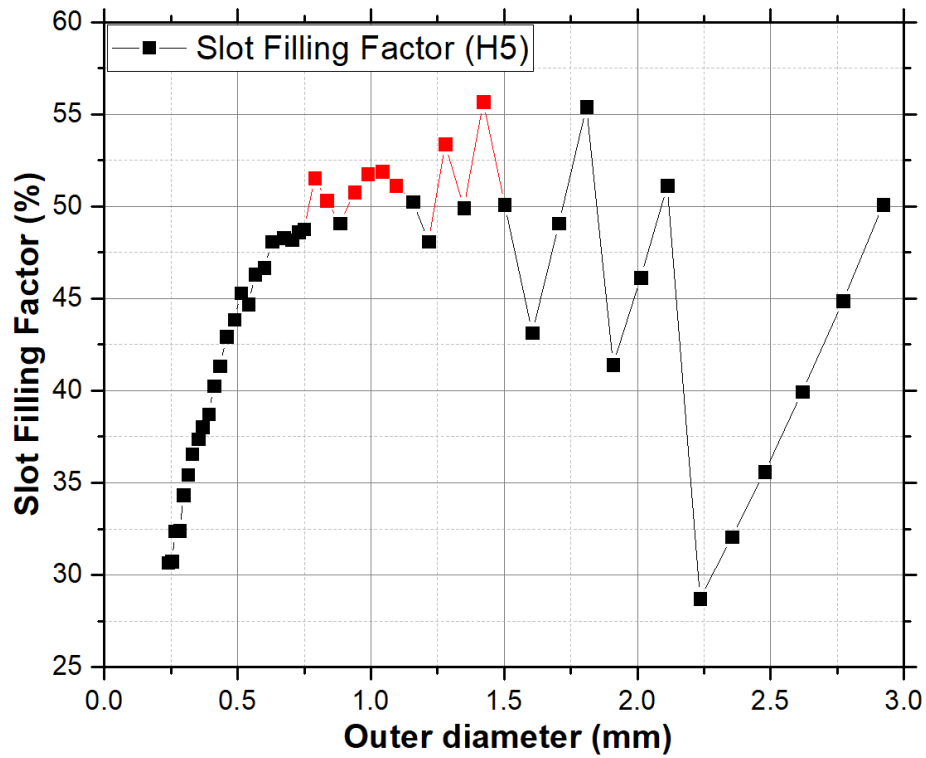
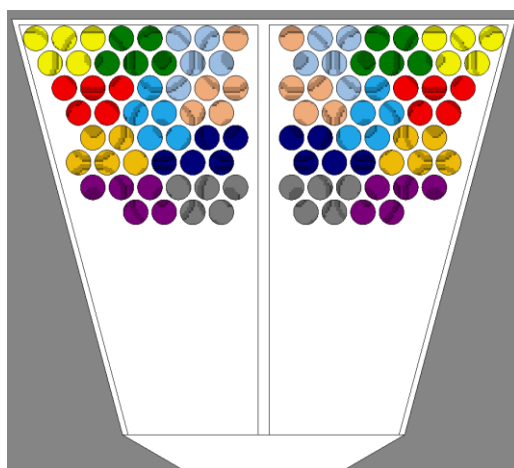


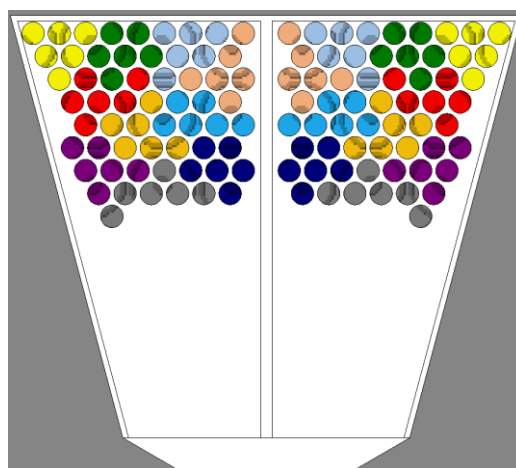
Fig. 4.21: Slot filling factor against the strand outer diameter (H5)

**TABLE 4.10: Strand diameters with high fill factor for H5**

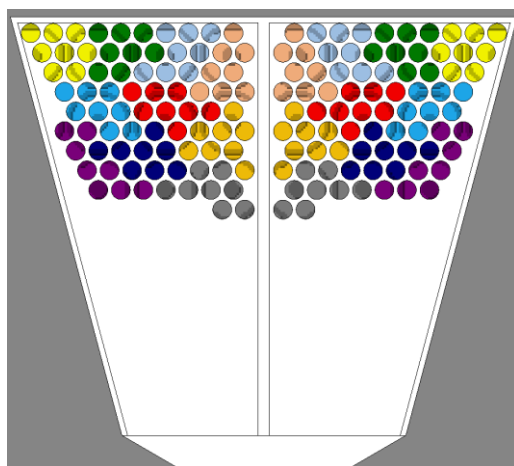
Strand nominal diameter (mm)	Total conductors per slot	Slot Filling Factor (%)	Number of parallel strands
1.32	100	55.67	5
1.18	120	53.38	6
1	160	51.12	8
0.95	180	51.90	9
0.9	200	51.76	10
0.85	220	50.48	11
0.75	280	50.52	14
0.71	320	51.54	16



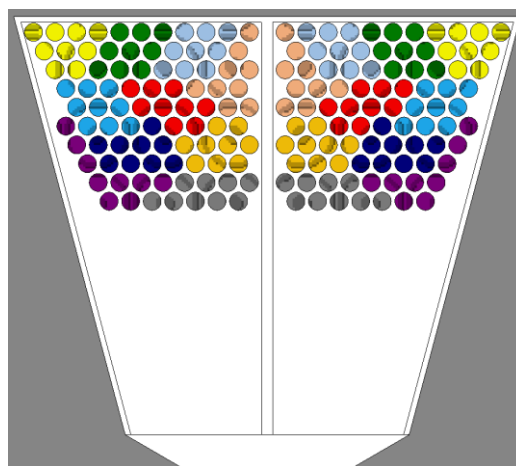
(a) 5 parallel strands



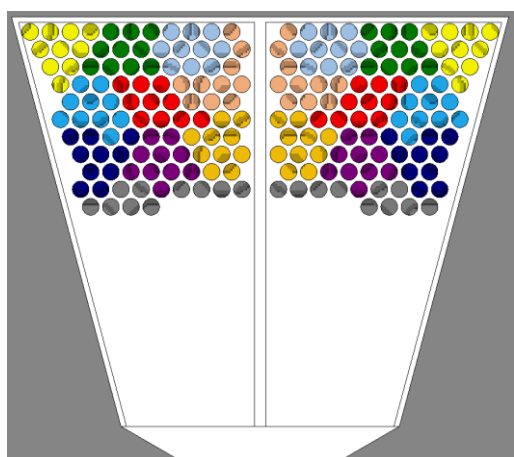
(b) 6 parallel strands



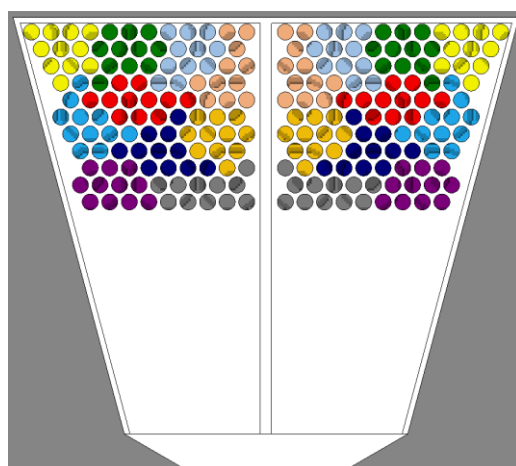
(c) 8 parallel strands



(d) 9 parallel strands



(e) 10 parallel strands



(f) 11 parallel strands

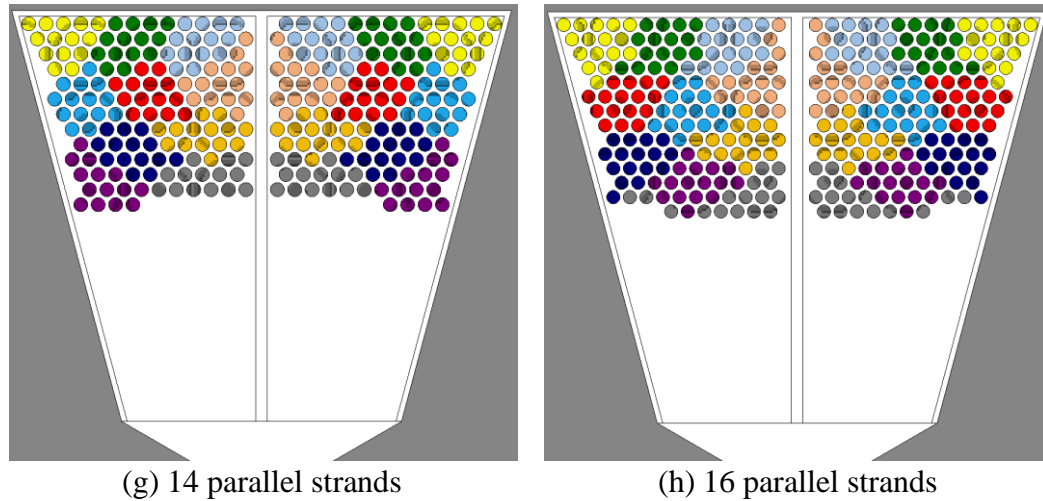


Fig. 4.22: Models used for analysis with slot height H5

**TABLE 4.11: Losses in the winding of the machine (H5)**

Model with parallel strands	Total Loss in Active Length (W)	DC loss in Active Length (W)	DC Loss in the endwinding (W)	Total loss (W)
5	820.76	610	295	1115.71
6	855.65	636	308	1163.23
8	885.57	664	321	1206.78
9	828.06	654	316	1144.42
10	813.66	656	317	1130.90
11	818.00	668	323	1141.33
14	847.56	647	326	1173.86
16	834.80	658	319	1153.39

TABLE 4.11 lists the losses in the winding of the machine with slot height H5. Here, the maximum total winding loss of approx. 1206 W is exhibited by 8 parallel strands model while the minimum total winding loss is shown by the 5 parallel strands model.

#### 4.4. Comparison and discussion

**TABLE 4.12: Comparison of losses in components for varying slot height (maximum total losses of each slot winding height)**

Height	Model with parallel strands	Active length Loss (W)	DC loss in active length (W)	DC loss in endwinding (W)	Total Loss (W)
H1	11	1604.31	348	168	1772.31
H2	27	1142.4	438	212	1354.4
H3	7	1070.58	435	211	1281.58
H4	10	905	531	257	1161.97
H5	8	885.57	664	321	1206.78

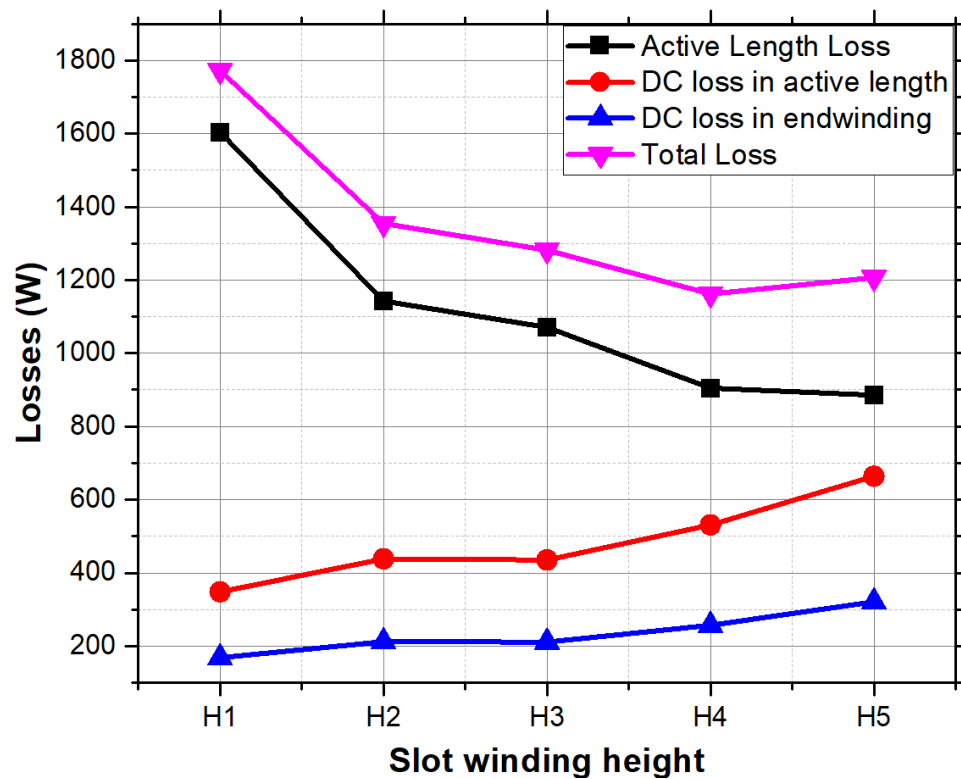


Fig. 4.23: Comparison of losses in components for varying slot heights (with maximum total losses for each winding height)

TABLE 4.12 lists comparison of losses in components for varying slot height. The models with maximum total losses in the winding for each slot height are selected for the comparison. Fig. 4.23 shows these comparisons of losses in graphical form. As the slot height reduces in steps (from H1 to H5), the available copper area reduces and thus the DC losses in the winding increase. This can be seen by the steady increase of the DC losses in the active length and the endwinding regions of the winding represented by the red and the blue curve in the Fig. 4.23. However, with the reduction in the winding slot height, the AC losses in the active length of the machine decrease markedly, which is represented by the black curve in the figure. Therefore, the total losses in the winding reduces from H1 till H4. For H5, although the losses in the active length reduces when compared to H4, the increase in DC losses overwhelms the net gain from the reduction of the AC losses in the active winding length and the total losses in the winding increases.

The slot winding height, H4, shows the minimum total losses for the comparison. From slot winding height H1 to H4, there is a 53% increase in the DC losses at the endwinding region. However, the losses in the active length reduces by approximately 43% from H1 to H4, while the net reduction in the total losses in the winding for the same is approximately 34%. Therefore, by optimising the slot winding height to H4, there is a net gain of 34% reduction in the total losses in the winding and 28% empty area near towards (compared to the winding area of H1), which can be further utilised for cooling the machine (using forced air or water cooling through the space).

**TABLE 4.13: Comparison of losses in components for varying slot height  
(minimum total losses of each slot winding height)**

Height	Model with parallel strands	Active length Loss (W)	DC loss in active length (W)	DC loss in endwinding (W)	Total Loss (W)
H1	13	1094.64	365.04	176	1270.64
H2	22	845.05	429	208	1053.05
H3	10	791.79	473	229	1020.79
H4	9	764.72	525	254	1018.83
H5	10	813.66	656	317	1130.90

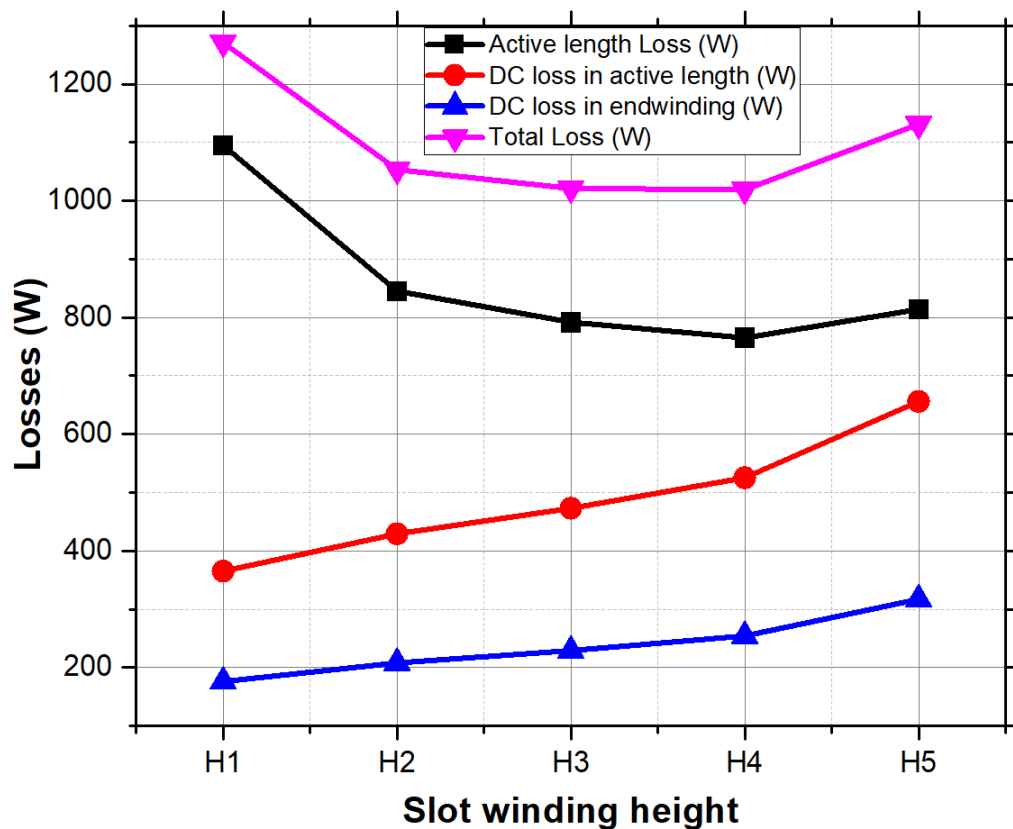


Fig. 4.24: Comparison of losses in components for varying slot heights (with minimum total losses for each winding height)

TABLE 4.13 lists the comparison of the losses in the components for varying slot winding height. The models with minimum total losses in the winding for each slot winding height were selected for this comparison. Slot winding height, H4, has the minimum total losses where the losses in the active length of the winding reduces by approximately 30% when compared to H1, with a net reduction in the total losses in the winding of 19.8%.

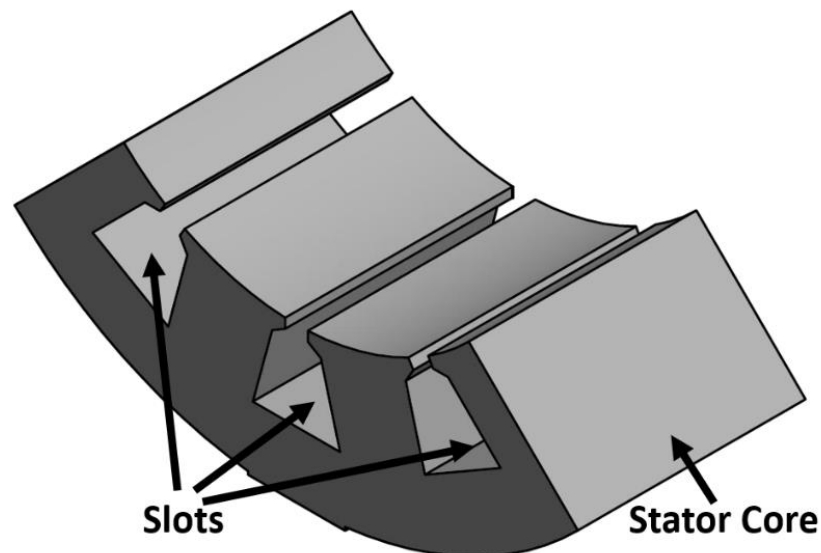
Therefore, by optimising the winding height in the slot and selecting appropriate wire size, the total losses in the winding can be significantly reduced and the leftover empty space (approximately 28% in this analysis) can be utilised for cooling the machine and thus indirectly increase the power density of the machine.

## Chapter 5

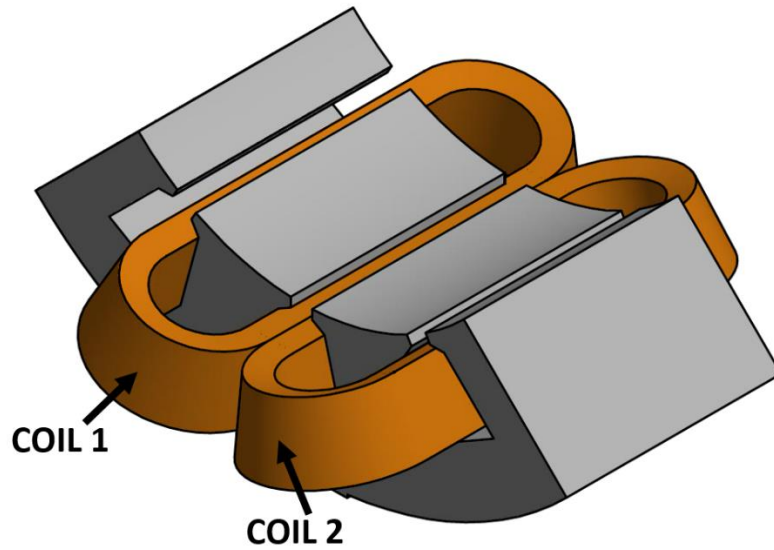
# Experimental validation of finite element modelling

## 5.1. Motorette with 33 'strands – in – hand'

In chapter 4 section 4.1, it is shown that the excitation field does not affect the losses in the winding significantly. Therefore, a quarter section motorette of the machine without the rotor is built. The 3D rendering of the motorette is shown in Fig. 5.1. The 3 slots in the motorette allow for two coil sides to be wound on the two full teeth, letting the central slot to be filled with conductors of two coil sides representing the 1 slot stranded model as shown in Fig. 5.1b.



(a) Representation of experimental motorette



(b) Representation of motorette with two coils wound

Fig. 5.1: 3D rendering of experimental motorette

**TABLE 5.1: Specification of motorette**

PARAMETER	SPECIFICATION
Stator core material	DI – MAX® HF-10
No. of slots	3
Core type	Laminated
Stack length	68 mm
Turns per slot	20
Strands – in - hand	33
Total strands in slot	660
Strand nominal diameter	0.63 mm
Strand Type	Gr-2, 200°C
Slot Filling factor	44%

The specifications of the motorette are listed in TABLE 5.1. The specifications are selected as such that the motorette resembles the prototype traction machine used in this thesis, except for the stack length which is reduced to half of the actual stack length of the machine.

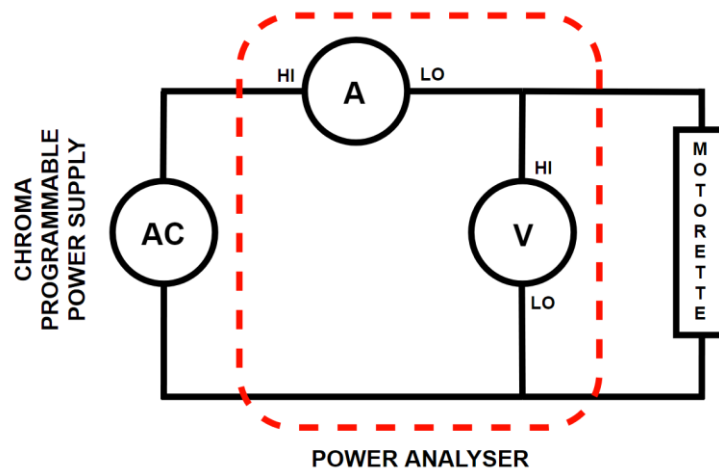


Fig. 5.2: Schematic diagram of the experimental setup

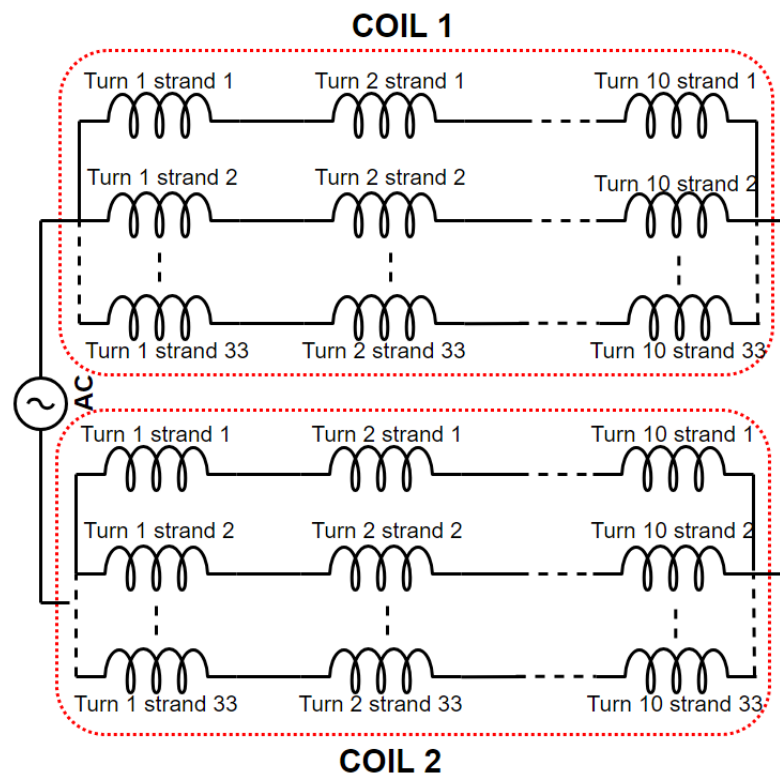
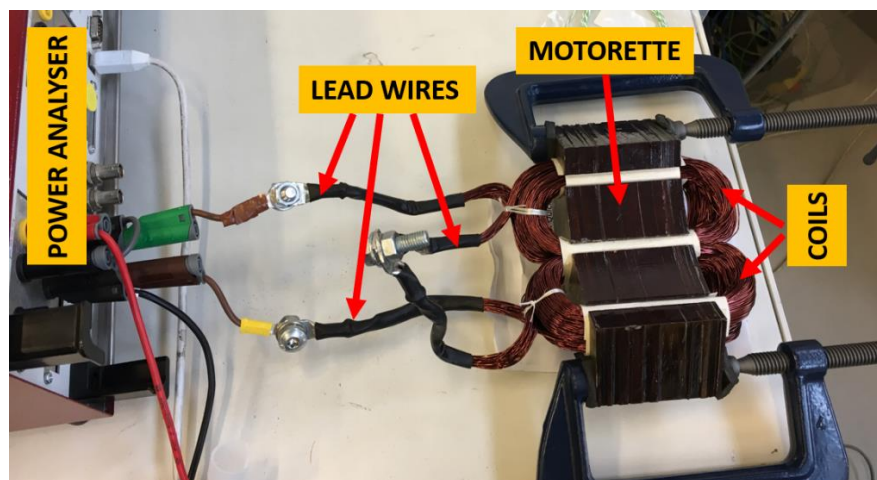


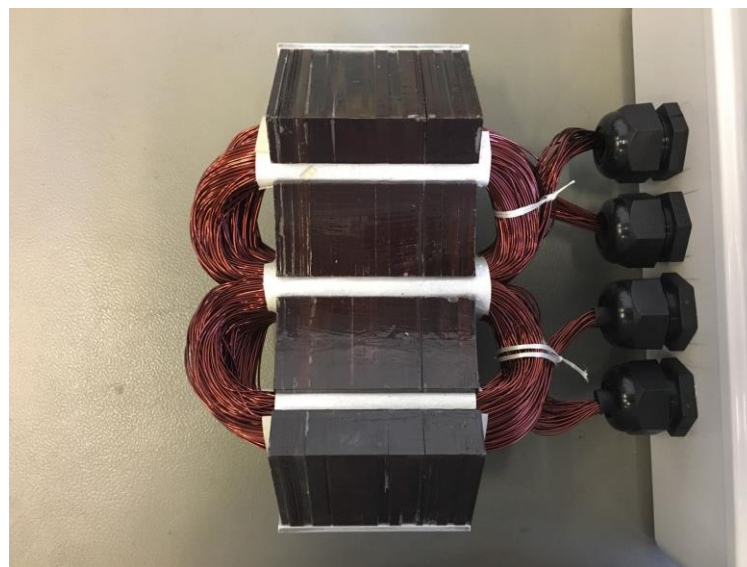
Fig. 5.3: Representation of circuitual connection of the motorette in the experimental setup

Fig. 5.2 shows the schematic diagram of the connections in the experimental setup. The motorette windings are connected to a precision power analyser (PPA 5530 from N4L [64]) to record the losses in the windings and is fed from a programmable AC power supply (Chroma programmable AC Source, 61511 [65]) which allow for

variable frequency inputs. Fig. 5.3 shows a representation of the circuitual connection of the windings in the motorette in the experimental setup.



(a) Experimental setup with motorette (33 strands – in – hand random winding)



(b) View of the coils in the motorette

Fig. 5.4: Experimental setup with test motorette (33 strands – in – hand random winding)

Fig. 5.4 shows the experimental setup with the motorette wound with 33 strands – in – hand random winding. Fig. 5.4a shows the motorette connection to the power analyser with the connecting cables with banana clip tips and lug nuts joining the

wires. A motorette model with 33 strands – in – hand representing the experimental motorette is generated for FEA and is shown in fig. 5.5 with two coils wound.

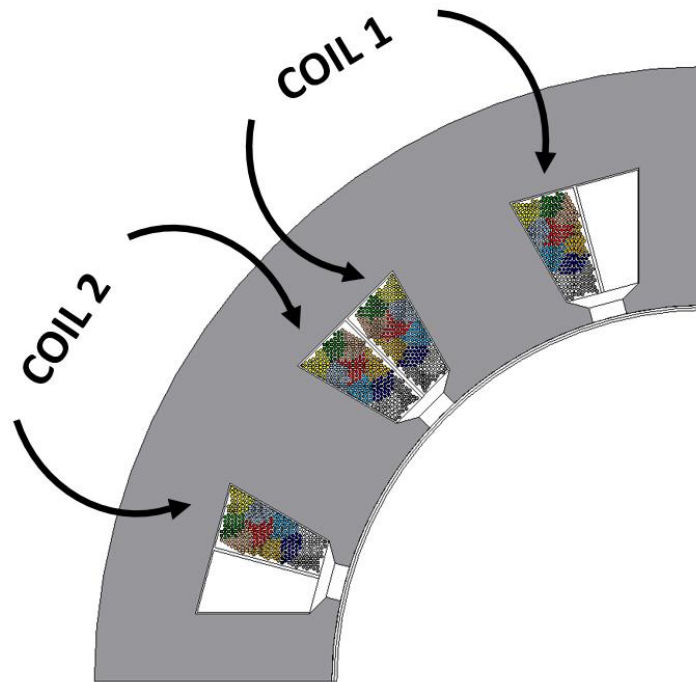


Fig. 5.5: Motorette representation for FEA

**TABLE 5.2: Experimental Losses of motorette**

Freq. (Hz)	Total Losses in the motorette at supply current (W)					
	5 A	10 A	15 A	20 A	25 A	30 A
186.67	0.51	2.19	4.55	8.82	12.43	19.12
300	0.64	2.75	5.85	11.06	16.04	23.79
500	1.02	4.11	8.96	16.42	24.57	36.13
666.67	1.28	5.49	11.86	21.48	32.71	48.05
1200	2.34	9.79	21.436	38.35	59.47	86.25

TABLE 5.2 lists the losses in the experimental total losses in the motorette for different current amplitude at various frequencies. Fig. 5.6 shows these losses as a function of the frequencies for each current amplitude. At higher frequencies, the losses are higher for larger current amplitudes as the flux density increase. To

compare the experimental losses with finite – element modelling, current amplitude of 30 A<sub>rms</sub> is selected and 2D FE simulations are run for various frequencies.

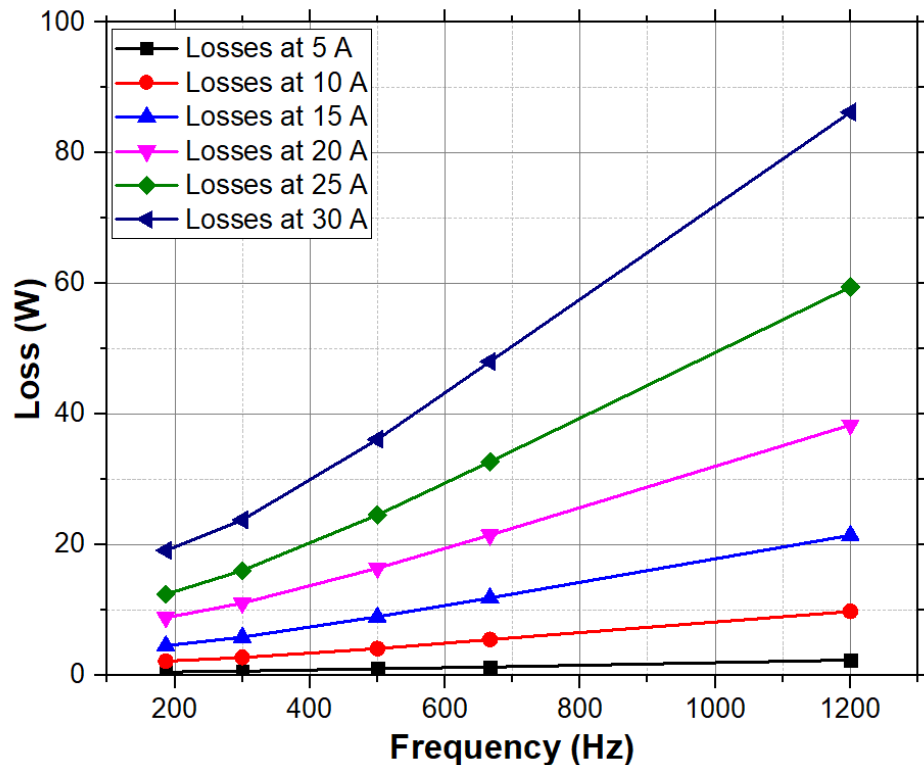


Fig. 5.6: Experimental total losses in the motorette at various frequencies for different current amplitude

Assuming no AC loss occurs at the endwinding, the leadwires and the connecting wires, the resistance of these components are calculated analytically and the DC loss in these components calculated. Therefore, the total loss for the simulated model is the summation of the active winding length (stack length) losses obtained from the FEA, the core losses (multiplied by factor of 2) from FEA and the calculated DC losses of the components (endwinding, lead wires, connecting wires).

**TABLE 5.3: Comparison of experimental loss and modelling loss**

Frequency (Hz)	Total Losses at 30 A		% difference
	Experimental (W)	Modelling (W)	
186.67	19.12	9.54	50.1
300	23.79	10.47	55.98
500	36.13	12.54	65.29
666.67	48.05	14.948	62.83

TABLE 5.3 shows the comparison of the total losses obtained at 30 A for experimental results with the modelling results. The difference between the experimental results and the modelling results is significant and the reason for this is sought after.

After carefully eliminating all other possible causes, it is predicted that the root cause for the vast mismatch to be due to dissimilar strands/bundle positions between the experimental motorette and the modelling. Since, the experimental motorette is randomly – wound, it is impossible to know the positions of the strands inside the slot. In order to verify this explanation of mismatched results, simpler models are required where the strand positions can be fixed in the experimental setup.

## **5.2. Motorette with slot formers**

In order to fix the strand position inside the slot, slot formers are made using 3D printing technology. The motorettes with varying degree of complexities are analysed both via finite – element and experimental verifications as detailed in the following sections.

### 5.2.1. Motorette 1

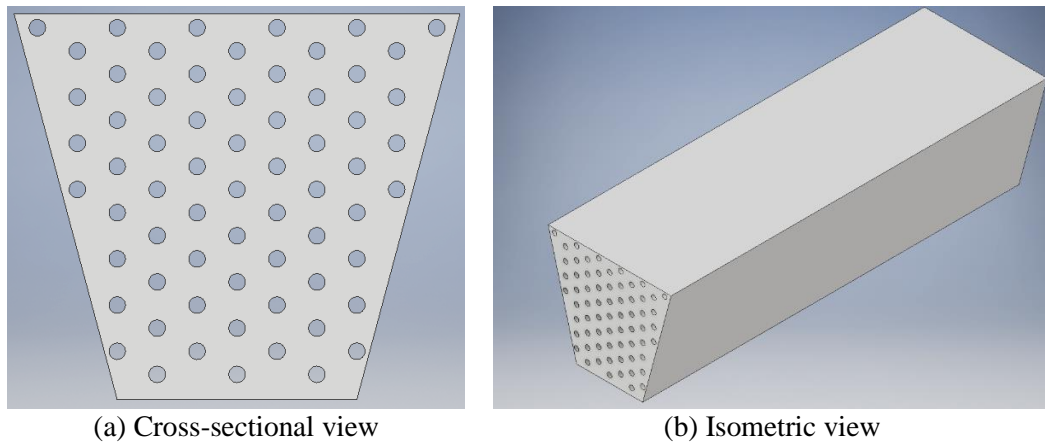


Fig. 5.7: Render of motorette slot former

**TABLE 5.4: Specification of slot in motorette 1**

PARAMETER	SPECIFICATION
Turns per half slot	7
Strands – in – hand	4
Total strands per slot	28
Strand nominal diameter	0.9 mm

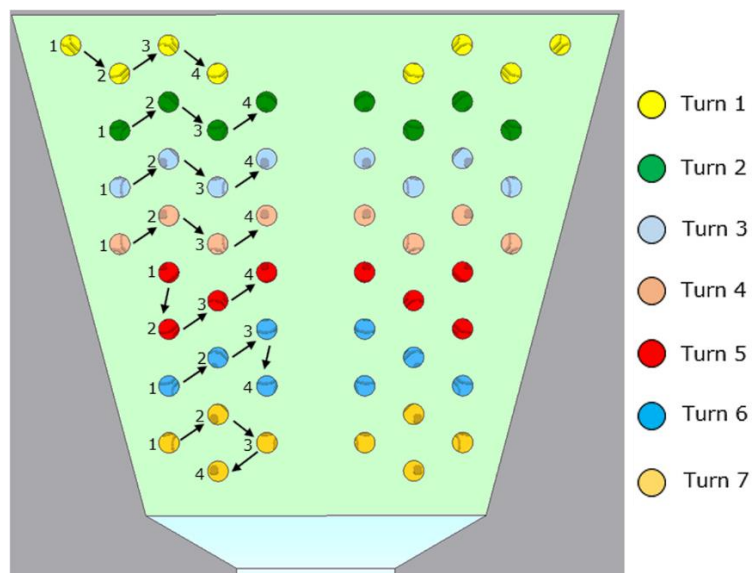
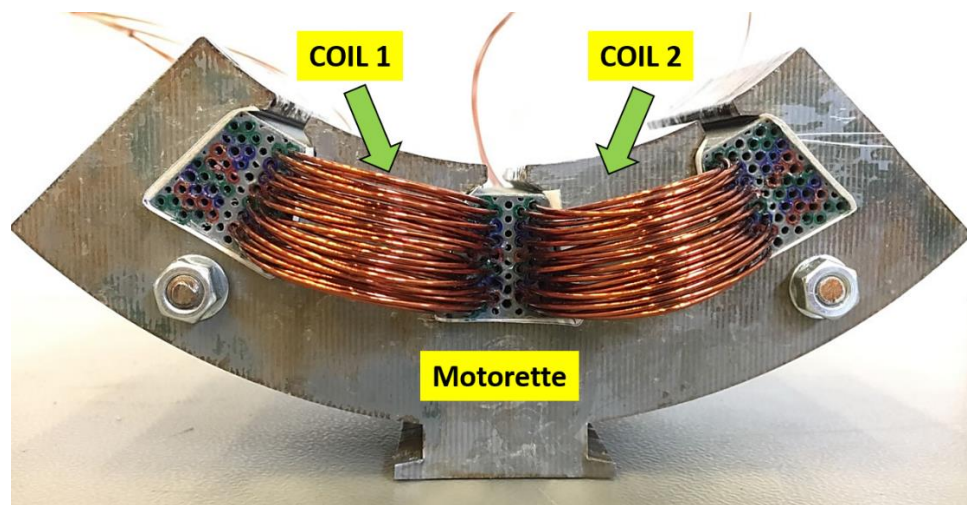
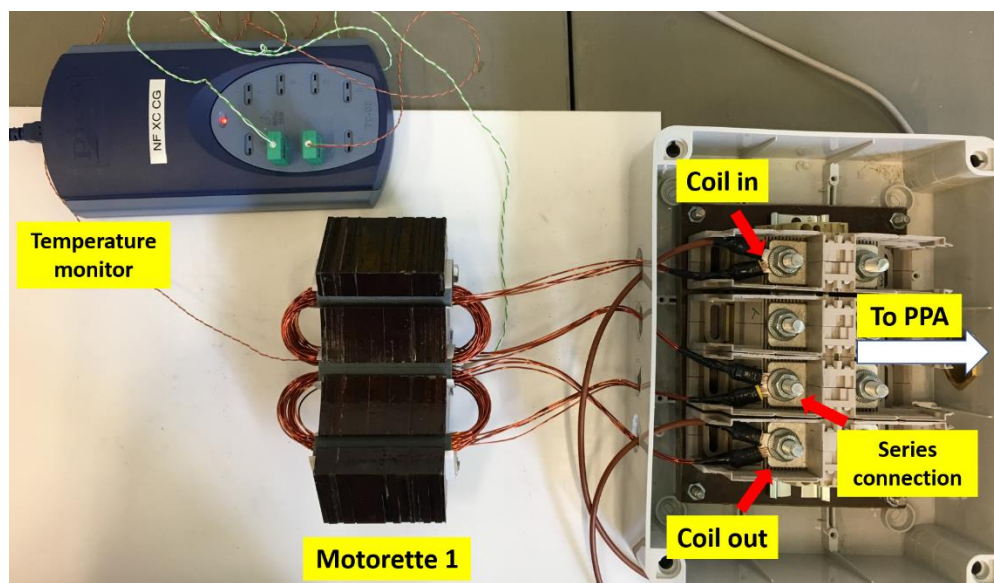


Fig. 5.8: Arrangement of strands in the slots of motorette 1

Fig. 5.7 shows the rendering of the slot formers for the motorette 1 and TABLE 5.4 lists the specifications of the slot former. Fig. 5.8 shows the arrangement of the strands inside the slot former. The strands are meticulously wound through the holes in the former so that they have the same positions inside the slot as in fig. 5.8. Similar to process described in the previous section, a 2D model of the motorette is generated with the exact positioning of the strands as the experimental motorette.



(a) Motorette 1 with coils in former



(b) Experimental setup for motorette 1

Fig. 5.9: Experimental motorette 1

Fig. 5.9 shows the experimental motorette 1. In Fig. 5.9a, the motorette with coils in the former is shown and in Fig. 5.9b, the experimental setup for measurement of losses in motorette 1 is shown. The measurements are carried out at  $30 A_{rms}$  and at frequencies (Hz): DC, 50, 500, 666.67, 1000 and 1500. Since, the former made of 3D printing material (which is generally polyester composite) have low malleability point, the temperature rise inside the slots is monitored using a data logger and k – type thermocouples. After each set of measurement, the motorette is allowed to cool down to the ambient temperature.

**TABLE 5.5: DC Losses in the components**

COMPONENT	LOSS VALUE (W)
Active winding length (calculated)	12.27
Endwinding + leadwires (calculated)	17.77
Wires to PPA (calculated)	5.09
Total DC loss (calculated)	35.13
Total DC loss (measured)	41.25
Stray loss	6.12

TABLE 5.5 lists the DC losses in the components of the motorette 1. The losses are obtained from analytical calculated and the total DC loss is compared against the actual measured DC loss. The calculation of the DC losses in the components is shown the appendix B. Total measured loss minus the total calculated loss results in a mismatch of 6.12 W. This stray loss maybe the result of the losses introduced by the contact resistance at the terminal box. However, since it is assumed that no AC loss is present in components except the active winding length, this stray DC loss value is being considered as a constant and is being factored in the further analysis.

**TABLE 5.6: Comparison of measured total loss and modelling loss**

Freq. (Hz)	Loss in components (W)					% difference	Total/DC loss (active length)
	Active length	Core (2x)	Total DC loss in components	Total (calculated)	Total (measured)		
DC	12.27	0	28.98	41.25	41.25	0	1
50	12.56	0.34	28.98	41.88	41.96	0.19	1.01
500	12.77	0.68	28.98	42.43	44.25	4.3	1.14
666.67	12.80	1	28.98	42.78	44.27	3.5	1.12
1000	13.23	1.82	28.98	44.03	45.45	3.2	1.11
1500	13.41	3.23	28.98	45.62	48.00	5.2	1.18

TABLE 5.6 shows the comparison of measured motorette losses with the calculated losses. The column highlighted in pale blue are the total losses incurred in the active winding length of the motorette. These results are obtained from FE simulations. The column highlighted in light gold shows the core loss (multiplied by factor of 2) obtained from FE simulations. The column highlighted in pale green contains the DC losses of components (endwinding + lead wires + wires to PPA + stray DC losses). The DC loss values of these components are considered constant across all the frequency measurements. The columns highlighted in orange lists the total losses (calculated) and the total losses (measured). The total losses (calculated) is the summation of active winding length loss, the core losses and the DC losses in the components for each frequency measurement. The total losses (measured) is the system loss measured for a frequency value listed in column 1. The column highlighted in green shows the percentage difference between the total calculated loss and the total measured loss, the largest difference being 5.2% at measured frequency of 1500 Hz. The column highlighted in blue shows the Total / DC loss ratio in the active length. Since, it is assumed that the AC loss is present only at the

active length, the numerator of the loss ratio is total measured loss minus the summation of core loss and the DC losses in the components.

The lower AC loss at high frequencies for the motorette 1 can be due to:

- (a) As presented in chapter 3, the combination of lesser number of parallel strands and horizontal arrangement of strands result in lower AC loss in the winding. Since the strands in motorette 1 is arranged in horizontal configuration and has only 4 parallel strands per turn, this may result in lesser circulating current.

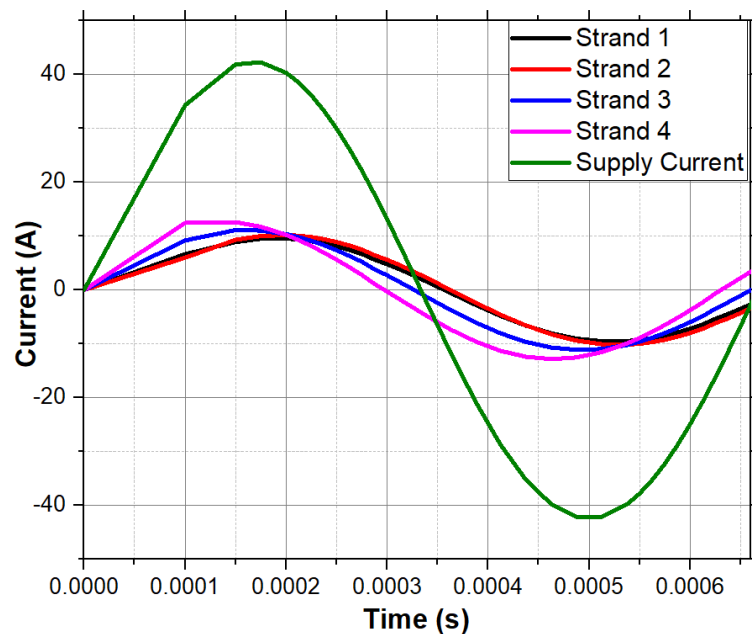


Fig. 5.10: Waveform of strand currents and supply current in motorette 1

Fig. 5.10 shows the waveform of the strand currents and the supply current at 1500 Hz. The main current is relatively evenly distributed among the strands and this asserts the reason for lower AC loss at high frequency.

- (b) The flux leaking into the slot links the strand in various positions in the slot differently and as a result the impedance seen by the strands is different depending on the position of the strand in slot. Due to smaller magnitude of current used in the experimental motorette, flux density in the teeth and the

back iron is small. As a result, the leakage flux will be insignificant to cause significant nonuniformity in impedance of the strands.

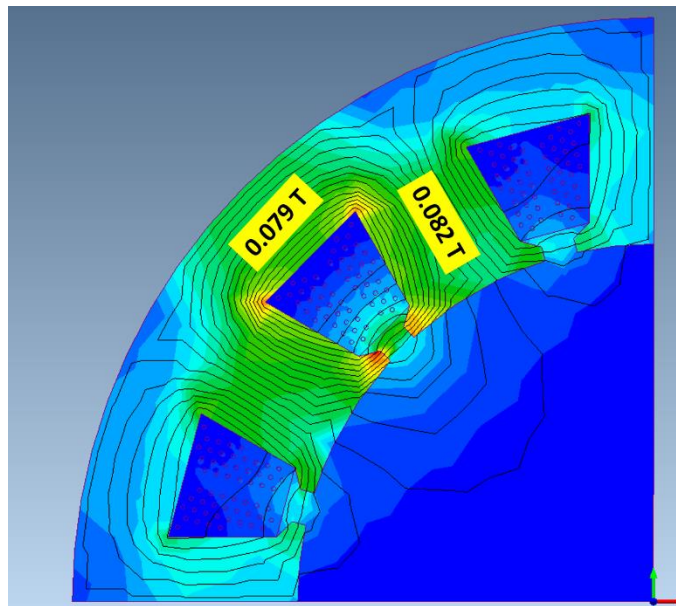
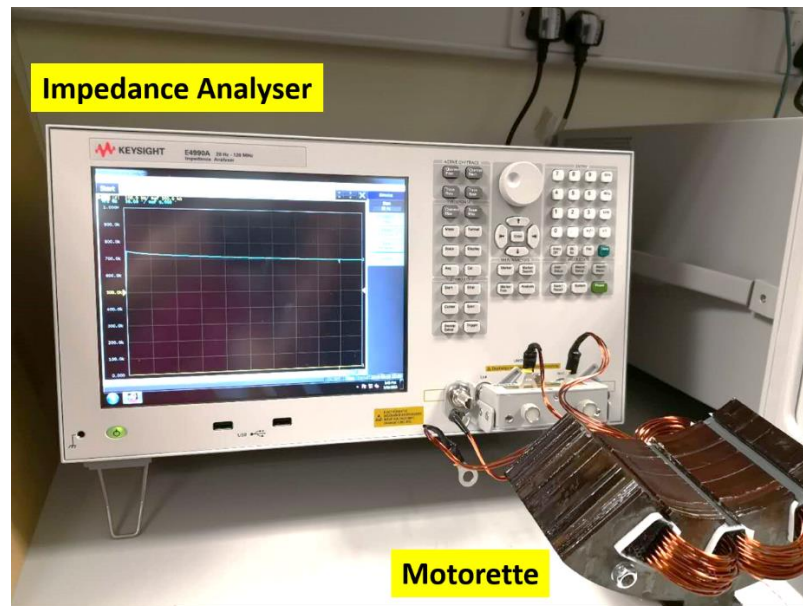


Fig. 5.11: Flux density  $|B|$  in the teeth and back iron of the motorette

Fig. 5.11 shows the flux density  $|B|$  in the teeth and the back-iron regions of the motorette 1 at the time instant when the current is peak. The value of flux density is very small and thus a very few fluxes will leak into the slot.

Another technique to estimate the high frequency losses in winding without taking into the core loss account is to measure the AC resistance of the coils in the motorette at various frequencies. To measure the AC resistance of the windings in the motorette, a precision impedance analyser (E4990A Impedance Analyzer from KEYSIGHT) is used. Fig. 5.12 the experimental measurement of the AC resistance of coils in the motorette. The results are obtained for frequency range (20 Hz – 2 kHz).



(a) Motorette with impedance analyser



(b) Frequency response of inductance and resistance of winding in the motorette

Fig. 5.12: Measurement of AC resistance of the motorette winding with impedance analyser

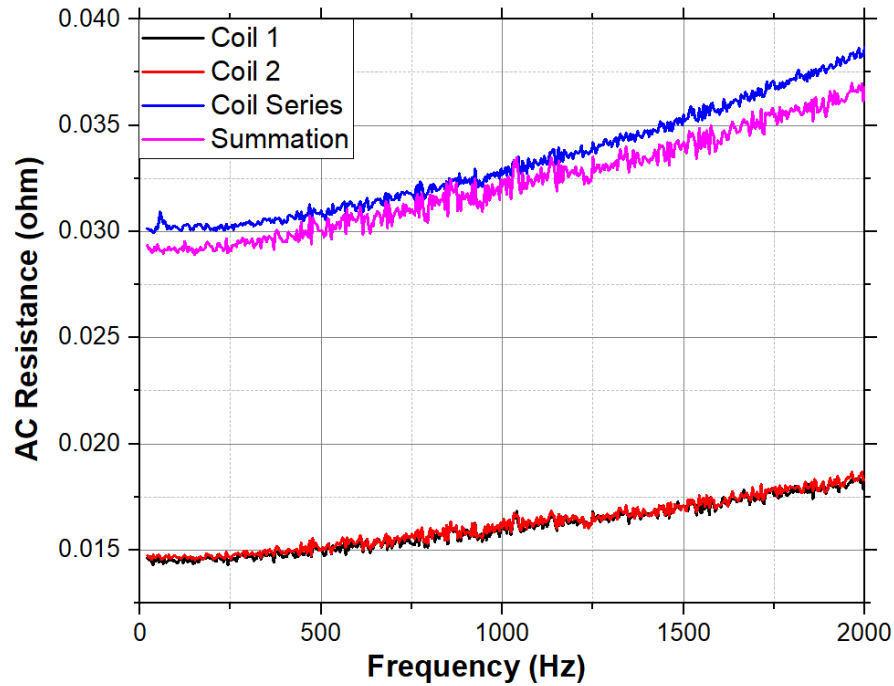


Fig. 5.13: AC resistance of the coils in the motorette as function of frequency

Fig. 5.13 shows the AC resistance of the individual coils and the coils in series as the function of frequency. The red and the black curves the AC resistance of the individual coils and the blue curve is the measured resistance of both the coils in series. The pink curve is the arithmetic sum of the resistances of the individual coils. A slight difference is observed between the actual measured series resistance and the arithmetic sum. This maybe due to the contact resistance introduced by the lugs at the terminals. The average value of the contact resistance is about  $1.03 \text{ m}\Omega$ .

Using the measured AC resistance of the series coil at specific frequencies and power loss equation (5.1), the losses incurred in the motorette winding can be calculated.

$$P_{Loss} = I^2 R_{AC} \quad (5.1)$$

**TABLE 5.7: Comparison of losses calculated from AC resistance with simulation loss**

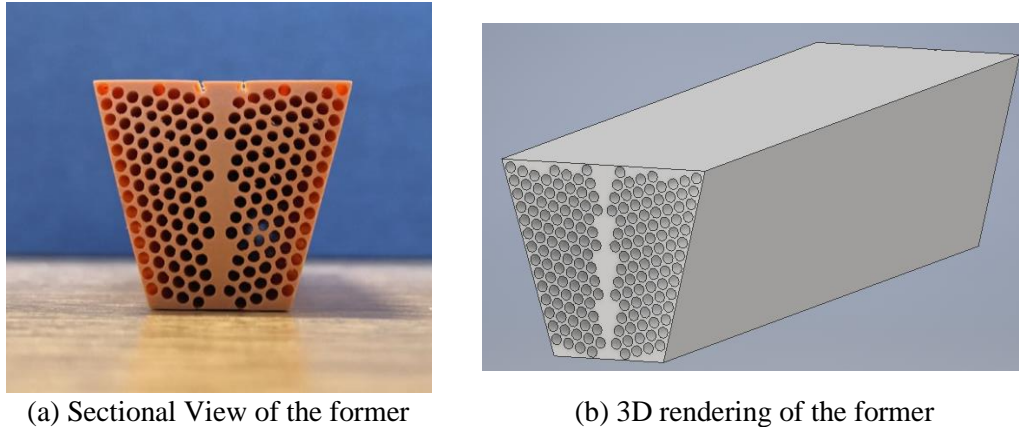
Freq. (Hz)	Losses (W)				% difference
	Active length	Endwinding + leadwires DC loss	Total (calculated)	Total (from AC resistance)	
50	12.56	17.77	30.33	28.13	7.80
500	12.77	17.77	30.54	28.26	8.07
666.67	12.80	17.77	30.57	28.86	5.93
1000	13.23	17.77	31.00	30.38	2.04
1500	13.41	17.77	31.18	33.21	-6.11

TABLE 5.7 shows the comparison of losses calculated using measured AC resistance with the results obtained from FE simulations. The total loss (calculated) is the aggregate of active winding length (from FEA) and the DC loss (calculated) of endwinding and leadwires combined. The Total loss (from AC resistance) are calculated at  $30 A_{rms}$  using eq. (5.1). The percentage difference between the total losses calculated using both methods is less than 10%.

The results obtained using the motorette 1 shows good co – relation between the simulated and the experimental results. However, the model is simple and the losses in the winding at high frequencies is not very significant. To validate the FE models at high frequencies, motorette with higher number of parallel strands are required.

### 5.2.2. Motorette 2

This section details a complex motorette and the validation of the AC loss modelling with finite – element with experimental results of the motorette.



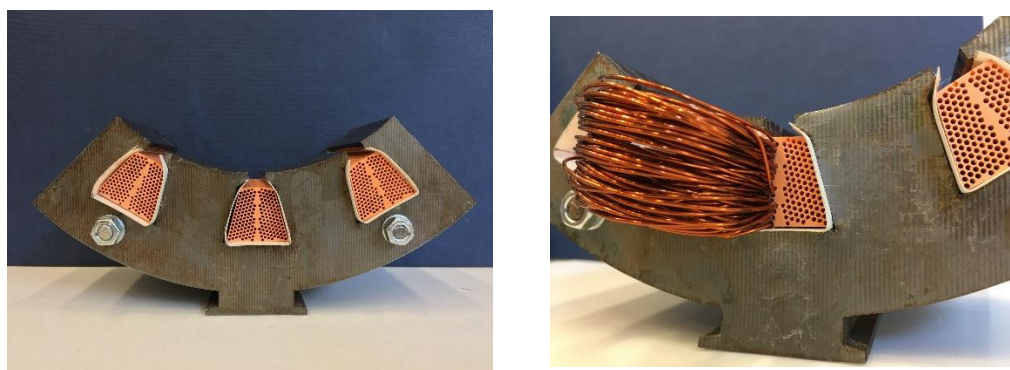
(a) Sectional View of the former

(b) 3D rendering of the former

Fig. 5.14: Former used for Motorette 2

**TABLE 5.8: Specification of slot former in motorette 2**

PARAMETER	SPECIFICATION
Turns per half slot	10
Strands – in – hand	9
Total strands per slot	180
Strand nominal diameter	0.8 mm
Slot filling factor	19.6%



(a) Motorette 2 with former

(b) Motorette with 1 coil wound

Fig. 5.15: Experimental Motorette 2

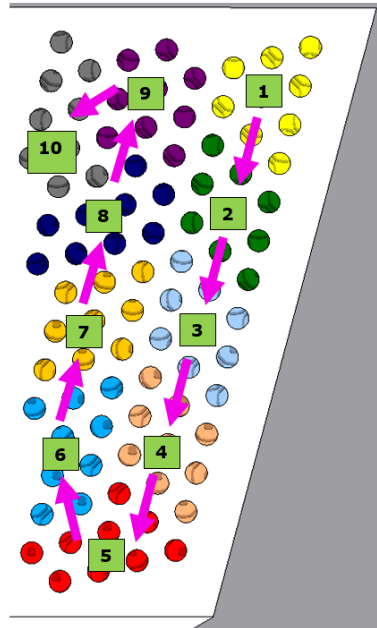
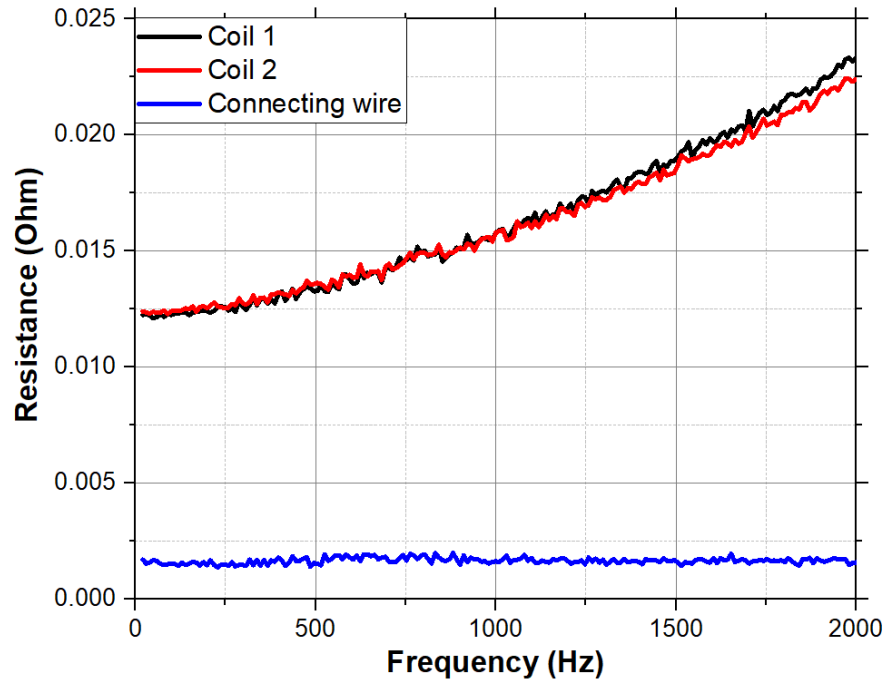
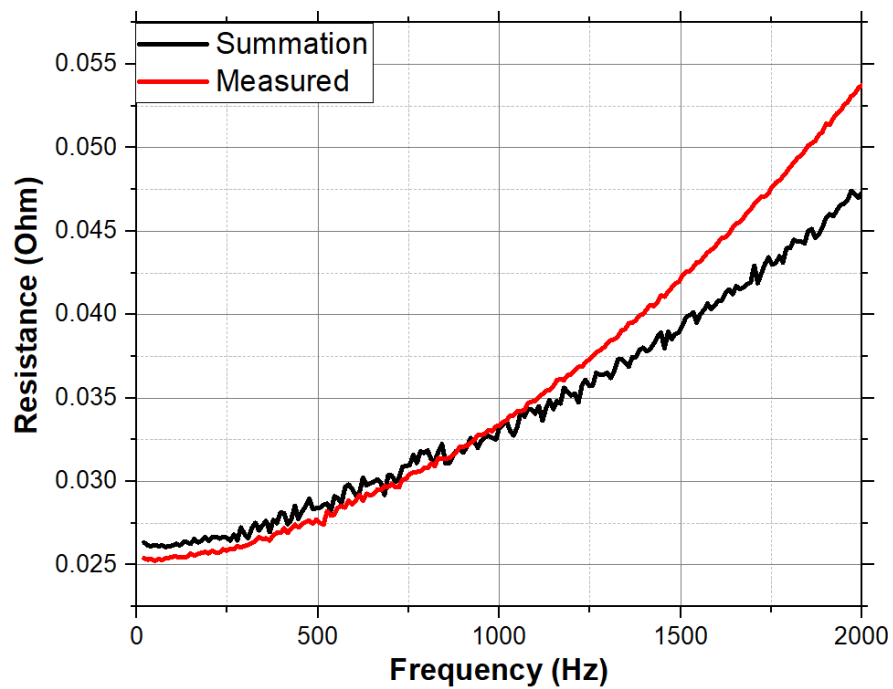


Fig. 5.16: Conductor positions and layout in mottorette 2

Fig. 5.14 shows the former used in mottorette 2. High precision 3D printers are used for printing holes with the minimum gap between them. Strong, high temperature resistant nanocomposite material, NanoCure RC25, is used for printing the precision formers [66]. TABLE 5.8 lists the specifications of the slot former in mottorette 2. The mottorette windings have 10 turns with 9 strands – in – hand. Fig. 5.15 shows the experimental mottorette 2 with the formers inserted in the slots. In Fig. 5.15b, one tooth of the mottorette is wound. Fig. 5.16 shows the conductor positions and their layout in the slot former. In the figure, the strands with same colour form one bundle and the number highlighted in green denotes the bundle number and its position in the slot former.



(a) Resistance of individual coils and connecting wire in motorette 2



(b) Comparison of summed series resistance of coils and measured resistance

Fig. 5.17: Measured resistance of the components in motorette 2 using impedance analyser

Fig. 5.17 shows the measured resistance of the components in motorette 2 using the impedance analyser described in previous section. In Fig. 5.17a, the black and the red plots represents the resistances of the coils measured individually. The blue plot is the resistance of the connecting wire used to link coil 1 and coil 2 in series. The resistance of the connecting wire does not change significantly with the increase in frequency and therefore it is considered as a constant. Fig. 5.17b shows the comparison of the measured series resistance and the summation of the resistances of the individual components. The series measured resistance represented by the red plot in Fig. 5.17b, is the equivalent resistances of coil 1 & 2 and the connecting wire, while the summation represented by the black plot, is the arithmetic sum of the individual resistances of coil 1 & 2 and the connecting wire. The discrepancy in both plots at high frequencies can be explained by the stray resistance introduced by the lugs and the lug nuts linking the coils in series.

The DC resistance of the experimental motorette setup can be split into following components: (a) Active length of the winding, (b) End windings, (c) Lead wires, (d) Connecting wire (the wire connecting two coils in series), and (e) supply wires (wires connecting the motorette to the power analyser).

The DC losses calculated as follows:

$$\text{DC resistance of the setup} = \text{Power loss at DC} / (\text{current})^2$$

The length of the connecting wire and the supply cables are equal, so the resistances are approximately equal.

DC resistance of the active length of the winding is calculated analytically.

DC resistance of (endwinding + leadwires + connecting wire) = DC resistance of the setup – DC resistance of (Active winding length + supply cables).

**TABLE 5.9: Comparison of measured total loss and modelling loss****(motorette 2)**

Freq. (Hz)	Losses in components (W)						Total /DC loss
	Active Length	Core (2x)	Total DC losses in components	Total Loss (calculated)	Total Loss (measured)	% difference	
DC	9.74	0	19.32	29.06	30.2	3.92	1
50	9.75	0.066	19.32	29.14	29.71	1.96	1.06
100	9.79	0.155	19.32	29.26	31.35	7.14	1.22
200	9.92	0.374	19.32	29.61	30.27	2.23	1.08
500	10.85	1.28	19.32	31.45	32.44	3.15	1.19
666.67	11.71	1.88	19.32	32.91	34.61	5.17	1.24
1000	14.13	3.44	19.32	36.89	40.47	9.70	1.51
1500	19.42	6.34	19.32	45.08	48.99	8.67	1.65

TABLE 5.9 shows the comparison of measured total loss with modelling loss of the motorette 2. The column highlighted in pale blue are the total losses incurred in the active winding length of the motorette. These results are obtained from FE simulations. The column highlighted in light orange shows the core loss (multiplied by factor of 2) obtained from FE simulations. The column highlighted in pale green contains the DC losses of components (endwinding + lead wires + connecting wires + supply cables to PPA). It is assumed that endwinding do not incur AC losses and only have DC loss. As shown in Fig. 5.17a, the resistance of the auxiliary cables (connecting wire and supply cables) do not change significantly. Therefore, DC loss values of these components are considered constant across all the frequency measurements. The columns highlighted in grey lists the total losses (calculated) and the total losses (measured). The total losses (calculated) is the summation of active winding length loss, the core losses and the DC losses in the components for each frequency measurement. The total losses (measured) is the system loss measured for a frequency value listed in column 1. The column highlighted in gold shows the

percentage difference between the total calculated loss and the total measured loss. The results of the measured losses with the modelling losses largely matchup with the largest difference being 9.7% at measured frequency of 1000 Hz. The column highlighted in green shows the Total / DC loss ratio in the active length. Since, it is assumed that the AC loss is present only at the active length, the numerator of the loss ratio is total measured loss minus the summation of core loss and the DC losses in the components.

### **5.3. Conclusion**

For random – wound machine, where the strands/bundles shapes and positions in the motorette cannot be predetermined, the modelling fails to estimate the total loss in the winding of the machine. However, for the motorettes where the strands/bundles position are same as finite – element models, the results show good co-relation between the experimental and the modelled losses. The models are able to predict the losses with accuracy of above 90%. The experimental verifications carried out in this chapter proves that the modelling of AC effects done in this thesis and is able to determine the loss incurred in windings due to AC effects with high degree of accuracy.

## Chapter 6

# **The Influence of bundle shapes and positions on the AC losses in the slot**

In this chapter, the influence of bundle shapes on the AC losses in the slot is investigated and a technique to reduce the AC losses in the slot is presented. To display the loss mitigation technique, a case model with 15 parallel strands is considered. An in -depth analysis of the loss reduction technique is carried out and experimental verification of the above technique is presented.

## **6.1. Methodology**

The methodology used in this chapter is as follows:

### **6.1.1. Selection of optimum strand diameter**

The methodology followed for selection of optimum strand size is similar to the one described in section 4.1.1 of chapter 4. However, the key difference for the method used in this chapter in comparison with the methodology in chapter 4 is the placement of the strands inside the slot geometry.

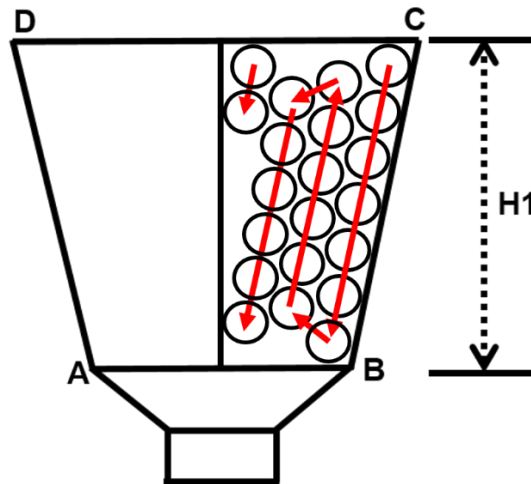


Fig. 6.1: Representation of strand layout in the slot geometry

Fig. 6.1 shows a representation of a slot of an electrical machine. The area marked with corners ABCD is the available area for winding with  $H_1$  being the height of the slot. The strands are placed inside the slot as shown in the figure with the red arrows marking the path of strand laying algorithm. Then, the slot filling factor obtained for each strand diameter is plotted against the strand diameter to select the magnet wire exhibiting high filling factor.

### 6.1.2. Clustering of strands into bundles and positioning

Similar to methodology described in section 4.2.2 of chapter 4, the strands are divided and grouped together into bundles to form parallel strands of conductors. Again, the shapes of the bundles are not constrained to allow for resemblance to winding of random – wound machine. The clustering of the strands is varied as such that the conductors occupy different location in the slot with varied shapes. This result in numerous plausible bundle positions and shapes. Then, these bundles are connected in external circuit to form turns and the strands within a bundle connected in parallel. Fig. 6.2 shows a representation of the process.

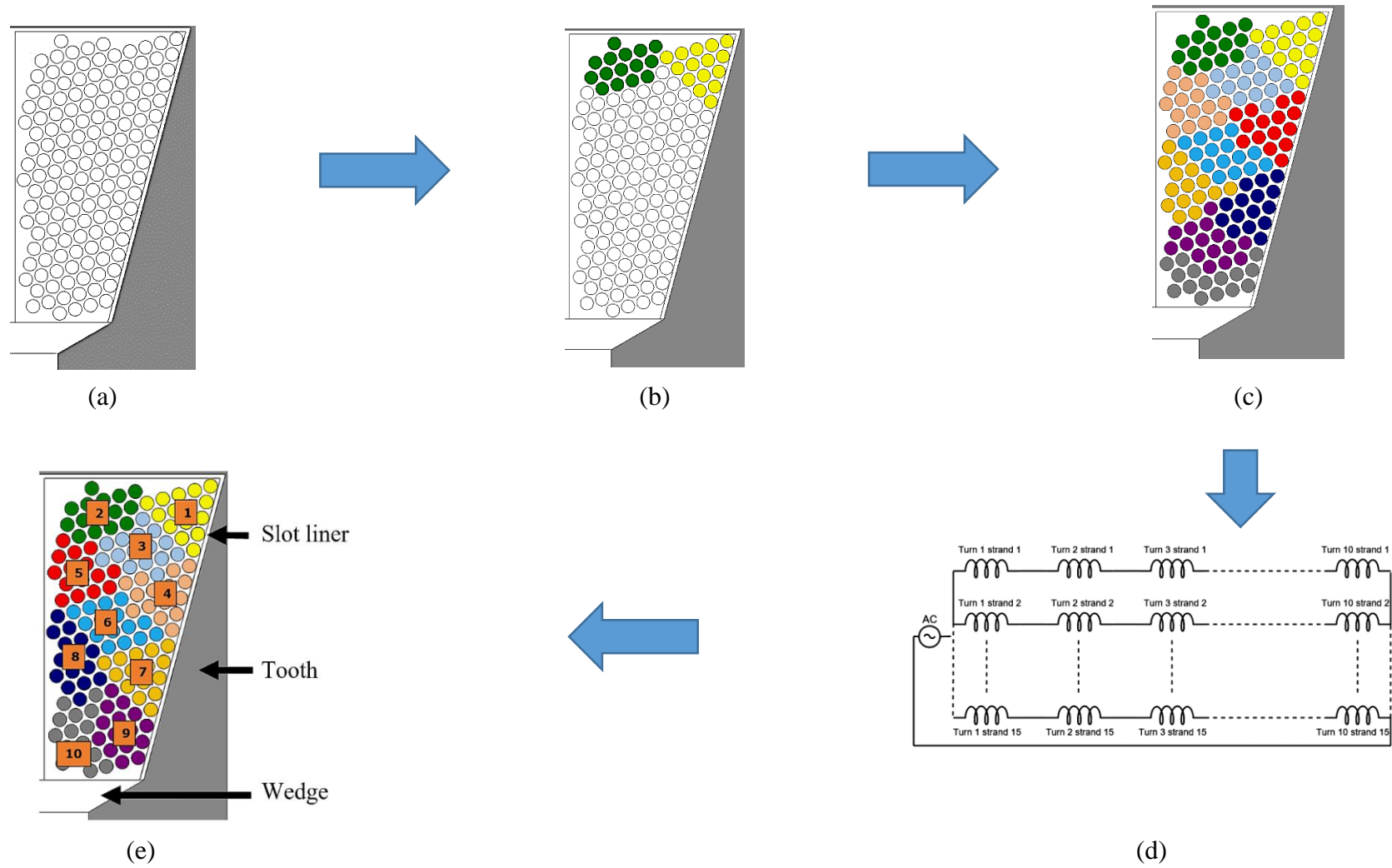


Fig. 6.2: Representation of the clustering and positioning process

## 6.2. Finite – Element model (15 parallel strands)

The analysis in this section is carried out using a model consisting of 10 turns per coil, with each bundle made up of 15 strands – in – hand resulting in 150 strands per half slot. Magnet wires with a nominal strand diameter of 1 mm are selected which results in a slot filling factor of 55%. A rms current amplitude of 84 A with a frequency of 1500 Hz is applied.

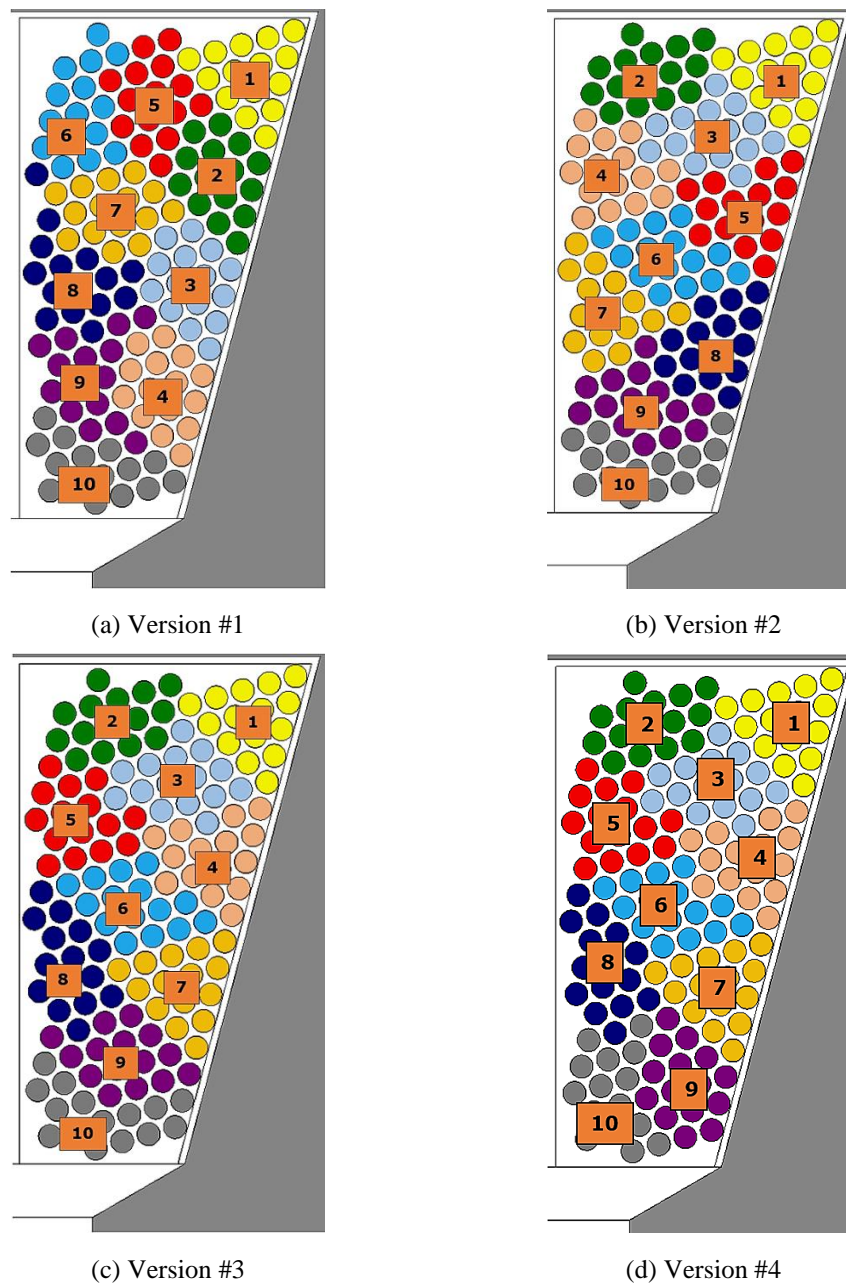


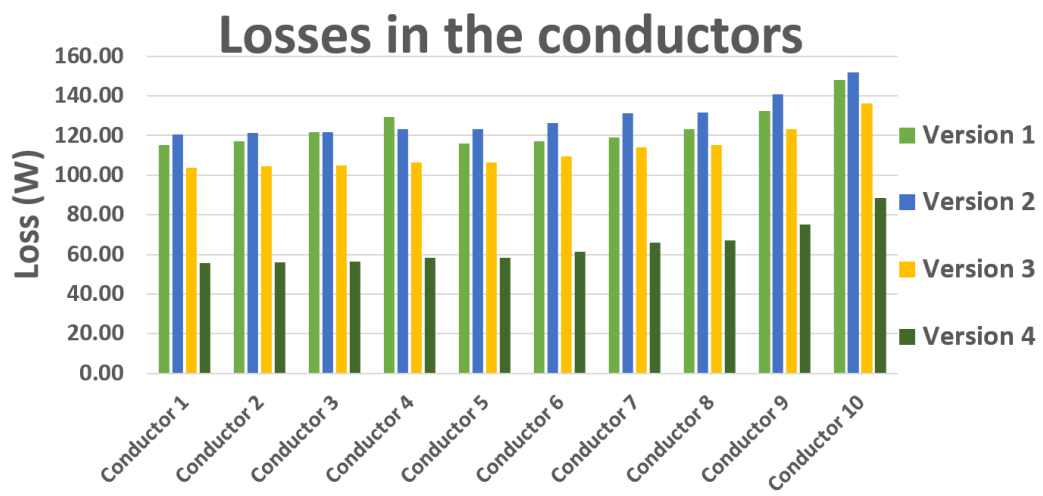
Fig. 6.3: Half side of a slot showing plausible versions of conductor positions

**TABLE 6.1: Comparison of total loss to DC loss**

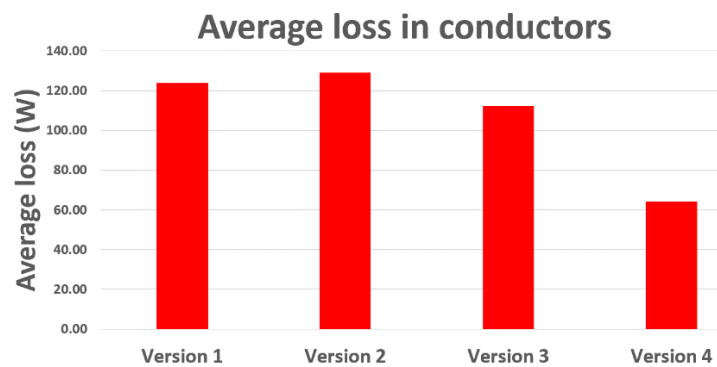
Versions	Total Loss (W)	Total Loss/ DC Loss
DC	355.5	1
Version #1	1238.62	3.49
Version #2	1289.48	3.63
Version #3	1122.42	3.16
Version #4	652.38	1.84

Fig. 6.3 shows four plausible versions of conductor positions inside the slot which are considered for the purpose of this analysis. The figures show the conductors holding different positions inside the slot geometry with colours representing the conductors and the numbers representing their positions within the slot geometry. TABLE 6.1 lists the total losses in the active length of the winding of the machine for each version along with the total loss to DC loss ratio, with the DC loss in the active length being 355.5 W. For versions #1, #2 and #3, the total loss to DC loss ratio is above 3 times. However, in case of version #4, the loss ratio is 1.84. Fig. 6.4a shows the comparison of the losses in the conductors for the four versions and Fig. 6.4b shows the averaged-out losses in the conductors for each version. The average reduction of losses in the conductors from the worst case (Version #2) to best case (Version #4) is approximately 50%. Also, as evident upon inspection of Fig. 6.3, comparing version #3 and #4, only the position of conductors 9 and 10 are changed. However, by doing so the total losses in the winding reduce by approximately 41%. Fig. 6.5a shows the supply current to one of the phases while Fig. 6.5b and Fig. 6.6c show the currents as shared by the strands for version #3 and #4 respectively. As can be observed from these figures, the currents in the strands are unevenly distributed

and are displaced in time. TABLE 6.2 further details quantitatively the comparison of currents as shared by the strands for version #3 and version #4.

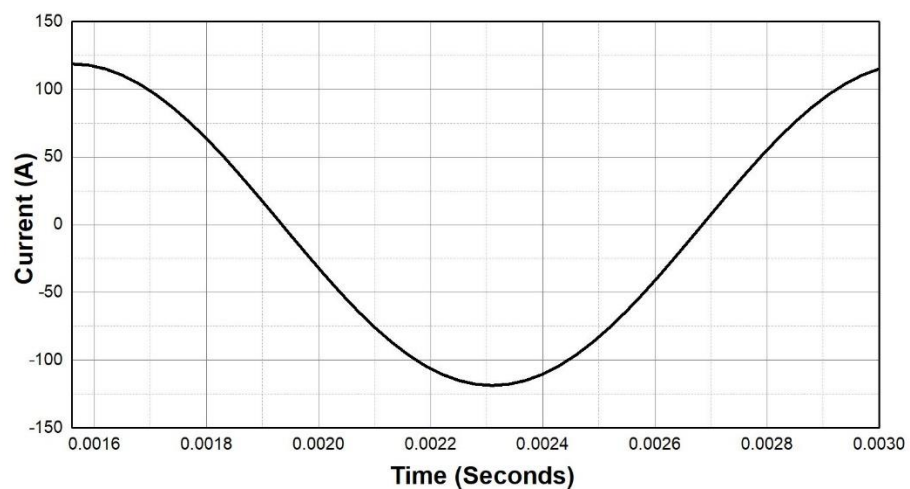


(a)

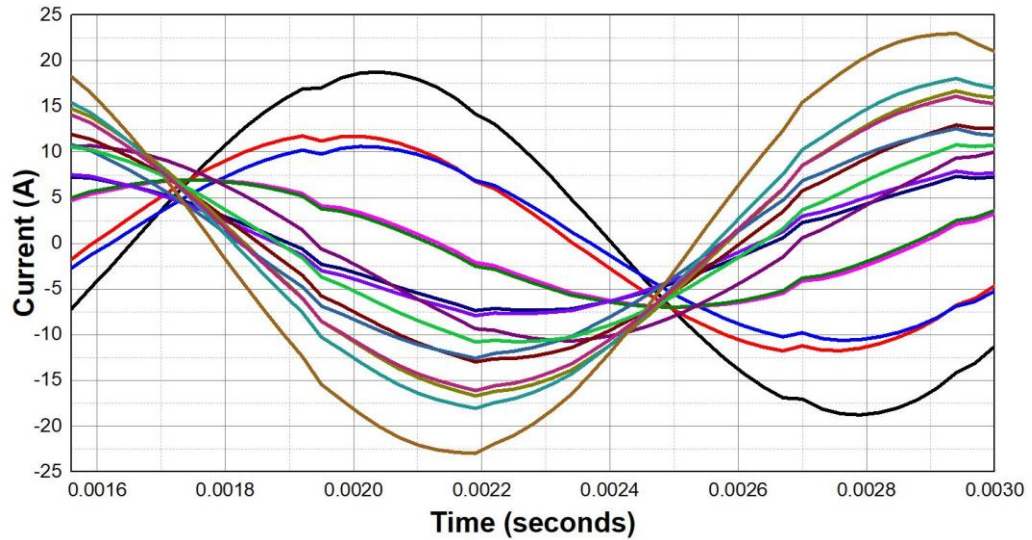


(b)

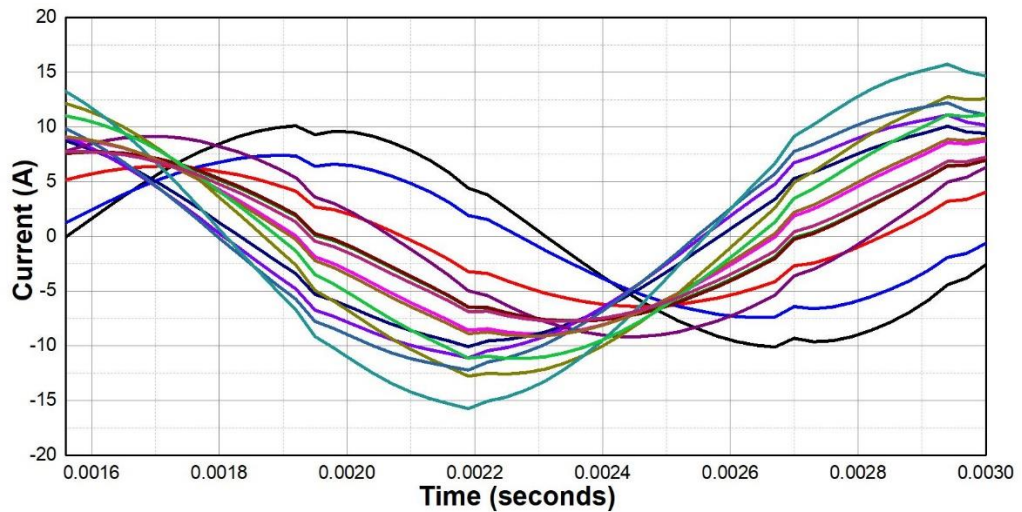
Fig. 6.4: (a) Losses in the conductors, (b) Average loss in the conductors



(a) Waveform of supply current



(b) Waveform of current in strands of Version #3



(c) Waveform of current in strands of Version #4

Fig. 6.5: Comparison of strands currents in Version #3 and #4 along with supply current

**TABLE 6.2: Comparison of strands currents**

	<b>Version #3</b>	<b>Version #4</b>
<b>Strand carrying max. current</b>	Strand 13	Strand 12
<b>Ideal current per strand (<math>A_{peak}</math>)</b>	7.92 A	
<b>Simulated current (<math>A_{peak}</math>)</b>	22.97 A	15.73 A
<b>Simulated / ideal current ratio</b>	2.9	1.86
<b>Strand carrying min. current</b>	Strand 5	Strand 2
<b>Simulated amplitude (<math>A_{peak}</math>)</b>	6.96 A	6.41 A
<b>% difference between max. and min.</b>	230%	145%

Indeed, from TABLE 6.2, if in an ideal scenario the supply current were to be evenly shared by the strands, then each strand should carry current with a peak amplitude of 7.92 A (peak supply current divided by the number of parallel strands). However, due to uneven current sharing, some strands carry more current compared to others. In case of version #3, the maximum peak current is carried by strand 13 with an amplitude of 22.97 A which is 2.9 times the ideal current the strands should be carrying. Strand 5 carries the minimum current, with an amplitude of 6.96 A and the percentage difference in current through strand 13 and strand 5 is 230%. In case of version #4, the maximum current of 15.73 A is carried by strand 12, which is 1.86 times the ideal current, while strand 2 carried the least current with a value of 6.41 A, which is 145.4 % less with respect to the current in strand 12.

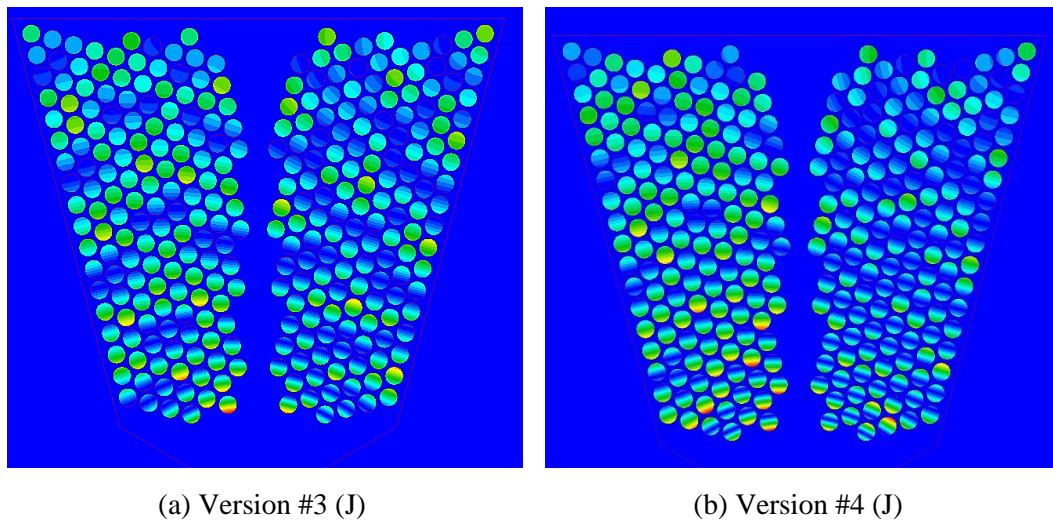


Fig. 6.6: Comparison of current density (J) in the strands (0.00294 s)

Fig. 6.6 shows the current density in the strands at a time instant when the currents are peak for both version #3 and #4. For version #3, the average current density (J) in strand 13 is 21.6 A/mm<sup>2</sup> which is 2.14 time or 113.86% more than the ideal current density of each strands. On the other hand, for version #4, the average value of (J) is

13.4 A/mm<sup>2</sup> which is 1.34 times or 32.67% higher than the ideal value of current density.

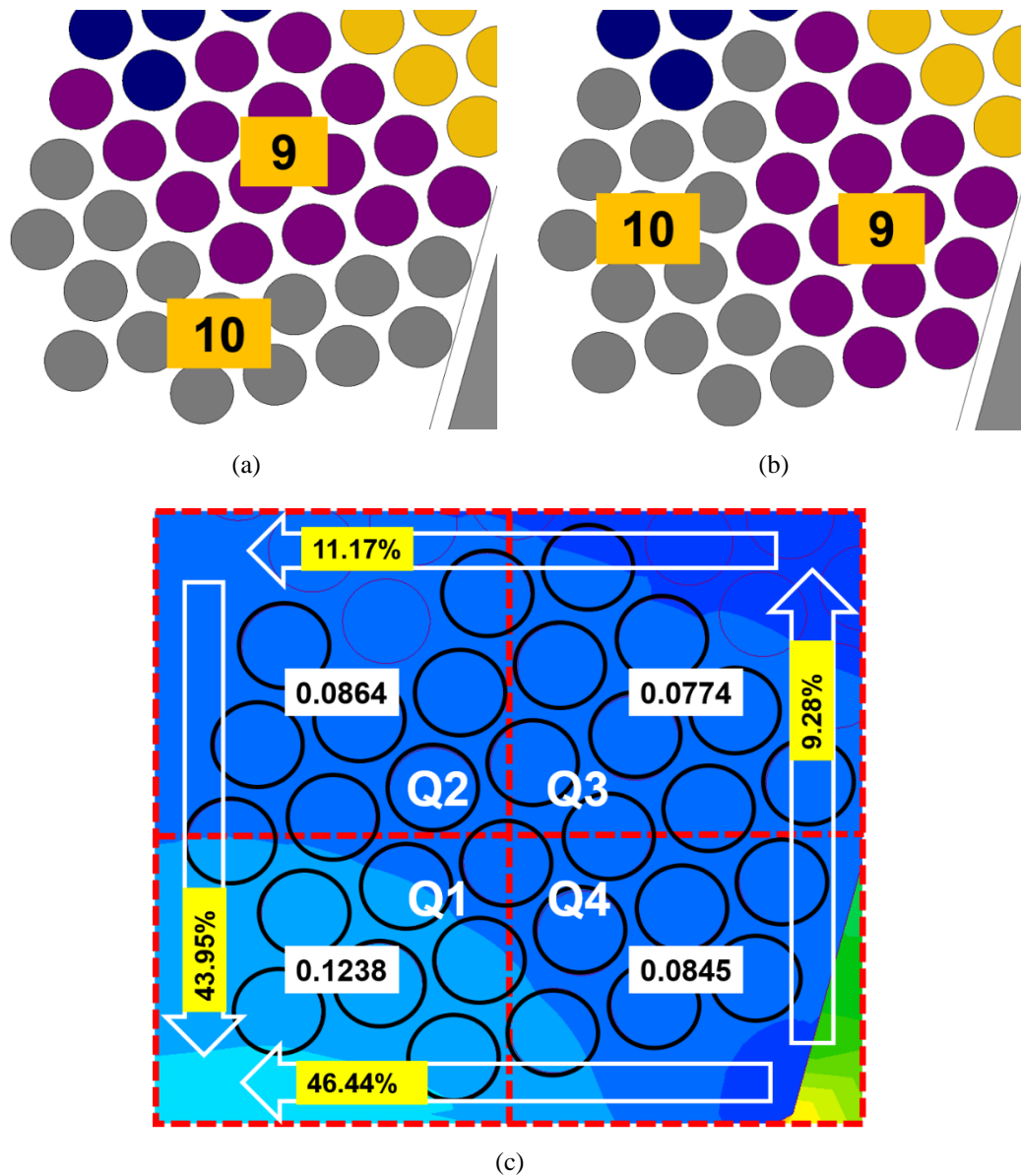


Fig. 6.7: (a) Conductor 9 and 10 in Version #3, (b) Conductor 9 and 10 in Version #4, and (c) Average value of flux density  $|B|$  in the quadrants

An explanation is sought as to why this notable difference between the two versions (#3 and #4). Fig. 6.7a and Fig. 6.7b shows the conductor 9 and 10 positions for version #3 and #4, respectively. The same strands in the slot geometry form the conductor 9 and conductor 10 in version #3 and #4. Considering this region of the

slot, in Fig. 6.7c, the flux density in the region of interest within the slot is plotted with the black bordered circles representing the strands that form conductors 9 and 10. The region of the slot occupied by these strands is divided into four quadrants, namely, Q1 to Q4. For each quadrant, the average flux density  $|B|$  is calculated over one electrical cycle the  $|B|$  for each quadrant is highlighted in white in Fig. 6.7c. The percentage change in  $|B|$  from one quadrant to another is highlighted in yellow and enclosed within white arrows. This change is quite noticeable from Q4 to Q1 at 46.44% and from Q2 to Q1 at 43.95%, when compared to Q3 to Q2 at 11.17% and Q4 to Q3 at 9.28%. In version #3, since the parallel strands of the conductors are placed across Q3 to Q2 and Q4 to Q1, they are subjected to an overall greater variation of flux density among them (11.17% for conductor 9 and 46.44% for conductor 10). This greater variation in flux linkage in parallel strands of a conductor results in the impedance of each parallel strand to vary significantly. This in turn leads to circulating currents in the strands causing the problem of higher uneven current sharing among the parallel strands. On the other hand, in version #4, the parallel strands of each conductor are grouped towards the vertical direction where the overall change in flux density is smaller and thus the parallel strands are linking more or less similar flux. The improved current sharing for version #4 with respect to that in version #3 is evident from fig. 6.5.

### **6.3. Validation**

In the previous section, interesting findings with regards to conductor positioning and AC losses was highlighted and an explanation was presented. For experimental validation purposes, a simpler motorette model is considered in this section as shown in Fig. 6.8 and detailed in TABLE 6.3. The model has 8 turns per phase and 5 strands – in – hand.

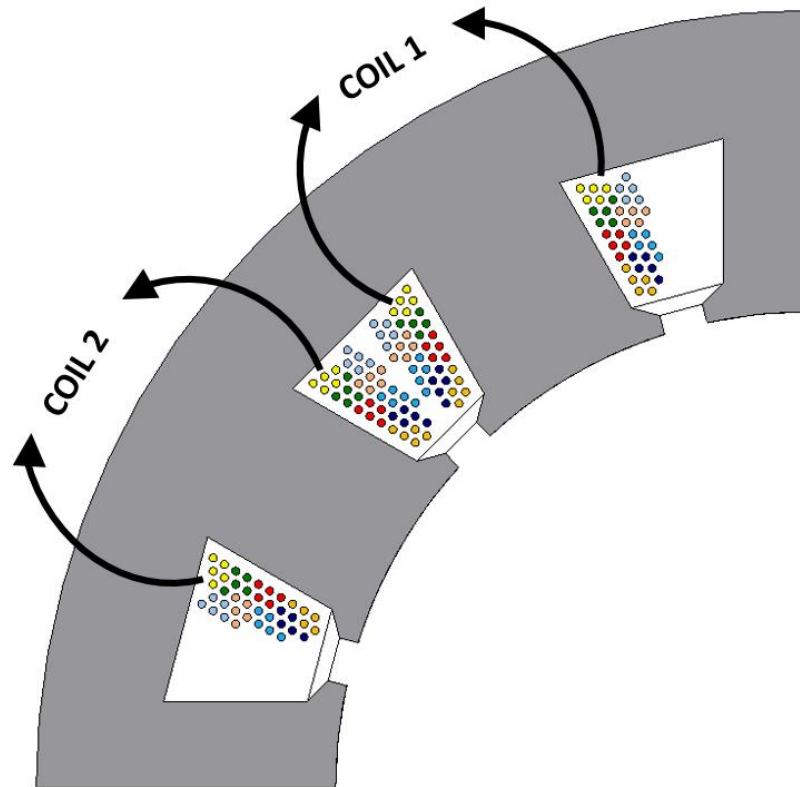


Fig. 6.8: Representation of motorette used for experimental validation

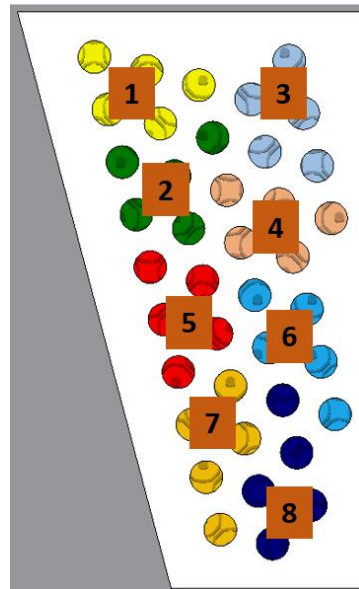
**TABLE 6.3: Specification of validation motorette**

PARAMETER	VALUE
Strands – in - hand	5
Turns per phase	8
Copper diameter (mm)	1.25
Total strands per slot	80
Slot Filling Factor (%)	20
Stack length (mm)	60

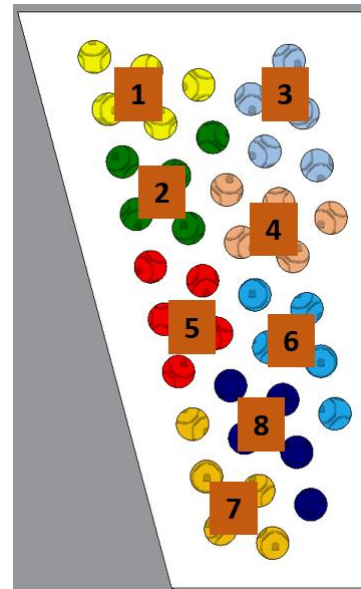
### 6.3.1. FE Modelling and Analysis

Five cases of conductor layout are modelled and analysed using FEA. Similar to the process described in section 6.2, only the shapes of two conductors (conductors

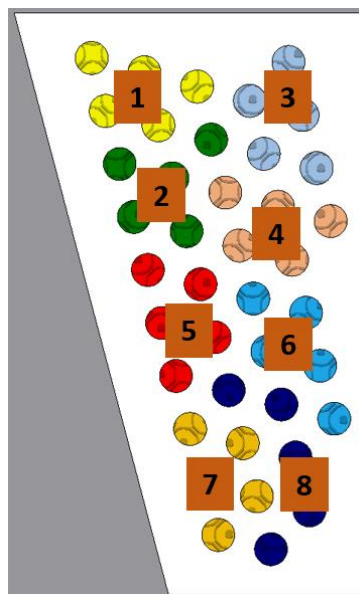
7 and 8) near the slot top are changed. A supply current of  $30 A_{rms}$  is used, with the five cases (Case #1 – Case #5) shown in Fig. 6.9 and the corresponding circuitual connection shown in Fig. 6.10.



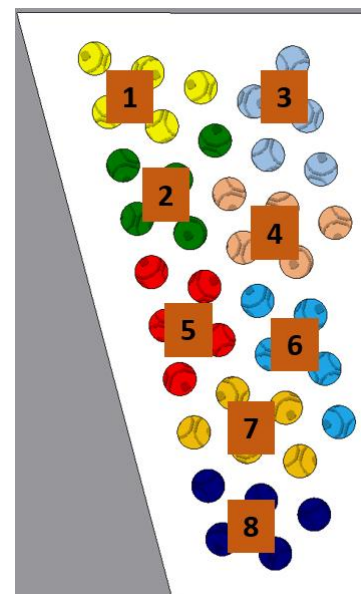
(a) CASE #1



(b) CASE #2



(c) CASE #3



(d) CASE #4

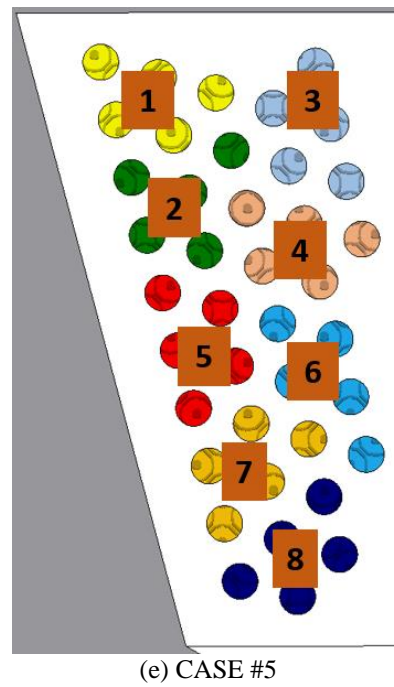


Fig. 6.9: Half side of the slot showing various cases with plausible conductor positions

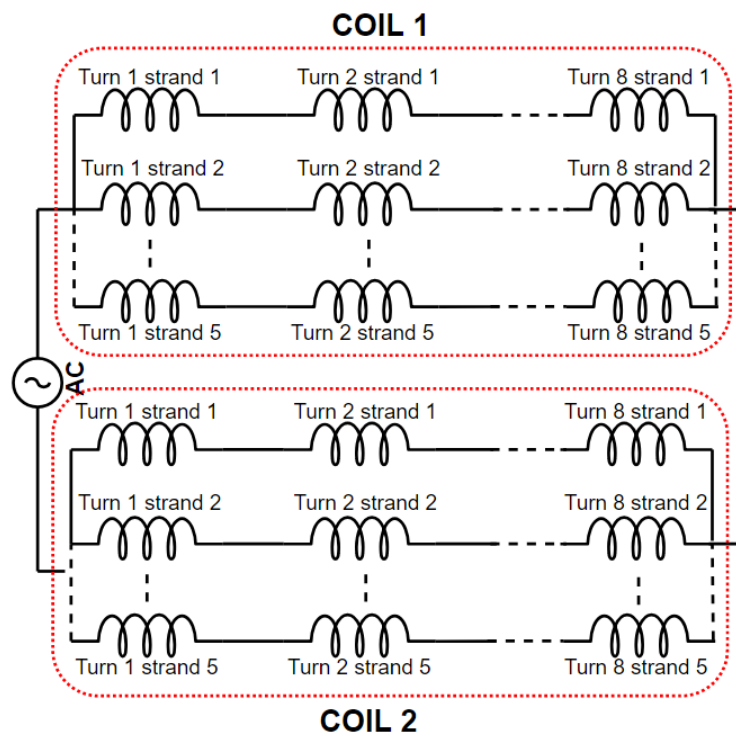
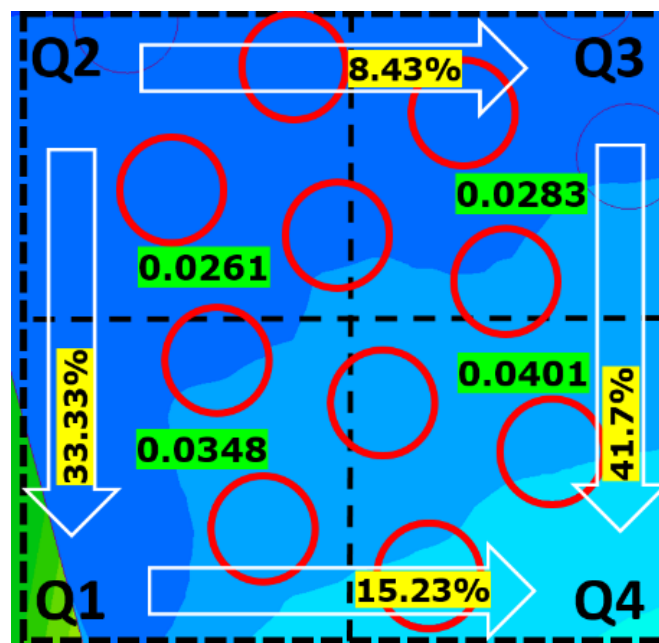


Fig. 6.10: Representation of circuitual connections of strands in the validation motorette

**TABLE 6.4: Comparison of Total / DC Loss in Active Machine Length**

CASE #	Active length Total Loss (W)	Total / DC Loss (Active Section)
CASE #1	21.86	4.27
CASE #2	23.18	4.53
CASE #3	19.31	3.78
CASE #4	13.39	2.62
CASE #5	13.24	2.59

TABLE 6.4 lists the calculated losses in the active length of the motorette corresponding to CASES # - #5 of Fig. 6.9. The DC loss of the motorette is 5.1 W. At 1500 Hz, CASE #2 has the highest active length loss of 23.18 W with a total to DC loss ratio of 4.53, while CASE #5 has the lowest loss of 13.24 W with a corresponding total to DC loss ratio of 2.59.



(a)

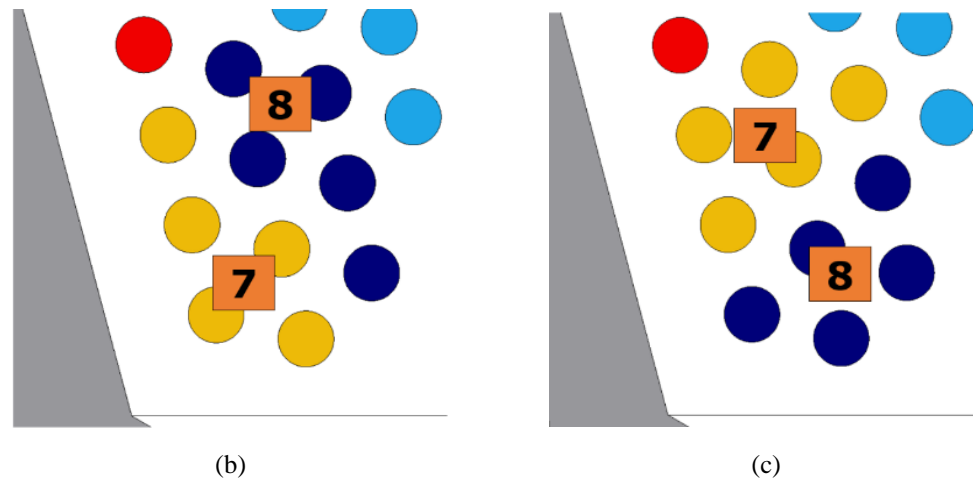
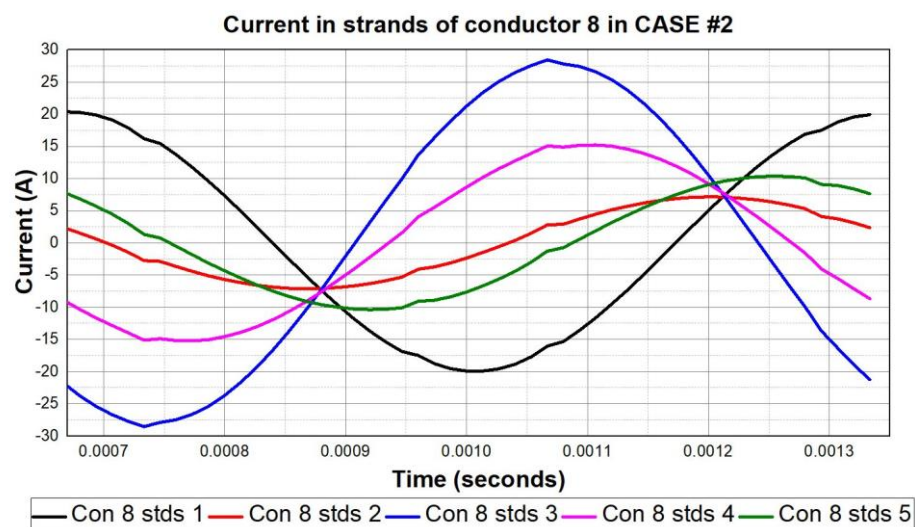


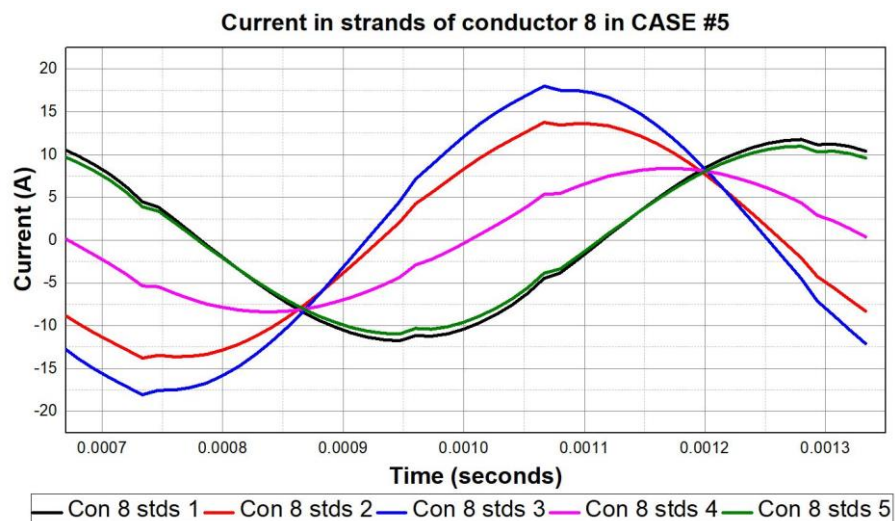
Fig. 6.11: (a) Average value of flux density  $|B|$  in the quadrants, (b) Conductor 7 and 8 in CASE #2, (c) Conductor 7 and 8 in CASE #5

As similar to the explanation described in section above, Fig. 6.11a shows the flux density in the region of interest within the slot is plotted, with the red circles representing the strands that form conductors 7 and 8. The region of the slot occupied by these strands is divided into four quadrants, namely, Q1 to Q4. For each quadrant, the average flux density  $|B|$  is calculated over one electrical cycle. The  $|B|$  for each quadrant is highlighted in green in Fig. 6.11a. The percentage change in  $|B|$  from one quadrant to another is highlighted in yellow and enclosed within the white arrows. This change is quite marked along the vertical direction i.e. from Q1 to Q2 at 33.33% and from Q3 to Q4 at 41.7%, when compared to that in the horizontal direction, with Q1 to Q4 being 15.23% and Q2 to Q3 being 8.43%. Figs. 6.11b and 6.11c show the conductor 7 and 8 positions for CASE #2 and CASE #5 respectively. In CASE #2, since the parallel strands of the conductors are vertically aligned, they are subjected to an overall greater variation of flux density among them. The greater variation in flux linkage in parallel strands of a conductor results in the impedance of each parallel strand to vary significantly. This in turn leads to circulating currents in the strands causing the problem of higher uneven current sharing among the parallel

strands. On the other hand, in CASE #5, the parallel strands of each conductor are grouped towards the horizontal direction where the change in flux density is smaller and thus the parallel strands are linking more or less similar flux. The improved current sharing for CASE #5 with respect to that in CASE #2 is evident from Fig. 6.12. As can be seen from this figure, in CASE #2, the peak current in the strands deviates from the ideal peak current by 92% while in CASE #5 it deviates by a significantly lower value of 48%.



(a) Waveform current in strands for CASE #2



(b) Waveform current in strands for CASE #5

Fig. 6.12: Comparison of strand currents in conductor 8 for CASE #2 and #5

### 6.3.2. Experimental validation

For the experimental verification, motorette CASE #2 and CASE #5 are considered. As earlier described in chapter 5, benefitting from the advancements in precision 3D printing, slot formers are manufactured (shown in Fig. 6.13), and used to fix exactly the positions of the individual strands in an identical fashion to the ones considered in the FE analysis.

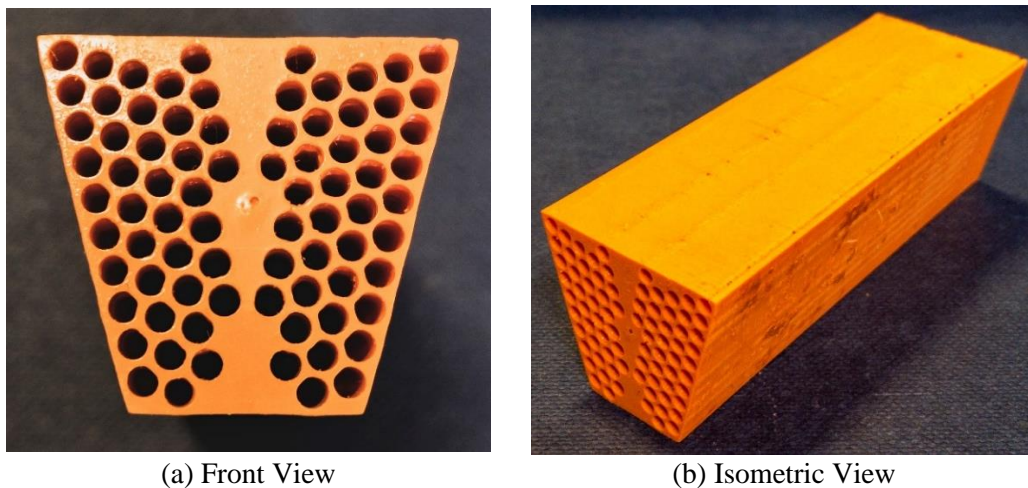


Fig. 6.13: Front and Isometric views for 3D printed former used within experimental validation

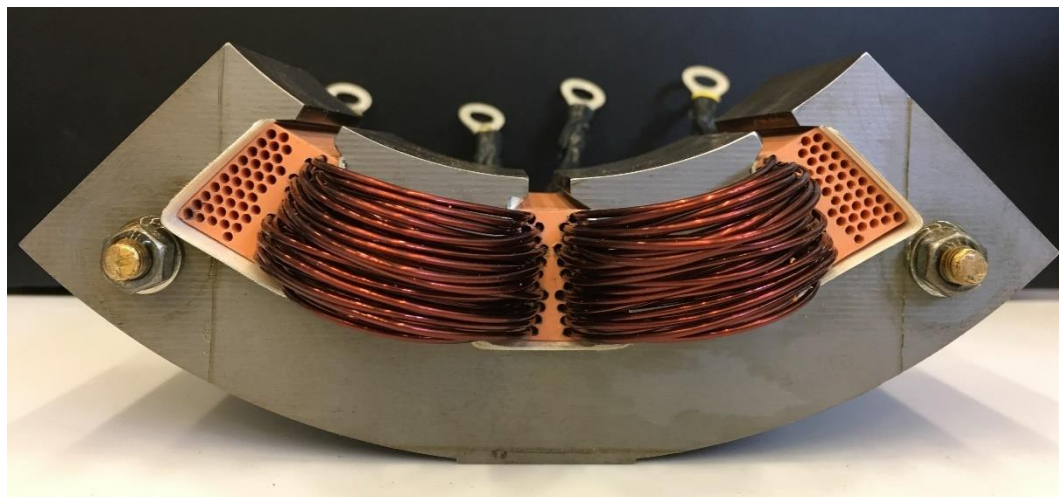


Fig. 6.14: A wound motorette with slot formers

Fig. 6.14 shows a wound motorette using the aforesaid formers. Similar as in case of chapter 5, an impedance analyser is used to measure the resistance of the leadwires,

crimp contacts and the connecting cables, up to very high frequencies (2 MHz) and it is observed that the resistance did not change significantly in the range of frequencies of interest for this study. Fig. 6.15 shows AC resistance of the connecting cable against the frequency.

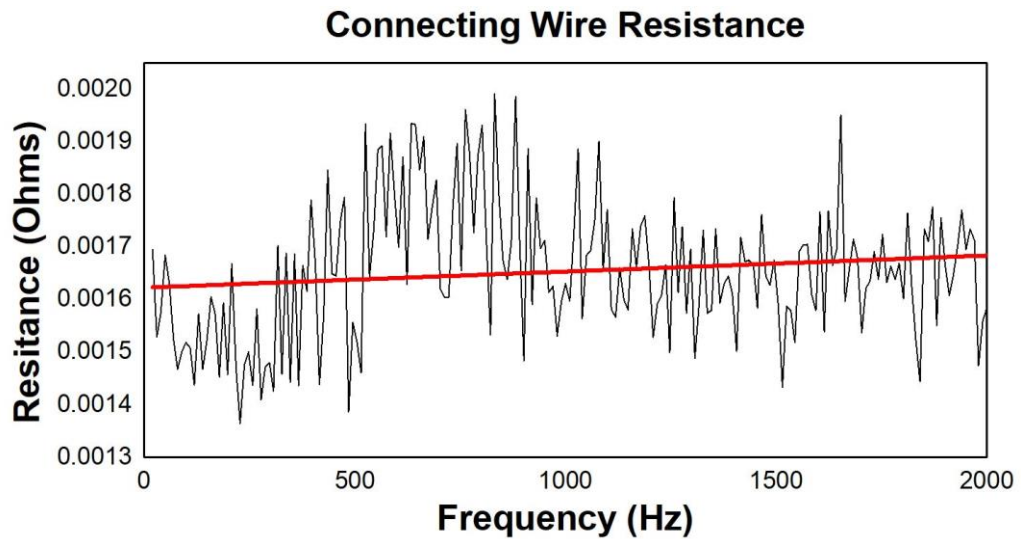


Fig. 6.15: AC resistance of connecting cable

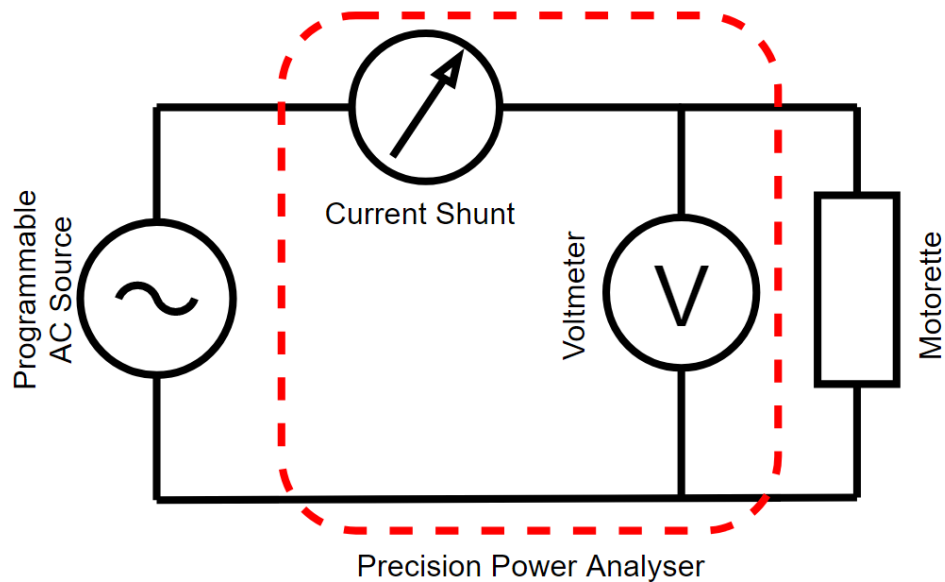
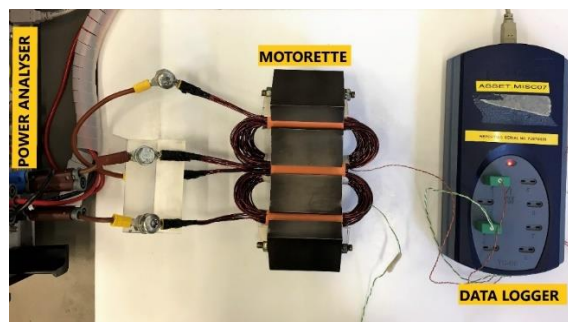
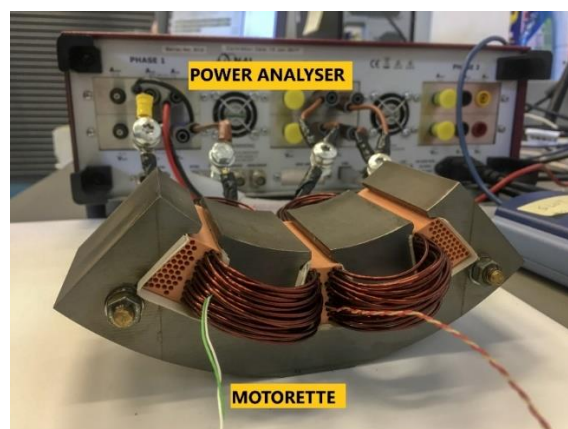


Fig. 6.16: Schematic diagram of experimental setup showing equipment and connection

Fig. 6.16 shows the schematic of the experimental setup and Fig. 6.17 shows the actual experimental setup for the AC loss measurement. A variable frequency power supply (Programmable AC source, CHROMA 61511) is used as the power source. A precision power analyser (PPA 5530 from N4L) is used for measuring the power loss in the experimental setup. Since, the power analyser has an overload capacity of 32 A, a current amplitude of  $30 A_{rms}$ , is injected into the coils for all the measured frequencies. Temperature is monitored in real – time using K – type thermocouples (connected to PICO TC – 08 data logger); placed inside the slot and at the endwindings. This ensures that the temperature effects on winding resistance can be accounted for. The specifications of the equipment used in the experimental setup is specified in the appendix.



(a) View 1



(b) View 2

Fig. 6.17: Views of experimental setup showing various equipment used in the tests along with the test motorette

**TABLE 6.5: Losses in Motorette CASE #2**

<b>Motorette CASE #2</b>				
<b>Freq.</b>	<b>Active Length</b>	<b>Total Sim.</b>	<b>Total Exp.</b>	<b>Total / DC</b>
<b>(Hz)</b>	<b>Loss (W)</b>	<b>Loss (W)</b>	<b>Loss (W)</b>	<b>Loss (Exp.)</b>
666.67	9.4	22.11	23.69	1.31
1500	23.89	39.10	42.35	2.24

**TABLE 6.6: Losses in Motorette CASE #5**

<b>Motorette CASE #5</b>				
<b>Freq.</b>	<b>Active Length</b>	<b>Total Sim.</b>	<b>Total Exp.</b>	<b>Total / DC</b>
<b>(Hz)</b>	<b>Loss (W)</b>	<b>Loss (W)</b>	<b>Loss (W)</b>	<b>Loss (Exp.)</b>
666.67	6.5	19.71	21.16	1.14
1500	13.24	28.49	34.00	1.73

TABLE 6.5 and 6.6 detail the comparison of simulated losses and experimentally measured losses at high frequencies (666.67 Hz and 1500 Hz). Here, the column ‘Active Length Loss’ represents the 2D – FEA – computed winding loss (only the part of the winding within the stator stack length considered, i.e. not including the endwindings). The column ‘Total Simulated Loss’ represents the active length loss added with the  $I^2R$  loss of the auxiliary components (endwinding, lead wires, crimp contacts, connecting cables) and the core losses as computed from FEA. The column ‘Total Experimental Loss’ represents the total experimentally – measured loss of the motorette setup (with the auxiliary components connected). Finally, the column ‘Total /DC loss (Exp.)’ represents the ratio of *total experimentally measured loss minus the 2D – FEA computed core loss at high frequency to the total experimentally – measured DC loss of the setup*. The simulated and the experimental total losses are in close matching. For clarity, it should be pointed out that in TABLE 6.5 and 6.6,

the endwinding losses are factored in. In agreement with the analysis prediction of the preceding section, there is a significant drop in the Total / DC loss ratio for CASE #5 when compared to CASE #2. Since, most of the AC losses occur within the active length of the machine, at 1500 Hz, the armature losses drop by a significant 36% in the active length of motorette for CASE #5 when compared to CASE #2.

#### **6.4. Conclusion**

Using the computationally efficient analysis model, various plausible versions of conductor positions and shapes were modelled. AC losses for each version were analysed and optimised, and a version where the AC losses in the active section reduce by around 50% with respect to the worst - case scenario was achieved. A detailed comparative analysis of the worst – case and best – case versions was made with some interesting observations. Most importantly, the aforesaid marked reduction of the AC losses can be rooted to the layout of the strands within the top section of the slot, where it is advised that within this section, the strands pertaining to the different conductors are organised as such that to minimise the variation of flux linkage within the strands of a conductor.

Benefitting from advancements in 3D printing technology, a precise coil former was printed and used to experimentally verify the hypothesis presented in this chapter and design recommendation on a simplified motorette section. A 36% reduction in the winding AC losses is experimentally verified simply by the accurate controlling of the strand positioning within the top of the slot. This finding can help with the improvement of power density in high frequency machines, and will inevitably further aided with the rapid advancements in printing and manufacturing techniques.

## Chapter 7

# Experimental Analysis

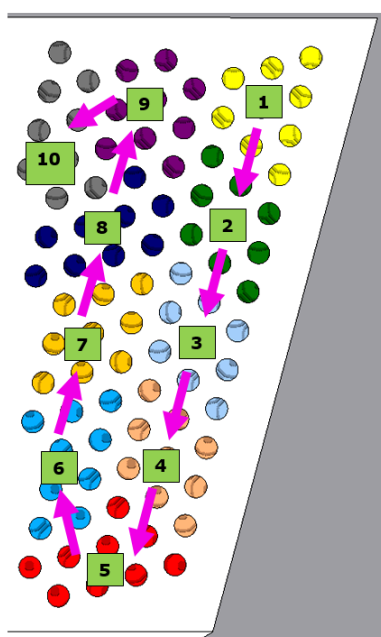
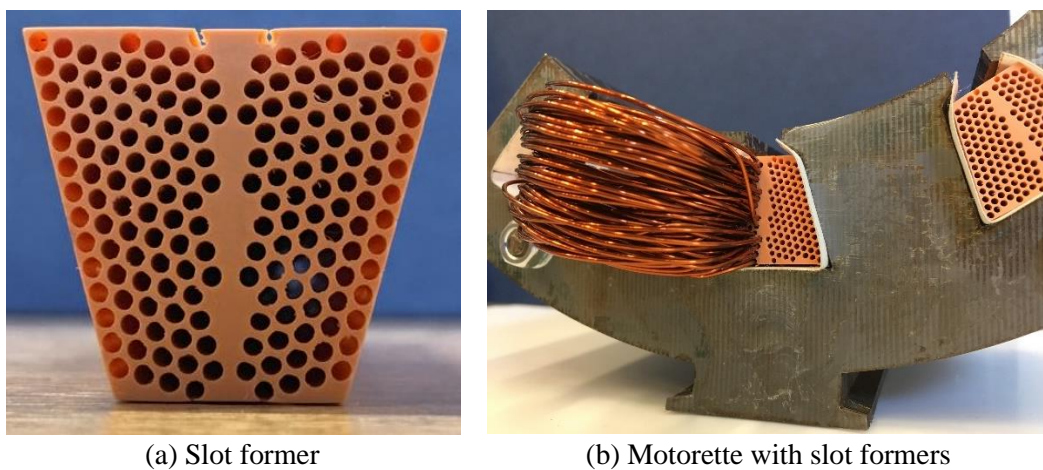
## 7.1. Comparative analysis of fixed strands positions and fixed conductor shapes motorette

In this section, experimental comparison of the AC losses in the motorette windings is analysed and presented. For the purpose of this comparison, two winding types in the slot are considered: (a) fixed strand positions (CASE A), and (b) fixed conductors shapes CASE B). For all the cases, the same parameters are used, i.e., magnet wire size, number of parallel strands and number of turns in the slot. The details of these parameters are listed in TABLE 7.1. The same motorette core detailed in TABLE 5.1 is used in this analysis.

**TABLE 7.1: Specifications of parameters used in the slot**

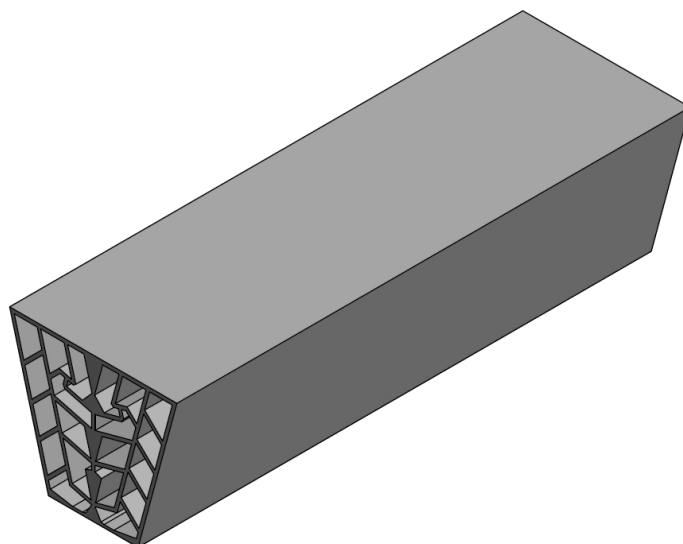
PARAMETER	SPECIFICATION
Turns per half slot	10
Strands – in – hand	9
Total strands per slot	180
Strand nominal diameter	0.8 mm
Slot filling factor	19.6%

Fig. 7.1 shows the motorette with fixed strands. This is the same motorette used for experimental analysis in chapter 5 and is detailed in subsection 5.2.2. Fig. 7.1a shows the 3D printed slot former used to fix the strands in the slot. Fig. 7.1b shows one coils side wound with the formers inside the slot of the motorette. Fig. 7.1c shows the conductor shapes and the positions in the slot former.

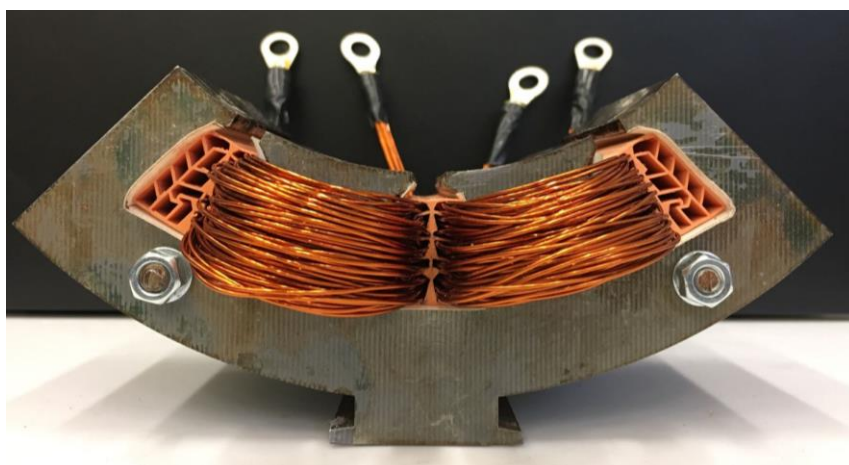


(c) Representation of fixed strands and conductor shapes in the former

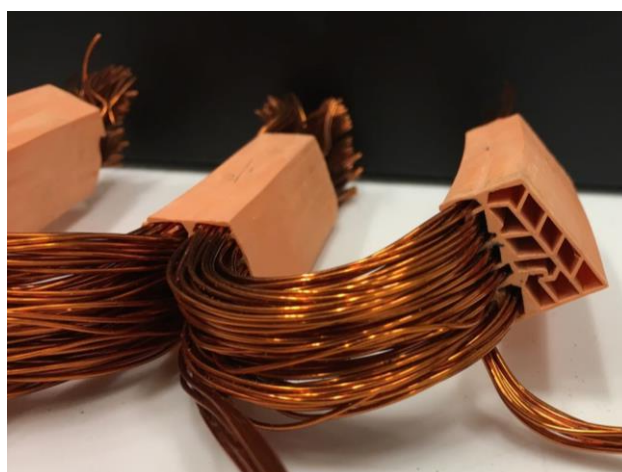
Fig. 7.1: Motorette with fixed strand positions (CASE A)



(a) 3D rendering of fixed conductor shapes former



(b) Wound motorette with fixed conductor shapes formers



(c) Winding in the slot former with fixed conductor shapes

Fig. 7.2: Formers and motorette with fixed conductor shapes (CASE B)

Fig. 7.2 shows the formers and the wound motorette with fixed conductor shapes. For this motorette (CASE B), the conductors shapes are fixed as same as CASE A, shown in Fig. 7.3.

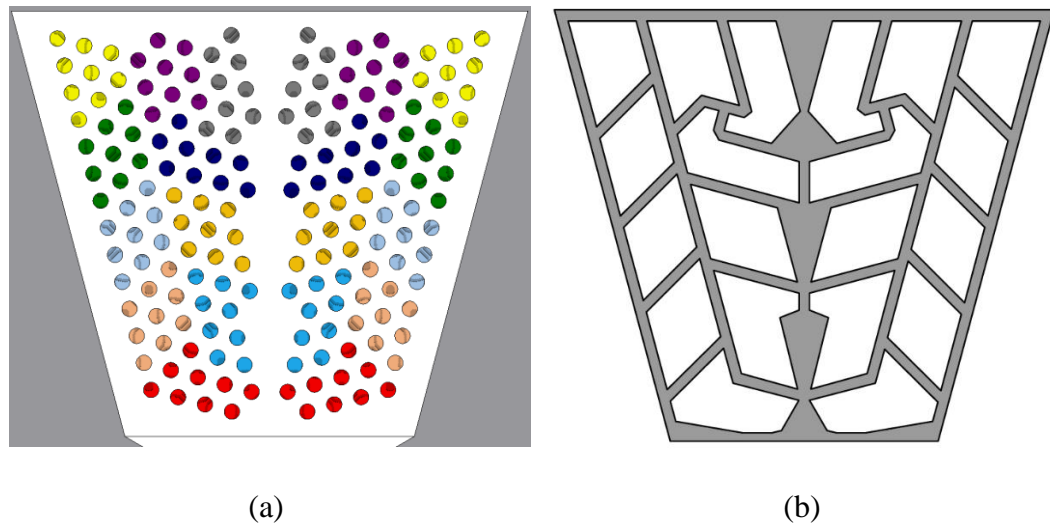


Fig. 7.3: Strands and conductor shapes in motorette (a) CASE A, (b) CASE B

Similar measurements procedures described in previous chapters are used for the analysis in this section. A supply current of  $30 A_{rms}$  is used. The coils sides are connected in series similar to as shown in Fig. 5.3 in chapter 5 and Fig. 6.10 in chapter 6. Precision power analyser (PPA 5530 from N4L) is used for the loss measurement and Programmable AC source (Chroma 61511) is used as the current source. The measurements are taken for frequencies (Hz): 20, 50, 100, 500, 666.67 and 1500 Hz.

**TABLE 7.2: Comparison of measured losses in motorette with winding configurations CASE A and CASE B**

Frequency (Hz)	Core Loss (2x) (W)	Measured total loss (W)		Losses in winding = Measured Total Loss – Core loss(2x)		Total/DC loss ratio (winding)		% difference
		CASE A	CASE B	CASE A	CASE B	CASE A	CASE B	
20	0.02	30.2	25.094	30.179	25.073	1.00	1.00	0.00
50	0.07	29.71	25.083	29.644	25.017	0.98	1.00	1.58
100	0.16	31.35	25.371	31.195	25.216	1.03	1.01	-2.70
500	1.28	32.435	26.217	31.155	24.937	1.03	0.99	-3.66
666.67	1.91	34.605	28.267	32.691	26.353	1.08	1.05	-2.97
1500	6.34	48.988	38.609	42.648	32.269	1.41	1.29	-8.93

TABLE 7.2 lists the comparison of the measured total losses in the motorette CASE A and CASE B. The column highlighted in 'grey' shows the core losses (multiplied by factor of 2) against the frequencies listed in column one. The core losses are obtained from finite – element analysis. The columns highlighted in 'green' shows the total measured losses of the motorette for CASE A and CASE B against the frequencies listed in the first column. These measured losses include all the losses of the motorette setup i.e., the winding losses, DC losses of the connecting wires and lead wires, core loss in the motorette. The columns in 'orange' lists the losses in the winding for both the cases. Here the losses in the winding is calculated by subtracting the core loss (2x) obtained from FEA from the measured total losses of the motorettes. The results of losses in the winding also includes the DC losses in the connecting cables, lead wires and endwindings. The columns highlighted 'yellow' shows the Total / DC loss ratio in the winding for both motorette cases. The measurements taken at 20 Hz are considered as DC value. Hence, the ratio of the losses in the winding at any frequency by the losses in the winding at 20 Hz gives the Total/DC loss ratio listed in the 'yellow' highlighted columns. The column highlighted in 'blue' shows the percentage difference between the Total/DC loss ratio of CASE B from CASE A.

The losses in the CASE B drops by approximately 9% at frequency of 1500 Hz, compared to CASE A. The transposition of the strands inside the conductor shape former in CASE B is the likely reason for the drop. However, this suggests that the positions of the individual strands are not vital if the shapes of the conductors are fixed. This drastically simplifies and accelerates the winding process. Aided by the possible better heat extraction and by the findings of chapter 6, whereby carefully

controlling the conductor shapes the losses were reduced by 36%, the power density in the machine can be further increased.

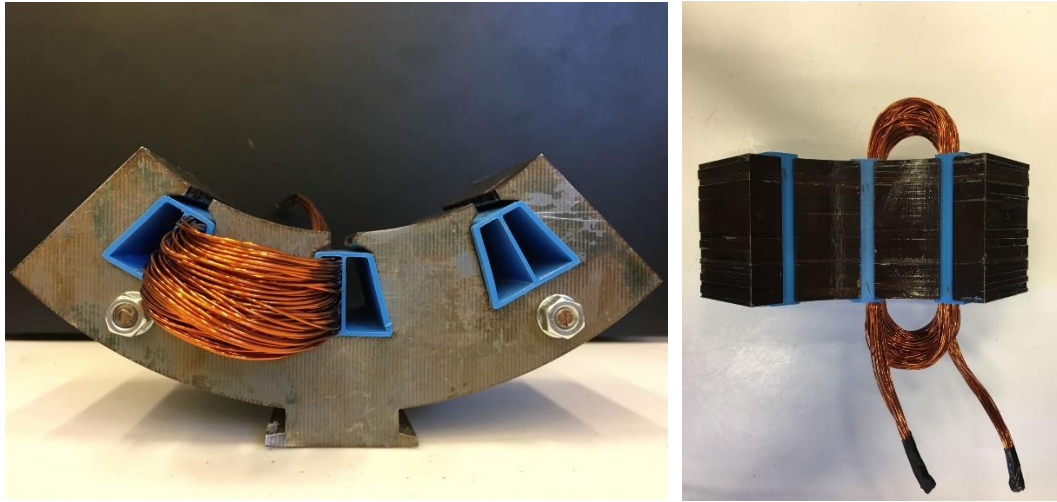
## **7.2. Relationship between copper filling factor and AC losses**

For this analysis, the slots in the motorette are random - wound with increasing copper slot filling factor: 20%, 30% and 40%. The AC losses in winding of the motorette for each of the cases is measured and finally the results are compared to the results obtained with using motorette with 33 ‘strands – in – hand’ detailed in chapter 5.

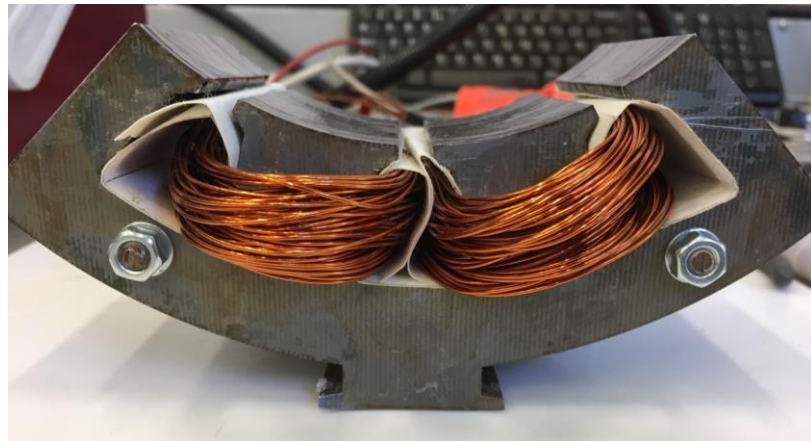
TABLE 7.3 lists the comparisons of the specifications in the slots of motorettes with the varying copper filling factor with the specifications in the slot of the motorette with 33 ‘strands – in – hand’. The column highlighted ‘grey’ lists the specifications for motorette with 20% Copper (Cu.) Filling Factor. The ‘blue’ highlighted column lists the specifications for 30% Cu. Filling Factor, the ‘gold’ column for 40%. In three of these above cases, the strand diameter and the number of turns is kept constant. So, as the copper filling factor change, the number of parallel strands or ‘strands – in – hand’ of a conductor change. The column highlighted ‘orange’ shows the specifications of the motorette with 33 ‘strands – in – hand’. Here, strand diameter of 0.63 mm is considered to be alike with the prototype traction machine described in chapter 3.

**TABLE 7.3: Specifications in the slot for motorettes with varied Copper filling factor**

PARAMETER	Specifications for motorettes with Copper Filling Factor			
	20%	30%	40%	44.5%
Turns per half slot	10	10	10	10
Strands – in – hand	9	14	18	33
Total strands per slot	180	280	360	660
Strand Copper diameter	0.8 mm	0.8 mm	0.8 mm	0.63 mm
Nominal Current Density	6.63 A/mm <sup>2</sup>	4.26 A/mm <sup>2</sup>	3.31 A/mm <sup>2</sup>	2.91 A/mm <sup>2</sup>



(a) 20% Cu. Filling Factor



(c) 30% Cu. Filling Factor



(d) 40% Cu. Filling Factor

Fig. 7.4: Experimental Motorette with varied Cu. Filling Factor

Fig. 7.4 shows the motorettes with varied copper filling factor used for experimental analysis in this section of the chapter.

**TABLE 7.4: Comparison of losses in the motorettes with varied Cu. Filling Factor**

Freq. (Hz)	Measured Total Losses (W)			Core loss (2x)	Losses in Winding = Measured Total Loss – Core Loss (2x) (W)			Total/DC Loss (Winding)		
	20%	30%	40%		20%	30%	40%	20%	30%	40%
20	24.28	19.95	15.64	0.02	24.26	19.93	15.62	1.00	1.00	1.00
50	24.32	20.50	15.95	0.07	24.25	20.43	15.88	1.00	1.03	1.02
100	24.32	20.56	16.63	0.16	24.17	20.41	16.48	1.00	1.02	1.05
500	26.31	22.44	19.42	1.28	25.03	21.16	18.14	1.03	1.06	1.16
666.67	27.65	23.96	20.79	1.91	25.74	22.04	18.87	1.06	1.11	1.21
1500	39.31	36.87	35.05	6.34	32.97	30.53	28.71	1.36	1.53	1.84

TABLE 7.4 lists the comparison of the losses in the motorettes and Total/DC loss ratio in the winding for the three copper filling factors. In TABLE 7.4, the columns highlighted in 'orange' shows the measured total losses in the motorette for the copper filling factors against the supplied frequencies listed in column one. The column highlighted 'blue' shows the core loss (multiplied by factor 2). The values of the core losses are obtained from finite – element analysis. The columns highlighted 'green' shows the losses in the winding. This includes the losses in the auxiliary components (considered DC losses), i.e., the endwinding, the connecting cables and the lead wires. The losses in the winding are calculated by subtracting the core loss value (2x) from the measured total loss of the motorette at any frequency. The columns highlighted in 'gold', shows the Total/DC loss ratio in the windings. The losses at 20 Hz are considered DC loss value. Therefore, the Total/DC loss ratio in the winding is the ratio of losses in the winding at any frequency to the losses in the winding at 20 Hz (considered DC loss).

This analysis shows that at lower frequencies, the relationship between the copper filling factor and AC losses in the winding is insignificant. However, at high frequencies, as the copper filling factor increase the AC losses in the winding increase. For instance, at the supplied frequency of 1500 Hz, the Total/DC loss ratio in the windings with 40% copper filling factor is approximately 35% higher than the Total/DC loss ratio with 20% copper filling factor.

Fig. 7.5 shows the comparison of Total/DC loss ratio in the winding for 20%, 30%, 40% Copper Filling Factor along with the Total/DC loss ratio in the winding of the 33 'strands – in – hand' motorette.

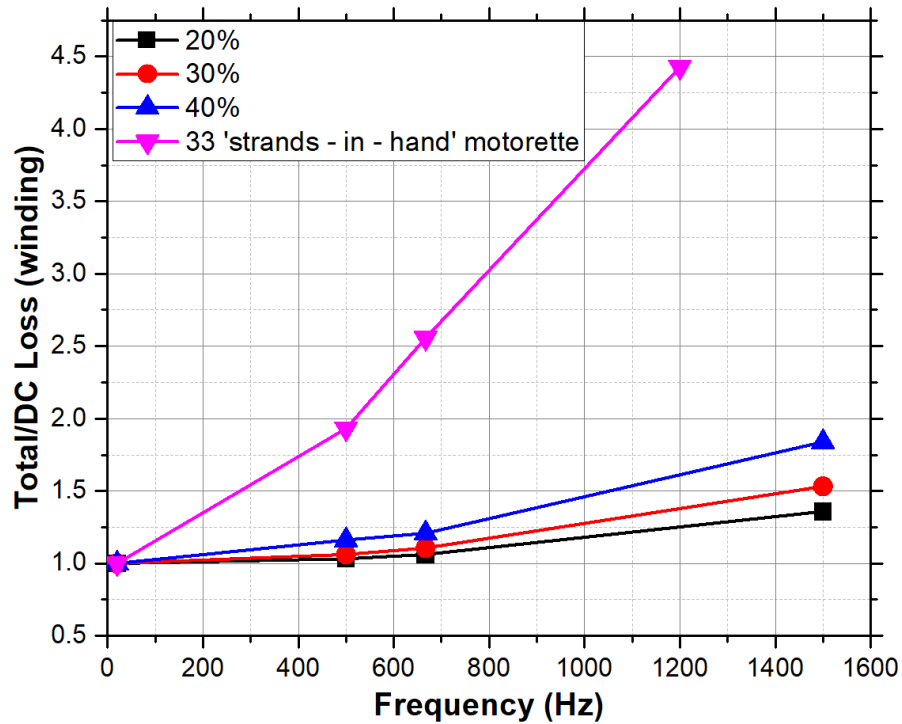


Fig. 7.5: Comparison of Total/DC Loss ratio of the motorettes

Comparing the 40% copper filling factor motorette with the 33 ‘strands – in – hand’ motorette, the later has a copper filling factor of 44.5%. However, with a smaller strand diameter for the later motorette, the number of parallel strands per conductors is 1.83 times than the motorette with 18 ‘strands – in – hand’. This has resulted in the total/DC loss ratio of approximately 4.42 at supply frequency of 1200 Hz compared to 1.84 for the motorette with 18 ‘strands – in – hand’ at frequency of 1500 Hz. This can be due to the greater circulating current effects in the motorette with more parallel strands. To conclude, for an increase in copper Filling factor of 11.25% with the smaller diameter, the Total/DC loss increase by approximately 140%.

Through experimental analysis, this section presents a relationship between the Copper Filling Factor and the AC losses in the winding. It shows that at lower frequencies, the relationship is insignificant. However, at higher frequencies, a

higher slot filling factor results in the higher AC losses in the winding. This analysis also shows that for random wound winding the losses in the winding can be unpredictable and with smaller strands diameters/ more strands – in – hand, the losses in the windings can be significantly high.

## Chapter 8

# Conclusion and Future Works

In this work, AC losses in the stator winding of an existing interior permanent magnet synchronous machines using numerical method approach were investigated. The main objective was to develop solutions in order to mitigate the AC losses in the winding occurring at high – frequency operation.

At first, a brief introduction to importance of cleaner and greener modes of transportation and its necessities were presented. An overview of the key components of an IPM machine were presented with prime focus on the components side the slots of the stator core. Properties of different kinds of winding types commercially available were discussed along with their advantages and disadvantages. The problem of AC losses in the windings of electrical machines and the necessity for their mitigation was presented in chapter 1. Losses in the electrical machines were presented in Chapter 2. Detailed aspects of the various losses in the stator core and the winding were presented, and a brief literature review on the subject by previous authors were presented.

In Chapter 3, the sensitivity of AC losses in the winding with varying strand numbers were analysed for an existing prototype traction machine. A methodology to segregate the total loss in the winding into components was described. Three different winding configurations (ARR1 – AAR3) were studied and the circulating current associated with them were investigated. Comparative case studies were made for some models and it is shown that even with strand diameter smaller than the skin depth, the skin and proximity effect exist, and it rapidly decreases with decrease in

the strand diameter. It is also shown by comparative analysis of the strands/bundles configurations that while the skin and proximity is largely independent of the bundle shape and position, the circulating current is significantly affected by the shaped of the bundle. Finally, it is presented by proving that the loss segregation equation holds true and re – confirmed that even with strands' diameter less than skin depth, the skin and proximity effects cannot be neglected.

In Chapter 4, a methodology to simplify the modelling of the machine was presented. For IPM machine with concentrated winding, the models can be simplified to just one slot. This resulted in substantial gain in saving computational time at a cost of loss in marginal amount of accuracy in calculating the losses. A methodology to optimize the winding height and strand size in order to minimize the losses in the windings was presented. It is shown by using finite – element analysis, that approximately 20% of the total losses in the winding can be reduced by optimizing the winding height and selecting appropriate wire size. Furthermore, approximately 28% of the available area for winding in the slot was left empty near the slot top which can be used to cool the machine by forcing air or coolant through the space.

In Chapter 5, experimental verifications of the AC loss modelling in this thesis were carried out using motorettes. It is shown that for randomly wound motorettes, where the strands/bundles shapes and positions inside the slot of the motorette cannot be predetermined, the modelling fails to estimate the losses in the winding. However, when the strands/bundles positions and shapes in the experimental mottorette matches with the FE modelling, the accuracy in predicting the losses was above 90%.

In Chapter 6, a methodology was proposed for modelling the strands and bundles inside the slot resembling winding of random – wound machines. The strands were

clustered together to form bundles which formed the different turns of the winding. The clustering of the strands varied as such that the conductors occupy different location in the slot with varied shapes. Using the computationally efficient analysis model, various plausible versions of conductor positions and shapes were modelled. AC losses for each version were analysed and an optimised version where the AC losses in the active section reduce by around 50% with respect to the worst - case scenario was achieved. It is shown that the aforesaid marked reduction of the AC losses can be rooted to the layout of the strands within the top section of the slot. Using experimental verification, a 36% reduction in the winding AC losses was achieved by the accurate controlling of the strand positioning within the top of the slot.

In Chapter 7, AC losses in the winding of experimental motorettes with fixed strands positions and fixed conductor shapes were investigated. It was shown that the exact position of the strands in a bundle shape do not have a significant effect on the AC losses, as for both motorettes the results were within 9% of each other. Using randomly – wound motorettes with increasing copper filling factor, it is shown that the AC losses in the randomly – wound motorette increases with increase in the copper filling factor. Also, the losses in the winding is unpredictable with randomly wound machine, as evident from the motorette with 33 ‘strands – in – hand’ with higher number of parallel strands where the losses increased by 140% compared to the motorette with 18 ‘strands – in – hand’.

The work in this thesis provided a comprehensive analysis of AC losses in the winding of an interior permanent magnet machine and successfully achieved the set goal of the thesis to mitigate the AC losses in winding at high – frequency operations by optimising the winding height in the slot and by optimising the winding

configuration at the slot top. These findings can help with the improvement of power density in high frequency machines, and with rapid advancements in 3D printing, additive manufacturing techniques and newer novel materials, precision placement of the strands in the slots at mass scale will be a significant source for performance enhancement.

Based on the findings of the thesis, following considerations should be made while designing and manufacturing stator windings with round magnet wires for high – speed applications:

- a. To minimise the effects of circulating currents, care should be taken to avoid vertical arrangements of strands/ bundles configurations such as ARR2, described in chapter 3.
- b. For a given slot geometry, selection of optimal winding height combined with optimal strand diameter and realistic modelling of strands/bundles arrangements can significantly reduce the AC losses in the windings.
- c. The arrangements of strands and shape of the bundles near the slot top (towards the slot opening) are very sensitive and can significantly affect the circulating current losses. By carefully controlling the bundle shapes near the slot top so that the strands within the bundle have minimum difference in flux linkage, the circulating currents losses can be significantly reduced.
- d. For randomly wound winding, the losses in the winding are unpredictable as the positions and shapes of the bundles are not known. However, the trend from the experimental analyses suggest that for similar slot filling factor, increasing the strands – in – hand can result in a significant increase

in the AC losses. Therefore, special care should be taken when selecting the size of strand diameter and number of strands – in – hand.

All the analyses of the AC losses in the winding in the thesis were carried out for the fundamental frequencies of the machine, considering pure sinusoidal waveform. However, in practise, most of the machine control involves power electronics with PWM waveform injection. Authors in [53] have already investigated the effect of high frequency current ripples induced by PWM on the proximity effect losses and concluded that the skin and proximity losses increase significantly due to PWM. To further the research work carried out in this thesis, PWM waveform will be considered for the analyses of AC losses carried out in this thesis and loss mitigation techniques will be proposed.

# References

- [1] "BP Energy Outlook 2018, British Petroleum," ed, 2018. Available: <https://www.bp.com/en/global/corporate/energy-economics/energy-outlook.html>.
- [2] "A technical summary of Euro 6/VI vehicle emission standards," ed, 2016, Available: [https://www.theicct.org/sites/default/files/publications/ICCT\\_Euro6-VI\\_briefing\\_jun2016.pdf](https://www.theicct.org/sites/default/files/publications/ICCT_Euro6-VI_briefing_jun2016.pdf)
- [3] "Global EV Outlook 2018, International Energy Agency," ed, 2018, Available: [https://www.theicct.org/sites/default/files/publications/ICCT\\_Euro6-VI\\_briefing\\_jun2016.pdf](https://www.theicct.org/sites/default/files/publications/ICCT_Euro6-VI_briefing_jun2016.pdf)
- [4] M. Barcaro, "Design and Analysis of Interior Permanent Magnet Synchronous Machines for Electric Vehicles," University of Padova, 2011.
- [5] "EU FP7 Marie\_Curie Initial Training network," ed, 2015, Available: <http://erean.eu/wordpress/rare-earth-magnets-still-optimum-choice-says-motor-design-expert/>
- [6] W. Tong, Mechanical Design of Electric Motors. Taylor & Francis, 2014.
- [7] "Technical Data for Copper Magnet Wire by Size acc. to IEC 60317," ed, 2012, Available: <https://www.sis.se/api/document/preview/571790/>
- [8] "NEMA Magnet Wire Thermal Class Ratings, Available: [https://www.superioressex.com/uploadedFiles/News/White\\_Papers/emcwa-nema\\_magnet-thermal-class-ratings.pdf](https://www.superioressex.com/uploadedFiles/News/White_Papers/emcwa-nema_magnet-thermal-class-ratings.pdf)," ed.
- [9] P. E. Alexander, "Thermal classification of magnet wire in NEMA MW-1000," in 1983 EIC 6th Electrical/Electrical Insulation Conference, 1983, pp. 110-113.
- [10] "Technical data for winding wire, Available: <http://www.lww.se/wp-content/uploads/2017/06/LWW-brochure-2016.pdf>," ed, 2016.
- [11] "Litz Wire," ed., Available: <https://www.packlitzwire.com/products/litz-wires/rupalit-safety>

- [12] P. Mellor, R. Wrobel, and N. Simpson, "AC losses in high frequency electrical machine windings formed from large section conductors," in 2014 IEEE Energy Conversion Congress and Exposition (ECCE), 2014, pp. 5563-5570.
- [13] D. Gerada, A. Mebarki, N. L. Brown, C. Gerada, A. Cavagnino, and A. Boglietti, "High-Speed Electrical Machines: Technologies, Trends, and Developments," *IEEE Transactions on Industrial Electronics*, vol. 61, no. 6, pp. 2946-2959, 2014.
- [14] D. Gerada et al., "Holistic electrical machine optimization for system integration," in 2017 IEEE 3rd International Future Energy Electronics Conference and ECCE Asia (IFEEC 2017 - ECCE Asia), 2017, pp. 980-985.
- [15] A. M. EL-Refaie, "Fractional-Slot Concentrated-Windings Synchronous Permanent Magnet Machines: Opportunities and Challenges," *IEEE Transactions on Industrial Electronics*, vol. 57, no. 1, pp. 107-121, Jan 2010.
- [16] R. Wrobel, P. H. Mellor, and D. Holliday, "Thermal Modeling of a Segmented Stator Winding Design," *IEEE Transactions on Industry Applications*, vol. 47, no. 5, pp. 2023-2030, 2011.
- [17] D. Bauer, P. Mamuschkin, H. Reuss, and E. Nolle, "Influence of parallel wire placement on the AC copper losses in electrical machines," in 2015 IEEE International Electric Machines Drives Conference (IEMDC), 2015, pp. 1247-1253.
- [18] I. Petrov, M. Polikarpova, P. Ponomarev, P. Lindh, and J. Pyrhönen, "Investigation of additional AC losses in tooth-coil winding PMSM with high electrical frequency," in 2016 XXII International Conference on Electrical Machines (ICEM), 2016, pp. 1841-1846.
- [19] P. Arumugam, "Design and modelling of permanent magnet machine's windings for fault-tolerant applications," University of Nottingham, 2013.
- [20] U. K. Advanced Propulsion Centre, "THE ROADMAP REPORT, Towards 2040: A Guide to Automotive Propulsion Technologies, Available: <https://www.apcuk.co.uk/app/uploads/2018/06/roadmap-report-26-6-18.pdf>," ed, 2018.
- [21] Benhaddadi et al., "Electric Machines and Drives," InTech: Rijeka, Croatia 2011, Available: <http://www.intechopen.com/download/pdf/14083>.

- [22] "GE Industrial Systems. 2002. Evaluation and application of energy efficient motors. Whitepaper publication number: e-GEA-M1019. [http://www.geindustrial.com/publibrary/checkout/e-GEA-M1019?TNR=White Papers|e-GEA-M1019|generic](http://www.geindustrial.com/publibrary/checkout/e-GEA-M1019?TNR=White%20Papers|e-GEA-M1019|generic)," 2002.
- [23] A. E. Fitzgerald, *Electric machinery* / A.E. Fitzgerald, Charles Kingsley, Jr., Stephen D. Umans, 6th ed. ed. (McGraw-Hill series in electrical engineering. Power and energy). Boston, Mass., 2003.
- [24] J. Pyrhonen, *Design of rotating electrical machines* / Juha Pyrhönen, Tapani Jokinen, Valéria Hrabovcová, Second edition. ed. 2014.
- [25] M. N. O. Sadiku, *Elements of electromagnetics* / Matthew N.O. Sadiku, 7th ed. ed. (Oxford series in electrical and computer engineering). New York; Oxford: Oxford University Press, 2018.
- [26] J. F. Gieras, *Permanent magnet motor technology: design and applications* / Jacek F. Gieras, 3rd ed. ed. Boca Raton, Fla., 2010.
- [27] M. G. MagNet Suite 7.8.3, "KB Article ID# MG601132," ed, 2018.
- [28] A. M. V.N. Mittle, *Design of Electrical Machines*. 2012.
- [29] M. Schiefer and M. Doppelbauer, "Indirect slot cooling for high-power-density machines with concentrated winding," in 2015 IEEE International Electric Machines Drives Conference (IEMDC), 2015, pp. 1820-1825.
- [30] M. van der Geest, H. Polinder, J. A. Ferreira, and D. Zeilstra, "Stator winding proximity loss reduction techniques in high speed electrical machines," in 2013 International Electric Machines Drives Conference, 2013, pp. 340-346.
- [31] A. Kampker, P. Burggräf, and C. Nee, "Costs, quality and scalability: Impact on the value chain of electric engine production," in 2012 2nd International Electric Drives Production Conference (EDPC), 2012, pp. 1-6.
- [32] M. Popescu and D. G. Dorrell, "Proximity Losses in the Windings of High Speed Brushless Permanent Magnet AC Motors with Single Tooth Windings and Parallel Paths," *IEEE Transactions on Magnetics*, vol. 49, no. 7, pp. 3913-3916, 2013.
- [33] H. M. Hamalainen, J. J. Pyrhonen, and J. Puranen, "Minimizing skin effect in random wound high-speed machine stator," in *IEEE EUROCON 2009*, 2009, pp. 752-757.
- [34] D. A. Gonzalez and D. M. Saban, "Study of the Copper Losses in a High-Speed Permanent-Magnet Machine with fForm-Wound Windings," *IEEE*

- Transactions on Industrial Electronics, vol. 61, no. 6, pp. 3038-3045, June 2014.
- [35] A. D. Podoltsev, I. N. Kucheryavaya, and B. B. Lebedev, "Analysis of effective resistance and eddy-current losses in multiturn winding of high-frequency magnetic components," *IEEE Transactions on Magnetics*, vol. 39, no. 1, pp. 539-548, Jan 2003.
- [36] R. P. Wojda and M. K. Kazimierczuk, "Analytical Optimization of Solid-Round-Wire Windings," *IEEE Transactions on Industrial Electronics*, vol. 60, no. 3, pp. 1033-1041, March 2013.
- [37] P. H. Mellor, R. Wrobel, and N. McNeill, "Investigation of Proximity Losses in a High Speed Brushless Permanent Magnet Motor," in *Conference Record of the 2006 IEEE Industry Applications Conference Forty-First IAS Annual Meeting, 2006*, vol. 3, pp. 1514-1518.
- [38] C. R. Sullivan, "Optimal choice for number of strands in a litz-wire transformer winding," *IEEE Transactions on Power Electronics*, vol. 14, no. 2, pp. 283-291, March 1999.
- [39] J. Haldemann, "Transpositions in stator bars of large turbogenerators," *IEEE Transactions on Energy Conversion*, vol. 19, no. 3, pp. 553-560, Sept 2004.
- [40] J. Gyselinck, P. Dular, N. Sadowski, P. Kuo-Peng, and R. V. Sabariego, "Homogenization of Form-Wound Windings in Frequency and Time Domain Finite-Element Modeling of Electrical Machines," *IEEE Transactions on Magnetics*, vol. 46, no. 8, pp. 2852-2855, Aug 2010.
- [41] H. Hämäläinen, J. Pyrhönen, J. Nerg, and J. Talvitie, "AC Resistance Factor of Litz-Wire Windings Used in Low-Voltage High-Power Generators," *IEEE Transactions on Industrial Electronics*, vol. 61, no. 2, pp. 693-700, Feb 2014.
- [42] X. Thang and C. R. Sullivan, "Stranded wire with uninsulated strands as a low-cost alternative to litz wire," in *IEEE 34th Annual Conference on Power Electronics Specialist, 2003. PESC '03, 2003*, vol. 1, pp. 289-295 vol.1.
- [43] X. Nan and C. R. Sullivan, "An Equivalent Complex Permeability Model for Litz-Wire Windings," *IEEE Transactions on Industry Applications*, vol. 45, no. 2, pp. 854-860, March 2009.
- [44] P. B. Reddy, T. M. Jahns, and T. P. Bohn, "Transposition effects on bundle proximity losses in high-speed PM machines," in *2009 IEEE Energy Conversion Congress and Exposition, 2009*, pp. 1919-1926.

- [45] M. van der Geest, H. Polinder, J. A. Ferreira, and D. Zeilstra, "Current Sharing Analysis of Parallel Strands in Low-Voltage High-Speed Machines," *IEEE Transactions on Industrial Electronics*, vol. 61, no. 6, pp. 3064-3070, June 2014.
- [46] F. Birnkammer, J. Chen, D. B. Pinhal, and D. Gerling, "Influence of the Modeling Depth and Voltage Level on the AC Losses in Parallel Conductors of a Permanent Magnet Synchronous Machine," *IEEE Transactions on Applied Superconductivity*, vol. 28, no. 3, pp. 1-5, April 2018.
- [47] Chetvorno, "Proximity effect," Available: [https://upload.wikimedia.org/wikipedia/commons/9/9b/Proximity\\_effect.svg](https://upload.wikimedia.org/wikipedia/commons/9/9b/Proximity_effect.svg)," ed: WikiMedia Commons, 2017.
- [48] P. B. Reddy, Z. Q. Zhu, S. H. Han, and T. M. Jahns, "Strand-level proximity losses in PM machines designed for high-speed operation," in 2008 18th International Conference on Electrical Machines, 2008, pp. 1-6.
- [49] P. B. Reddy, T. M. Jahns, and T. P. Bohn, "Modeling and analysis of proximity losses in high-speed surface permanent magnet machines with concentrated windings," in 2010 IEEE Energy Conversion Congress and Exposition, 2010, pp. 996-1003.
- [50] M. Klauz and D. G. Dorrell, "Eddy Current Effects in a Switched Reluctance Motor," *IEEE Transactions on Magnetics*, vol. 42, no. 10, pp. 3437-3439, Oct 2006.
- [51] M. Spang and M. Albach, "Optimized Winding Layout for Minimized Proximity Losses in Coils With Rod Cores," *IEEE Transactions on Magnetics*, vol. 44, no. 7, pp. 1815-1821, July 2008.
- [52] R. Wrobel, A. Mlot, and P. H. Mellor, "Contribution of End-Winding Proximity Losses to Temperature Variation in Electromagnetic Devices," *IEEE Transactions on Industrial Electronics*, vol. 59, no. 2, pp. 848-857, Feb 2012.
- [53] S. Iwasaki, R. P. Deodhar, Y. Liu, A. Pride, Z. Q. Zhu, and J. J. Bremner, "Influence of PWM on the Proximity Loss in Permanent-Magnet Brushless AC Machines," *IEEE Transactions on Industry Applications*, vol. 45, no. 4, pp. 1359-1367, 2009.
- [54] A. Fatemi, D. M. Ionel, N. A. O. Demerdash, D. A. Staton, R. Wrobel, and Y. C. Chong, "A computationally efficient method for calculation of strand

- eddy current losses in electric machines," in 2016 IEEE Energy Conversion Congress and Exposition (ECCE), 2016, pp. 1-8.
- [55] F. Jiancheng, L. Xiquan, B. Han, and K. Wang, "Analysis of Circulating Current Loss for High-Speed Permanent Magnet Motor," *IEEE Transactions on Magnetics*, vol. 51, no. 1, pp. 1-13, Jan 2015.
- [56] A. Lehikoinen and A. Arkkio, "Efficient Finite-Element Computation of Circulating Currents in Thin Parallel Strands," *IEEE Transactions on Magnetics*, vol. 52, no. 3, pp. 1-4, March 2016.
- [57] A. Tessarolo, F. Agnolet, F. Luise, and M. Mezzarobba, "Use of Time-Harmonic Finite-Element Analysis to Compute Stator Winding Eddy-Current Losses Due to Rotor Motion in Surface Permanent-Magnet Machines," *IEEE Transactions on Energy Conversion*, vol. 27, no. 3, pp. 670-679, 2012.
- [58] H. Rossmanith, M. Doebroenti, M. Albach, and D. Exner, "Measurement and Characterization of High Frequency Losses in Nonideal Litz Wires," *IEEE Transactions on Power Electronics*, vol. 26, no. 11, pp. 3386-3394, Nov 2011.
- [59] P. B. Reddy and T. M. Jahns, "Analysis of bundle losses in high speed machines," in *The 2010 International Power Electronics Conference - ECCE ASIA -*, 2010, pp. 2181-2188.
- [60] M. Vetuschi and F. Cupertino, "Minimization of Proximity Losses in Electrical Machines With Tooth-Wound Coils," *IEEE Transactions on Industry Applications*, vol. 51, no. 4, pp. 3068-3076, July 2015.
- [61] P. Arumugam, "Design Optimization on Conductor Placement in the Slot of Permanent Magnet Machines to Restrict Turn–Turn Short-Circuit Fault Current," *IEEE Transactions on Magnetics*, vol. 52, no. 5, pp. 1-8, May 2016.
- [62] A. Lehikoinen, N. Chiodetto, E. Lantto, A. Arkkio, and A. Belahcen, "Monte Carlo Analysis of Circulating Currents in Random-Wound Electrical Machines," *IEEE Transactions on Magnetics*, vol. 52, no. 8, pp. 1-12, 2016.
- [63] J. Lähteenmäki, "Design and voltage supply of high-speed induction machines," ed, 2002, p. 140.
- [64] "PPA55xx User Manual" ed., Available: <https://www.newtons4th.com/wp-content/uploads/2014/07/PPA55xx-User-Manual2.pdf>

- [65] "Chroma Programmable AC Source 61511/61512 User's Manual" ed, 2009., Available: <https://www.chromausa.com/product/high-power-programmable-ac-source-61510/#Documentation>
- [66] "Slot Former Material - NanoCure RC25", ed, 2007, Available: <http://www.aytasarim.com/nano-cure-rc25.pdf>
- [67] "Precision Power Analyzers PPA55xx Series" ed, Available: [https://www.newtons4th.com/wp-content/uploads/2014/07/PPA45\\_5500-Brochure-July-2017-low-res-1.pdf](https://www.newtons4th.com/wp-content/uploads/2014/07/PPA45_5500-Brochure-July-2017-low-res-1.pdf)
- [68] K. E. Y. S. I. G. H. T. Technologies, "E4990A, Brochure, 5991-3888EN," ed., Available: <https://literature.cdn.keysight.com/litweb/pdf/5991-3888EN.pdf?id=2465255>
- [69] A. K. Steel, "DI-MAX HF-10 Cold Rolled Fully Processed Nonoriented Electrical Steel," ed., Available: [https://www.aksteel.com/sites/default/files/2018-01/dimaxhf10201204\\_1.pdf](https://www.aksteel.com/sites/default/files/2018-01/dimaxhf10201204_1.pdf)

# APPENDICES

## Appendix – A

Mesh condition in Finite – Element Simulations

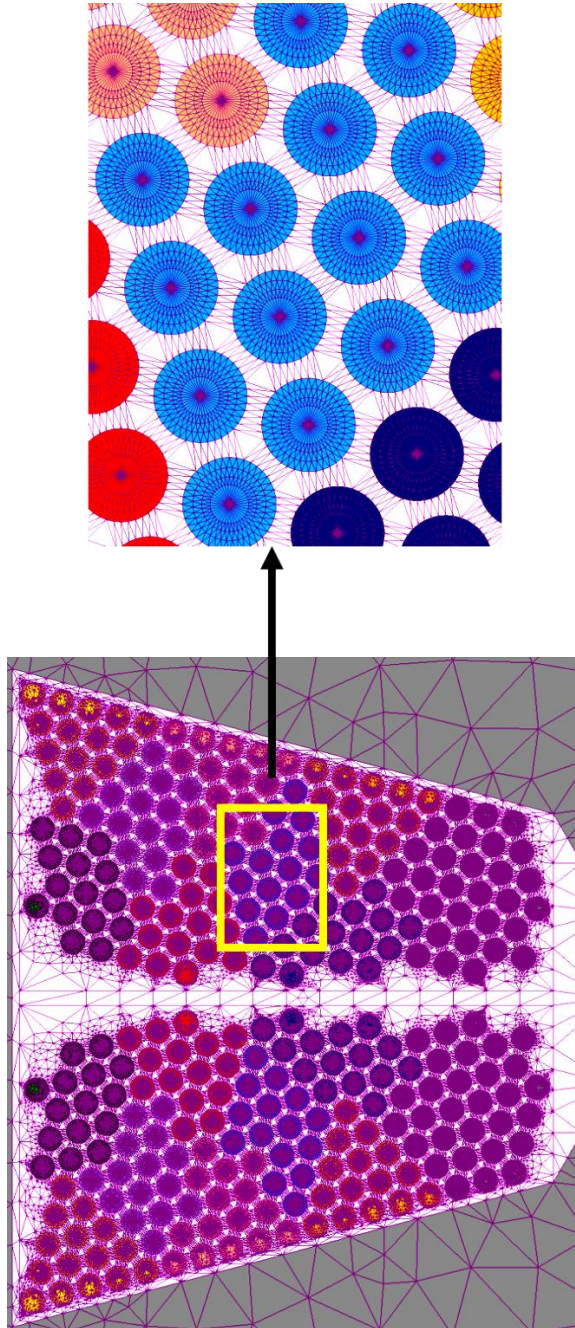


Fig. A1: Refined mesh in the strands of the FE models

## Appendix – B

### Calculation of DC resistance

Calculation of DC resistances of the components in the motorette 1, described in subsection 5.2.1.

Length of one coil,  $L_{coil} = 2330 \text{ m}$

Resistivity of copper at 20°C,  $\rho_{20} = 1.7953 \times 10^{-8}$

Temperature coefficient of copper,  $\alpha = 0.004041$

Using equation (2.7),  $\rho_{27} = 1.80907 \times 10^{-8}$

Area of conductor,

$$A_{con} = \pi \left( \frac{\text{strand diameter}}{2} \right)^2 \times (\text{parallel strands}) = 2.54469 \text{ mm}^2$$

$$R_{coil} = \rho_{27} \times \frac{L_{coil}}{A_{con}} = 0.01654 \Omega$$

$$R_{Total} = 2 \times R_{coil} = 0.033128 \Omega$$

Length of end winding + extension = Total length of coil – active length

Therefore, total endwinding+ extension resistance = 0.019593  $\Omega$

Length of supply cable from PPA to motorette = 1240 mm

Area = 4 mm<sup>2</sup>

$$R_{cable} = 5.61 \times 10^{-3} \Omega$$

## Appendix – C

### C 1. Specifications of Programmable AC power supply (chroma 61511)

*Programmable AC Source 61511/61512 User's Manual*

Model	61511	61512
<b>AC OUTPUT RATING</b>		
Single Phase Power	12K VA	18K VA
3-Phase Power	12K VA	18K VA
Power per Phase	4K VA	6K VA
<b>VOLTAGE</b>		
Range	150V/300V/Auto	
Output Voltage	0~150V / 0~300V	
Accuracy	0.2%+0.2%F.S.	
Resolution	0.1 V	
Distortion *1	0.3% @50/60Hz , 1%@15- 1KHz , 1.5%@>1KHz	
Line Regulation	0.1%	
Load Regulation *2	0.2%	
Temp. Coefficient	0.02% per degree from 25°C	
<b>MAXIMUM CURRENT (single phase)</b>		
RMS	96A / 48A	144A / 72A
Peak (CF=4)	384A / 192A	576A / 288A
<b>MAXIMUM CURRENT (each of 3-phase)</b>		
RMS	32A / 16A	48A / 24A
Peak (CF=4)	128A / 64A	192A / 96A
<b>FREQUENCY</b>		
Range	DC, 15-1.5KHz	
Accuracy	0.15%	
<b>PHASE ANGLE</b>		
Range	0 ~ 360°	
Resolution	0.3°	
Accuracy	<0.8°@50/60Hz	
<b>DC OUTPUT RATING (single phase)</b>		
Power	6K VA	9K VA
Voltage	212V / 424V	212V / 424V
Current	48A / 24A	72A / 36A
<b>DC OUTPUT RATING (each of 3-phase)</b>		
Power	2K VA	3K VA
Voltage	212V / 424V	212V / 424V
Current	16A / 8A	24A / 12A
<b>INPUT 3-PHASE RATING (per phase)</b>		
Power Type	3-phase, Delta or Y connection	
Voltage Range	190-250V (Delta: L-L, Y: L-N)	
Frequency Range	47-63 Hz	
Max. Current	Delta: 80A Y: 70A	Delta: 120A Y: 90A
<b>MEASUREMENT</b>		
<b>VOLTAGE</b>		
Range	150V / 300V	
Accuracy	0.2%+0.2%F.S.	
Resolution	0.1 V	

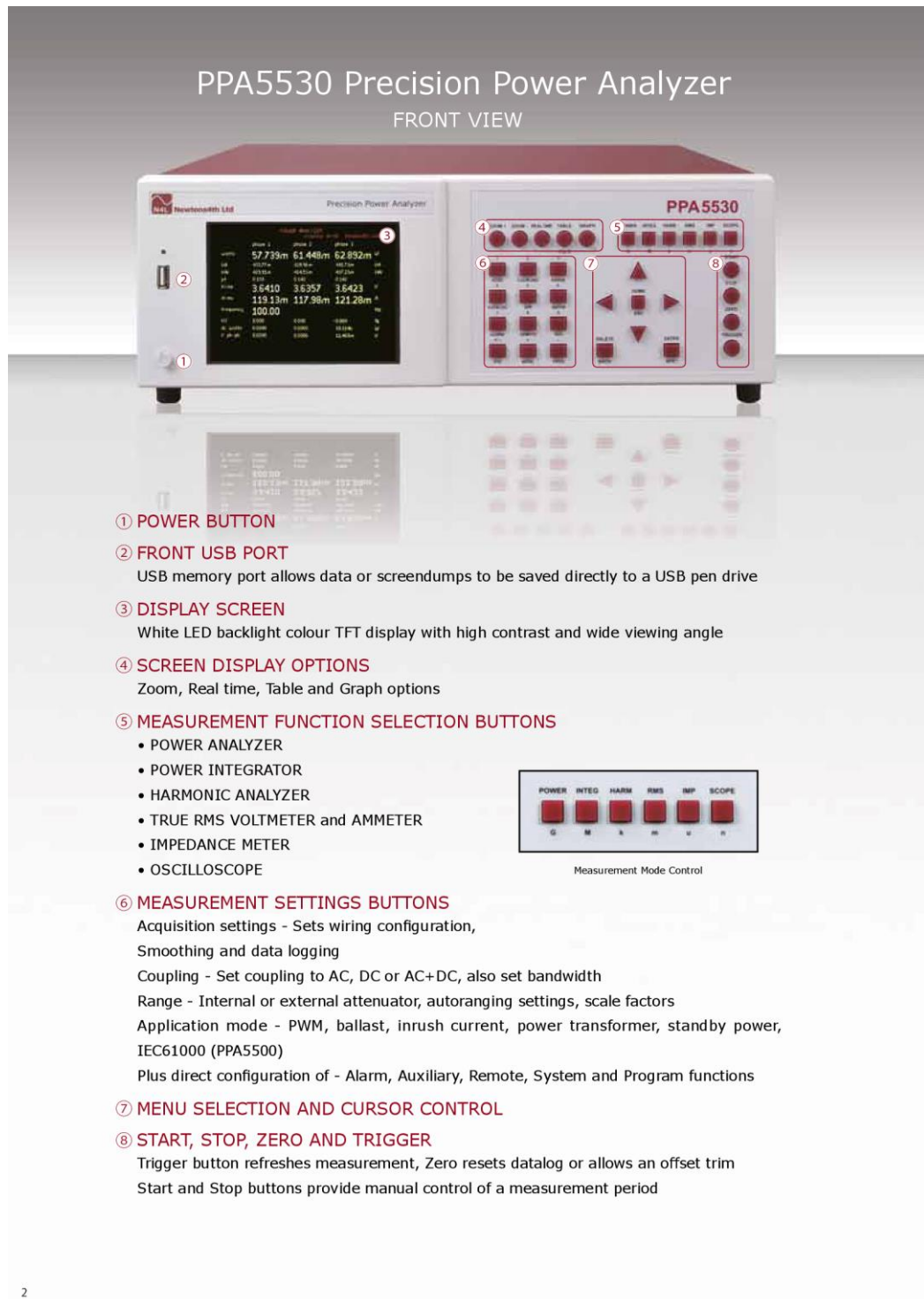
*General Information*

<b>CURRENT (per phase)</b>		
Range	8A/32A/128Apeak	12A/48A/192Apeak
Peak per Phase	128A	192A
Accuracy (rms)	0.4%+0.3% F.S.	
Accuracy (peak)	0.4%+0.6% F.S.	
Resolution	0.006A / 0.025A / 0.1A	
<b>POWER</b>		
Accuracy	0.4%+0.4% F.S.	
Resolution	0.1 W	
<b>OTHERS</b>		
Efficiency <sup>*3</sup>	0.75 (Typical)	
Size (H×W×D)	1163×546×700 mm 45.78×21.5×27.56 inch	1163×546×700 mm 45.78×21.5×27.56 inch
Weight	220 kg / 505.29 lbs	240 kg / 533.92 lbs
Protection	OVP, OCP, OPP, OTP, FAN-FAIL	
Remote Interface	GPIB, RS-232, USB, Ethernet	
<b>TEMPERATURE RANGE</b>		
Operation	0 °C to 40 °C	
Storage	-40 °C to 85 °C	
Humidity	30 % to 90 %	
Safety & EMC	CE	

**Notes:**

- \*1 : Maximum distortion is tested under output 125VAC (150V RANGE) and 250VAC (300V RANGE) with maximum current to linear load.
- \*2 : Load regulation is tested by sine wave and remote sense.
- \*3 : Efficiency is tested on input voltage: 230V.

## C 2. Specification of Precision Power Analyzer (PPA 5530) [67]





### C 3. Wiring configuration of PPA 5530

Wiring configuration of PPA5530 [66]

#### PPA55xx "KinetiQ" user manual

## 8 Measurement options

### 8.1 Wiring configuration

The three phase version of KinetiQ, the PPA5530, can be used in a variety of wiring configurations. Other versions, PPA5520 and PPA5510, accept a subset of these configurations:

configuration	5530	5520	5510
single phase 1	✓	✓	✓
2 phase	✓	✓	
3 phase 2 wattmeter	✓	✓	
3 phase 3 wattmeter	✓		
single phase 2	✓	✓	
single phase 3	✓		
3 phase 2 wattmeter + phase 3	✓		

In the single phase modes (phase 1, phase 2, phase 3) the other phase inputs are completely ignored and the selected phase acts as a completely independent single phase power analyser.

In the 3 phase 2 wattmeter configuration, the voltages are measured relative to phase 3. The phase 1 voltage input is connected across phase 1 and phase 3, and phase 2 voltage input is connected across phase 2 and phase 3, thus measuring phase to phase voltage directly. Phase 1 and 2 current inputs are connected normally. There is no need to measure the current in phase 3 as phase 3 has no voltage relative to itself so the power contribution is zero. In this mode, the neutral channel displays the synthesised phase 3 current.

## PPA55xx "KinetiQ" user manual

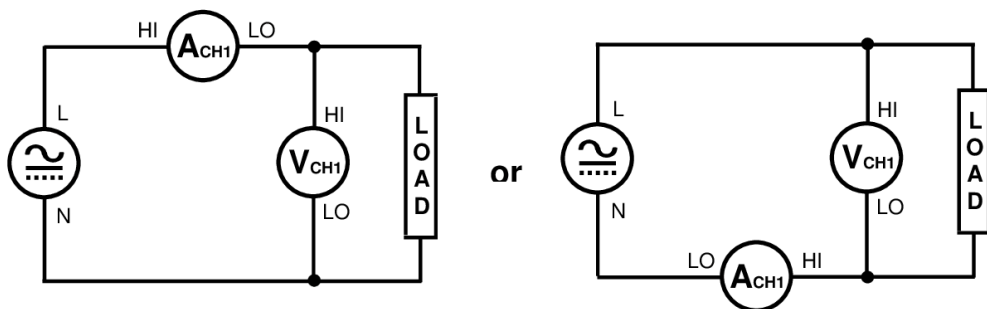
The advantage of this connection method is that 3 phase power can be measured with only 2 wattmeters. This frees up phase 3 of a 3 phase instrument to simultaneously measure the power of a single phase input (3 phase 2 wattmeter + phase 3 configuration). This allows direct measurement of efficiency in a 3 phase motor drive or 3 phase inverter application. The frequency reference for the independent phase 3 may be selected to be voltage, current, the mains line frequency, or the same as phase 1 & 2. In this mode, frequencies up to 1kHz can be measured with phase 3.

With the 3 phase 3 wattmeter configuration, each measurement phase is connected to a phase of the load with the voltage inputs measuring to neutral. In this mode, phase to neutral voltages are measured directly and phase to phase voltages are also computed.

The wiring configuration is the first item to be selected under the ACQU menu.

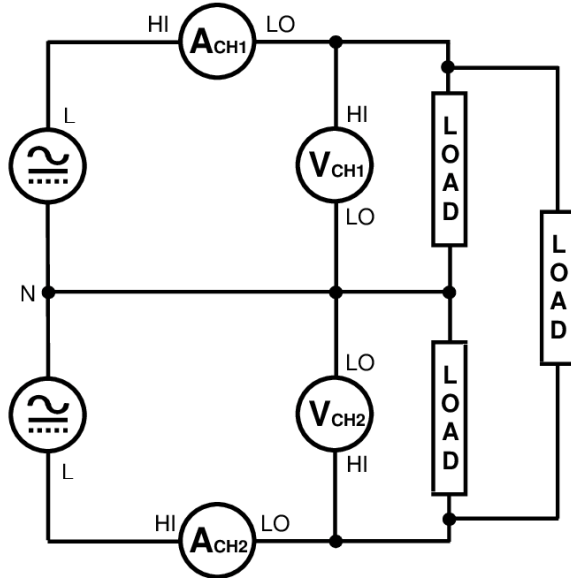
## 8.1.1 Wiring diagrams

## Single Phase

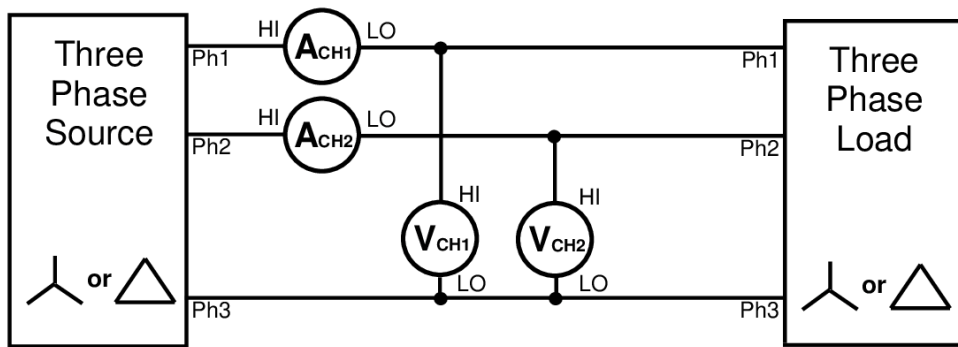


PPA55xx "KinetiQ" user manual

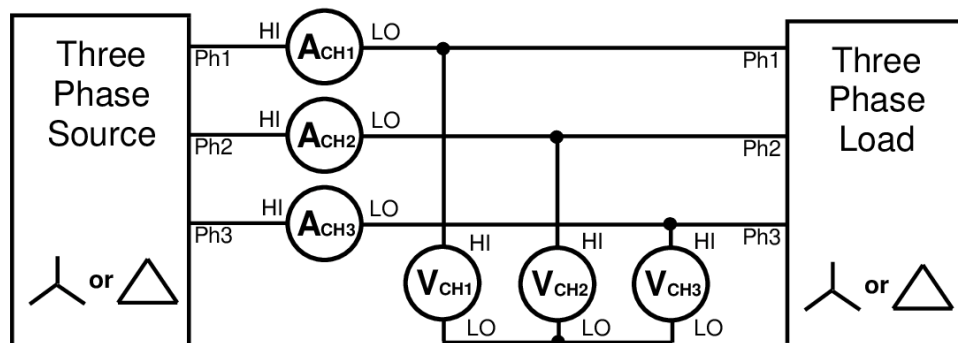
Two Phase Two Wattmeter



Three Phase Two Wattmeter

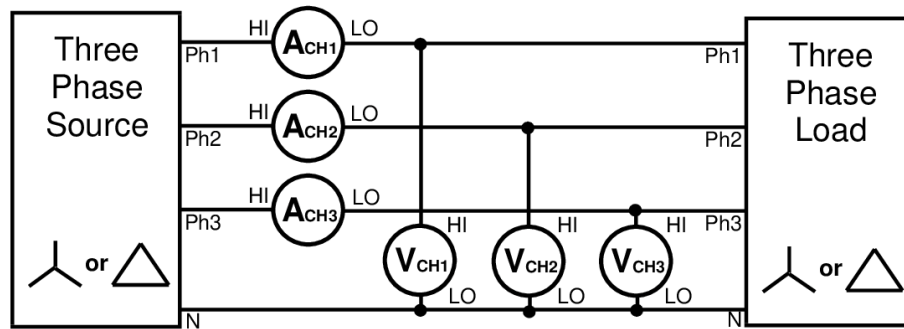


Three Phase Three Wattmeter - simulated neutral

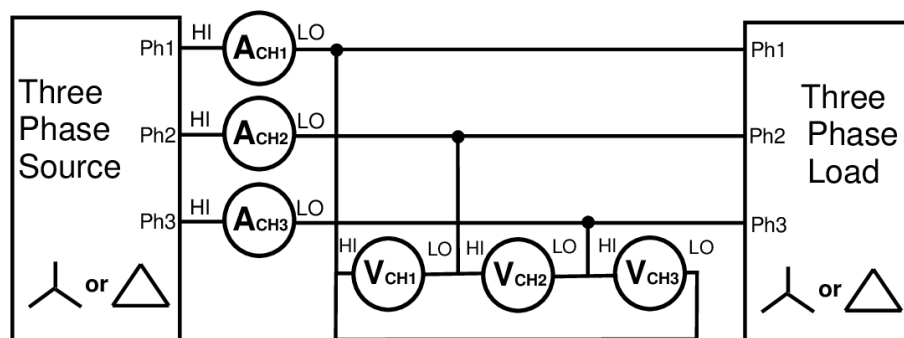


## PPA55xx "KinetiQ" user manual

## Three Phase Three Wattmeter – Star Connections



## Three Phase Three Wattmeter– Delta Connections



On a multi phase instrument all the phases usually use the same input control data – internal/external, scaling factor etc. It is possible to select "independent" so that the phases can be set up differently. This is useful if different scaling factors are required for external shunts or if one phase is using internal shunt when others are external.

## C 4. Specification of Precision Impedance Analyzer (KEYSIGHT E4990A)

### Keysight E4990A Impedance Analyzer

The E4990A impedance analyzer has a frequency range of 20 Hz to 120 MHz. The E4990A provides an industry best 0.045% (typical) basic accuracy over a wide impedance range with a 40 V built-in DC bias source. The equivalent circuit analysis function supports seven different multi-parameter models and helps you to simulate your own equivalent parameter values of components.

Five frequency options (20 Hz to 10/20/30/50/120 MHz) and frequency upgrades allow you to choose the most appropriate option with the least amount of investment.

The E4990A supports a variety of test accessories that are designed to make measurements simple and reliable.

Whether you are in R&D, QA, or inspection, the E4990A is an ideal solution for characterizing and evaluating electronic components, semiconductor devices, and materials.

#### Application examples

##### Passive components

Impedance measurement of capacitors, inductors, ferrite beads, resistors, transformers, or crystal/ceramic resonators

##### Semiconductor components

C-V characteristics analysis of varactor diodes. Impedance evaluation of diodes, transistors, amplifiers, or MEMS.

##### Other components

Impedance evaluation of components on printed circuit boards.

##### Materials measurements

Dielectric and magnetic materials can be measured on the E4990A up to 120 MHz with the appropriate fixtures. The N1500A Option 005/006 provides versatile materials measurements using the 16451B, 16452A and 16454A fixtures. The easy-to-use user interface for calibration, limit test, and report generation functions assure comprehensive and accurate measurements on the E4990A. The N1500A software can run either on E4990A or an external PC.



### Summary of Key Specifications

Operating frequency	20 Hz to 10/20/30/50/120 MHz (Option 010/ 020 /030/ 050/120 respectively)
Measurement parameters	Z ,  Y , q, R, X, G, B, L, C, D, Q, Complex Z, Complex Y, Vac, Iac, Vdc, Idc
Basic impedance accuracy	± 0.08% (typical ± 0.045%)
Q accuracy	± 3% (typical) at Q = 100, frequency ≤ 10 MHz
Impedance range	25 mΩ to 40 MΩ (10% accuracy)
Measurement time <sup>1</sup>	3 msec/point at Option 120, and 010/020/030/050 with Option 001, frequency ≥ 100 kHz, measurement time = 1 (fast)
Measurement type	Four-terminal-pair measurement (standard) 7-mm 1-port measurement with 42942A measureable grounded devices <sup>2</sup> Impedance probe measurement with 42941A measureable grounded devices <sup>2</sup>
Voltage/current signal level	5 mVrms to 1 Vrms /200 μArms to 20 mArms, 1 mV/20 μA resolution
DC bias	0 to ± 40 V± 100 mA, 1 mV/40 μA resolution
Auto level control (ALC)	Signal level voltage/current, DC bias voltage/current
Sweep parameters	Frequency, signal voltage/current, DC bias voltage/current
Sweep type	Linear frequency, log frequency, linear signal level, linear DC bias, log DC bias, segment
Number of measurement points	2 to 1601
Number of channels/traces	4-channel/4-trace
Marker	10 independent markers per trace, delta marker, marker search, marker analysis
Data analysis	Equivalent circuit analysis, limit line test
Interface	USB (front 2, rear 4), LAN, USBTMC, GPIB, 24 bit I/O
Display	10.4 inch TFT color LCD with touch screen

- Option 001 is available with the E4990A-010, 020, 030, 050 only.
- Option 120 only.

Fig. C1: KEYSIGHT Impedance Analyzer (E4990A) [68]

## Appendix – D

Specification of material used for motorette stator core [69].



**DI-MAX® HF-10** COLD ROLLED FULLY PROCESSED NONORIENTED ELECTRICAL STEEL

### SPECIFICATIONS

#### COMPOSITION (typical)

2.65% Si, 0.70% Al

#### GUARANTEED MAXIMUM AND TYPICAL MAGNETIC PROPERTIES

Release grading is based on as-sheared Epstein test and based on core loss at 1.0 T and 400 Hz in accordance with ASTM A343 (reference data at frequencies above 400 Hz were developed in conformance with ASTM A348). Representative properties using stress relief annealing are shown for reference.

#### CORE LOSS

	Typical	Maximum
As-Sheared	14.5 W/kg (6.6 W/lb)	15.5 W/kg (7.0 W/lb)
After 830 °C SRA	13.7 W/kg (6.2 W/lb)	14.5 W/kg (6.6 W/lb)

#### OTHER MAGNETIC PROPERTIES\*

Magnetic Induction at 5000 A/m	1.65 T
Volume Resistivity	54 - 56 µhm-cm
Saturation Induction	1.99 T

#### INSULATIVE COATING

Type	ASTM A976 C-5
Components	Aluminum phosphate, inorganic silicate fillers, acrylic resin
Thickness*	2.5 - 2.8 µm (100 - 110 µin)
Space factor	Minimum 95.0%
	Typical 96.5%
Franklin Current	Maximum 0.30 A
	Typical 0.02 A
Weldability	Good (minimal porosity)

A976 C-5-A type (CARLITE® 3 ANTI-STICK™ Electrical Steel) is available upon request

#### MECHANICAL AND PHYSICAL PROPERTIES

Density	7.65 gm/cm <sup>3</sup>
Yield Strength*	350 MPa (50,000 psi)
Tensile Strength*	450 MPa (65,000 psi)
Elongation, % in 2"	20%
Hardness, Rockwell B*	78
Thickness Aim	0.25 mm (0.010 in)
Tolerance	±0.02 mm (±0.00075 in)
Strip Crown*	0.005 - 0.006 mm (0.00020 - 0.00025 in)

Density determination conducted in compliance with ASTM A34. Typical mechanical and physical properties as noted.

\*Typical values


**DI-MAX® HF-10** COLD ROLLED FULLY PROCESSED NONORIENTED ELECTRICAL STEEL

## CORE LOSS AND EXCITING POWER TABLES AS-SHEARED

Flux Density (T)	CORE LOSS (W/kg) @ Frequency (Hz) - ASTM A343; ASTM A348; 50/50; As-Sheared										
	50	60	100	200	400	700	1000	1500	2500	5000	10000
0.1	0.0123	0.0151	0.0271	0.0648	0.17	0.396	0.699	1.36	3.23	10.4	32.7
0.2	0.0556	0.0683	0.123	0.289	0.736	1.66	2.86	5.43	12.4	37.5	113.0
0.4	0.205	0.252	0.46	1.09	2.78	6.23	10.6	19.8	43.8	128.0	395.0
0.7	0.528	0.651	1.20	2.91	7.55	17.1	29.4	55.3	125.0	380.0	
1.0	0.972	1.20	2.22	5.43	14.4	33.4	58.3	112.0	265.0	842.0	
1.2	1.38	1.71	3.16	7.7	20.4	48.3	85.2	168.0			
1.3	1.66	2.05	3.78	9.18	24.3	56.9	101.0	200.0			
1.4	2.02	2.49	4.58	11.1	29.0						
1.5	2.45	3.03	5.53	13.3	35.0						
1.6	2.87	3.54	6.47	15.5	40.1						
1.7	3.25	4.00	7.23	17.1							

Flux Density (T)	EXCITING POWER (VA/kg) @ Frequency (Hz) - ASTM A343; ASTM A348; 50/50; As-Sheared										
	50	60	100	200	400	700	1000	1500	2500	5000	10000
0.1	0.0498	0.06	0.101	0.207	0.433	0.809	1.24	2.06	4.09	12.5	36.8
0.2	0.143	0.173	0.294	0.617	1.34	2.62	4.14	7.12	14.7	43.2	126.0
0.4	0.389	0.471	0.811	1.75	3.97	8.07	13.1	23.0	48.4	143.0	432.0
0.7	0.905	1.10	1.90	4.16	9.72	20.4	33.8	61.0	134.0	425.0	
1.0	1.76	2.13	3.67	7.98	18.6	39.7	66.7	124.0	285.0	965.0	
1.2	2.94	3.55	6.06	12.9	29.1	61.0	102.0	190.0			
1.3	4.31	5.20	8.79	18.3	39.9	81.5	133.0	242.0			
1.4	8.32	10.0	16.7	34.1	71.2						
1.5	24.2	29.4	49.0	98.6	203.0						
1.6	68.2	82.5	137.0	276.0	574.0						
1.7	150.0	181.0	301.0	604.0							



**DI-MAX® HF-10** COLD ROLLED FULLY PROCESSED NONORIENTED ELECTRICAL STEEL

**D-C MAGNETIZATION CURVE - AS-SHEARED**

